Quantum Vector Magnetometry based on the Voigt Effect

Tadas Pyragius

Advisor: Dr. Thomas Fernholz

Department of Physics & Astronomy

University of Nottingham

A thesis submitted in partial fulfilment
of the requirements for the degree of

Doctor of Philosophy

January 22, 2020

Aušrai ir Andriui.

Abstract

Magnetism plays a fundamental role in nature existing in almost every conceivable domain of the physical world ranging from stars and planets to our brains and hearts. Some magnetic phenomena are easy to observe and measure, whilst others are small and subtle making them almost impossible to detect. Developments in precision magnetometry, utilising the quantum nature of atoms has given access to the world of small and subtle enabling the understanding of such signals as well as pushing the boundaries of knowledge of the fundamental forces of nature. In this thesis we describe theoretical and experimental methods to dispersively detect all three vector components of an external magnetic field using radio-frequency dressed alkali atoms based on the Voigt effect. To achieve this, we measure the linear birefringence of the radio frequency dressed atomic medium via polarization homodyning. This gives rise to modulated polarization signals at the first and second harmonic of the dressing frequency. The vector components of the external magnetic field are mapped onto the quadratures of these harmonics. Our scheme requires only one frequency of modulation and has a simple single axis beam geometry making it advantageous for miniature magnetic field sensors. Furthermore, we extend our Voigt effect scheme to dressed microwave spectroscopy and show that it can be used to infer the prepared state populations paving the way towards partial quantum state tomography.

Contents

Chapter 1

Introduction

1.1 Review of Optically Pumped Magnetometry

The phenomena of light-matter interaction in the presence of magnetic fields have been known and studied since the beginning of modern physics [1]. The two most well known of these so-called magneto-optical interactions are the Faraday and the Voigt effects. In the Faraday effect, the light-matter interaction results in a rotation of the polarisation of light in the presence of a longitudinal magnetic field while for the Voigt effect, the polarisation rotation occurs in the presence of a transverse field. In both cases the magnitude of the angular rotation depends on the magnitude of the external magnetic field and occurs as a consequence of phase shifts experienced by the different polarisations of the probe light. Magneto optical effects have been exploited extensively in commercial optical isolators utilising the Faraday effect. They rely on solid state based materials such as flint glass which posses a typical Verdet constant $V \approx 3 \times 10^{-5}$ rad $\mathrm{G}^{-1}\mathrm{cm}^{-1}$ which describes the amount of polarisation rotation per unit field and length [2]. The pioneering work in optical pumping of alkali atoms has enabled access to precisely control and enhance optical properties of vapour based systems with non-linear magneto optical rotations exceeding $V \approx 10^4$ rad $\mathrm{G}^{-1}\mathrm{cm}^{-1}$ [2–5]. This has spawned the field of optically pumped magnetometers. To put things into perspective, optically pumped rubidium vapour produces a factor 10^{20} larger rotation per atom compared to flint glass. With the advent of narrow-line frequency stabilised lasers and techniques to produce optically dense atomic vapours with long spin-coherence lifetimes it became possible to achieve magnetic field sensitivities exceeding 10^{-15} $\mathrm{T}/\sqrt{\mathrm{Hz}}$ [7, 8].

With such ultra-high levels of sensitivity, optically pumped magnetometers (OPMs) have become the state of the art magnetic field sensors out-competing other types of magnetic field sensing devices such as superconducting quantum interference devices

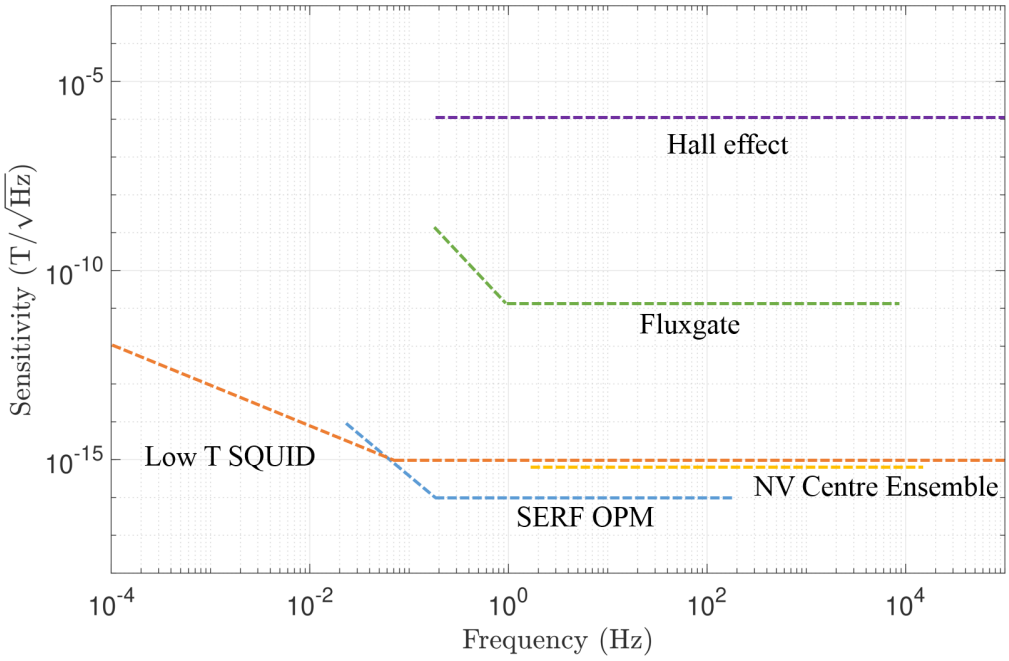

Figure 1.1: Typical noise performance and bandwidth characteristics of some magnetic field sensors. Low T SQUID - low temperature liquid helium cooled super conducting quantum interference device. SERF OPM - spin-exchange-relaxation-free optically pumped magnetometer.

(SQUIDs), Nitrogen Vacancy (NV) centres as well as the more conventional fluxgate and Hall effect based magnetometers, see Fig. 1.1 for performance [10]. Of course, the reasons behind such a huge interest in OPMs goes beyond their ultra-high sensitivity. One of the key advantages of OPMs over other devices is their simplicity and compactness making them ideal for making miniature and portable devices. Moreover, they can be tuned to work across a very large magnetic field range making them a very flexible tool across many disciplines, something that SQUID based sensors or fluxgate sensors would not be able to do. In addition, they can have a frequency independent gain meaning that they can reliably detect fields across a large range of frequencies - again, this is a major limitation in flux based magnetic field sensors. Often times, measurements of absolute fields require a precise calibration of the sensor which can be difficult and expensive to acquire, not to mention the fact that the architecture of some of the magnetic field sensors have dependence on the external environment (e.g. thermally induced drifts) which necessitates for repeated calibration a routine task. This is especially suboptimal in applications with remote sensing. The inherent advantage of OPMs is that they can be configured to measure the magnetic field through fundamental physical constants thus completely removing any need for calibration. These inherent advantages have ushered a new era of precision magnetic field sensing with extremely broad areas of applications ranging from fundamental

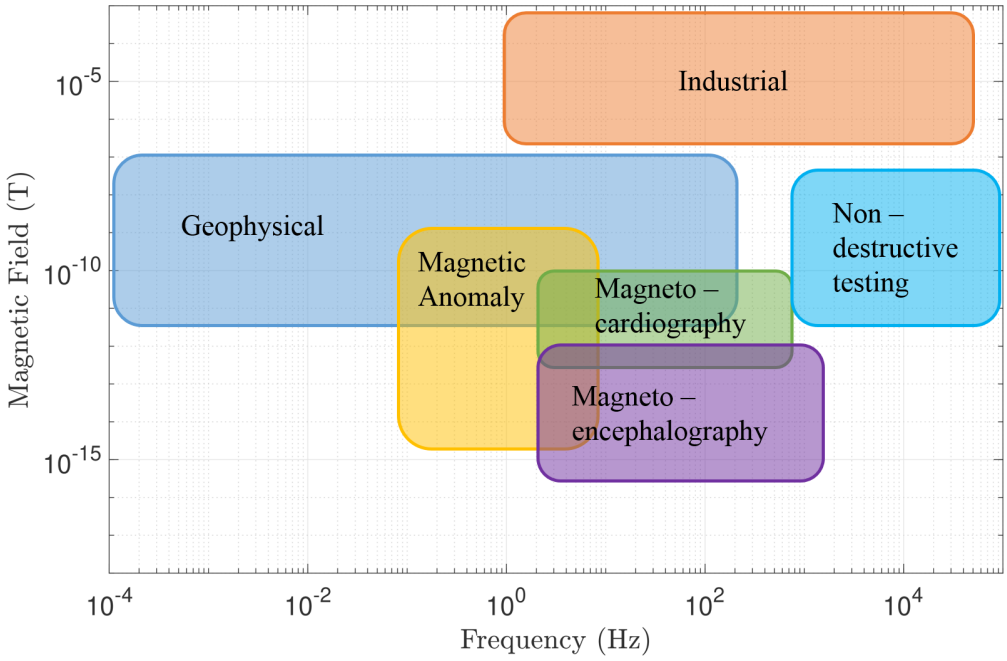

Figure 1.2: Field range and frequencies of various magnetic field phenomena. Adapted from [9].

physics experiments to medical physics. Examples include measurements of the electric dipole moment (EDM) [11, 12] and searches for exotic physics [13] as well as magneto-encephalography (MEG) [14, 15] and magneto-cardiography [16–18]. Some of the applications with field and frequency range are given in Fig. 1.2.

In its simplest operation, an OPM uses a pump-probe laser to measure the atomic Larmor frequency, i.e. the frequency of spin precession due to an external magnetic field. This is achieved by the probe light interacting with atoms that have been prepared in a magnetically sensitive state through optical pumping. The light-matter interaction between the probe light and the optically pumped atoms results in a magneto optical effect which rotates the polarisation of the probe beam i.e., the polarisation of the probe is modulated by the atomic Larmor precession which allows one to infer the external magnetic field by measuring this frequency. To date, most of the OPM schemes are based on pump-probe configurations that rely on measuring the Faraday effect. As a result, the majority of such schemes require an orthogonal pump-probe geometry for high efficiency of detection and typically enable the measurement of two orthogonal magnetic field components [19]. However, this geometry adds complexity towards developing miniature sensors, because it requires additional space for optical access to accommodate the orthogonal pump/probe beams. This makes the cell fabrication process complex, requiring precision glass blowing techniques which are difficult to realise on a large scale. On the other hand, a parallel pump/probe architecture is

compatible with chip-scale and compact atomic magnetometers, especially because the cells can be easily mass produced to a high degree of homogeneity through anodically bonded processes [20].

In some applications it may be desirable to be able to extract full vector field information. Some OPM schemes employ a scalar magnetometer that runs as a vector magnetometer by applying a rotating low frequency bias magnetic field [21, 22]. Another possible approach uses multiple radio-frequency modulations to map the three vector components onto the harmonics of the signal [23, 24]. The effects of the field orientation on the resulting signal phase have been studied for different configurations of a modulating field and may be used for full vector magnetometry [25]. Also an all-optical scheme with crossed beams was demonstrated to extract the three field components [26]. However, the schemes described above largely rely on measuring the Faraday effect which requires an orthogonal pump/probe beam geometry as well as multiple radio-frequency fields making the detection as well as the signal interpretation into its constituent field components not trivial.

1.2 Motivation

The motivation of this work has been a curiosity driven serendipitous scientific discovery. The first stage of this PhD program, was focused on theoretical and experimental work on dispersive detection of radio-frequency dressed clock-states using cold atomic gases of ^{87}Rb [27]. The primary motivation of this work was centred around non-destructive probing of atomic states and the measurement of their corresponding atomic populations for use in applications in atomic clock schemes as well as atom interferometers. The latter part is a key area of focus in our experimental research group developing matter-wave Sagnac interferometer [28, 29]. During the process of the experimental work undertaken to measure the populations of the clock states it was realised that vector information of the external field could be mapped onto the polarisation of the probe beam interacting with the dressed atoms. Follow up theoretical work allowed us to compute what the field response would be which was soon confirmed experimentally using cold atoms. A cold atomic system for measuring magnetic fields is not of practical use due to its complexity and size and limited bandwidth, as a result, this motivated us to build a hot vapour setup and investigate these ideas and observations further which ultimately led to this thesis.

The magnetometer described in this thesis is a Bell-Bloom type, free induction decay, three-dimensional vector magnetometer based on the Voigt effect of radio-frequency dressed aligned states [5, 6]. It operates in a pump/probe regime with a single radio-frequency field dressing the atomic medium. This gives rise to modulated polarisation signals at the first and second harmonic of the dressing frequency. The demodulation of the probe's ellipticity onto orthogonal quadratures of the first and second harmonic of the dressing frequency yields information about external magnetic fields, see Fig. 1.3. For small external fields, the field mapping is linear.

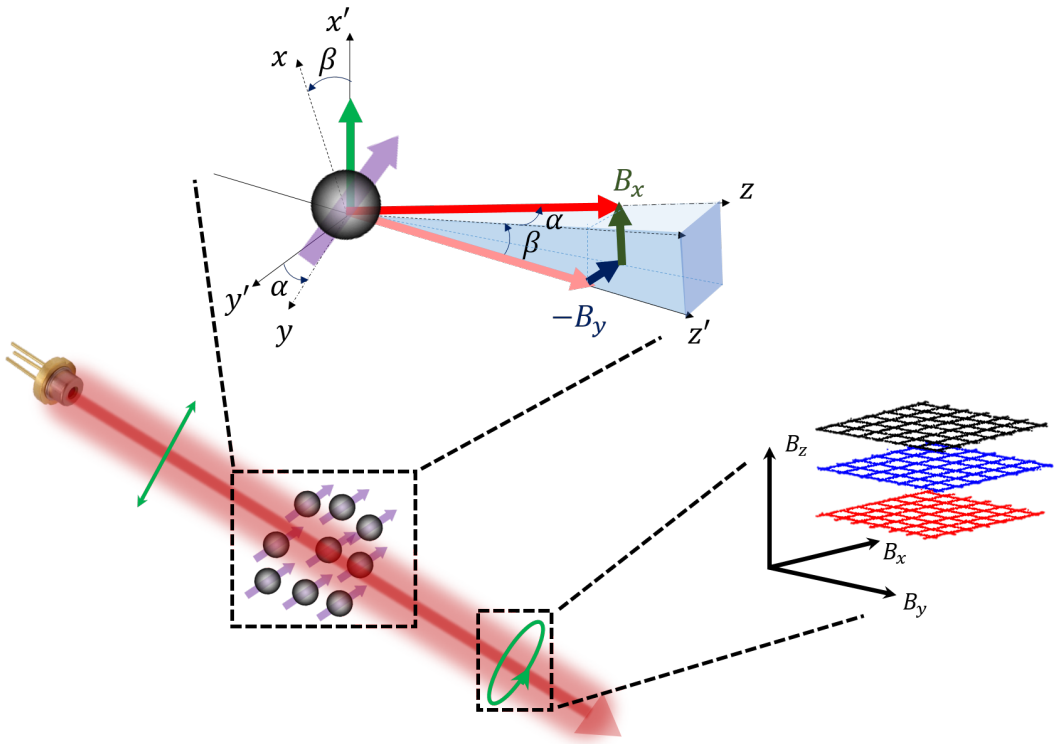

Figure 1.3: Illustration of the Voigt-effect based three-dimensional vector magnetometer. Atomic spin precession dressed with a radio-frequency field encodes the external field information onto the polarisation of light during the light-matter interaction. For small external magnetic fields, the polarisation rotation is linearly proportional to applied fields.

Actively driving the atoms with a radio-frequency field gives rise to a phase-locked spin precession resulting in low technical noise from the operation at radio-frequencies and the use of lock-in detection. Moreover, operating the magnetometer in a pump/probe regime, we are able to minimise pump induced light shifts and noise. Furthermore, a pump/probe architecture allows us to reset the spin state for each measurement point avoiding hysteresis in the system [30]. The probing is done with a low-power off-resonant probe beam to minimise spin-decoherence effects as a result of the measurement process. The radio-frequency dressing can be arbitrarily tuned providing a high dynamic range of operation both in shielded and unshielded environments with a flat frequency response. Finally, the single beam pump/probe geometry makes this sensor architecture ideal for miniaturisation.

This thesis is organised as follows:

Chapter 2 outlines the main theoretical ideas behind light-matter interaction in

off-resonant regime. In particular, it lays out the formalism of Stokes vectors to experimental observables and how they can be used to measure external magnetic fields through birefringent light-matter interactions. We discuss the scope and limitations of the proposed models as well as various optical broadening mechanisms pertinent in thermally broadened atomic vapours. We quantitatively discuss the state preparation process via optical pumping and the effects on the prepared state via the interaction with an off resonance probe.

Chapter 3 is devoted to a new and previously unexplored theoretical description of radio-frequency dressed states in an external magnetic field and how the resultant atomic spin dynamics measured via the Voigt effect maps the three vector components of the external field. The chapter discusses the various theoretical approaches used to model the magnetometer response with their scope and limitations. We further extend the theoretical work in showing how the Voigt effect signal can be used to perform partial state tomography using microwave spectroscopy.

Chapter 4 lays out the experimental apparatus, its intricacies and performance in terms of the laser system, optics, electronic and magnetic shielding hardware. Experimental sequence, data acquisition and processing methods are discussed in relation to magnetometer bandwidth, noise performance as well as the limitations.

Chapter 5 summarises the experimental results obtained in both unshielded and shielded operation of the magnetometer and compares them to the theoretical results. Scope and limitations are discussed in relation to the theory and experiment.

Chapter 6 concludes the thesis and where possible, provides an outlook on future work.

List of Publications

[I] S. Jammi, T. Pyragius, M. G. Bason, H. Marin Florez, T. Fernholz, *Dispersive detection of radio-frequency-dressed states*, Phys. Rev. A, **97**, 043416, (2018).

[II] T. Pyragius, H. Marin Florez, T. Fernholz, *Voigt-effect-based three-dimensional vector magnetometer*, Phys. Rev. A, **100**, 023416, (2019).

CHAPTER 2

Light-Matter interaction

This chapter outlines the theory of light matter interaction. In particular, the discussion centres around resonant and off-resonant light matter interactions in the context of optical pumping - during the state preparation process and dispersive light matter interaction - during probing of the prepared state. Attention is given to a number of optical broadening and decoherence mechanisms.

2.1 Stokes Variables

A common technique used to detect the atomic spin precession around an external magnetic field of an optically pumped magnetometer is by measuring the change in polarisation through the light-matter interaction [32]. This change in light polarisation can be conveniently parametrised using the Stokes vector formalism. This is achieved by decomposing the polarisation of light into its polarisation intensity components (see Fig. 2.1). For classical coherent and monochromatic light of intensity I, Stokes vector is given by

$$S_0 = \frac{1}{2} cn\epsilon_0 |E|^2 = I, \tag{2.1}$$

$$S_x = I_x - I_y, \tag{2.2}$$

$$S_y = I_{+45^\circ} - I_{-45^\circ}, \tag{2.3}$$

$$S_z = I_+ - I_-, \tag{2.4}$$

where c is the speed of light in vacuum, n is the refractive index of the medium, ϵ_0 is the permittivity of free space and E is the amplitude of the electric field. Here the I_i terms are the intensity decomposed polarisation components, see Fig. 2.1 for illustration. The Stokes vector satisfies

$$S_0^2 = S_x^2 + S_y^2 + S_z^2. \tag{2.5}$$

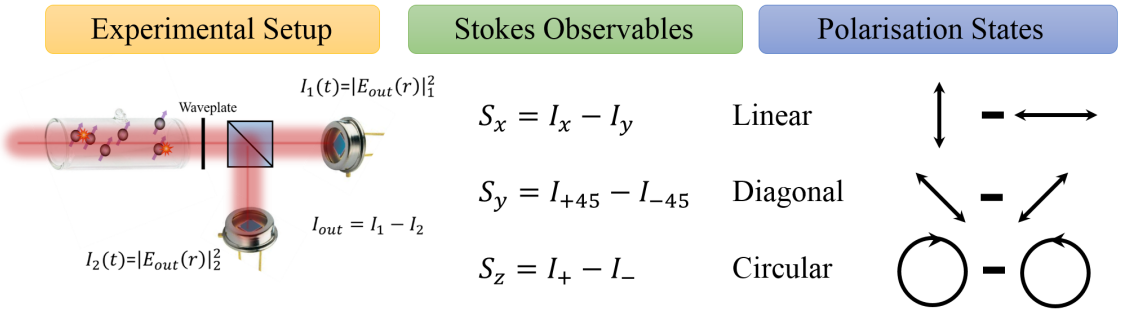

Figure 2.1: Light-matter interaction causes a polarisation rotation. The rotation in polarisation is analysed by decomposing the light into its constituent components using a waveplate and a polarising beam-splitter which allows us to measure Stokes vectors in terms of the intensity of the decomposed light polarisations.

In certain conditions, where for example quantum effects play a dominant role, the classical observables have to be appropriately transformed for a proper quantum mechanical treatment. This is readily achieved by applying the second postulate of quantum mechanics by replacing our classical observables with linear Hermitian operators. Here we follow a continuous description of electromagnetic fields previously described in ref. [33]. Since our Stokes vectors are defined in terms of light intensity, we can apply the second quantisation to the electric field

$$\hat{\mathbf{E}} = \sum_j (\hat{\mathcal{E}}_j + \hat{\mathcal{E}}_j^\dagger), \tag{2.6}$$

where the operators take the following form in the Fourier space (taking propagation only along the z-direction)

$$\hat{\mathcal{E}}_j(z,t) = g\mathbf{e}_j \frac{1}{\sqrt{2\pi}} \int \hat{a}_{k,j} e^{i(kz-\omega_L t)} dk, \tag{2.7}$$

where $\hat{a}_{k,j}$ is the lowering operator of the electromagnetic field in the second quantisation, $k = 2\pi/\lambda_L$ is the wave vector of the laser light with λ_L being the wavelength of the laser with

$$g = \sqrt{\frac{\hbar\omega_L}{2\epsilon_0 A}}, \tag{2.8}$$

where ω_L is the frequency of the monochromatic light source, A is the cross-sectional area of the atomic medium and ϵ_0 is the permittivity of free space. The quantity g, scales the field strength per photon, and $\mathbf{e}_j$ are unit polarisation vectors. Using the expressions above allows us to write the quantised electric field in terms of creation and annihilation operators

$$\hat{\mathbf{E}}_j(z,t) = g[\hat{a}_j(z,t)\mathbf{e}_j + \hat{a}_j^\dagger(z,t)\mathbf{e}_j^*], \tag{2.9}$$

where the commutation relations read

$$[\hat{a}_i(z,t), \hat{a}_j^\dagger(z,t')] = \delta_{i,j}\delta_z(z)\delta(t-t'). \tag{2.10}$$

Using the quantised expression for the electric field in eq. (2.9) and substituting it into eqns. (2.1)-(2.4) yields the quantum mechanical Stokes operators

$$\begin{pmatrix} \hat{S}_x \\ \hat{S}_y \\ \hat{S}_z \end{pmatrix} = \frac{c}{2} \begin{pmatrix} \hat{a}_x^\dagger \hat{a}_x - \hat{a}_y^\dagger \hat{a}_y \\ \hat{a}_{+45^\circ}^\dagger \hat{a}_{+45^\circ} - \hat{a}_{-45^\circ}^\dagger \hat{a}_{-45^\circ} \\ \hat{a}_+^\dagger \hat{a}_+ - \hat{a}_-^\dagger \hat{a}_- \end{pmatrix} = \frac{c}{2} \begin{pmatrix} \hat{a}_+^\dagger \hat{a}_- + \hat{a}_-^\dagger \hat{a}_+ \\ i\hat{a}_-^\dagger \hat{a}_+ - i\hat{a}_+^\dagger \hat{a}_- \\ \hat{a}_+^\dagger \hat{a}_+ - \hat{a}_-^\dagger \hat{a}_- \end{pmatrix}, \tag{2.11}$$

where we have defined

$$\hat{a}_{+,-} = \frac{1}{\sqrt{2}}(\hat{a}_x \mp i\hat{a}_y), \tag{2.12}$$

$$\hat{a}_{+45^\circ,-45^\circ} = \frac{1}{\sqrt{2}}(\pm\hat{a}_x + \hat{a}_y), \tag{2.13}$$

with $\hat{a}_{+45^\circ,-45^\circ}$, and $\hat{a}_{x,y}$ describing circular $\sigma^\pm$, linear $\pm 45^\circ$, and horizontal/vertical polarisations, respectively. In addition, the Stokes vector components obey commutation rules of angular momentum, i.e.,

$$[\hat{S}_i(t), \hat{S}_j(t')] = i\delta(t-t')\epsilon_{ijk}\hat{S}_k(t), \tag{2.14}$$

where ϵ_{ijk} is the Levi-Civita tensor

$$\epsilon_{ijk} = \begin{cases} +1 & \text{if } (i,j,k) \text{ is } (1,2,3),(2,3,1), \text{ or } (3,1,2), \\ -1 & \text{if } (i,j,k) \text{ is } (3,2,1),(1,3,2), \text{ or } (2,1,3), \\ 0 & \text{if } i=j, \text{ or } j=k, \text{ or } k=i. \end{cases} \tag{2.15}$$

2.2 Off-resonant light-matter interaction

2.2.1 Birefringence effects in light-matter interaction in the semi-classical limit

In general, the optical properties of a material are largely governed by their intrinsic electron energy level structure. For gaseous media, the effects of light-atom interaction are well described by the first order susceptibility $\chi^{(1)}$ with the real, $\mathrm{Re}[\chi^{(1)}]$ and imaginary parts $\mathrm{Im}[\chi^{(1)}]$ containing the response of the refractive index n and the coefficient of absorption α as a function of frequency of the applied field, respectively. In classical terms, an electromagnetic wave propagating through a homogeneous dielectric medium can be described by Maxwell's wave equation [34, 35]

$$c^2\nabla^2\vec{\mathbf{E}} = \frac{\partial^2\vec{\mathbf{E}}}{\partial t^2} + \frac{1}{\epsilon_0}\frac{\partial^2\vec{\mathbf{P}}}{\partial t^2}, \tag{2.16}$$

where $\vec{\mathbf{E}}$ is the electric field vector, $\vec{\mathbf{P}} = \epsilon_0\chi^{(1)}\vec{\mathbf{E}}$ is the polarisability vector, c is the speed of light in vacuum and ϵ_0 is the permitivity of free space. Considering a 3D case, the wave equation (2.16) has a general solution given by

$$\vec{\mathbf{E}} = \vec{\mathbf{E}}_0 e^{-\mathbf{k_I}\cdot\mathbf{r}} e^{i(\mathbf{k_R}\cdot\mathbf{r}-\omega_L t)}, \tag{2.17}$$

with $\mathbf{k_I}$ and $\mathbf{k_R}$ being the momentum propagation constants which relate to the complex refractive index $\tilde{\mathbf{n}}$ and further by the sum of ordinary refractive index $\mathbf{n_R}$ and the extinction coefficient $\mathbf{n_I}$ which is responsible for the absorption

$$\mathbf{k} = \mathbf{k_R} + \mathbf{k_I} = \frac{\omega_L}{c}\tilde{\mathbf{n}} = \frac{\omega_L}{c}(\mathbf{n_R} + i\mathbf{n_I}). \tag{2.18}$$

We can relate the first order susceptibility $\chi^{(1)}$ to the complex refractive index by the following relation [36]

$$\tilde{\mathbf{n}} = (\mathbf{n_R} + i\mathbf{n_I}) = \sqrt{1 + \chi^{(1)}}. \tag{2.19}$$

In the case where the light-matter interaction results in no light absorption (far off-resonant beam), we can neglect the contribution from $\mathbf{n_I} \approx 0$ and the resultant classical electromagnetic wave only experiences phase shifts which are dependent on the refractive index $\mathbf{n_R}$

$$\vec{\mathbf{E}} = \vec{\mathbf{E}}_0 e^{i(\mathbf{k_R}\cdot\mathbf{r} - \omega_L t)}. \tag{2.20}$$

If the polarisability of the dielectric medium is directional (i.e. anisotropic) due to $\chi^{(1)}$, then the different polarisations of the electromagnetic wave will experience phase shifts due to the fact that the refractive indices for the different polarisations are different. This phenomena is known as birefringence. Quantum mechanically, the atomic polarisability of the medium can be expressed using the density operator [37]

$$P_{ij} = N\vec{d}_{ij}\rho_{ij}, \tag{2.21}$$

where N is the atomic number density, $\vec{d}_{ij}$ is the transition dipole moment which depends on the Clebsch-Gordan coefficients [38]

$$\vec{d}_{ij} = \left\langle F_i, m_i \middle| \vec{d} \middle| F_j, m_j \right\rangle = (-1)^{F_i - m_i} \left\langle F_i \middle\| \vec{d} \middle\| F_j \right\rangle \begin{pmatrix} F_i & 1 & F_j \\ -m_i & q & m_j \end{pmatrix}, \tag{2.22}$$

where q corresponds to the polarisation state such that

$$q = \begin{cases} 0, & \pi\text{-polarisation}, \\ +1, & \sigma^+\text{-polarisation}, \\ -1, & \sigma^-\text{-polarisation}. \end{cases} \tag{2.23}$$

Using the classical definition of polarisability together with the quantum mechanical one, we can derive a semi-classical version of the first order susceptibility

$$\chi^{(1)} = \frac{1}{\Omega_{ij}}\frac{N}{\epsilon_0\hbar}d_{ij}^2\rho_{ij}, \tag{2.24}$$

where the Rabi frequency Ω_{ij} is given by

$$\Omega_{ij} = \frac{\vec{d}_{ij}\cdot\vec{\mathbf{E}}_0}{\hbar}. \tag{2.25}$$

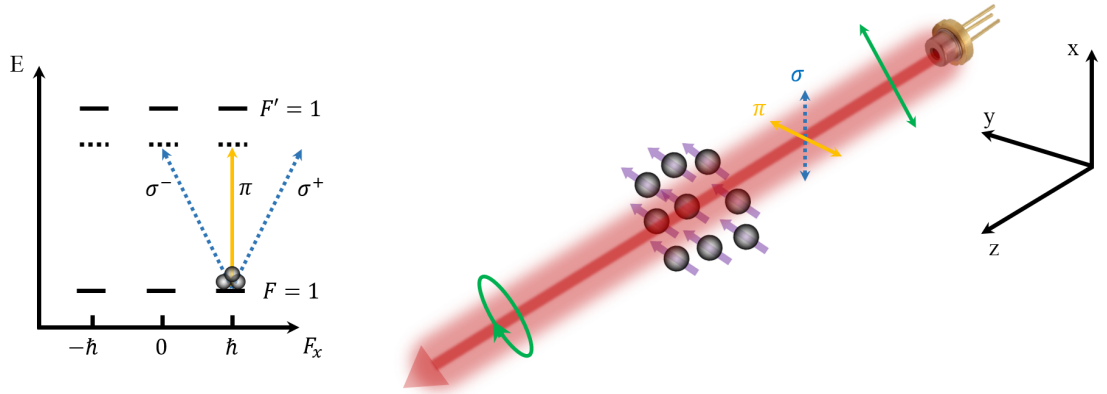

Figure 2.2: Phase shift of the polarisation as a consequence of the light-matter interaction. Here an off-resonant light beam of a well defined polarisation interacts with atoms prepared in a stretched state. The different polarisation components of the light have different Clebsch-Gordan coefficients and as a result, different refractive indices which introduce phase shifts in the polarisation during the light-matter interaction.

Combining equations (2.19) and (2.24) and assuming the limit of no absorption, the refractive index is given by

$$n_R^{ij} = \sqrt{1 + \frac{1}{\Omega_{ij}} \frac{N}{\epsilon_0 \hbar} d_{ij}^2 \rho_{ij}}. \tag{2.26}$$

From the equation above we can observe the following; different polarisations of light will yield different Clebsch-Gordan coefficients, and as a result, will give different refractive indices which will introduce phase shifts in the outgoing electromagnetic wave rotating the polarisation, Fig. 2.2 illustrates the basic principle schematically. For light of wavelength λ interacting with a birefringent sample of length l, the plane of polarisation between e.g. two circular components of light rotates by an angle ϕ given by [41]

$$\phi = (n_R^+ - n_R^-) \frac{\pi l}{\lambda}. \tag{2.27}$$

This naïve toy model is effective in giving a qualitative explanation of how the light-matter interaction results in phase shifts of the polarisation of light. However, it lacks descriptive power relating the effects to observable quantities such as the Stokes vectors. Moreover, the energy level structure of the atoms is in general complex, and as a result may have additional contributions to the polarisation phase shifts. Finally, our goal is to be able to encode the spin-magnetic field interaction onto the light matter interaction which would allows us to optically probe the local magnetic field information sensed by the atomic medium.

2.2.2 Birefringence effects in light-matter interactions in the quantum limit

In quantum mechanics, the general light-atom interaction Hamiltonian is given by the scalar product between the dipole transition moment operator $\hat{\mathbf{d}}$ and the quantised electric field

$$\hat{H}_E = -\hat{\mathbf{d}} \cdot \hat{\mathbf{E}}(z,t), \tag{2.28}$$

where as before, the electric field in the second quantisation reads

$$\hat{\mathbf{E}}(z,t) = \sum_j (\hat{\mathcal{E}}_j(z,t) + \hat{\mathcal{E}}_j^\dagger(z,t)). \tag{2.29}$$

Here we have explicitly considered the light propagation to be along z in one dimension [33]. In our case we are interested in describing light-matter interaction in the off-resonant regime where absorption of the fields can be neglected. As a result of this, the interaction reduces to spin and polarisation dependent dispersion, governed by the frequency dependent polarisability tensor $\hat{\boldsymbol{\alpha}}$ of the atomic medium. The interaction energy can be expressed as a second-order perturbation with state-dependent dipole density $\hat{\mathbf{d}}$, i.e., as a light-shift of atomic ground states. The effective Hamiltonian can be stated as [27, 38]

$$\hat{H}_{\text{eff}} = -\int (\hat{\mathcal{E}}^\dagger \hat{\boldsymbol{\alpha}} \hat{\mathcal{E}}) A dz = \sum_n \int \frac{\hat{\mathcal{E}}^\dagger \hat{\mathbf{d}}_n \hat{\mathbf{d}}_n^\dagger \hat{\mathcal{E}}}{\hbar \Delta_n} A dz, \tag{2.30}$$

where the sum is over the contributions from transitions to excited states with resonant frequencies ω_n and corresponding detunings $\Delta_n = \omega_L - \omega_n$. Here A is the cross-sectional area of the interaction medium. For alkali atoms in their electronic ground state, the atomic dipole moment depends on the individual spin $\hat{\mathbf{F}}_i$, which we describe by a continuous operator function $\hat{\mathbf{f}}(z)$ for dimensionless spin per atom. The collective spin of N atoms distributed over any finite length L with density $\rho(z)$ are expressed as

$$\sum_{i=1}^{N} \hat{\mathbf{F}}_i = \int_L \rho(z) \hat{\mathbf{f}}(z) \hbar A dz. \tag{2.31}$$

Using this description, the effective interaction Hamiltonian for an atomic (sub)ensemble in one of the electronic ground-state hyperfine manifolds ($L = 0, J = \frac{1}{2}$) of certain F, can be expressed with irreducible tensor components (see references [27, 33, 42–44] for detailed description)

$$\begin{aligned} \hat{H}_{\text{eff}} = \frac{g^2}{c} \int_0^L \Big[& \underbrace{2\alpha_F^{(0)} \hat{S}_0 + 2\alpha_F^{(2)} \hat{S}_0 \left(\hat{f}_z^2 - \frac{1}{3} \hat{f}^2 \right)}_{\text{Stark Shift}} \\ & + \underbrace{2\alpha_F^{(1)} \hat{S}_z \hat{f}_z}_{\text{Faraday Effect}} + \underbrace{\alpha_F^{(2)} \left(\hat{S}_+ \hat{f}_-^2 + \hat{S}_- \hat{f}_+^2 \right)}_{\text{Voigt Effect}} \Big] \rho A dz, \end{aligned} \tag{2.32}$$

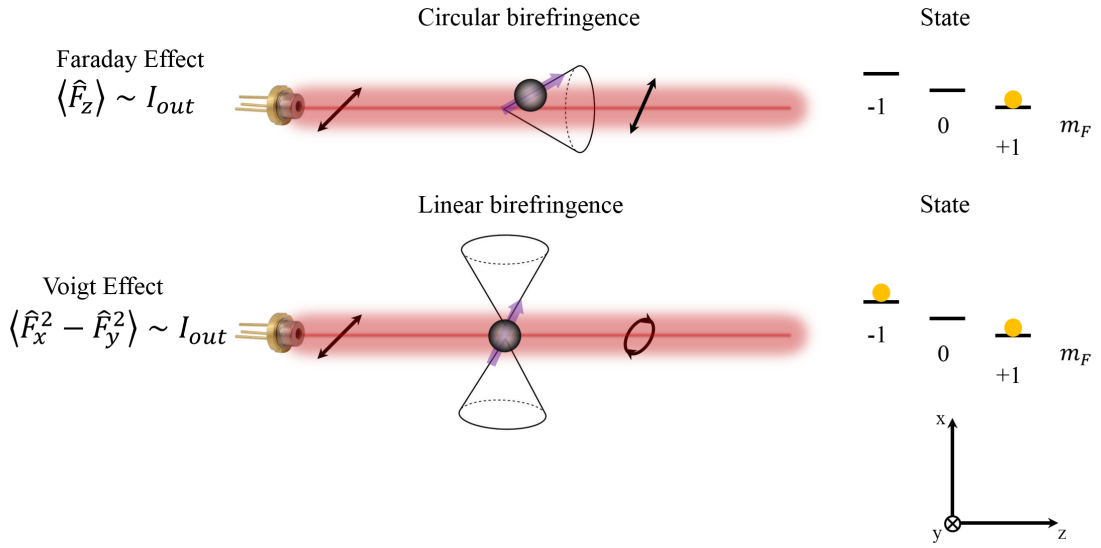

Figure 2.3: a) For the circular birefringence, we have a polarised state where the atomic spins precess around some static field. A light pulse propagating along z with a 45° polarisation will experience a polarisation phase shift when interacting with the sample due to the fact that the indices of refraction $n_{\sigma^+} \neq n_{\sigma^-}$. The rotation will occur between $\hat{S}_x$ and $\hat{S}_y$ whilst $\hat{S}_z$ will remain constant. b) For the case of linear birefringence where the sample is in an aligned state, the same light polarisation will experience a phase shift due to the fact that $n_x \neq n_y$. The rotation will occur between $\hat{S}_y$ and $\hat{S}_z$ whilst $\hat{S}_x$ will remain constant. A linearly polarised beam will acquire ellipticity.

where the quantities in the equation above are defined as follows

$$\hat{f}_\pm = \hat{f}_x \pm i\hat{f}_y, \tag{2.33}$$

$$\hat{S}_\pm = \hat{S}_x \pm i\hat{S}_y. \tag{2.34}$$

Here the effective interaction Hamiltonian contains three terms describing phase shifts in light polarisation relating to the Stokes vectors, $\hat{S}_i$, polarisibailities, $\alpha_F^{(i)}$ as well as the atomic spin $\hat{f}_i$. The first two terms coupled to the Stokes vector S_0 describe global phase shifts of the light beam, without any change in polarisation, also known as the Stark shift. The third term, containing the Stokes vector $\hat{S}_z$ describes the circular birefringence of the atomic medium, known as the Faraday Effect. Here the phase shifts in light polarisation are caused by the difference in interaction strengths between the atomic medium and the two circularly polarised components of light. The last term in the interaction Hamiltonian containing the $\hat{S}_\pm$ Stokes vectors corresponds to the linear birefringence of the atomic medium, also known as the Voigt effect. The Voigt effect causes light polarisation phase shifts between vertical and horizontal polarisation components and the atomic medium. See Fig. 2.3 for illustration of the two effects. The quantities $\alpha_F^{(k)}$ are scalar, vector and tensor polarisabilities and they

depend on the frequency detuning from the energy levels as well as their transition dipole moments. In the off-resonant case, satisfying electric dipole transition rules $F \to F' = F, F \pm 1$ the polarisabilities are given by

$$\alpha_F^{(0)} = \mathcal{A}_F^{F-1} + \mathcal{A}_F^F + \mathcal{A}_F^{F+1}, \tag{2.35}$$

$$\alpha_F^{(1)} = \frac{3}{2}\left[-\frac{\mathcal{A}_F^{F-1}}{F} - \frac{\mathcal{A}_F^F}{F(F+1)} + \frac{\mathcal{A}_F^{F+1}}{F+1}\right], \tag{2.36}$$

$$\alpha_F^{(2)} = \frac{3}{2}\left[\frac{\mathcal{A}_F^{F-1}}{F(2F-1)} - \frac{\mathcal{A}_F^F}{F(F+1)} + \frac{\mathcal{A}_F^{F+1}}{(F+1)(2F+3)}\right], \tag{2.37}$$

where the three scalar polarisabilities $\mathcal{A}_F^{F'}$ for transitions from F to F' are expressed in terms of the reduced dipole moments (which, by isotropy convention, sum up three orthogonal polarisations) and the respective detunings

$$\mathcal{A}_F^{F'} = \frac{1}{3}\cdot\frac{|\langle J, F||\mathbf{d}||J', F'\rangle|^2}{\hbar\Delta_{F,F'}} = \frac{\pi\epsilon_0 c^3\Gamma_{J'}}{\Delta_{F,F'}\omega_{J'}^3}(2J'+1)(2F'+1)\begin{Bmatrix} J & J' & 1 \\ F' & F & I\end{Bmatrix}^2,$$

where we have used a Wigner 6-j symbol and introduced decay rate $\Gamma_{J'}$ and frequency $\omega_{J'}$ of spontaneous emission from the excited J' levels [48]. We also defined detunings $\Delta_{F,F'} = \omega_L - \omega_{F,F'}$ of the light field with respect to the optical $F \to F'$ transition frequencies. We assume $A_F^{F'} = 0$ for non-existing transitions and the higher order terms are $\alpha_F^{(1)} = \alpha_F^{(2)} = 0$. In our experiments we use ^{87}Rb with nuclear spin $I = 3/2$ in $F = 2$ driven near the D1 lines ($J' = 1/2$) the resulting tensor components are explicitly given by

$$\alpha_2^{(0)} = \frac{\alpha_{J'}}{2}\left[\frac{1}{\Delta_{2,1}} + \frac{1}{\Delta_{2,2}}\right], \tag{2.38}$$

$$\alpha_2^{(1)} = -\frac{\alpha_{J'}}{8}\left[\frac{3}{\Delta_{2,1}} + \frac{1}{\Delta_{2,2}}\right], \tag{2.39}$$

$$\alpha_2^{(2)} = \frac{\alpha_{J'}}{8}\left[\frac{1}{\Delta_{2,1}} - \frac{1}{\Delta_{2,2}}\right], \tag{2.40}$$

where the far-detuned, scalar polarisability coefficient is given by

$$\alpha_{J'} = \frac{\epsilon_0\lambda_{J'}^3\Gamma_{J'}}{8\pi^2}, \tag{2.41}$$

which depends on the D1-line parameters $\Gamma_{J'} = 2\pi \times 5.75$ MHz and $\lambda_{J'} = 795$ nm. In our case, the thermal atoms are in a Doppler broadened medium, and as a result each atom sees different detuning of the light. Typically in the experiments (outlined in later sections) the probe detuning is $\Delta_{2,1} = 550$ MHz red detuned from the $F = 2 \to F' = 1$ transition of the D1 line ($\Delta_{2,2} = 1366$ MHz for $F = 2 \to F' = 2$). The Doppler valley at full-width-half-maximum (FWHM) of room temperature ^{87}Rb of the D1 line is $\Gamma_D \approx 560$ MHz. As a result, the fraction of atoms being in a velocity class experiencing resonant interactions due to the Doppler effect with the probing beam

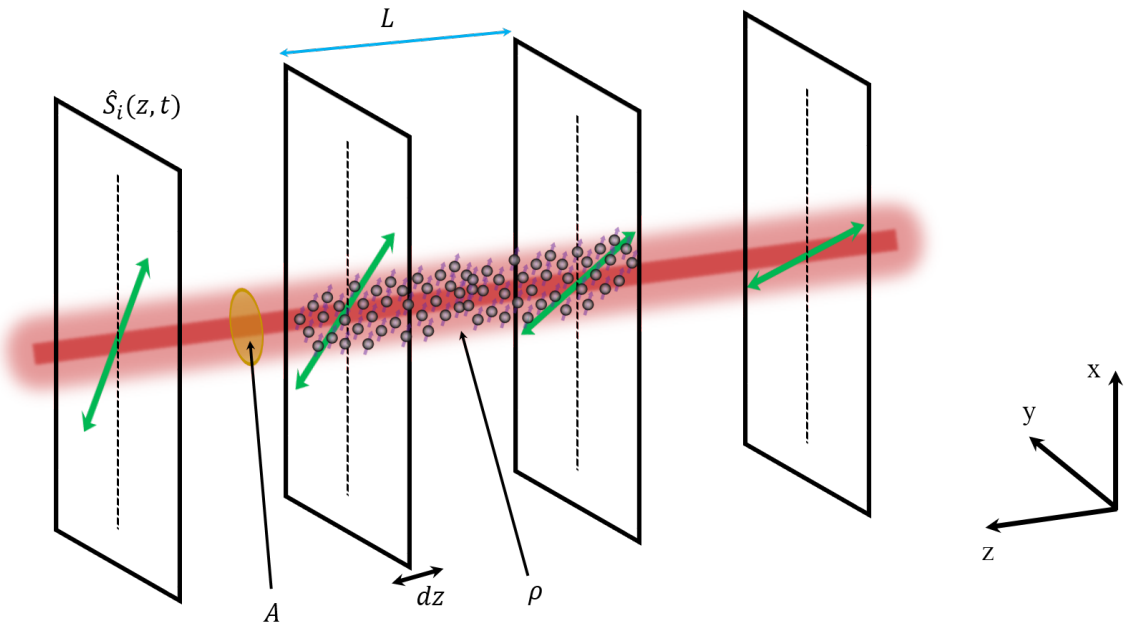

Figure 2.4: An illustration of the polarisation rotation due to the circular birefringence of the atomic medium. Here at each atomic layer characterised by the atomic number $dn = \rho A dz$ the light polarisation rotates by a small angle $d\theta$.

will be negligible and as a result can be ignored.

We want to understand how our observables, i.e. Stokes vectors evolve in time and space given the light-matter interaction Hamiltonian described above. This can be computed using the Heisenberg equation of motion

$$(\partial_t + c\partial_z)\hat{\mathbf{S}}(z,t) = \frac{1}{i\hbar}[\hat{\mathbf{S}}(z,t), \hat{H}_{\text{eff}}]. \tag{2.42}$$

Here the the non-zero time derivative in the Heisenberg equation describes the effects of light retardation. The speed of light in a medium is inversely proportional to the refractive index of that medium, $v = c/n$. In our case, the Clebsch-Gordan coefficients for the different polarisations are not equal and as a result, the effective refractive indices and the speed of light for the two light polarisation components will be different. Moreover, as the light propagates through the atomic medium, the atomic state will be randomly perturbed as a result of the measurement - this is known as quantum back-action [45]. This will consequently change the strength of the light-matter interaction because the initially prepared atomic state has changed. The quantum back-action effects increase in strength as the probe detuning, $\Delta \to 0$ where the probe light comes into resonance with the atomic transitions.

Inserting the expressions for the Stokes vectors defined in the previous section with the off-resonant light matter interaction Hamiltonian, $\hat{H}_{\text{eff}}$, and neglecting the light retardation effects, i.e. $\partial_t \hat{\mathbf{S}}(z,t) = 0$, the Heisenberg equations of motion for the

Stokes vectors read

$$\frac{\partial \hat{S}_x}{\partial z} = \frac{2g^2\rho A}{\hbar c}\left[-\alpha_F^{(1)}\hat{S}_y\hat{f}_z + \alpha_F^{(2)}\hat{S}_z(\hat{f}^2_{+45^\circ} - \hat{f}^2_{-45^\circ})\right], \tag{2.43}$$

$$\frac{\partial \hat{S}_y}{\partial z} = \frac{2g^2\rho A}{\hbar c}\left[\alpha_F^{(1)}\hat{S}_x\hat{f}_z - \alpha_F^{(2)}\hat{S}_z(\hat{f}^2_x - \hat{f}^2_y)\right], \tag{2.44}$$

$$\frac{\partial \hat{S}_z}{\partial z} = \frac{2g^2\rho A}{\hbar c}\alpha_F^{(2)}\left[\hat{S}_y(\hat{f}^2_x - \hat{f}^2_y) - \hat{S}_x(\hat{f}^2_{+45^\circ} - \hat{f}^2_{-45^\circ})\right], \tag{2.45}$$

where

$$\hat{f}_{+45^\circ,-45^\circ} = \frac{1}{\sqrt{2}}(\pm\hat{f}_x + \hat{f}_y). \tag{2.46}$$

Recall that the collective spin of N atoms distributed over any finite length L with density $\rho(z)$ are expressed as

$$\sum_{i=1}^{N}\hat{\mathbf{F}}_i = \int_L \rho(z)\hat{\mathbf{f}}(z)\hbar A dz. \tag{2.47}$$

Assuming that the thermal atoms have a uniform density distribution, $\rho(z) \to \rho$ and further neglecting the back-action effects on the atomic spin states due to the far-off resonant probing and low light intensity, for small optical phase shifts in polarisation ($\ll 1$ rad) the spin operator terms in equations (2.43, 2.44, 2.45) can be approximated to

$$\hat{X}_x = \int \rho(\hat{f}^2_x - \hat{f}^2_y)\hbar^2 A dz = \sum_i^N(\hat{F}^2_{x,i} - \hat{F}^2_{y,i}), \tag{2.48}$$

$$\hat{X}_y = \int \rho(\hat{f}^2_{+45^\circ} - \hat{f}^2_{-45^\circ})\hbar^2 A dz = \sum_i^N(\hat{F}^2_{+45^\circ,i} - \hat{F}^2_{-45^\circ,i}), \tag{2.49}$$

$$\hat{T}_z = \int \rho\hat{f}_z\hbar A dz = \sum_i^N \hat{F}_{z,i}. \tag{2.50}$$

Using these definitions and integrating equations (2.43, 2.44, 2.45) yields the form of the Stokes operators after the off-resonant probe interaction with the atomic medium

$$\hat{S}_x^{\text{out}} = \hat{S}_x - \frac{2g^2}{c\hbar^2}\alpha_F^{(1)}\hat{S}_y\hat{T}_z + \frac{2g^2}{c\hbar^3}\alpha_F^{(2)}\hat{S}_z\hat{X}_y, \tag{2.51}$$

$$\hat{S}_y^{\text{out}} = \hat{S}_y + \frac{2g^2}{c\hbar^2}\alpha_F^{(1)}\hat{S}_x\hat{T}_z - \frac{2g^2}{c\hbar^3}\alpha_F^{(2)}\hat{S}_z\hat{X}_x, \tag{2.52}$$

$$\hat{S}_z^{\text{out}} = \hat{S}_z + \frac{2g^2}{c\hbar^3}\alpha_F^{(2)}\left[\hat{S}_y\hat{X}_x - \hat{S}_x\hat{X}_y\right]. \tag{2.53}$$

In our experiments the probe light is linearly polarised at 45° in the x-y plane, hence, $\hat{S}_x = \hat{S}_z \approx 0$ (refer to Fig. 2.1 on page 8 for illustration). In addition, we assume that the probe light is sufficiently strong in intensity such that the correspondence

principle applies giving $\hat{S}_y \approx S_y$ i.e. the probe beam is classical. With these further assumptions, the above equations reduce to

$$\hat{S}_x^{\text{out}} = -\frac{2g^2}{c\hbar^2}\alpha_F^{(1)} S_y \sum_i^N \hat{F}_{z,i}, \tag{2.54}$$

$$\hat{S}_y^{\text{out}} = S_y, \tag{2.55}$$

$$\hat{S}_z^{\text{out}} = \frac{2g^2}{c\hbar^3}\alpha_F^{(2)} S_y \sum_i^N (\hat{F}_{x,i}^2 - \hat{F}_{y,i}^2), \tag{2.56}$$

where we have made the substitutions for $\hat{X}_x$ and $\hat{T}_z$ given in equations (2.48-2.50). The experimental observables which are our Stokes vectors are then found by computing their expectation values. Assuming that all of our atoms, n_F are prepared in the same quantum state, the expectation values are given by

$$\left\langle \hat{S}_x^{\text{out}} \right\rangle = -g_F^{(1)} S_y n_F \left\langle \hat{F}_z \right\rangle, \tag{2.57}$$

$$\left\langle \hat{S}_z^{\text{out}} \right\rangle = g_F^{(2)} S_y n_F \left\langle \hat{F}_x^2 - \hat{F}_y^2 \right\rangle, \tag{2.58}$$

here n_F is the atomic number density. Furthermore, we have let

$$g_F^{(k)} = \frac{2g^2\alpha_F^{(k)}}{c\hbar^{k+1}}. \tag{2.59}$$

The equations (2.57) and (2.58) describe the Faraday and Voigt effects respectively. We can immediately observe that the birefringence effects of both the Faraday and Voigt effects depend on the vector and tensor polarisabilities which in turn depend on probe detuning and the line transition strength. In addition, the signals are proportional to the number of atoms prepared in a state that maximises the expectation values. In the case of the Faraday effect, the expectation value, $\left\langle \hat{F}_z \right\rangle$, is maximised, when the prepared state is a stretched state

$$\left\langle \hat{F}_z \right\rangle = \left\langle F, F_z \middle| \hat{F}_z \middle| F, F_z \right\rangle = \hbar m, \tag{2.60}$$

where m is the magnetic quantum number of the hyperfine Zeeman states. For the Voigt effect the expectation value using pure states in the x-basis is given by

$$\left\langle \hat{F}_x^2 - \hat{F}_y^2 \right\rangle = \left\langle F, F_x \middle| \hat{F}_x^2 - \hat{F}_y^2 \middle| F, F_x \right\rangle = \frac{1}{2}\hbar^2(F(F+1) - 3m^2). \tag{2.61}$$

For a fixed hyperfine state manifold F, the maximum expectation value is achieved for pure states in cases where $m = 0$ and $m = \pm F$. The case for $m = 0$ is sensitive to external fields via the Voigt effect, but does not yield maximum sensitivity. On the other hand, a state, $|\psi\rangle$ constructed to satisfy $m = \pm 2$ would yield maximal sensitivity to the external fields. Prepared in the x-basis, an example ansatz state that would satisfy such properties would be an equal statistical mixture of $|F = 2, m \pm 2\rangle$ states. Such statistical mixture cannot be expressed in the standard ket basis, but can be trivially defined using the density matrix approach

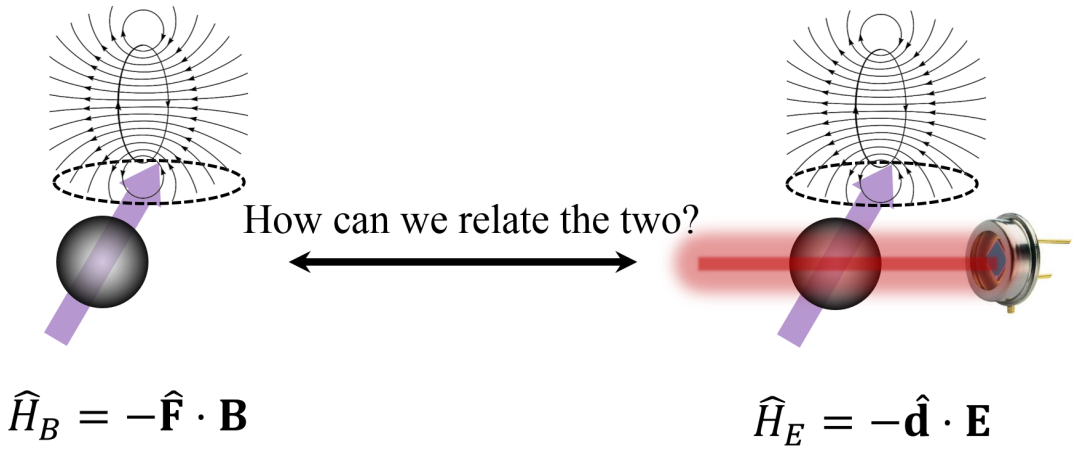

Figure 2.5: An atomic spin precesses around a weak external field with an interaction Hamiltonian given by the linear Zeeman effect. The spin precession of the atom affects the transition dipole moment and therefore the light-matter interaction Hamiltonian. The dynamics of the interaction Hamiltonian can be measured using Stokes vectors which then allow us to extract the magnetic field information.

$$\hat{\rho} = \sum_i p_i \left|\psi_i\right\rangle \left\langle\psi_i\right| = \frac{1}{2}\left(\left|\downarrow\right\rangle \left\langle\downarrow\right| + \left|\uparrow\right\rangle \left\langle\uparrow\right|\right), \tag{2.62}$$

where the $|\uparrow\rangle = |F = 2, m = +2\rangle$ and $|\downarrow\rangle = |F = 2, m = -2\rangle$. The expectation value for the Voigt effect is given by

$$\left\langle \hat{F}_x^2 - \hat{F}_y^2 \right\rangle = \mathrm{Tr}\left[\hat{\rho}\left(\hat{F}_x^2 - \hat{F}_y^2\right)\right]. \tag{2.63}$$

We can now relate the hyperfine spin operators $\hat{F}_i$ to external magnetic field. For weak external fields, the spin-field interaction Hamiltonian is given by the linear Zeeman effect

$$H_B = -\frac{\mu_B g_F}{\hbar}\hat{\mathbf{F}} \cdot \mathbf{B}, \tag{2.64}$$

which can be used to compute the spin dynamics and substituted into the light-matter expression for the Voigt effect. The details of the field-spin interaction Hamiltonian and the corresponding dynamics will be discussed in detail in Chapter 3.

It is noteworthy to reiterate the scope of the light-matter interaction Hamiltonian presented here. The model assumes far-off resonant interaction between light and the atomic ensemble and low light power which allows us to neglect the back-action effects as a result of the weak perturbation of the atomic state during the measurement. This assumption will break down if the probe becomes close to the atomic resonance. If we assume that the probe is sufficiently detuned such that the system can be treated as a two-level atom, then the spin decoherence rate due to the probe beam, Γ_{probe}, can be

described using the following relation [46]

$$\Gamma_{\text{probe}} = \frac{\Gamma}{2}\frac{s}{1+s} \approx \frac{3\lambda^3\Gamma^2}{16\pi^2\hbar c\Delta^2}I, \tag{2.65}$$

where the saturation parameter is given by

$$s = \frac{I}{I_{\text{sat}}\left(1+\left(\frac{2\Delta}{\Gamma}\right)^2\right)}, \tag{2.66}$$

with

$$I_{\text{sat}} = \frac{2\pi^2\hbar c\Gamma}{3\lambda^3}. \tag{2.67}$$

Moreover, the picture is more complicated by the fact that we have a Doppler broadened medium which means that the back-action effects vary across the different atomic velocity classes since they experience different probe detunings. Another physical aspect that was neglected in order to simplify the theoretical analysis was the retardation of light. In principle, if the sample is short, and the light-matter interactions are weak, the retardation effects will be small for the different light polarisations. However, for strong fields and/or high atomic density (large interaction volume) the birefringence effects may be strong enough to produce sufficiently significant light retardation influencing the dynamic effects of the Stokes vectors.

2.3 Optical Broadening Mechanisms

2.3.1 Doppler Broadening

Optically pumped magnetometry experiments are commonly carried out using room temperature alkali vapours which act as the field sensing medium. Unfortunately, thermal motion of the individual atoms in the vapour complicate the light-matter interaction picture. Consider a single atom moving with a velocity $v_z\vec{e}_z$ along the direction of propagation of a laser beam of frequency ω_L. The light perceived by the atom acquires a frequency shift where the new frequency ω' is given by the Doppler effect

$$\omega' = \omega_L\left(1 \pm \frac{v_z}{c}\right), \tag{2.68}$$

where the $\pm$ sign indicates whether the atom is co- or counter-propagating with respect to the travelling light beam and c is the speed of light. However, the atomic vapour has many atoms and as a result, the velocities have a statistical distribution which is given by the Maxwell's probability distribution

$$P(v_z)dv_z = \frac{m}{2\pi k_B T}e^{-\frac{mv_z^2}{2k_BT}}, \tag{2.69}$$

where m is the atomic mass and T is the temperature of the vapour and k_B is the Boltzmann's constant. If the atoms are at rest, the absorption cross-section of a

two-level atom is given by

$$\sigma(\Delta) = \sigma_0 \frac{\Gamma_0}{4\Delta^2 + \Gamma_0^2}, \tag{2.70}$$

where $\Delta = \omega_L - \omega_0$ is the light detuning from the resonance of the transition, ω_0, σ_0 is the absorption cross section on resonance

$$\sigma_0 = \frac{\hbar\omega_0\Gamma_0}{2I_{\text{sat}}}, \tag{2.71}$$

and Γ_0 is the natural linewidth of the transition which can be computed using [48]

$$\Gamma_0 = \frac{\omega_0^3}{3\pi\epsilon_0\hbar c^3}\frac{2J+1}{2J'+1}|\langle J \parallel d \parallel J' \rangle|^2, \tag{2.72}$$

where d is the dipole transition moment, J and J' are the angular momenta of the states. In the limit where the Doppler width is much larger than the natural linewidth of the atomic transition, $\Gamma_D \gg \Gamma$, the absorption cross-section takes the following form

$$\sigma(\delta) = \sigma_D e^{-\left(\frac{\Delta}{\Gamma_D}\right)^2}, \tag{2.73}$$

where σ_D is given by [61]

$$\sigma_D = \frac{\sqrt{\pi}}{2}\frac{\Gamma_0}{\Gamma_D}\sigma_0. \tag{2.74}$$

For room temperature ^{87}Rb isotope, the Doppler broadened linewidth is on the order of 560 MHz. Here the thermally broadened Doppler linewidth, Γ_D, is given by

$$\Gamma_D = \frac{\omega_0}{c}\sqrt{\frac{8k_BT\ln 2}{m}}. \tag{2.75}$$

2.3.2 Transit-Time Broadening

Another effect that contributes to the line broadening is the transit-time broadening. This effect occurs due to a finite interaction time between the atom and the laser. Consider the case where thermal atoms are travelling through a monochromatic laser beam of diameter d and frequency ω_0, the transit time is defined by $\tau = d/|v_\perp|$, where $v_\perp$ is the mean velocity perpendicular to the beam's direction of propagation. For a monochromatic laser source, the electric field is given by $E(t) = E_0\cos(\omega_L t)$. For an atom traversing this electric field the intensity spectrum is given by computing its Fourier transform

$$E(\omega) = \frac{1}{\sqrt{2\pi}}\int_0^\tau E_0\cos(\omega_L t)e^{-i\omega t}dt, \tag{2.76}$$

with the intensity profile given by $I(\omega) = E^*(\omega)E(\omega)$. In the limit where $(\omega - \omega_L) \ll \omega_L$ the intensity profile yields [61, 66]

$$I(\omega) = I_0\frac{\sin^2[(\omega-\omega_L)\tau/2]}{(\omega-\omega_L)^2}, \tag{2.77}$$

where I_0 is a normalisation constant. In reality, the field distribution across a laser beam is not uniform. If our beam intensity profile has a Gaussian beam shape described by TEM_{00} transverse electromagnetic mode then the electric field is given by

$$E = E_0 e^{-r^2/w_0^2} \cos(\omega_L t), \tag{2.78}$$

where $2w_0$ gives the diameter of the Gaussian beam profile where $z_R = \pi w_0^2/\lambda$ is the Rayleigh length. If we apply the same recipe as before by computing the Fourier transform of the electric field and then the corresponding intensity profile in the Fourier plane, we obtain

$$I(\omega) = I_0 \exp\left(-(\omega - \omega_L)^2 \frac{w_0^2}{2v_\perp^2}\right), \tag{2.79}$$

which gives a transit–time limited linewidth (FWHM) of

$$\Gamma_t = \frac{1}{\tau} = \sqrt{2}\frac{v_\perp}{w_0}. \tag{2.80}$$

We therefore have two possibilities to tune the effects of transit–time broadening. The diameter of the laser beam can be changed or the thermal speed of the atoms. Increasing the beam diameter is useful in the context of optical pumping since it maximises the pumped atomic volume and reduces the transit time broadening. On the other hand, reducing the temperature to reduce the atomic velocities reduces the transition broadening but has the technical disadvantage of decreasing atomic number density compromising signal strength. Typically, for room temperature ^{87}Rb atoms interacting with a pump beam of $1/e^2$ diameter of ≈ 7 mm the transit time broadening is of the order $\Gamma_t \approx 0.04$ MHz. In other words, the transit-time broadening dominates the natural lifetime of our state, $\tau \gg 1/\Gamma_0$. This assumes a gas with a pressure in the unsaturated regime.

2.3.3 Pressure Broadening

Another spectral line broadening effect that is common in gaseous media is pressure broadening. It arises due to collisions between atoms or the atoms colliding with the walls of the container. In cases where buffer gases are used, then heterogeneous atom-buffer atom collisions are also present. When the two atoms are in close proximity, the interaction between their electrostatic potentials results in polarisation of their respective dipole moments which result in spectral line shifting and broadening. Since the interactions are non-linear, the resultant broadened line shape tends to be non–Lorentzian [39].

Atomic collisions can be elastic or inelastic in nature. For inelastic collisions, there exists spectral line broadening. This is due to the fact that each collision result in additional depopulation of the excited state along with the natural spontaneous emission. The collision rate is directly related to the pressure of the gas, and as a result a change in pressure will change the transition probability and therefore the

linewidth of the state. Thus, for inelastic collisions, the optical transition linewidth changes according to [40]

$$\Gamma = \Gamma_0 + \Gamma_{\text{press}} = \Gamma_0 + n_{\text{Rb}}\sigma_c\bar{v}, \tag{2.81}$$

where σ_c is the collisional cross section, $\bar{v}$ is the average relative thermal velocity and n_{Rb} is the atomic number density of rubidium. The number density is temperature dependent and is given by [48, 49]

$$n_{\text{Rb}}(T) = \frac{1}{T}10^{21.866+A-\frac{B}{T}}, \tag{2.82}$$

in units (cm^{-3}), where A and B are alkali-specific coefficients [50]. On the other hand, in elastic collisions, the linewidth of the transitions is not affected. However, the peak of the resonance position changes. This is due to the fact that for each collision, the atom acquires a random phase kick which when averaged over an entire ensemble, the emitted radiation acquires a frequency shift in the intensity peak [61]. When we consider both types of elastic and inelastic collisions, the combined intensity profile takes the form [66]

$$I(\omega) \sim \frac{(\Gamma_0 + \Gamma_{\text{press}})^2}{4(\omega - \omega_L - \Delta\omega)^2 + (\Gamma_0 + \Gamma_{\text{press}})^2}, \tag{2.83}$$

where, $\Delta\omega$ is the line shift proportional to the cross section of elastic collisions. Increasing the atomic density increases the degree of rotation in the Stokes vectors (see eq. 2.58 on page 17), thus, increasing the temperature would increase the signal strength. However, the increase in atomic density increases the collision rate, which further increases the rate of depopulation of the magnetically sensitive atomic states. Therefore it is possible that the competition between the two effects may produce some limit where a further increase in the atomic density does not improve the signal strength. This will be discussed in more detail the next chapter.

2.3.4 Power Broadening

So far the optical broadening mechanisms outlined in this section originate from the thermal motion of the atoms with the somewhat partial exception to the transit time broadening where the size of the beam also plays a role. There also exists a spectral line broadening mechanism which is dependent upon the intensity of the optical field. This arises as a consequence of reduced absorption cross section near resonance where the intensity of the optical field is larger than the saturation intensity [65]. The natural linewidth, Γ_0 of a two level atom has a Lorentzian profile. If we take into account of the power broadening effects then we need to include a frequency dependant saturation parameter, S which also has a Lorentzian profile of the following form [66]

$$S(\omega) = S(\omega_0)\frac{(\Gamma_0/2)^2}{(\omega - \omega_0)^2 + (\Gamma_0/2)^2}. \tag{2.84}$$

Using the equation above, the corresponding intensity profile of a power broadened medium is then given by

$$I_S(\omega) = I_0(\omega_0)\frac{(\Gamma_0/2)^2}{(\omega-\omega_0)^2+(\Gamma_0/2)^2}. \tag{2.85}$$

With this modified intensity profile, the new linewidth in a power broadened medium takes the following form [65]

$$\Gamma_I = \Gamma_0\sqrt{1+\frac{I}{I_{\text{sat}}}} = \Gamma_0\sqrt{1+2\left(\frac{\Omega}{\Gamma_0}\right)^2}, \tag{2.86}$$

where I_{sat} and I are the saturation intensity and laser intensities respectively and Ω is the Rabi frequency of the transition. In the case where the intensity of the optical field is comparable to the saturation intensity, $I \approx I_{\text{sat}}$, the linewidth can be approximated to $\Gamma_I = \sqrt{2}\Gamma_0$ [51]. Table 2.1 summarises the various broadening mechanisms and their respective contributions.

Table 2.1: Summary of broadening mechanisms and typical values for ^{87}Rb D2 $5^2S_{1/2} \rightarrow 5^2P_{3/2}$ on resonance transitions at $T = 295$ K, $P = 2$ mW with beam diameter $d = 7.1$ mm.

Type of Broadening	Relation	Value
Transit Broadening	$\Gamma_t = \sqrt{2}(v_\perp/w)$	≈ 0.04 MHz
Pressure Broadening	$\Gamma_p = n_{\text{Rb}}\sigma_c\bar{v}$	≈ 0.5 MHz
Power Broadening	$\Gamma_I = \Gamma_0\sqrt{1+2(\Omega/\Gamma_0)^2}$	≈ 8 MHz
Doppler Broadening	$\Gamma_D = \omega_0/(2\pi c)\sqrt{8k_BT\ln 2/m}$	≈ 560 MHz

2.4 Optical Pumping and Probing

2.4.1 State Preparation with Optical Pumping

A crucial part in being able to measure the Voigt effect and detect external magnetic fields is to efficiently prepare a magnetically sensitive state. As we discussed in the previous subsection 2.2.2 on page 12, an ansatz optimal state that is sensitive to external magnetic fields that also maximises our Voigt effect signal is an equal statistical mixture of the ^{87}Rb hyperfine ground state $|F = 2, m_F = \pm 2\rangle$. By inspection of the energy level structure of the D1 and D2 lines of ^{87}Rb such a state can be prepared by using a combination of $\pi-$polarised pump and repump beams addressing the $F = 1$ and $F = 2$ ground states via optical pumping.

Table 2.2: Gyromagnetic ratios g_F for the D1 and D2 ground and excited states

State / Line	$5^2S_{1/2}$	$5^2P_{1/2}$	$5^2P_{3/2}$
$F = 1$	$g_F = -1/2$	$g_F = -1/6$	$g_F = 2/3$
$F = 2$	$g_F = 1/2$	$g_F = 1/6$	$g_F = 2/3$

Typically, the optical pumping processes are modelled via the Liouville-von Neumann equation using the density matrix approach [52]. The advantage of this approach is that it contains the populations of the states as well as the coherences which contains the full picture of our system. It can also take into account of various optical broadening mechanisms, collisions, magnetic field influence to name just a few. However, for systems containing many non-degenerate energy levels, the process becomes complicated and computationally intense [53]. In addition, depending on the complexity of the system (e.g. Doppler broadening) and the interactions involved, a number of approximations can be made allowing for a significant simplification of the optical pumping processes with minimal sacrifice of the accuracy of the results.

In our case, the optical fields used to drive the atomic transitions to prepare the sensitive states as well as probe them have optical field intensities below the saturation intensity of the states, $I < I_{\text{sat}}$. As a result, due to the low light intensities, the rate of absorption of light by atoms, Ξ, is much slower than the atomic decay due to spontaneous emission, Γ_0, such that $\Xi < \Gamma_0$. Consequently, the light-matter interaction process is dominated by the rate of absorption of light. This allows us to model the optical pumping processes with simple rate equations and ignore the effects of coherences [38, 54]. The scattering rate for a ground state level $|g_j\rangle$ excited to $|e_k\rangle$ is given by

$$\Xi_{j,k}(I, \Delta) = \frac{I/I_{\text{sat}}}{1 + I/I_{\text{sat}} + (2\Delta_{j,k}/\Gamma_k)^2} \frac{\gamma_{j,k}\Gamma_k}{2}, \tag{2.87}$$

where Γ_k is the natural linewidth of the excited state. Here $\Delta_{j,k}$ is the light detuning from resonance and I is the intensity of the optical field. The branching ratios, $\gamma_{j,k}$, are computed using

$$\gamma_{e,g}(|J_e, I, F_e, m_e\rangle \to |J_g, I, F_g, m_g\rangle) = \gamma_{g,e}(|J_g, I, F_g, m_g\rangle \to |J_e, I, F_e, m_e\rangle) = (2F_e + 1)(2J_g + 1)(2J_e + 1) \times \begin{Bmatrix} J_g & I & F_g \\ F_e & 1 & J_e \end{Bmatrix}^2 \times \begin{pmatrix} F_g & 1 & F_e \\ m_g & q & -m_e \end{pmatrix}^2, \tag{2.88}$$

where the curly and round brackets around the matrices represent the Wigner-6j and Wigner-3j symbols respectively. The element q corresponds to the polarisation state such that

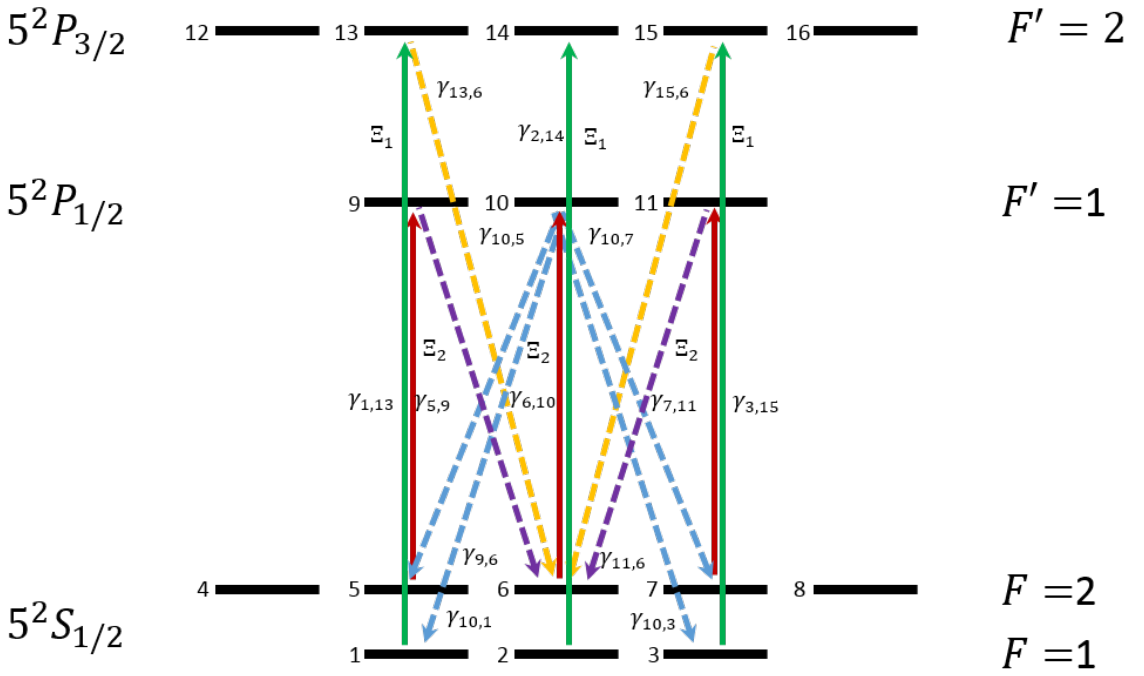

Figure 2.6: Branching ratio diagram for $|F = 2, m_F = 0\rangle$ state with $\pi-$polarised light pump and repump light in the x-basis with scattering rates Ξ_2 and Ξ_1 respectively. Here, Ξ_1 corresponds to the pumping/scattering rate of the repump beam, Ξ_2 is the pumping rate for the pump with $I/I_{\text{sat}} = 1$ and $\Delta = 0$ MHz for both beams. The branching ratios $\gamma_{j,k}$ are computed using eq. (2.88), see Appendix A.1 on page 171 for the corresponding values.

$$q = \begin{cases} 0, & \pi\text{-polarisation}, \\ +1, & \sigma^+\text{-polarisation}, \\ -1, & \sigma^-\text{-polarisation}, \end{cases} \tag{2.89}$$

with the natural lifetimes for the D1 and D2 lines given by

$$\Gamma_k = \begin{cases} 2\pi \times 5.746\text{MHz}, & \text{D1-line}, \\ 2\pi \times 6.065\text{MHz}, & \text{D2-line}. \end{cases} \tag{2.90}$$

The branching ratios, $\gamma_{j,k}$ are normalised against the D2 line transition strength

$$|F_g = I + 1/2, m_g = F_g\rangle \rightarrow |F_e = I + 3/2, m_e = F_e\rangle\,, \tag{2.91}$$

to be unity. See tables in Appendix A.1 on page 171 for the relevant branching ratios.

The time dependent population for each ground level ρ_n is governed by the following rate equation [54]

$$\partial_t \rho_n(t) = \sum_{j \neq n} \rho_j(t) \left(\sum_k \Xi_{j,k} \gamma_{j,k} \gamma_{n,k} \right) - \rho_n(t) \sum_k \Xi_{n,k} \gamma_{n,k} (1 - \gamma_{n,k}), \tag{2.92}$$

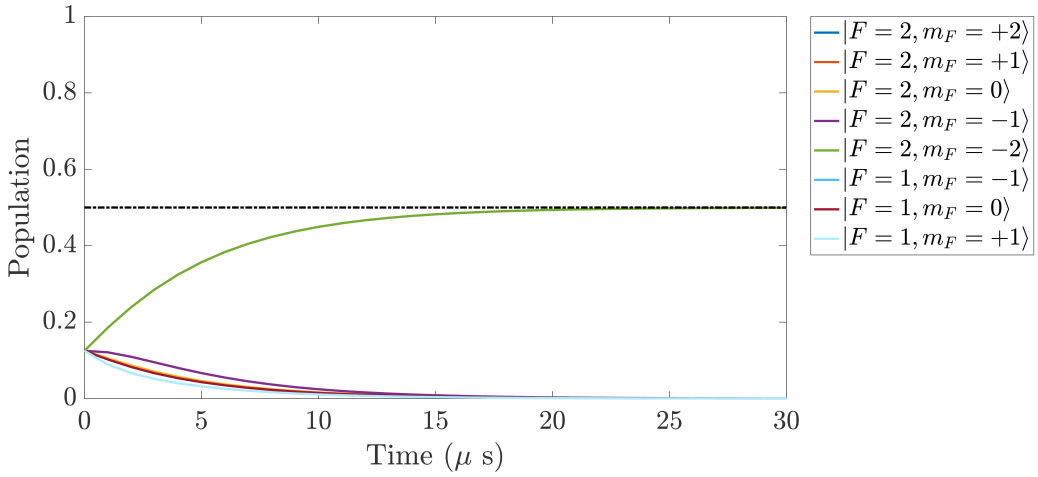

Figure 2.7: Pump and Repump dynamics on during the state preparation process on resonance. For our experimental parameters, we have $I/I_{\text{sat}} = 1$ and both the pump and repump have $\pi-$polarisation. This model assumes an initial input state to be a thermal state with equally distributed populations in the $F = 1$ and $F = 2$ manifolds. Some of the colours of the populations are not visible because they overlap with other state colour labels.

where the sum over j is over the ground state levels and the sum over k is for the excited state levels. In our case, we take the pump to address $|F = 2\rangle \rightarrow |F' = 1\rangle$ of the D1 line with $\pi-$polarisation and on resonance with the transition. The repump beam addresses $|F = 1\rangle \rightarrow |F' = 2\rangle$ of the D2 line also having $\pi-$polarisation and on resonance with the transition. For example, the rate equation for the population of $|F = 2, m_F = 0\rangle$ state represented by ρ_6 reads (see Fig. 2.6 for the contributions to the population for $|F = 2, m_F = 0\rangle$ state)

$$\begin{aligned}\partial_t\rho_6(t) = &-\rho_6(t)\gamma_{6,10}(\gamma_{10,5}+\gamma_{10,7}+\gamma_{10,1}+\gamma_{10,3})\Xi_2\\ &+(\rho_5(t)\gamma_{5,9}\gamma_{9,6}+\rho_7(t)\gamma_{7,11}\gamma_{11,6})\Xi_2\\ &+(\rho_1(t)\gamma_{1,13}\gamma_{13,6}+\rho_3(t)\gamma_{3,15}\gamma_{15,6})\Xi_1,\end{aligned} \tag{2.93}$$

where for example ρ_5 represents the state population of the $|F = 2, m_F = -1\rangle$ state and ρ_1, ρ_2 and ρ_3 correspond to the state populations of the $|F = 1, m_F = -1\rangle$, $|F = 1, m_F = 0\rangle$ and $|F = 1, m_F = +1\rangle$ respectively. The full set of coupled differential equations are given in Appendix A.1 on page 171. These can be solved analytically using any symbolic/numeric math package. In the absence of collisional depolarisation, other broadening mechanisms and the fact that $I < I_{\text{sat}}$ we find that during the state preparation process using $\pi-$polarised light for the pump and the repump beams we achieve a steady state corresponding to an equal statistic mixture of $|F = 2, m_F = \pm 2\rangle$, see Fig. 2.7. However, our model has several limitations. Experimentally, the pump is pulsed in phase with the radio-frequency dressing field with a duty cycle of 9%. This is due to the fact that the radio-frequency field driving the atomic precession constantly changes the quantisation axis in the lab frame. As a result, efficient pumping occurs

when the polarisation of the pump is sufficiently well aligned with the quantisation axis of the precessing spins. The overlap between the rotating quantisation axis and polarisation of the pump during the 9% duty cycle means that some of the atoms will be pumped to a different state which this model does not take into account. This may pose a limitation in understanding how efficient our state preparation process is. Moreover, experimentally, the pump and repump beams travel along a relatively long cell, as a result of the resonant interaction between the light and the atoms, significant absorption can occur given by the Beer-Lambert law

$$I(z) = I_0 e^{-n_{\mathrm{Rb}}\sigma_0 z}, \tag{2.94}$$

where I_0 is the initial intensity, n_{Rb} is the atomic density (cm^{-3}), σ_0 is the resonant absorption cross section and z is distance travelled by the beam across the atomic medium. From this we can observe that scattering rate given by eq. (2.87) on page 24 will be influenced as the beam propagates across the atomic medium. As a result, the state preparation may not be homogeneous across the atomic medium. This limitation can be avoided by using a short cell. These effects will be explored further in the following chapters.

2.4.2 Far-off-resonant probing of the prepared state

The state preparation process is followed by a probing cycle where a far-off resonant beam interacts with the atomic ensemble. The probe acquires a phase shift in polarisation which is dependent on the external magnetic field. Whilst the probe beam is detuned to be far-off resonance of the $|F = 2\rangle \rightarrow |F' = 1\rangle$ transition of the D1 line there nevertheless will be some light scattering which will have optical pumping effects. This will affect our prepared state. To understand the impact of the probe on our state we employ the rate model outlined above. The probe is weak and below the saturation limit of the state, $I/I_{\mathrm{sat}} = 0.6$. Our probe light has 45° polarisation and a detuning of $\Delta = -550$ MHz. Here the 45° polarisation enters the calculation via the branching ratios where the light can be decomposed into $\pi-$ and $\sigma^{\pm}$ polarisations with the branching ratios calculated according to eq. (2.88) on page 24 for the given polarisations. The rate equation for the $|F = 2, m_F = -2\rangle$ population is given by

$$\begin{aligned}\partial_t \rho_4(t) = &-\rho_4(t)\gamma_{4,9}(\gamma_{9,5} + \gamma_{9,6} + \gamma_{9,1} + \gamma_{9,2})\Xi_2 \\ &+ \rho_5(t)\gamma_{5,9}\gamma_{9,4}\Xi_2 + \rho_6(t)\gamma_{6,9}\gamma_{9,4}\Xi_2,\end{aligned} \tag{2.95}$$

see Fig. 2.8 for the breakdown. The rest of the equations can be found in Appendix A.2 on page 173. Solving this set of equations and taking their time evolution allows us to see how the state populations change during the probe cycle. Experimentally, the probe cycle lasts roughly 3 ms. Looking at Fig. 2.9 we observe that by the end of the probe cycle, the $|F = 2, m_F = \pm 2\rangle$ populations drop by 20% to a population fraction of 0.4. The $|F = 2, m_F = 0, \pm 1\rangle$ states acquire a population fraction of 0.01 and 0.05 respectively with the ground state $|F = 1\rangle$ having a near equal distribution of the remaining fraction. To reduce the depopulation through pumping one could further increase the probe detuning which would decrease the scattering rate. However, this

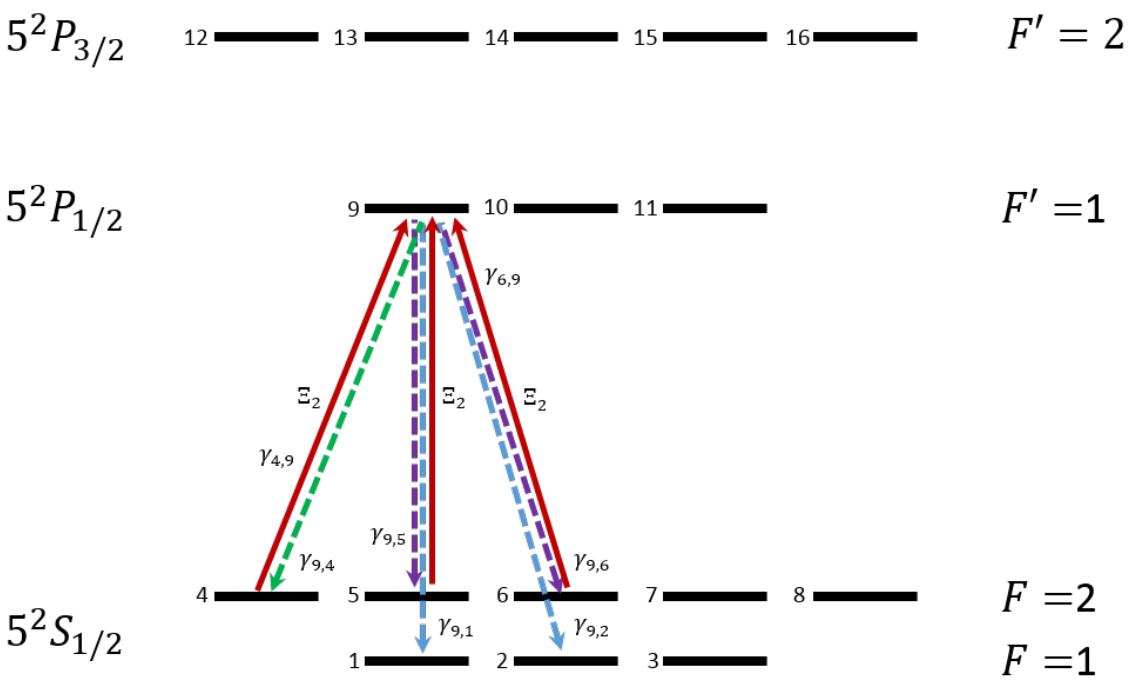

Figure 2.8: Branching ratio diagram for $|F = 2, m_F = -2\rangle$ state corresponding to the $\rho_4(t)$ population with 45° polarised light in the x-basis. Here, Ξ_2 corresponds to the scattering rate of the probe beam with $I/I_{\text{sat}} = 0.6$ and $\Delta = -550$ MHz. The branching ratios $\gamma_{j,k}$ are computed using eq. (2.88), see Appendix A.1 on page 171 for the corresponding values.

has a diminishing return since that would also reduce our light-matter interaction due to the fact that the second-order polarisability tensor, $\alpha^{(2)}$, is dependent upon the detuning of the probe. Alternatively, we could reduce the power of the probe which would reduce the scattering and as a result, the depopulation rate. Again, whilst this is also a valid strategy, the limit is imposed by the electronic and light shot noise dominating at low light powers. The effects of probe detuning and light power will be explored experimentally in the subsequent chapters.

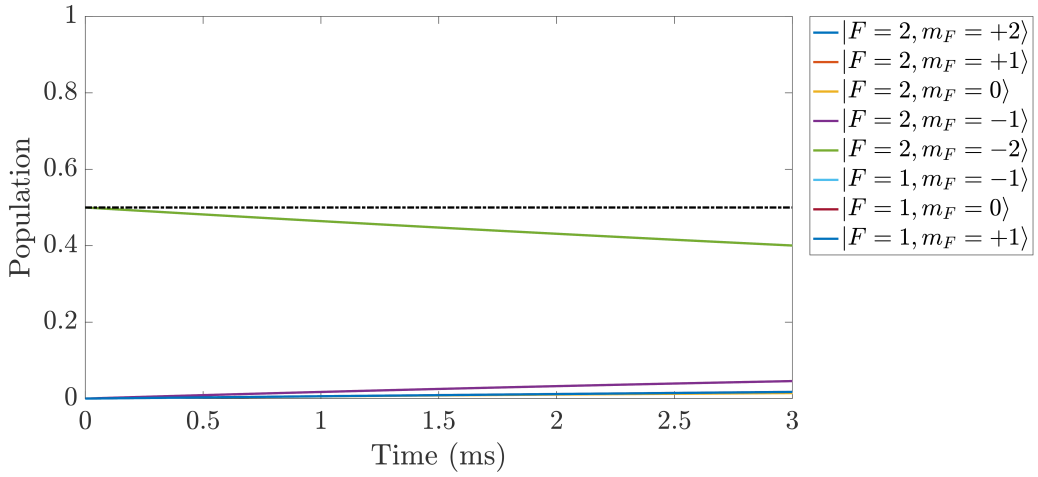

Figure 2.9: Evolution of the populations with $\Delta = -550$ MHz probe detuning from $|F = 2\rangle \rightarrow |F' = 1\rangle$ on the D1 line with $I/I_{\text{sat}} = 0.6$. The initial state is the statistical mixture prepared during the pump/repump cycle. Here the probe has a 45° polarised light. Here the 3 ms duration of the evolution during the probe coincides with our experimental probe duration. Some of the colours of the populations are not visible because they overlap with other state colour labels.

CHAPTER 3

Spin Dynamics in an external magnetic field

This chapter outlines the generalised theory of the dynamics of a radio-frequency (rf) dressed spin-1 particle in an external magnetic field. It consists of three sections discussing three novel and separate models which are used to describe the magnetometer response due to the Voigt effect. All three sections carefully detail the general assumptions, theory, scope and limitations of the proposed models. In each case, we outline theoretical predictions which can be experimentally falsified.

3.1 Geometric interpretation of spin dynamics in a rf-dressed field

An atom with a non-zero magnetic moment $\boldsymbol{\mu}$ subjected to an external magnetic, $\mathbf{B}$ field will begin to precess about that field at a Larmor frequency $\omega_{\text{rf}} = \gamma\mathbf{B}$, where γ is the gyromagnetic ratio of the atom. If the magnetic field is small, then the magnetic moment $\boldsymbol{\mu}$ is independent from the external field and the atom acquires energy given by

$$E = -\boldsymbol{\mu} \cdot \mathbf{B}. \tag{3.1}$$

If we consider the total angular momentum of the atom $\mathbf{F} = \mathbf{I} + \mathbf{J}$ with $\mathbf{I}$ being the nuclear spin angular momentum and $\mathbf{J} = \mathbf{L} + \mathbf{S}$ total angular momentum of the electron consisting of the orbital and spin angular momenta, then the Hamiltonian of the atom in a weak external magnetic field yields

$$\hat{H} = -\frac{\mu_B g_F}{\hbar}\hat{\mathbf{F}} \cdot \mathbf{B}, \tag{3.2}$$

where μ_B is the Bohr magneton, $\hbar$ is the reduced Planck's constant and g_F is the nuclear Landé g-factor which is given by

$$g_F = g_J \frac{F(F+1) + J(J+1) - I(I+1)}{2F(F+1)} + g_I \frac{F(F+1) + I(I+1) - J(J+1)}{2F(F+1)}, \tag{3.3}$$

where we have explicitly included the effects of the magnetic moment of the nucleus. In our case, we consider atoms interacting with a static field $\mathbf{B}_{\mathrm{dc}} = B_{\mathrm{dc}}\mathbf{e}_z$ and a field oscillating at a radio-frequency ω_{rf} in a transverse direction $\mathbf{B}_{\mathrm{rf}}(t) = B_{\mathrm{rf}}\cos(\omega_{\mathrm{rf}}t - \mathbf{k}_{\mathrm{rf}}\cdot\mathbf{r})\mathbf{e}_x$. For weak fields, the time-dependent interaction Hamiltonian of an atom with spin $\hat{\mathbf{F}}$ of constant magnitude can be approximated by

$$\hat{H} = -\frac{\mu_B g_F}{\hbar}\hat{\mathbf{F}}\cdot(\mathbf{B}_{\mathrm{rf}}(t,\mathbf{r}) + \mathbf{B}_{\mathrm{dc}})\,. \tag{3.4}$$

Here, the spin operator $\hat{\mathbf{F}}$ is given by

$$\hat{\mathbf{F}} = \begin{bmatrix}\hat{F}_x\\ \hat{F}_y\\ \hat{F}_z\end{bmatrix}, \tag{3.5}$$

where $\hat{F}_i$ are the spin-1 matrices (see Appendix B.6.1 on page 187 and onwards for details). Physically, the wavelength of the rf-field, λ_{rf}, is much larger than the atom size, thus we can approximate the rf-dressing field to

$$\mathbf{B}_{\mathrm{rf}}(t) \approx B_{\mathrm{rf}}\cos(\omega_{\mathrm{rf}}t)\mathbf{e}_x \quad \text{for} \quad \lambda_{\mathrm{rf}} \gg r. \tag{3.6}$$

After the approximations, the Hamiltonian takes the form

$$\hat{H} = -\frac{\mu_B g_F}{\hbar}\hat{\mathbf{F}}\cdot(\mathbf{B}_{\mathrm{rf}}(t) + \mathbf{B}_{\mathrm{dc}})\,. \tag{3.7}$$

We want to remove the time dependence and solve the Hamiltonian in the rotated frame. Depending on the sign of the g_F factor, using positive ω_{rf}, we transform the coordinates to a frame rotating about the z-axis with a unitary rotation operator

$$\hat{U} = e^{i\omega_{\mathrm{rf}}t\hat{F}_z/\hbar}, \tag{3.8}$$

where ω_{rf} is the angular frequency of the rf-field. Note that this unitary transformation is time dependent. As a result, the transformed Hamiltonian takes the following form (see Appendix B.1 on page 175 for detailed evaluation)

$$\hat{H}' = i\hbar\frac{d\hat{U}}{dt}\hat{U}^\dagger + \hat{U}\hat{H}\hat{U}^\dagger. \tag{3.9}$$

Neglecting counter-rotating terms and applying the rotating wave approximation (RWA), the transformed, effective Hamiltonian takes the form

$$\hat{H}_{\mathrm{eff}} = -\frac{\mu_B g_F}{\hbar}\hat{\mathbf{F}}\cdot\mathbf{B}_{\mathrm{eff}}. \tag{3.10}$$

The effective magnetic field in this frame is given by

$$\mathbf{B}_{\mathrm{eff}} = B_\rho\mathbf{e}_x + (B_{\mathrm{dc}} - B_{\mathrm{res}})\mathbf{e}_z, \tag{3.11}$$

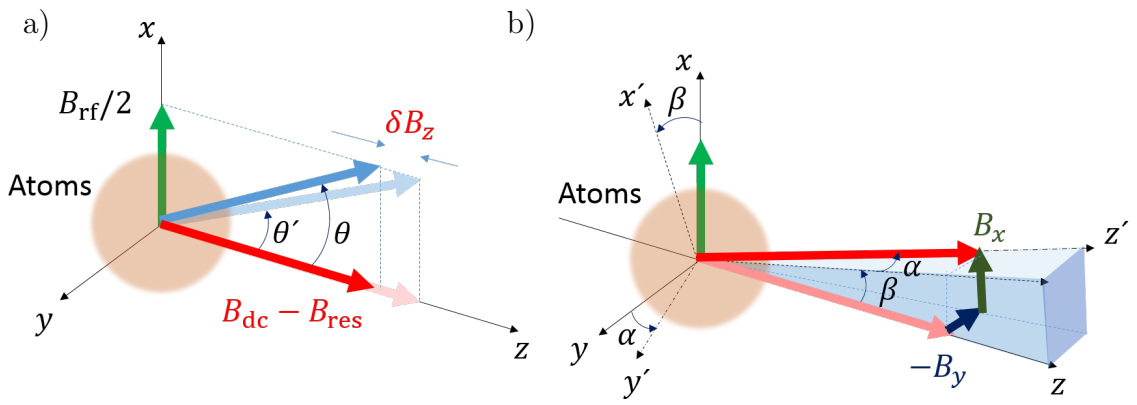

Figure 3.1: Geometrical depiction of the effective field in the rotating frame. a) The effective field encloses an angle θ with the z-axis. An external field variation B_z^{ext} changes the angle $\theta \to \theta'$. b) The presence of transverse external fields B_y and B_x also changes the orientation of the effective field, rotating it by angles α and β, respectively.

where $B_\rho = B_{\text{rf}}/2$, and $B_{\text{res}} = \pm\hbar\omega_{\text{rf}}/\mu_B g_F$ corresponds to a fictitious magnetic field that defines a resonance condition for the Larmor precession. As depicted in Fig. 3.1 a), the angle enclosed by the effective field and the z-axis is

$$\theta = \frac{\pi}{2} - \tan^{-1}\frac{B_{\text{dc}} - B_{\text{res}}}{B_\rho}. \tag{3.12}$$

Here the angle θ defines the direction of the effective magnetic field $\mathbf{B}_{\text{eff}}$ which our dressed state follows adiabatically. To satisfy the adiabaticity condition the rate of change of the adiabatic field angle, $|\dot{\theta}|$ needs to be much smaller than the effective magnetic field such that the state can follow it [27]

$$|\dot{\theta}| \ll \mu_B g_F |\mathbf{B}_{\text{eff}}|/\hbar. \tag{3.13}$$

In other words, if the rate of change of the amplitude of the rf-field, B_ρ, the static field B_{dc} or the B_{res} field change faster than the $|\mathbf{B}_{\text{eff}}|$ field, the state will no longer be able to follow these changes adiabatically and as a result, will no longer be an eigenstate of the Hamiltonian. In the rotated frame, the dressed state takes the form

$$|\Psi_{\text{rot}}\rangle = e^{i\theta\hat{F}_y/\hbar}\,|F, F_z\rangle\,. \tag{3.14}$$

Here the dressed state refers to the eigenstate of the radio-frequency dressed atom-spin Hamiltonian. We can transform this state into the lab frame

$$|\Psi(t)\rangle = \hat{U}^{-1}(t)\,|\Psi_{\text{rot}}\rangle = e^{-i\omega_{\text{rf}}t\hat{F}_z/\hbar}e^{-i\theta\hat{F}_y/\hbar}\,|F, F_z\rangle = \hat{R}(t)\,|F, F_z\rangle\,. \tag{3.15}$$

Experimentally, the lab measurements take the form of the expectation values of our observable operators. Thus, it is conducive to translate from the Schrödinger picture to the Heisenberg picture where the states are constant in time and the operators evolve in time. We can write this as follows

$$\langle\Psi(t)|\,\hat{O}\,|\Psi(t)\rangle = \langle F, F_z|\,\hat{R}(t)\hat{O}\hat{R}^{-1}(t)\,|F, F_z\rangle\,. \tag{3.16}$$

Using the Baker-Hausdorff Lemma [55]

$$e^{\hat{A}}\hat{B}e^{-\hat{A}} = \hat{B} + [\hat{A},\hat{B}] + \frac{1}{2!}[\hat{A},[\hat{A},\hat{B}]] + ..., \tag{3.17}$$

it can be shown that for a Cartesian vector operator, the corresponding Heisenberg operator is given by a geometric rotation, i.e. (see Appendix B.2 on page 177)

$$\hat{\mathbf{O}}'(t) = \hat{R}(t)\hat{\mathbf{O}}\hat{R}^{-1}(t) = \mathbf{R}(t)\hat{\mathbf{O}}. \tag{3.18}$$

If we take $\hat{O} = \hat{F}_i$ to be our spin operators with the definition of $\hat{R}(t) = e^{-i\omega_{\mathrm{rf}}t\hat{F}_z/\hbar}e^{-i\theta\hat{F}_y/\hbar}$, then, the time dependent geometric rotation is given by

$$\hat{\mathbf{F}}'(t) = \hat{R}(t)\hat{\mathbf{F}}\hat{R}^{-1}(t) = \mathbf{R}(t)\hat{\mathbf{F}} \tag{3.19}$$

$$\begin{bmatrix} \hat{F}'_x(t) \\ \hat{F}'_y(t) \\ \hat{F}'_z(t) \end{bmatrix} = \begin{bmatrix} \cos\theta\cos\omega_{\mathrm{rf}}t & -\sin\omega_{\mathrm{rf}}t & -\sin\theta\cos\omega_{\mathrm{rf}}t \\ \cos\theta\sin\omega_{\mathrm{rf}}t & \cos\omega_{\mathrm{rf}}t & -\sin\theta\sin\omega_{\mathrm{rf}}t \\ \sin\theta & 0 & \cos\theta \end{bmatrix} \cdot \begin{bmatrix} \hat{F}_x \\ \hat{F}_y \\ \hat{F}_z \end{bmatrix},$$

where $\mathbf{R}(t) = \mathbf{R}_z(\omega_{\mathrm{rf}}t)\mathbf{R}_y(-\theta)$ are standard rotation matrices, namely

$$\mathbf{R}_z(\omega_{\mathrm{rf}}t) = \begin{bmatrix} \cos\omega_{\mathrm{rf}}t & -\sin\omega_{\mathrm{rf}}t & 0 \\ \sin\omega_{\mathrm{rf}}t & \cos\omega_{\mathrm{rf}}t & 0 \\ 0 & 0 & 1 \end{bmatrix}, \tag{3.20}$$

$$\mathbf{R}_y(-\theta) = \begin{bmatrix} \cos\theta & 0 & -\sin\theta \\ 0 & 1 & 0 \\ -\sin\theta & 0 & \cos\theta \end{bmatrix}. \tag{3.21}$$

From the definition of the adiabatic angle θ we see that the an external magnetic field in the z-direction will affect the spin evolution which is nothing else but an effective rotation. The presence of transverse fields can also be represented by effective rotations as shown in Fig. 3.1 b). Field components B_x^{ext} and B_y^{ext} rotate the static field about the x, y-axes by angles β and α, respectively. Hence, we can use a sequential rotation $\mathbf{M}(\alpha,\beta) = \mathbf{R}_x(\alpha)\mathbf{R}_y(\beta)$, which transforms the atomic spin operator in the laboratory frame as

$$\hat{\mathbf{F}}' = \mathbf{M}(\alpha,\beta)\hat{\mathbf{F}} = \begin{bmatrix} 1 & 0 & 0 \\ 0 & \cos\alpha & -\sin\alpha \\ 0 & \sin\alpha & \cos\alpha \end{bmatrix} \cdot \begin{bmatrix} \cos\beta & 0 & -\sin\beta \\ 0 & 1 & 0 \\ -\sin\beta & 0 & \cos\beta \end{bmatrix} \cdot \begin{bmatrix} \hat{F}_x \\ \hat{F}_y \\ \hat{F}_z \end{bmatrix}, \tag{3.22}$$

where unprimed the coordinates are aligned with the actual field. The angles α and β are given by

$$\alpha = \arctan\left(\frac{-B_y^{\mathrm{ext}}}{B_z'^{\mathrm{ext}}}\cos(\beta)\right), \tag{3.23}$$

$$\beta = \arctan\left(\frac{B_x^{\mathrm{ext}}}{B_z'^{\mathrm{ext}}}\right), \tag{3.24}$$

where $B_z^{\prime\text{ext}} = B_z^{\text{ext}} + B_{\text{res}} + B_\rho$. With the small angle approximation the above reduces to

$$\alpha \approx \frac{-B_y^{\text{ext}}}{B_z^{\prime\text{ext}}}, \tag{3.25}$$

$$\beta \approx \frac{B_x^{\text{ext}}}{B_z^{\prime\text{ext}}}. \tag{3.26}$$

For a complete description at larger angles, we need to include the fact that the transverse fields increase the actual static field strength to

$$B_{\text{dc}} = \sqrt{(B_z^{\prime\text{ext}})^2 + (B_x^{\text{ext}})^2 + (B_y^{\text{ext}})^2}, \tag{3.27}$$

and that the applied rf-field is not co-rotated, leading to a reduction of its effective amplitude in the rotating frame, given by $B_\rho = (B_{\text{rf}}/2)\cos\beta$. With this, the total rotation due to external fields in the lab frame is given by

$$\hat{\mathbf{F}}''_{\text{Lab}} = \mathbf{M}(\alpha,\beta)\mathbf{R}(t)\hat{\mathbf{F}} = \mathbf{R}_x(\alpha)\mathbf{R}_y(\beta)\mathbf{R}_z(\omega_{\text{rf}}t)\mathbf{R}_y(-\theta)\hat{\mathbf{F}}. \tag{3.28}$$

If we let s_ν (c_ν) to stand for $\sin(\nu)$ ($\cos(\nu)$) with $\nu \in \{\alpha, \beta, \theta, \omega_{\text{rf}}t\}$ the transformed operators take the following form

$$\hat{F}_x^{\text{Lab}}(t) = (c_{\omega_{\text{rf}}t}c_\beta c_\theta + s_\beta s_\theta)\hat{F}_x - s_{\omega_{\text{rf}}t}c_\beta \hat{F}_y - (c_{\omega_{\text{rf}}t}c_\beta s_\theta + c_\theta s_\beta)\hat{F}_z, \tag{3.29}$$

$$\begin{aligned}\hat{F}_y^{\text{Lab}}(t) = {} & (c_\beta s_\alpha c_\theta + (c_{\omega_{\text{rf}}t}s_\alpha s_\beta + c_\alpha c_\theta s_{\omega_{\text{rf}}t}))\hat{F}_x - (s_{\omega_{\text{rf}}t}s_\alpha s_\beta - c_{\omega_{\text{rf}}t}c_\alpha)\hat{F}_y \\ & - (s_\alpha c_\beta c_\theta + s_\theta(c_{\omega_{\text{rf}}t}s_\alpha s_\beta + s_{\omega_{\text{rf}}t}c_\alpha))\hat{F}_z,\end{aligned} \tag{3.30}$$

$$\begin{aligned}\hat{F}_z^{\text{Lab}}(t) = {} & ((s_{\omega_{\text{rf}}t}s_\alpha c_\theta - c_{\omega_{\text{rf}}t}c_\alpha s_\beta) - c_\alpha c_\beta s_\theta)\hat{F}_x + (s_{\omega_{\text{rf}}t}c_\alpha s_\beta + c_{\omega_{\text{rf}}t}s_\alpha)\hat{F}_y \\ & + (c_\alpha c_\beta c_\theta + (c_{\omega_{\text{rf}}t}c_\alpha s_\beta - s_{\omega_{\text{rf}}t}s_\alpha s_\theta))\hat{F}_z.\end{aligned} \tag{3.31}$$

3.1.1 Linear Birefringence of the rf-dressed spin

In order to detect the spin evolution due to the presence of external magnetic fields, we incorporate the formalism of the light-matter interaction discussed in the previous chapter. The interaction between the atomic medium and the off-resonant light field leads to linear or circular birefringence which depends on the atomic-spin dependent polarisability tensor. After the propagation through the medium, neglecting absorption and assuming sufficiently small phase angles, the resulting Voigt rotation can be described by Stokes operators

$$\left\langle \hat{S}'_z(t) \right\rangle = g_F^{(2)} S_y n_F \left\langle \hat{F}_x^2(t) - \hat{F}_y^2(t) \right\rangle, \tag{3.32}$$

where $\hat{S}'_z$ represent the polarisation's ellipticity as photon flux imbalances of the output light, measured in linear basis. The coupling strengths $g_F^{(k)}$ depend on light detuning, interaction cross section, and the rank-k components of the polarisability tensor. In these equations, we assume interaction with n_F atoms in the same spin state within one hyperfine F-manifold and neglect dispersive back-action on the atoms (Stark

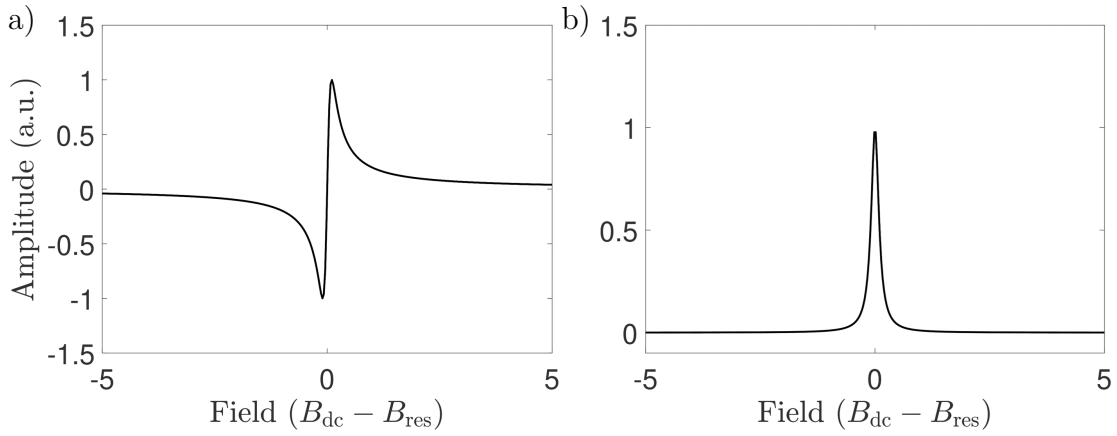

Figure 3.2: Spectral decomposition of Voigt rotation proportional to $\left\langle \hat{F}_x^2 - \hat{F}_y^2 \right\rangle$, with harmonics $n = 1$ a), $n = 2$ b) given by eq. (3.38) where θ is given in eq. (3.12).

shifts) [27].

We square the operators, $\left(\hat{F}_i^{\rm Lab}(t)\right)^2$, obtained in eqs. (3.29-3.31) on page 34 and substitute them into the expression for the Voigt rotation eq. (3.32). Evaluating this we obtain spectral decomposition of the signal which leads to

$$\left\langle \hat{S'}_z(t) \right\rangle = \frac{1}{2} g_F^{(2)} S_y n_F \hbar^2 \xi_F(F_z) \sum_{n=0}^{2} h_n(\theta) e^{in\omega_{\rm rf}t} + c.c., \tag{3.33}$$

where

$$\langle F, F_z | \, \hat{F}_x^2 - \hat{F}_y^2 \, | F, F_z \rangle = \hbar^2 (F(F+1) - 3F_z^2)/2 = \hbar^2 \xi_F(F_z). \tag{3.34}$$

The spectral amplitudes, h_i vary as

$$h_0 = \frac{1 + 3\cos 2\theta}{4} \left(\frac{\cos^2\beta}{2} - \frac{(3 - \cos 2\beta)\cos 2\alpha}{4} \right), \tag{3.35}$$

$$h_1 = \left(\frac{1}{2} \cos\alpha \sin 2\beta \mp \frac{i}{4} \sin 2\alpha (3 - \cos 2\beta) \right) \sin 2\theta, \tag{3.36}$$

$$h_2 = -\left(\frac{1}{4} \cos^2\alpha (3 - \cos 2\beta) + \frac{1}{2} \cos 2\beta \mp \frac{i}{2} \sin\alpha \sin 2\beta \right) \sin^2\theta. \tag{3.37}$$

In the small external field approximation, where the transverse fields are small, i.e. $\alpha, \beta \leq 1$, the spectral components h_n can be reduced to the following

$$(h_0, h_1, h_2)^T(\theta) \approx \begin{pmatrix} 0 \\ (\beta \mp i\alpha) \sin 2\theta \\ -\sin^2\theta \end{pmatrix}. \tag{3.38}$$

The principal behaviour of these functions is shown in Fig. 3.2. The transverse field components are mapped onto the quadratures of the first harmonic $\beta - i\alpha \approx$

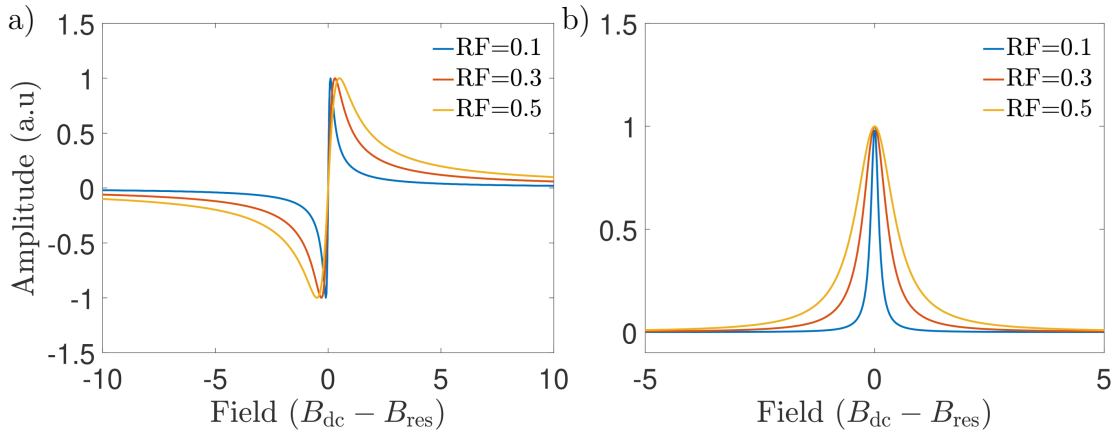

Figure 3.3: Magnetometer dispersive and resonant profiles at different radio-frequency field amplitudes. As can be observed increasing the rf-field amplitude increases the linewidth of the resonance profile as well as decreasing the steepness of the dispersive curves.

$(B_x^{\text{ext}} + iB_y^{\text{ext}})/B_z'^{\text{ext}}$, with a dispersive shape and an oscillation amplitude proportional to $\sin 2\theta$. Maximal amplitude is reached at $\theta = \pi/4$ and $\theta = 3\pi/4$, i.e. when the static field is $B_{\text{dc}} = B_{\text{sense}}^{\pm} = B_{\text{res}} \pm B_\rho$. The maximum sensitivity and approximately linear response to B_z^{ext} is also met at $B_{\text{dc}} = B_{\text{sense}}^{\pm}$. Hence, the Voigt rotation enables detection of all three magnetic components by evaluating the first and second signal harmonics.

3.1.2 Magnetometer response to external fields (Geometric Model)

In order to measure external magnetic fields, we extract three quadratures from the first and second harmonic signals. We separate the first harmonic, h_1 into real and imaginary parts, and evaluate the real part of the second harmonic, h_2. The result is given by

$$h_x = \text{Re}(h_1) = \frac{1}{4}(3 - \cos 2\beta) \sin 2\alpha \sin 2\theta, \tag{3.39}$$

$$h_y = \text{Im}(h_1) = \frac{1}{2} \cos\alpha \sin 2\beta \sin 2\theta, \tag{3.40}$$

$$h_z = \text{Re}(h_2) = -\frac{1}{4}\left((3 - \cos 2\beta)\cos^2\alpha + 2\cos 2\beta\right)\sin^2\theta. \tag{3.41}$$

The characteristic shape of the functions h_x, h_y and h_z are shown in Fig. 3.4. For the Voigt effect measurements where we have small longitudinal and transverse field perturbations due to external field sources, i.e. $B_{x,y,z}^{\text{ext}} \ll B_{\text{sense}}^{+}$, we work on the high field side of the rf resonance, by applying a field in the z-direction of strength

$$B_{\text{sense}}^{+}(\alpha = \beta = 0) = B_{\text{res}} + B_\rho, \tag{3.42}$$

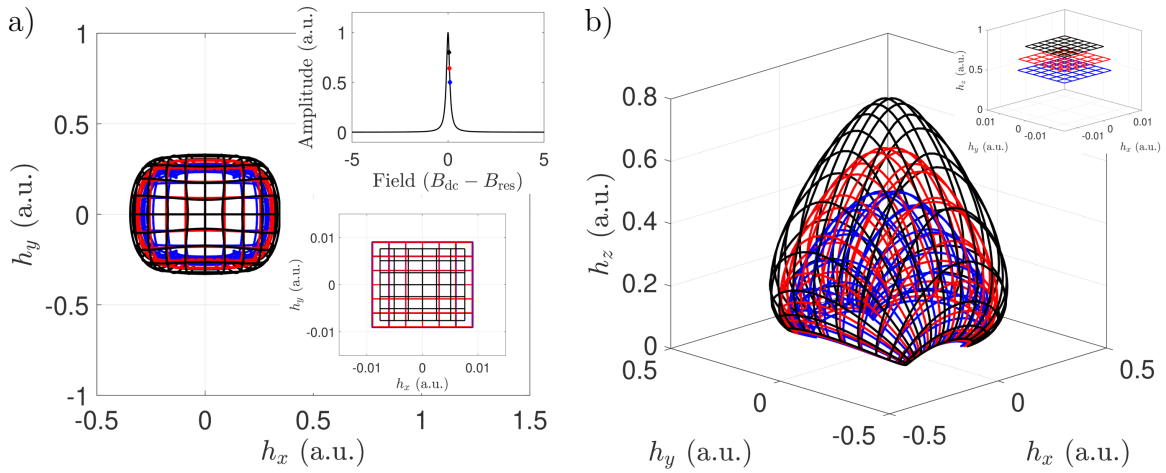

Figure 3.4: Atomic response, mapping the external magnetic field vectors onto harmonic signal components on the sensitive field point $B^{+}_{\text{sense}} = B_{\text{res}} + B_{\rho}$. a) Theoretical response of the signal quadratures at frequency ω_{rf}, as a function of the transverse field components B^{ext}_{x} and B^{ext}_{y} for constant B^{ext}_{z}. b) Full 3-dimensional response, including the real part of the signal amplitude at frequency $2\omega_{\text{rf}}$, which allows for the measurement of the longitudinal field B^{ext}_{z}. Here the insets in a) and b) show the OPM response in the case where the external fields are small described by equations (3.43-3.45). The response in the insets is obtained by linearly sweeping $B^{\text{ext}}_{x,y}$ fields for a given B^{ext}_{z} where $B^{\text{ext}}_{x,y,z} \ll B^{+}_{\text{sense}}$.

which enables full 3D vector field sensitivity. At this setting, the explicit second order Taylor expansion of the three relevant signal quadratures is given by

$$h_x \approx + \left(\frac{1}{B^{+}_{\text{sense}}} - \frac{B^{\text{ext}}_{z}}{B^{2}_{\text{sense}}} \right) B^{\text{ext}}_{x}, \tag{3.43}$$

$$h_y \approx - \left(\frac{1}{B^{+}_{\text{sense}}} - \frac{B^{\text{ext}}_{z}}{B^{2}_{\text{sense}}} \right) B^{\text{ext}}_{y}, \tag{3.44}$$

$$\begin{aligned} h_z \approx & - \frac{1}{2} + \frac{B^{\text{ext}}_{z}}{B_{\text{rf}}} - \left(\frac{B^{\text{ext}}_{z}}{B_{\text{rf}}} \right)^{2} \\ & + \frac{2B^{+}_{\text{sense}} + B_{\text{rf}}}{4B^{2}_{\text{sense}} B_{\text{rf}}} (B^{\text{ext}}_{x})^{2} + \frac{B^{+}_{\text{sense}} + B_{\text{rf}}}{2B^{2}_{\text{sense}} B_{\text{rf}}} (B^{\text{ext}}_{y})^{2}, \end{aligned} \tag{3.45}$$

where B^{ext}_{i} components correspond to the measured external magnetic fields. According to this model, the sensitivity of the magnetometer to the external magnetic fields can be tuned. One of the parameters to tune this sensitivity is the amplitude of the radio-frequency dressing field, B_{ρ}. Increasing the radio-frequency field amplitude increases the linewidth of the $2\omega_{\text{rf}}$ resonance profile which in turn reduces the slope of the resonance at the B^{+}_{sense} point, see Fig. 3.3. Moreover, this reduces the sensitivity in the transverse field sensing directions which are mapped onto the ω_{rf} dispersive resonance. The reduction in sensitivity to all three components can be seen more clearly in the low external field perturbation limit given in equations (3.43-3.45) where increasing the

rf-field amplitude decreases the signal quadrature values in h_x, h_y and h_z for the same external fields. Another parameter that tunes the sensitivity of the OPM, in this case, only in the transverse field directions i.e. the h_x and h_y components is the frequency of the dressing field, ω_{rf}. In order to achieve sensitive field measurements we need to tune the OPM $B^{+}_{\mathrm{sense}} = B_{\mathrm{res}} + B_{\rho}$, however, the resonance field $B_{\mathrm{res}} = \hbar\omega_{\mathrm{rf}}/\mu_B g_F$ depends linearly on the frequency of the dressing field. Increasing the rf-dressing field frequency increases B_{res} field and consequently B^{+}_{sense} which in effect reduces the $h_{x,y}$ signal quadrature values since they are inversely proportional the B^{+}_{sense} field. The strategy to increase the sensitivity of the OPM in the transverse field directions would be to simply reduce the dressing field frequency, ω_{rf}, which effectively increases the magnitude of the geometric angles α and β for the transverse fields. However, this poses a limitation on the bandwidth of the magnetometer as well as efficient state preparation process because the spin coherence lifetime becomes comparable to the rf-field time period. This will be discussed in more detail in the following chapters. On the other hand, increasing the frequency poses an upper limit where the effects of the second order Zeeman effect will become relevant since the sensitive field point, $B^{+}_{\mathrm{sense}} = B_{\mathrm{res}} + B_{\rho}$, becomes large enough resulting in non-linear energy level splitting.

3.1.3 Scope and Limitations of the Geometric model

The geometric model described in this section gives a rough estimation of the magnetometer response to various field parameters. It predicts that higher rf-dressing frequencies linearly decrease the OPM response in the transverse field directions as well as the fact that at higher rf-dressing amplitudes, the OPM resonance and dispersive curves broaden further decreasing the OPM sensitivity to transverse and longitudinal fields. Moreover, we find that at higher transverse and longitudinal fields, the orthogonality between the field mapping quadratures becomes compromised and, as a result, a characteristic ovoid shape is observed when the field scan range is comparable to B^{+}_{sense}. For low external fields, the model predicts linear response, ideal for magnetic field measurements.

Despite a number of assumptions that have been made to derive this model, we find that it gives us a broad understanding of the various properties of the system. However, it may be hiding some important details in explaining the experimental results. One of the assumptions that we have made in this model is that we are dealing with pure quantum states. This is not the case since (as will be discussed in later chapters) the state that we prepare is a mixed state in the hot vapour case. Furthermore, the assumed choice of the input state may not be fully accurate since the model gives no description on the state preparation process with various decoherence effects due atomic collisions, gradient fields, light power, temperature effects etc. This makes it difficult to assess the contribution these important parameters may have and how they influence the OPM response over a range of values that may be present in the experiment. Moreover, another important assumption that we have made in our model is that our prepared dressed-state follows the effective field $\mathbf{B}_{\mathrm{eff}}$ adiabatically allowing us to define the adiabatic angle θ. In reality, this assumption is valid only

in cases where the rate of change of the effective field $\mathbf{B}_{\text{eff}}$ is much smaller than the Larmor frequency of precession, namely

$$|\dot{\theta}| \ll \mu_B g_F |\mathbf{B}_{\text{eff}}|/\hbar. \tag{3.46}$$

In the next section, we develop an approach which takes into account of most of the effects which we have neglected so far. The model is based on the Heisenberg equation of motion of the atomic spin $\hat{F}$ which includes phenomenological state preparation/pumping terms as well as decoherence effects due to collisions and gradient fields.

3.2 Heisenberg interpretation of spin dynamics in a rf-dressed field

3.2.1 The Hamiltonian of a Spin in a radio-frequency dressed field

We begin with the same assumption outlined in the previous section about the spin-field interaction Hamiltonian

$$\hat{H} = -\frac{\mu_B g_F}{\hbar}\hat{\mathbf{F}} \cdot \mathbf{B}. \tag{3.47}$$

In the radio-frequency dressed scenario, we set the magnetic field to have the following form

$$\mathbf{B} = (B_{\text{rf}} \cos\omega_{\text{rf}} t + B_x^{\text{ext}})\mathbf{e}_x + B_y^{\text{ext}}\mathbf{e}_y + (B_{\text{dc}} + B_z^{\text{ext}})\mathbf{e}_z, \tag{3.48}$$

where B_{rf} is the amplitude of the rf-field and B_{dc} is the static field along the longitudinal direction which are experimentally controlled. Additionally, we have the external fields B_i^{ext} with $i = x, y$ and z, which originate from external sources. Substituting the expression for the field and letting $g'_F = g_F/\hbar$ and $\Omega_i = \mu_B g'_F B_i$ with $i = \text{rf}, \text{dc}, x, y$ and z the Hamiltonian takes the following form

$$\hat{H}(t) = (\Omega_{\text{rf}} \cos(\omega_{\text{rf}} t) + \Omega_x^{\text{ext}})\hat{F}_x(t) + \Omega_y^{\text{ext}}\hat{F}_y(t) + (\Omega_{\text{dc}} + \Omega_z^{\text{ext}})\hat{F}_z(t). \tag{3.49}$$

We want to understand how the spin operators evolve in time subject to these external fields, i.e. we want to obtain a time dependent equation of motion of the spin operators, since they are our experimental observables. To do this, we apply the formalism of the Heisenberg representation

$$\frac{d\hat{F}_i(t)}{dt} = -\frac{i}{\hbar}\left[\hat{F}_i(t), \hat{H}(t)\right], \tag{3.50}$$

which after evaluation we obtain

$$\frac{d\hat{F}_x(t)}{dt} = -(\Omega_{\text{dc}} + \Omega_z^{\text{ext}})\hat{F}_y(t) + \Omega_y^{\text{ext}}\hat{F}_z(t), \tag{3.51}$$

$$\frac{d\hat{F}_y(t)}{dt} = (\Omega_{\text{dc}} + \Omega_z^{\text{ext}})\hat{F}_x(t) - (\Omega_{\text{rf}} \cos(\omega_{\text{rf}} t) + \Omega_x^{\text{ext}})\hat{F}_z(t), \tag{3.52}$$

$$\frac{d\hat{F}_z(t)}{dt} = -\Omega_y^{\text{ext}}\hat{F}_x(t) + (\Omega_{\text{rf}} \cos(\omega_{\text{rf}} t) + \Omega_x^{\text{ext}})\hat{F}_y(t). \tag{3.53}$$

a) Collisions b) Pumping

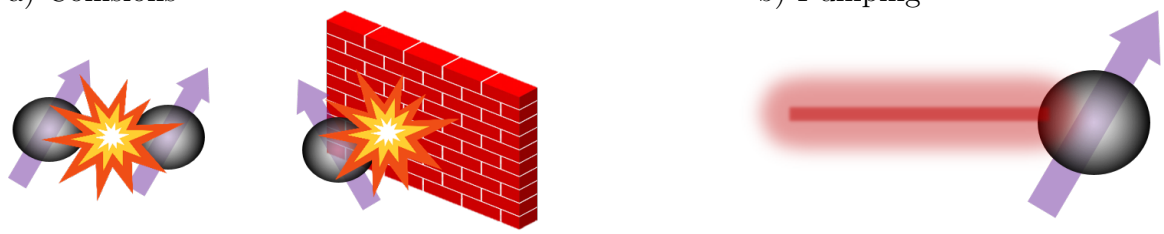

Figure 3.5: a) Due to the thermal motion of the atoms, there will be collisions between the atoms themselves as well as the collisions between the atoms and the cell walls. These two processes introduce decoherence by depolarising the atoms from the initially prepared state. b) Atoms, initially in a thermal state are optically pumped in order to make the spin precession sensitive to the external magnetic fields. The pumping may have a time dependent and arbitrary intensity profile which influences the final atomic state to which the atoms will be prepared.

The above system of equations can be conveniently expressed in the matrix form

$$\begin{bmatrix} \partial_t \hat{F}_x(t) \\ \partial_t \hat{F}_y(t) \\ \partial_t \hat{F}_z(t) \end{bmatrix} = \begin{bmatrix} 0 & -\Omega_{\mathrm{dc}} - \Omega_z^{\mathrm{ext}} & \Omega_y^{\mathrm{ext}} \\ \Omega_{\mathrm{dc}} + \Omega_z^{\mathrm{ext}} & 0 & -\Omega_{\mathrm{rf}} \cos(\omega_{\mathrm{rf}} t) - \Omega_x^{\mathrm{ext}} \\ -\Omega_y^{\mathrm{ext}} & \Omega_{\mathrm{rf}} \cos(\omega_{\mathrm{rf}} t) + \Omega_x^{\mathrm{ext}} & 0 \end{bmatrix} \cdot \begin{bmatrix} \hat{F}_x(t) \\ \hat{F}_y(t) \\ \hat{F}_z(t) \end{bmatrix}, \tag{3.54}$$

which we can write in a more compact form

$$\left. \frac{d\hat{\mathbf{F}}(t)}{dt} \right|_{\mathrm{coher}} = (\mathbf{B}_0(t) + \mathbf{B}_{\mathrm{ext}}^{(0)})\hat{\mathbf{F}}(t), \tag{3.55}$$

where

$$\mathbf{B}_0(t) = \begin{bmatrix} 0 & -\Omega_{\mathrm{dc}} & \\ \Omega_{\mathrm{dc}} & 0 & -\Omega_{\mathrm{rf}} \cos(\omega_{\mathrm{rf}} t) \\ 0 & \Omega_{\mathrm{rf}} \cos(\omega_{\mathrm{rf}} t) & 0 \end{bmatrix}, \tag{3.56}$$

$$\mathbf{B}_{\mathrm{ext}}^{(0)} = \begin{bmatrix} 0 & -\Omega_z^{\mathrm{ext}} & \Omega_y^{\mathrm{ext}} \\ \Omega_z^{\mathrm{ext}} & 0 & -\Omega_x^{\mathrm{ext}} \\ -\Omega_y^{\mathrm{ext}} + & \Omega_x^{\mathrm{ext}} & 0 \end{bmatrix}. \tag{3.57}$$

This equation of motion governs the dynamics of the spin in a radio-frequency dressed field and can be solved using the Floquet expansion which will be discussed in detail in the follow up sections. However this picture is not complete since experimentally, a number of processes including the pumping cycle and collisions affect the spin dynamics and therefore will influence the magnetometer response.

3.2.2 Spin dynamics with Collisions and Pumping

The most common approach used to describe the evolution of the spin dynamics is through the Bloch equations [56]. It is a powerful phenomenological model that

takes into account pumping and decoherence of precessing spins. For a polarised spin $P_i = \left\langle \hat{F}_i \right\rangle$ the optical Bloch equation of motion is given by

$$\frac{d\mathbf{P}}{dt} = \gamma \mathbf{B} \times \mathbf{P} - \frac{1}{T_2}(P_x \mathbf{e}_x + P_y \mathbf{e}_y) - \frac{1}{T_1}(P_z - P_0), \tag{3.58}$$

where γ is proportional to the Larmor frequency and the polarisation vector is $\mathbf{P} = (P_x, P_y, P_z)$ with $P_i = \left\langle \hat{F}_i \right\rangle$. The decoherence T_1 accounts for relaxation of the spins along the longitudinal direction from magnetic field gradient, collisions with the walls and atoms that are pumped with spin polarisation P_0. From the results derived in our light-matter interaction chapter, solving the Bloch equations would allows us to model the magnetometer response for the Faraday effect

$$\left\langle \hat{S}_x^{\text{out}} \right\rangle = -g_F^{(1)} S_y n_F \left\langle \hat{F}_z \right\rangle. \tag{3.59}$$

However, the observables that determine the Voigt effect are not linear like in the Faraday effect, but instead are bi-linear $\left\langle \hat{F}_i^2(t) \right\rangle$ and so their dynamics cannot be modelled using the Bloch equations. Thus, we need a new approach in order to see how the decoherence and pumping enter the equations of motion of the second order moments.

We begin to describe our approach by first starting with decoherence effects. Thermal atoms colliding in a space of finite volume (without any buffer gases) have ballistic trajectories and occasionally collide with each other as well as the cell walls. These collisions result in the atomic spin depolarisation. The energy provided by the thermal bath is driving these collisions which in turn dissipate this energy - in other words, there exists a fluctuation-dissipation type process which is random by nature. We can model this random process using the Langevin equation of motion [57]. We take the spin operator term and embed it into a large reservoir which causes the system to relax due to the interaction with the Langevin forces which in our case are the collisions with the assumption that they can be modelled by a pure white noise process. Thus, the Langevin forces of our operators can be written as follows (excluding the coherent spin dynamics terms) [32, 57]:

$$\left.\frac{d\hat{\mathbf{F}}(t)}{dt}\right|_{\Gamma_{\text{rel}}} = -\mathbf{\Gamma}_{\text{rel}} \hat{\mathbf{F}}(t) + \hat{\mathcal{F}}(t), \tag{3.60}$$

where the Langevin force satisfies the following relations

$$\left\langle \hat{\mathcal{F}}(t) \right\rangle = 0, \tag{3.61}$$

$$\left\langle \hat{\mathcal{F}}(t) \hat{\mathcal{F}}(t') \right\rangle = \mathbf{\Gamma}_{\text{rel}} \delta(t - t'), \tag{3.62}$$

with the relaxation matrix given by

$$\mathbf{\Gamma}_{\text{rel}} = \begin{bmatrix} \Gamma_x & 0 & \\ 0 & \Gamma_y & 0 \\ 0 & 0 & \Gamma_z \end{bmatrix}, \tag{3.63}$$

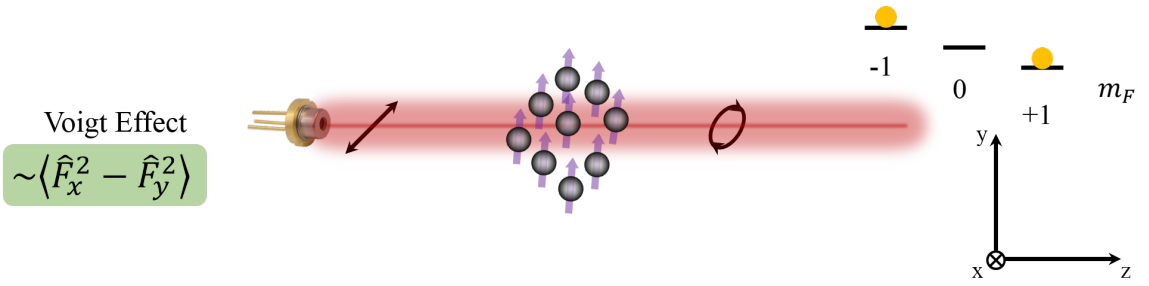

Figure 3.6: In the Voigt effect measurements, the state preparation process results in a mixed state with atoms accumulating in the extreme ends of the their corresponding hyperfine states. This prepared state has a mean value of $\left\langle \hat{F}_z(t) \right\rangle = 0$ so the dynamics described by the first order equation of motion would not be able to give us useful information about the magnetometer response.

where the relaxation processes in general have relaxation rates that are different in transverse and longitudinal directions. Commonly it is considered that the transverse direction is affected equally by spin exchange collisions such that $\Gamma_x = \Gamma_y = \Gamma_2$. On the other hand, processes like wall collisions, decoherence induced by the pump and magnetic field gradients, may relax the longitudinal direction at a different rate, given by $\Gamma_z = \Gamma_1$ [49, 56].

To describe the pumping, we employ a similar model based also on Langevin dynamics where we introduce some average input state, $\left\langle \hat{\mathbf{F}}^{\text{in}} \right\rangle$ (state that we ideally expect to prepare) that is not dependent on the input dynamics with a randomly fluctuating force $\hat{\mathcal{F}}^{\text{in}}(t)$ which causes spin flips satisfying the following relations

$$\left\langle \hat{\mathcal{F}}^{\text{in}}(t) \right\rangle = 0, \tag{3.64}$$

$$\left\langle \hat{\mathcal{F}}^{\text{in}}(t) \hat{\mathcal{F}}^{\text{in}}(t') \right\rangle = \Gamma_p(t) \delta(t - t'). \tag{3.65}$$

The Langevin equation for pumping then takes the form

$$\left. \frac{d\hat{\mathbf{F}}(t)}{dt} \right|_{\Gamma_p} = -\Gamma_p(t) \left(\hat{\mathbf{F}}(t) - \left\langle \hat{\mathbf{F}}^{\text{in}} \right\rangle \right) + \hat{\mathcal{F}}^{\text{in}}(t), \tag{3.66}$$

where $\Gamma_p(t)$ is a time dependent pumping rate. The operator $\hat{\mathbf{F}}^{\text{in}}$ is given simply by the spin-1 angular momentum operators:

$$\hat{\mathbf{F}}^{\text{in}} = \begin{bmatrix} \hat{F}_x(0) \\ \hat{F}_y(0) \\ \hat{F}_z(0) \end{bmatrix}. \tag{3.67}$$

By combining the coherent, pumping and collisional spin dynamics, we obtain the full equation of motion of the spin operators

$$\left.\frac{d\hat{\mathbf{F}}(t)}{dt}\right|_{\text{Tot}} = \left.\frac{d\hat{\mathbf{F}}(t)}{dt}\right|_{\text{coher}} + \left.\frac{d\hat{\mathbf{F}}(t)}{dt}\right|_{\Gamma_p} + \left.\frac{d\hat{\mathbf{F}}(t)}{dt}\right|_{\Gamma_{\text{rel}}}. \tag{3.68}$$

Substituting in the terms yields

$$\left.\frac{d\hat{\mathbf{F}}(t)}{dt}\right|_{\text{Tot}} = (\mathbf{B}_0(t) + \mathbf{B}_{\text{ext}}^{(0)})\hat{\mathbf{F}}(t) - \Gamma_p(t)\left(\hat{\mathbf{F}}(t) - \left\langle\hat{\mathbf{F}}^{\text{in}}\right\rangle\right) + \hat{\mathcal{F}}^{\text{in}}(t) - \mathbf{\Gamma}_{\text{rel}}\hat{\mathbf{F}}(t) + \hat{\mathcal{F}}(t). \tag{3.69}$$

In principle, solving this equation of motion in some conditions, whether being in the steady state or time dependent and dynamical form it would allow us to extract the necessary information of the spin dynamics of the magnetometer. This would mean that to solve the equation above we would need to choose some state by taking the expectation value

$$\left\langle\frac{d\hat{\mathbf{F}}(t)}{dt}\right\rangle = (\mathbf{B}_0(t) + \mathbf{B}_{\text{ext}}^{(0)})\left\langle\hat{\mathbf{F}}(t)\right\rangle - \Gamma_p(t)\left(\left\langle\hat{\mathbf{F}}(t)\right\rangle - \left\langle\hat{\mathbf{F}}^{\text{in}}\right\rangle\right) + \left\langle\hat{\mathcal{F}}^{\text{in}}(t)\right\rangle - \mathbf{\Gamma}_{\text{rel}}\left\langle\hat{\mathbf{F}}(t)\right\rangle + \left\langle\hat{\mathcal{F}}(t)\right\rangle. \tag{3.70}$$

As a consequence of the Langvein dynamics, the stochastic forces are zero, and so the equation of motion above reduces to

$$\left\langle\frac{d\hat{\mathbf{F}}(t)}{dt}\right\rangle = (\mathbf{B}_0(t) + \mathbf{B}_{\text{ext}}^{(0)})\left\langle\hat{\mathbf{F}}(t)\right\rangle - \Gamma_p(t)\left(\left\langle\hat{\mathbf{F}}(t)\right\rangle - \left\langle\hat{\mathbf{F}}^{\text{in}}\right\rangle\right) - \mathbf{\Gamma}_{\text{rel}}\left\langle\hat{\mathbf{F}}(t)\right\rangle. \tag{3.71}$$

Which corresponds to the Bloch equation (3.58) on page 41. However, recall that the measurement of the Voigt effect in terms of Stokes' operators is given by

$$\left\langle\hat{S}_z'(t)\right\rangle = g_F^{(2)} S_y n_F \left\langle\hat{F}_x^2(t) - \hat{F}_y^2(t)\right\rangle, \tag{3.72}$$

and in general $\left\langle\hat{F}_i(t)\right\rangle^2 \neq \left\langle\hat{F}_i^2(t)\right\rangle$. As a result, we cannot use the equation of motion derived above which is typically used in the Faraday type magnetometry in order to model the magnetometer response in the Voigt configuration. We need to be able to derive the second order moment equation which governs the time dependent dynamics of $\left\langle\partial_t\hat{F}_i^2(t)\right\rangle$.

3.2.3 Covariance Matrix and the Second Order Moments

Experimentally, our observables correspond to the second moments of the angular momentum operators i.e. in the lab frame the measurements have the form of $\langle\hat{F}_x^2(t) - \hat{F}_y^2(t)\rangle$. The autocorrelation function $\sigma(t, t+\tau)$ provides the information about the correlation of the second moments and how they evolve in time. In our case,

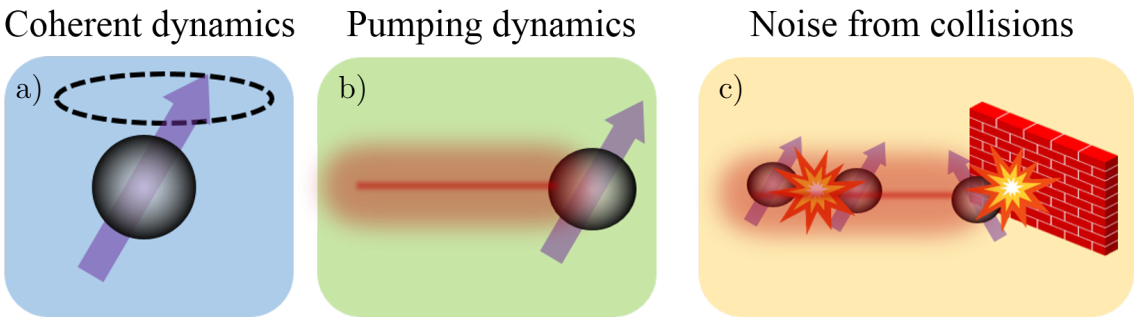

Figure 3.7: Three components that govern the total spin dynamics. a) Spin-Field interaction. b) Spin-Pump Field interaction. c) Spin Depolarisation through pumping and atomic collisions.

we define the autocorrelation function function in terms of our angular momentum operators:

$$\sigma(t, t+\tau) = \left\langle \hat{\mathbf{F}}(t)\ \hat{\mathbf{F}}^T(t+\tau) \right\rangle$$

$$= \begin{bmatrix} \left\langle \hat{F}_x(t)\hat{F}_x^T(t+\tau)\right\rangle & \left\langle \hat{F}_x(t)\hat{F}_y^T(t+\tau)\right\rangle & \left\langle \hat{F}_x(t)\hat{F}_z^T(t+\tau)\right\rangle \\ \left\langle \hat{F}_y(t)\hat{F}_x^T(t+\tau)\right\rangle & \left\langle \hat{F}_y(t)\hat{F}_y^T(t+\tau)\right\rangle & \left\langle \hat{F}_y(t)\hat{F}_z^T(t+\tau)\right\rangle \\ \left\langle \hat{F}_z(t)\hat{F}_x^T(t+\tau)\right\rangle & \left\langle \hat{F}_z(t)\hat{F}_y^T(t+\tau)\right\rangle & \left\langle \hat{F}_z(t)\hat{F}_z^T(t+\tau)\right\rangle \end{bmatrix}. \tag{3.73}$$

Since we are interested in the pure second moments and not the time correlation, we can set $\tau = 0$ which gives a simple expression for the matrix elements

$$\sigma_{ij}(t) = \left\langle \hat{F}_i(t)\ \hat{F}_j^T(t) \right\rangle, \tag{3.74}$$

where we can see that now our autocorrelation matrix contains the terms $\left\langle \hat{F}_x^2(t)\right\rangle$ and $\left\langle \hat{F}_y^2(t)\right\rangle$ that are contained in our expression for the Voigt effect. In addition, we want to understand the dynamics of the time evolution of the covariance matrix since it contains time dependent fields such as the rf-field and the pumping. To get the dynamics of the correlation function we simply take the time derivative of it. From the spin dynamics we can determine the dynamics of the second moment

$$\frac{d\sigma(t)}{dt} = \left\langle \frac{d\hat{\mathbf{F}}(t)}{dt}\ \hat{\mathbf{F}}^T(t) \right\rangle + \left\langle \hat{\mathbf{F}}(t)\ \frac{d\hat{\mathbf{F}}^T(t)}{dt} \right\rangle. \tag{3.75}$$

Substituting eq.(3.69) into the above expression yields

$$\frac{d\sigma(t)}{dt} = \mathbf{B}(t)\sigma(t) + \sigma(t)\mathbf{B}^T(t) - \Gamma_p(t)\left[2\sigma(t) - \left\langle \hat{\mathbf{F}}^{\text{in}} \right\rangle \left\langle \hat{\mathbf{F}}^T(t) \right\rangle - \left\langle \hat{\mathbf{F}}(t) \right\rangle \left\langle \hat{\mathbf{F}}^{\text{in}T} \right\rangle\right]$$
$$+ \left\langle \hat{\mathcal{F}}^{\text{in}}(t)\ \hat{\mathbf{F}}^T(t) \right\rangle + \left\langle \hat{\mathbf{F}}(t)\ \hat{\mathcal{F}}^{\text{in}T}(t) \right\rangle + \left\langle \hat{\mathcal{F}}(t)\ \hat{\mathbf{F}}^T(t) \right\rangle + \left\langle \hat{\mathbf{F}}(t)\ \hat{\mathcal{F}}^T(t) \right\rangle, \tag{3.76}$$

where we have defined $\mathbf{B}(t) = \mathbf{B}_0(t) + \mathbf{B}_{\text{ext}}^{(0)} - \Gamma_{\text{rel}}$. For states with $\left\langle \hat{\mathbf{F}}^{\text{in}} \right\rangle = 0$ (which are the kind of states we prepare in the experiment), the equation above reduces to (see Fig. 3.7 for illustration)

$$\begin{aligned}\frac{d\sigma(t)}{dt} = &\underbrace{\mathbf{B}(t)\sigma(t) + \sigma(t)\mathbf{B}^T(t)}_{\text{Coherent}} - \underbrace{2\Gamma_p(t)\sigma(t)}_{\text{Pumping}} \\ &+ \underbrace{\left\langle \hat{\mathcal{F}}^{\text{in}}(t)\ \hat{\mathbf{F}}^T(t) \right\rangle + \left\langle \hat{\mathbf{F}}(t)\ \hat{\mathcal{F}}^{\text{in}T}(t) \right\rangle}_{\text{Pump Noise}} \\ &+ \underbrace{\left\langle \hat{\mathcal{F}}(t)\ \hat{\mathbf{F}}^T(t) \right\rangle + \left\langle \hat{\mathbf{F}}(t)\ \hat{\mathcal{F}}^T(t) \right\rangle}_{\text{Thermal Noise}}. \end{aligned} \tag{3.77}$$

The first terms on the right hand side of the equation above containing $\mathbf{B}(t)$, describe the coherent dynamics between the spin and the magnetic field. The second expression containing $\Gamma_p(t)$ models the dynamics of the pumping process. The last two terms of the equation can be interpreted as the stochastic contributions due to the noise generated during the pumping process and the thermal state contribution from depolarised atoms which is a consequence of collisional effects.

Whilst we know the form of the coherent and pumping terms of the spin dynamics, the last two terms describing the noise induced due to the pump and collisions are unknown to us. Therefore, we need to find their exact contribution which we shall do in the following sections.

3.2.4 Spin Operator Collisional Diffusion Matrix

We want to derive an expression for the thermal noise component (which acts as a momentum diffusion coefficient) in the second moment equation of motion which takes the form

$$\mathcal{D} = \left\langle \hat{\mathcal{F}}(t)\ \hat{\mathbf{F}}^T(t) \right\rangle + \left\langle \hat{\mathbf{F}}(t)\ \hat{\mathcal{F}}^T(t) \right\rangle. \tag{3.78}$$

As described in the previous section, the spin relaxation process can be modelled using the Langevin equation of motion

$$\left.\frac{d\hat{\mathbf{F}}(t)}{dt}\right|_{\Gamma_{\text{rel}}} = -\mathbf{\Gamma}_{\text{rel}}\hat{\mathbf{F}}(t) + \hat{\mathcal{F}}(t), \tag{3.79}$$

where as before the relaxation matrix takes the form

$$\mathbf{\Gamma}_{\text{rel}} = \begin{bmatrix} \Gamma_x & 0 & \\ 0 & \Gamma_y & 0 \\ 0 & 0 & \Gamma_z \end{bmatrix}, \tag{3.80}$$

and the stochastic force operator satisfies

$$\left\langle \hat{\mathcal{F}}(t) \right\rangle = 0, \tag{3.81}$$

$$\left\langle \hat{\mathcal{F}}_i(t)\hat{\mathcal{F}}_j(t')\right\rangle = (\tilde{\mathbf{\Gamma}})_{ij}\delta(t-t'), \tag{3.82}$$

where the last expression corresponds to the relaxation matrix associated to the correlation matrix of the stochastic operators. This correlation matrix becomes relevant when the dynamics of the second order moment need to be considered. Here $\tilde{\mathbf{\Gamma}}$ is our diffusion matrix which we will now begin to calculate. Since the linear birefringence of the Voigt effect depends on the square operator dynamics, the stochastic effects, which are given by the mean square value, are not zero and therefore need to be accounted for in the spin dynamics. The Langevin equation of motion has a general solution of the form [57]:

$$u(t) = u(0)e^{-\gamma t} + e^{-\gamma t}\int_0^t e^{\gamma t'}\mathcal{F}_i(t')dt'. \tag{3.83}$$

Thus, if we take our operator equations from the above, we obtain the following general solution:

$$\hat{F}_i(t) = \hat{F}_i(0)e^{-\Gamma_i t} + e^{-\Gamma_i t}\int_0^t e^{\Gamma_i t'}\hat{\mathcal{F}}(t')dt'. \tag{3.84}$$

We assume that the reservoir has no memory i.e. it has a Markov property which is satisfied by the following relation

$$\langle \hat{\mathcal{F}}_i(t)\hat{\mathcal{F}}_j(t)\rangle = \Gamma_{ij}\delta(t-t'). \tag{3.85}$$

Here we adopt the approach from [33], to determine the diffusion matrix by integrating the solution of the spin operators given by eq. (3.79). Using this approach and the standard angular momentum commutator relations

$$\left[\hat{F}_i(t), \hat{F}_j(t)\right] = \epsilon_{ijk}\hat{F}_k(t), \tag{3.86}$$

where ϵ_{ijk} is the Levi-Civita tensor, after some algebra (see Appendix B.4 on page 181 for detailed calculation), the full $\tilde{\mathbf{\Gamma}}$-matrix reads:

$$\tilde{\mathbf{\Gamma}} = \begin{bmatrix} \Gamma_{xx} & \Gamma_{xy} & \Gamma_{xz} \\ \Gamma_{yx} & \Gamma_{yy} & \Gamma_{yz} \\ \Gamma_{zx} & \Gamma_{zy} & \Gamma_{zz} \end{bmatrix} = \begin{bmatrix} 2\Gamma_x\sigma^0_{xx} & (\Gamma_x+\Gamma_y)\sigma^0_{xy} & (\Gamma_x+\Gamma_z)\sigma^0_{xz} \\ (\Gamma_x+\Gamma_y)\sigma^0_{yx} & 2\Gamma_y\sigma^0_{yy} & (\Gamma_y+\Gamma_z)\sigma^0_{yz} \\ (\Gamma_x+\Gamma_z)\sigma^0_{zx} & (\Gamma_z+\Gamma_y)\sigma^0_{zy} & 2\Gamma_z\sigma^0_{zz} \end{bmatrix}, \tag{3.87}$$

which we can write in a simplified form

$$\tilde{\mathbf{\Gamma}} = \mathbf{\Gamma}_{\text{rel}}\sigma_0 + \sigma_0\mathbf{\Gamma}_{\text{rel}}, \tag{3.88}$$

where we have defined $\left\langle \hat{F}_i(t)\hat{F}_j^T(t)\right\rangle = \sigma_{ij}$. The $\tilde{\mathbf{\Gamma}}$ matrix is analogous to the diffusion coefficient which characterises the fluctuations of the Langevin forces acting on the operators $\hat{F}_i$ with Γ_i characterising the dissipation force acting on $\hat{F}_i$ [58]. In general each direction is subjected to different decoherence rates. As a result, it is commonly considered that the transverse direction is affected equally by spin exchange collisions such that $\Gamma_x = \Gamma_y = \Gamma_2$. On the other hand, processes like wall collision, decoherence induced by the pump and magnetic field gradients, may relax the longitudinal direction at a different rate, given by $\Gamma_z = \Gamma_1$.

Now we can substitute the solution to the first order moment spin dynamics into the momentum diffusion expression

$$\mathcal{D} = \left\langle \hat{\mathcal{F}}(t)\ \hat{\mathbf{F}}^T(t) \right\rangle + \left\langle \hat{\mathbf{F}}(t)\ \hat{\mathcal{F}}^T(t) \right\rangle, \tag{3.89}$$

with

$$\hat{\mathbf{F}}(t) = \int_{t_0}^{t} dt'\ \frac{d\hat{\mathbf{F}}(t')}{dt'}\bigg|_{\text{Tot}}, \tag{3.90}$$

substituting eq. (3.69) and integrating gives

$$\begin{aligned}\hat{\mathbf{F}}(t) =& \hat{\mathbf{F}}(t_0) + \int_{t_0}^{t} dt'[\mathbf{B}(t') + \mathbf{B}_{\text{ext}}(0) - \Gamma_p(t')]\hat{\mathbf{F}}(t') \\ &+ \int_{t_0}^{t} dt' \left[\Gamma_p(t') \left\langle \hat{\mathbf{F}}^{\text{in}} \right\rangle + \hat{\mathcal{F}}^{\text{in}}(t')\right] + \int_{t_0}^{t} dt' \hat{\mathcal{F}}(t').\end{aligned} \tag{3.91}$$

We can substitute this solution into the momentum diffusion eq. (3.89) terms

$$\begin{aligned}\left\langle \hat{\mathbf{F}}(t)\mathcal{F}^T(t) \right\rangle =& \left\langle \hat{\mathbf{F}}(t_0)\hat{\mathcal{F}}^T(t) \right\rangle + \int_{t_0}^{t} dt' \left[\mathbf{B}(t') + \mathbf{B}_{\text{ext}}^{(0)} - \Gamma_p(t')\right] \left\langle \hat{\mathbf{F}}(t')\hat{\mathcal{F}}^T(t) \right\rangle \\ &+ \int_{t_0}^{t} dt' \Gamma_p(t') \left\langle \hat{\mathbf{F}}^{\text{in}} \right\rangle \left\langle \hat{\mathcal{F}}^T(t) \right\rangle + \int_{t_0}^{t} dt' \left\langle \hat{\mathcal{F}}^{\text{in}}(t')\hat{\mathcal{F}}^T(t) \right\rangle + \int_{t_0}^{t} dt' \left\langle \hat{\mathcal{F}}(t')\hat{\mathcal{F}}^T(t) \right\rangle.\end{aligned} \tag{3.92}$$

We note that for white noise type stochastic operator, the correlation function between the stochastic operator and an observable $\hat{O}$ is zero, i.e.

$$\left\langle \hat{\mathbf{O}}(t')\hat{\mathcal{F}}^T(t) \right\rangle = \left\langle \hat{\mathbf{O}}(t') \right\rangle \left\langle \hat{\mathcal{F}}^T(t) \right\rangle = 0, \quad \forall\,[t, t']\,. \tag{3.93}$$

Physically, this is due to the fact that the system is embedded into an infinite size and memoryless bath, which produces the random force fluctuations. If the system possessed non-Markov property meaning that it had memory, the correlation between the observable and the stochastic forces would be non-zero. In other words, the interaction between the observable quantity $\hat{O}$ and the bath has no effect on the statistical properties of the bath. Additionally, the correlation between separate baths is also zero, thus

$$\left\langle \hat{\mathcal{F}}^{\text{in}}(t')\hat{\mathcal{F}}^T(t) \right\rangle = 0, \quad \forall\,[t, t']\,. \tag{3.94}$$

Once again, the stochastic processes with different physical origins are statistically independent of each other and mutually exclusive, resulting in no effective correlations between them since the two baths are not coupled through any physical process. We further note that for Langevin type forces $\left\langle \hat{\mathcal{F}}(t) \right\rangle = 0$. With this, eq. (3.92) reduces to

$$\left\langle \hat{\mathbf{F}}(t)\hat{\mathcal{F}}^T(t) \right\rangle = \int_{t_0}^{t} dt' \left\langle \hat{\mathcal{F}}(t')\hat{\mathcal{F}}^T(t) \right\rangle. \tag{3.95}$$

The operation for the transposed element is identical. This correlation function satisfies the Markov property which we derived in eq. (B.117). Substituting it for both terms gives (see eq. B.84 on page 181)

$$\left\langle \hat{\mathcal{F}}(t)\ \hat{\mathbf{F}}^T(t) \right\rangle + \left\langle \hat{\mathbf{F}}(t)\hat{\mathcal{F}}^T(t) \right\rangle = \int_{t_0}^{t} dt' \tilde{\mathbf{\Gamma}}(t)\ \delta(t'-t) + \int_{t_0}^{t} dt' \tilde{\mathbf{\Gamma}}(t')\ \delta(t-t'). \quad (3.96)$$

Now we apply a change of variables $t'' = t' - t$ for the first integral and $t'' = t - t'$ for the second integral. This yields

$$\left\langle \hat{\mathcal{F}}(t)\ \hat{\mathbf{F}}^T(t) \right\rangle + \left\langle \hat{\mathbf{F}}(t)\hat{\mathcal{F}}^T(t) \right\rangle = \int_{0}^{t-t_0} dt'' \tilde{\mathbf{\Gamma}}(t)\ \delta(t'') + \int_{-(t-t_0)}^{0} dt'' \tilde{\mathbf{\Gamma}}(t''+t)\ \delta(t''). \quad (3.97)$$

In our case, the relaxation process which models the rate of atomic collisions is a time independent process $\tilde{\mathbf{\Gamma}}(t) \to \tilde{\mathbf{\Gamma}}$ hence, the above integral reduces to

$$\left\langle \hat{\mathcal{F}}(t)\ \hat{\mathbf{F}}^T(t) \right\rangle + \left\langle \hat{\mathbf{F}}(t)\hat{\mathcal{F}}^T(t) \right\rangle = \tilde{\mathbf{\Gamma}} = \mathbf{\Gamma}_{\text{rel}}\sigma_0 + \sigma_0\mathbf{\Gamma}_{\text{rel}}. \quad (3.98)$$

Now, since the collisions depolarise our prepared state, we make the assumption that this depolarised state is thermal. In other words we let $\sigma \to \sigma_0$ such that

$$\hat{\rho}_0 = \frac{1}{2F+1} \begin{pmatrix} 1 & 0 & \cdots & 0 \\ 0 & 1 & \cdots & 0 \\ \vdots & \vdots & \ddots & \vdots \\ 0 & 0 & \cdots & 1 \end{pmatrix}, \quad (3.99)$$

with the thermal second order matrix element given by

$$\sigma_0^{ij} = \text{Tr}\left[\hat{\rho}_0 \hat{F}_i \hat{F}_j\right]. \quad (3.100)$$

Thus, the relaxation term of the second moment reads

$$\tilde{\mathbf{\Gamma}} = \left\langle \hat{\mathcal{F}}(t)\ \hat{\mathbf{F}}^T(t) \right\rangle + \left\langle \hat{\mathbf{F}}(t)\hat{\mathcal{F}}^T(t) \right\rangle = \mathbf{\Gamma}_{\text{rel}}\sigma_0 + \sigma_0\mathbf{\Gamma}_{\text{rel}}. \quad (3.101)$$

3.2.5 Spin Operator Pumping Diffusion Matrix

The next term we want to find a form for is the term due to the noise induced by the pumping process which results in random spin flips. In eq. (3.77) it is given by

$$\mathcal{D}_p = \left\langle \hat{\mathcal{F}}^{\text{in}}(t)\ \hat{\mathbf{F}}^T(t) \right\rangle + \left\langle \hat{\mathbf{F}}(t)\ \hat{\mathcal{F}}^{\text{in}_T}(t) \right\rangle. \quad (3.102)$$

As before, using the solution given in eq. (3.91) and substituting into the expression above and expanding (showing the work on the second term) gives

$$\left\langle \hat{\mathbf{F}}(t)\hat{\mathcal{F}}^{\text{in}_T}(t) \right\rangle = \left\langle \hat{\mathbf{F}}(t_0)\hat{\mathcal{F}}^{\text{in}_T}(t) \right\rangle + \int_{t_0}^{t} dt' \left[\mathbf{B}(t') + \mathbf{B}_{\text{ext}}^{(0)} - \Gamma_p(t')\right] \left\langle \hat{\mathbf{F}}(t')\hat{\mathcal{F}}^{\text{in}_T}(t) \right\rangle$$
$$+ \int_{t_0}^{t} dt' \Gamma_p(t') \left\langle \hat{\mathbf{F}}^{\text{in}} \right\rangle \left\langle \hat{\mathcal{F}}^{in_T}(t) \right\rangle + \int_{t_0}^{t} dt' \left\langle \hat{\mathcal{F}}^{\text{in}}(t')\hat{\mathcal{F}}^{\text{in}_T}(t) \right\rangle + \int_{t_0}^{t} dt' \left\langle \hat{\mathcal{F}}(t')\hat{\mathcal{F}}^{\text{in}_T}(t) \right\rangle. \quad (3.103)$$

Following the same reasoning, we assume the stochastic forces that produce random spin flips have the Markov property and are memoryless with no correlations between the observables $\hat{O}$ and the stochastic terms. In addition, other stochastic processes that are present in the system, but have different physical origin (i.e. collisions) are mutually exclusive and do not correlate, this implies

$$\left\langle \hat{\mathcal{F}}^{\text{in}_T}(t) \right\rangle = 0, \tag{3.104}$$

$$\left\langle \hat{\mathbf{F}}(t_0)\hat{\mathcal{F}}^{\text{in}_T}(t) \right\rangle = \left\langle \hat{\mathcal{F}}^{\text{in}}(t)\hat{\mathbf{F}}^{T}(t_i) \right\rangle = 0, \tag{3.105}$$

$$\left\langle \hat{\mathcal{F}}(t')\hat{\mathcal{F}}^{\text{in}_T}(t) \right\rangle = \left\langle \hat{\mathcal{F}}^{\text{in}}(t)\hat{\mathcal{F}}^{T}(t') \right\rangle = 0. \tag{3.106}$$

Thus, the spin operator pumping diffusion matrix reduces to

$$\mathcal{D}_p = \int_{t_0}^{t} dt' \left\langle \hat{\mathcal{F}}^{\text{in}}(t)\hat{\mathcal{F}}^{\text{in}_T}(t') \right\rangle + \int_{t_0}^{t} dt' \left\langle \hat{\mathcal{F}}^{\text{in}}(t')\hat{\mathcal{F}}^{\text{in}_T}(t) \right\rangle. \tag{3.107}$$

Using the correlation function derived in eq. (B.117) and substituting it for both terms given in the above

$$\left\langle \hat{\mathcal{F}}^{\text{in}}(t)\ \hat{\mathbf{F}}^{T}(t) \right\rangle + \left\langle \hat{\mathbf{F}}(t)\hat{\mathcal{F}}^{\text{in}_T}(t) \right\rangle = \int_{t_0}^{t} dt' \tilde{\mathbf{\Gamma}}_p(t)\ \delta(t'-t) + \int_{t_0}^{t} dt' \tilde{\mathbf{\Gamma}}_p(t')\ \delta(t-t'). \tag{3.108}$$

Applying a change of variables $t'' = t' - t$ (and $t'' = t - t'$ for the second integral) we have

$$\mathcal{D}_p = \int_{0}^{t-t_0} dt''\ \tilde{\mathbf{\Gamma}}_p(t)\delta(t'') + \int_{-(t-t_0)}^{0} dt''\ \tilde{\mathbf{\Gamma}}_p(t''+t)\delta(t''). \tag{3.109}$$

Now, our diffusion matrix for the spin flips is time dependent since it is dependent upon the rate of optical pumping $\Gamma_p(t)$. For a time dependent case it is then convenient to apply an $\epsilon > 0$ around zero, for a proper definition of the integral with a $\delta(t)$ function, such that

$$\mathcal{D}_p = \int_{\epsilon}^{t-t_0} dt''\ \tilde{\mathbf{\Gamma}}_p(t)\delta(t'') + \int_{-\epsilon}^{\epsilon} dt''\ \tilde{\mathbf{\Gamma}}_p(t)\delta(t'') + \int_{-(t-t_0)}^{-\epsilon} dt''\ \tilde{\mathbf{\Gamma}}_p(t''+t)\delta(t'') + \int_{-\epsilon}^{\epsilon} dt''\ \tilde{\mathbf{\Gamma}}_p(t''+t)\delta(t''). \tag{3.110}$$

From this, the first and third terms are zero since they are evaluated in a range of time where $\delta(t'') = 0$. The only non-zero contribution is given by

$$\mathcal{D}_p = \int_{-\epsilon}^{\epsilon} dt''\ [\tilde{\mathbf{\Gamma}}_p(t)\delta(t'') + \tilde{\mathbf{\Gamma}}_p(t''+t)\delta(t'')], \tag{3.111}$$

and consequently, we have

$$\mathcal{D}_p = 2\tilde{\mathbf{\Gamma}}_p(t) = (\mathbf{\Gamma}_p(t)\sigma_{\text{in}} + \sigma_{\text{in}}\mathbf{\Gamma}_p(t)). \tag{3.112}$$

Here $\Gamma_p(t)$ is the pump matrix rate, which can take any form in time. For convenience, we can express this arbitrary pump rate as harmonic superposition, namely

$$\Gamma_p(t) = \Gamma_p^{(0)} + \Gamma_p^{(1)} e^{i\omega_{\rm rf} t} + \Gamma_p^{(-1)} e^{-i\omega_{\rm rf} t} + \Gamma_p^{(2)} e^{2i\omega_{\rm rf} t} + \Gamma_p^{(-2)} e^{-2i\omega_{\rm rf} t} + \cdots . \tag{3.113}$$

The spectral distribution and the values of these coefficients depends on the pumping profile that is used to prepare the atomic state, such that for example, for a square wave intensity profile of frequency $\omega_{\rm rf}$ and duty cycle, d, the coefficients take the form

$$\Gamma_p^{(0)} = \Gamma_b \; d, \tag{3.114}$$

$$\Gamma_p^{(n)} = \Gamma^{(-n)} = \frac{\Gamma_b}{n\pi} \sin(n\pi d). \tag{3.115}$$

where Γ_b is the amplitude of the pumping rate. For completeness, the pumping rate matrix is simply given by

$$\mathbf{\Gamma}_p(t) = \Gamma_p(t)\mathbf{I}, \tag{3.116}$$

where $\mathbf{I}$ is the identity matrix. Using the expression above and combining it with eq. (3.112), the diffusion matrix for spin flips is given by

$$\mathcal{D}_p = 2\Gamma_p(t)\mathbf{I}\sigma_{\rm in}. \tag{3.117}$$

In the ideal scenario, the pumping process prepares the state such that it is sensitive to the external magnetic fields. In our experiment, we choose such a state to be a mixed state which when prepared in the x-basis has the following density operator form

$$\hat{\rho}_{\rm in}^x = \begin{pmatrix} \frac{1}{2} & 0 & 0 & 0 & 0 \\ 0 & 0 & 0 & 0 & 0 \\ 0 & 0 & 0 & 0 & 0 \\ 0 & 0 & 0 & 0 & 0 \\ 0 & 0 & 0 & 0 & \frac{1}{2} \end{pmatrix}. \tag{3.118}$$

Now the light propagation is along the z-basis so we need to transform the above state. In order to transform to another basis, we need to perform a unitary transformation on $\hat{\rho}_{\rm in}^x$

$$\hat{\rho}_{\rm in}^z = \hat{U}^\dagger \hat{\rho}_{\rm in}^x \hat{U}, \tag{3.119}$$

where

$$\hat{U} = |\psi\rangle_z \langle\psi|_z , \tag{3.120}$$

which is an outer product of the normalised eigenvectors of the $\hat{F}_x$ matrix in the z-basis. The unitary transformation has the form:

$$\hat{U} = \begin{pmatrix} \frac{1}{4} & \frac{1}{2} & \frac{\sqrt{6}}{4} & \frac{1}{2} & \frac{1}{4} \\ -\frac{1}{2} & -\frac{1}{2} & 0 & \frac{1}{2} & \frac{1}{2} \\ \frac{\sqrt{6}}{4} & 0 & \frac{1}{2} & 0 & \frac{\sqrt{6}}{4} \\ -\frac{1}{2} & \frac{1}{2} & 0 & -\frac{1}{2} & \frac{1}{2} \\ \frac{1}{4} & -\frac{1}{2} & \frac{\sqrt{6}}{4} & -\frac{1}{2} & \frac{1}{4} \end{pmatrix}. \tag{3.121}$$

Thus, the stochastic nature of the interaction between the pump beam and the input state will flip such a spin. In this case, we define our second order moment input state σ_{in} matrix element

$$\sigma_{\text{in}}^{ij} = \left\langle \hat{F}_i(0)\hat{F}_j^T(0) \right\rangle = \text{Tr}\left[\hat{\rho}_{\text{in}}^z \hat{F}_i \hat{F}_j\right], \tag{3.122}$$

where the $\hat{\rho}_{\text{in}}^z$ is expressed in the basis where the measurement takes place. Hence, the final diffusion matrix form that models random spin flips due to the pump process is

$$\mathcal{D}_p = 2\Gamma_p(t)\mathbf{I}\sigma_{\text{in}}. \tag{3.123}$$

We have derived the expressions for the decoherence effects due to atomic collisions and pumping based on the Langevin dynamics where the stochastic forces have a zero mean value and a delta function correlation which is stationary in time. Moreover, the random forces follow a Gaussian distribution of values. The second order moment equation is now fully defined. The next steps are to solve it with some well defined boundary conditions that are experimentally meaningful.

3.2.6 Spin Dynamics in the Liouville Space

The complete second order moment dynamics reads

$$\frac{d\sigma(t)}{dt} = \mathbf{B}(t)\sigma(t) + \sigma(t)\mathbf{B}^T(t) - 2\Gamma_p(t)\left[\sigma(t) - \sigma_{\text{in}}\right] + \mathbf{\Gamma}_{\text{rel}}\sigma_0 + \sigma_0\mathbf{\Gamma}_{\text{rel}}. \tag{3.124}$$

We would like to solve the second moment dynamics for σ which contains the information about the operators $\left\langle \hat{F}_i^2(t) \right\rangle$ used for the Voigt effect. However, the equation above cannot be trivially solved for a number of reasons. First of all, the second order moments σ are square matrices. The form of this equation does not have a simple set of coupled linear equations of motion which would be trivial to solve by finding an inverse matrix. Moreover, matrix multiplication is non-commutative i.e. $\mathbf{AB} \neq \mathbf{BA}$ and so we can not trivially rearrange the equation above for the σ_i terms to be on the right hand side of the other operators. A standard procedure to overcome this is to transform the above equation of motion into Liouville space. This converts σ_i which is a square matrix ($n \times n$, where n is the matrix dimension) into $\sigma_i \rightarrow \mathbf{X}$ which is a vector ($n^2 \times 1$). Consider the following, we have a case where an $n \times n$ operator acts on an $n \times n$ state which in our case is σ_i. Trivially, this can be expressed as

$$\sigma' = \mathbf{A}\sigma\mathbf{B}, \tag{3.125}$$

where $\mathbf{A}$, $\mathbf{B}$ and σ are all square matrices of the same dimension. For example, using the terms in eq. (3.124) we could write

$$\sigma_0\mathbf{\Gamma}_{\text{rel}} = \mathbf{I}\sigma_0\mathbf{\Gamma}_{\text{rel}}, \tag{3.126}$$

and

$$\mathbf{\Gamma}_{\text{rel}}\sigma_0 = \mathbf{\Gamma}_{\text{rel}}\sigma_0\mathbf{I}, \tag{3.127}$$

where $\mathbf{I}$ is the identity matrix. In the Liouville space, we can find a superoperator such that

$$\hat{\hat{\mathcal{L}}}\sigma_{\mathcal{L}} = \left(\mathbf{B}^T \otimes \mathbf{A}\right)\sigma_{\mathcal{L}}, \tag{3.128}$$

where $\hat{\hat{\mathcal{L}}}$ is an $n^2 \times n^2$ square matrix operating on the density operator transformed in the Liouville space which is now a $n^2 \times 1$ vector. Here the tensor product for square matrices is defined as

$$\begin{bmatrix} a_{1,1} & a_{1,2} \\ a_{2,1} & a_{2,2} \end{bmatrix} \otimes \begin{bmatrix} b_{1,1} & b_{1,2} \\ b_{2,1} & b_{2,2} \end{bmatrix} = \begin{bmatrix} a_{1,1}\begin{bmatrix} b_{1,1} & b_{1,2} \\ b_{2,1} & b_{2,2} \end{bmatrix} & a_{1,2}\begin{bmatrix} b_{1,1} & b_{1,2} \\ b_{2,1} & b_{2,2} \end{bmatrix} \\ a_{2,1}\begin{bmatrix} b_{1,1} & b_{1,2} \\ b_{2,1} & b_{2,2} \end{bmatrix} & a_{2,2}\begin{bmatrix} b_{1,1} & b_{1,2} \\ b_{2,1} & b_{2,2} \end{bmatrix} \end{bmatrix}$$

$$= \begin{bmatrix} a_{1,1}b_{1,1} & a_{1,1}b_{1,2} & a_{1,2}b_{1,1} & a_{1,2}b_{1,2} \\ a_{1,1}b_{2,1} & a_{1,1}b_{2,2} & a_{1,2}b_{2,1} & a_{1,2}b_{2,2} \\ a_{2,1}b_{1,1} & a_{2,1}b_{1,2} & a_{2,2}b_{1,1} & a_{2,2}b_{1,2} \\ a_{2,1}b_{2,1} & a_{2,1}b_{2,2} & a_{2,2}b_{2,1} & a_{2,2}b_{2,2} \end{bmatrix}. \tag{3.129}$$

Additionally, we distinguish the Liouville operators in cases where the matrix operators act on the operator σ_i from the left or the right, i.e.

$$\hat{\mathbf{O}}\ \sigma \rightarrow \mathcal{L}(\hat{\mathbf{O}})\mathbf{X}, \tag{3.130}$$

$$\sigma\ \hat{\mathbf{O}} \rightarrow \mathcal{R}(\hat{\mathbf{O}})\mathbf{X}. \tag{3.131}$$

Using these results and applying them to eq. (3.124) we transform into the Liouville space

$$\frac{d\mathbf{X}(t)}{dt} = \mathbf{C}(t)\mathbf{X}(t) - 2\Gamma_p(t)\ [\mathbf{X}(t) - \mathbf{X}_{\text{in}}] + \Lambda_{\text{rel}}\ \mathbf{X}_0, \tag{3.132}$$

where we have defined

$$\mathbf{C}(t) = \mathcal{L}(\mathbf{B}(t)) + \mathcal{R}(\mathbf{B}(t)^T), \tag{3.133}$$

$$\Lambda_{\text{rel}} = \mathcal{L}(\mathbf{\Gamma}_{\text{rel}}) + \mathcal{R}(\mathbf{\Gamma}_{\text{rel}}), \tag{3.134}$$

with the second moment matrices which now have a vector form

$$\mathbf{X}(t) = \begin{bmatrix} \left\langle \hat{F}_x(t)\hat{F}_x^T(t) \right\rangle \\ \left\langle \hat{F}_x(t)\hat{F}_y^T(t) \right\rangle \\ \vdots \\ \left\langle \hat{F}_z(t)\hat{F}_z^T(t) \right\rangle \end{bmatrix}, \tag{3.135}$$

and

$$\mathbf{X}_{\text{in}} = \begin{bmatrix} \left\langle \hat{F}_x(0)\hat{F}_x^T(0) \right\rangle \\ \left\langle \hat{F}_x(0)\hat{F}_y^T(0) \right\rangle \\ \vdots \\ \left\langle \hat{F}_z(0)\hat{F}_z^T(0) \right\rangle \end{bmatrix} = \begin{bmatrix} \text{Tr}(\hat{\rho}_{\text{in}}^z \hat{F}_x \hat{F}_x) \\ \text{Tr}(\hat{\rho}_{\text{in}}^z \hat{F}_x \hat{F}_y) \\ \vdots \\ \text{Tr}(\hat{\rho}_{\text{in}}^z \hat{F}_z \hat{F}_z) \end{bmatrix} = \begin{bmatrix} 4 \\ 0 \\ 0 \\ 0 \\ 1 \\ 0 \\ 0 \\ 0 \\ 1 \end{bmatrix}, \tag{3.136}$$

with the thermal state given by

$$\mathbf{X}_0 = \begin{bmatrix} \mathrm{Tr}(\hat{\rho}_0 \hat{F}_x \hat{F}_x) \\ \mathrm{Tr}(\hat{\rho}_0 \hat{F}_x \hat{F}_y) \\ \vdots \\ \mathrm{Tr}(\hat{\rho}_0 \hat{F}_z \hat{F}_z) \end{bmatrix} = \begin{bmatrix} 2 \\ 0 \\ 0 \\ 0 \\ 2 \\ 0 \\ 0 \\ 0 \\ 2 \end{bmatrix}, \tag{3.137}$$

where $\hat{\rho}_0$ is given in eq. (3.99) on page 48. Note that we didn't need to change the basis for the thermal state since it has a form of an identity matrix with a numerical factor, and any matrix transformation on an identity matrix produces no effect on the identity matrix itself.

Now, the eq. (3.132) which we transformed in the Liouville space has a form that could in principle be solved using matrix methods in some conditions. However, we immediately encounter a problem because the radio-frequency field as well as the pumping fields have a time dependent profile which prevent us from using trivial methods to solve this first order differential equation.

3.2.7 Spin Dynamics in the Floquet Space

Recall that in the Liouville space the second moment dynamics are given by

$$\frac{d\mathbf{X}(t)}{dt} = \mathbf{C}(t)\mathbf{X}(t) - 2\Gamma_p(t)\,[\mathbf{X}(t) - \mathbf{X}_{\mathrm{in}}] + \Lambda_{\mathrm{rel}}\,\mathbf{X}_0. \tag{3.138}$$

In order to solve this time dependent dynamical equation, we propose to employ a Floquet expansion. We start by showing that we can spectrally decompose the coherent dynamics and the pumping into its harmonics, namely, we can write

$$\mathbf{C}(t) = \mathbf{C}^{(0)} + \mathbf{C}^{(1)}\, e^{i\omega_{\mathrm{rf}}t} + \mathbf{C}^{(-1)}\, e^{-i\omega_{\mathrm{rf}}t}, \tag{3.139}$$

and

$$\Gamma_p(t) = \Gamma_p^{(0)} + \Gamma_p^{(1)} e^{i\omega_{\mathrm{rf}}t} + \Gamma_p^{(-1)} e^{-i\omega_{\mathrm{rf}}t} + \Gamma_p^{(2)} e^{2i\omega_{\mathrm{rf}}t} + \Gamma_p^{(-2)} e^{-2i\omega_{\mathrm{rf}}t} + \cdots = \sum_{n=0} \Gamma_p^{(n)} e^{in\omega_{\mathrm{rf}}t}. \tag{3.140}$$

Note that that these operator functions obey periodic properties which satisfy

$$\mathbf{C}(t+T) = \mathbf{C}(t), \tag{3.141}$$

$$\Gamma_p(t+T) = \Gamma_p(t), \tag{3.142}$$

where T is the time period of the system. The properties of periodicity of our dynamical system satisfy Floquet's theorem. In the context of quantum mechanics and more

specifically, the formalism of the Heisenberg equation of motion which we are dealing with here, the theorem states that if we have first-order linear differential equation of the form

$$\begin{aligned}\partial_t \hat{F}(t) &= -i[\hat{H}(t), \hat{F}(t)] \\ &= -i\hat{\hat{\mathcal{L}}}(t)\mathbf{X}(t),\end{aligned} \tag{3.143}$$

where $\hat{\hat{\mathcal{L}}}(t)$ is the Liouvillian superoperator and $\mathbf{X}(t)$ is our second order moment in the Liouville space, then we can transform the time dependent Liouvillian $\hat{\hat{\mathcal{L}}}(t)$ into a time independent Liouvillian by expanding the original Liouvillian as a Fourier series [59, 60].

$$\hat{\hat{\mathcal{L}}}(t) = \sum_{j=-\infty}^{\infty} \hat{\hat{\mathcal{L}}}_j e^{ij\omega_{\mathrm{rf}}t}, \tag{3.144}$$

where the time dependent Liouvillian satisfies the periodicity condition $\hat{\hat{\mathcal{L}}}(t+T) = \hat{\hat{\mathcal{L}}}(t)$ and T is the time period of the system. Now the spectral decomposition of the Liouvillian removes the time dependence at the expense of significantly increasing the matrix space where we must solve for each Liouvillian $\hat{\hat{\mathcal{L}}}_j$ component simultaneously. We note that, in principle, there exists an infinite number of spectral components which for practical means is not reasonable when solving such an equation. The typical approach is to truncate the problem at twice the frequency of the highest frequency component present in the Hamiltonian [60]. This is somewhat akin to the Nyquist criteria. In our case, the magnetic field information is encoded in the first and the second harmonic, so as a good rule of thumb, we can truncate the solution at the fourth harmonic. However, this criteria for truncation does not consider our pumping profile which has a square shape in the time domain, and as a result, high harmonic composition in the Fourier space. This may impact the calculations of the state preparation process and the consequent spin-dynamics. Therefore, it may not be sufficient to base the truncation process solely on the coherent part of the dynamical system without considering the potential impact of the driving terms in the system.

The next part of the Floquet expansion is the form of the propagator $\mathbf{\Pi}(t)$ which operates on our observables, i.e. $\mathbf{X}(t)$. This propagator can also be decomposed in the Fourier series

$$\mathbf{X}(t) = \mathbf{\Pi}(t)\mathbf{X}(0) = \sum_{k=-\infty}^{\infty} \mathbf{\Pi}_k(t) e^{ik\omega_{\mathrm{rf}}t}\mathbf{X}(0), \tag{3.145}$$

which allows us to spectrally decompose our second order moment expression transformed in the Liouville space

$$\mathbf{X}(t) = \mathbf{X}^{(0)}(t) + \mathbf{X}^{(1)}(t)\ e^{i\omega_{\mathrm{rf}}t} + \mathbf{X}^{(-1)}(t)\ e^{-i\omega_{\mathrm{rf}}t} + \mathbf{X}^{(2)}(t)e^{2i\omega_{\mathrm{rf}}t} + \mathbf{X}^{(-2)}(t)\ e^{-2i\omega_{\mathrm{rf}}t} + \cdots . \tag{3.146}$$

Taking eqns. (3.139, 3.205, 3.146) and substituting them into eq. (3.138) and expanding (see Appendix B.5.1 on page 186 for details) and by grouping the terms with the same

harmonic frequency, we can generalise the expansion to an n^{th} harmonic which has the following relation

$$\begin{aligned}\frac{d\mathbf{X}^{(n)}(t)}{dt} =&\mathbf{C}_n^{(0)}\mathbf{X}^{(n)}(t) + \mathbf{C}^{(1)}\mathbf{X}^{(n-1)}(t) + \mathbf{C}^{(-1)}\mathbf{X}^{(n+1)}(t) - 2\sum_i \Gamma_p^{(n-i)}\mathbf{X}^{(i)}(t) \\ &+ 2\Gamma_p^{(n)}\mathbf{X}_{\text{in}} + \Lambda_{\text{rel}}\ \mathbf{X}_0\ \delta_{n,0}. \end{aligned} \tag{3.147}$$

We can express the recursive relation given in eq. (3.147) in a more compact form by defining a new linear space. We define a harmonic vector $\mathbb{X}$ such that

$$\mathbb{X} = \begin{bmatrix} \mathbf{X}^{(-n)}e^{-in\omega_{\text{rf}}t} \\ \vdots \\ \mathbf{X}^{(-1)}e^{-i\omega_{\text{rf}}t} \\ \mathbf{X}^{(0)} \\ \mathbf{X}^{(1)}e^{i\omega_{\text{rf}}t} \\ \vdots \\ \mathbf{X}^{(n)}e^{in\omega_{\text{rf}}t} \end{bmatrix}, \tag{3.148}$$

and by defining a matrix $\mathbb{N}$ with matrix elements $\mathbb{N}_{ij} = j\delta_{ij}$ and j spanning for all possible harmonics, the spin operator can be written as

$$\mathbb{X}(t) = e^{i\omega_{\text{rf}}\mathbb{N}t}\mathbb{X}_F, \tag{3.149}$$

where

$$\mathbb{X}_F = \begin{bmatrix} \mathbf{X}^{(-n)} \\ \vdots \\ \mathbf{X}^{(-1)} \\ \mathbf{X}^{(0)} \\ \mathbf{X}^{(1)} \\ \vdots \\ \mathbf{X}^{(n)} \end{bmatrix}. \tag{3.150}$$

If we additionally define a vector $\mathbb{V}$ with $\mathbb{V}_i = 1$ for all i's, the second order moment operator can be written as $\mathbf{X}(t) = \mathbb{V}\cdot\mathbb{X}(t)$. With these definitions we can write the eq. (3.147) in a more compact form

$$\frac{d\mathbf{X}(t)}{dt} = \mathbb{V}\cdot e^{i\mathbb{N}\omega_{\text{rf}}t}\left([\mathbb{C} - \mathbb{\Gamma}]\ \mathbb{X}_F + \mathbb{\Gamma}_{\text{in}}\mathbb{X}_{\text{in}} + \mathbb{\Lambda}_{\text{rel}}\mathbb{X}_0\right), \tag{3.151}$$

where the pump matrix term reads

$$(\mathbb{\Gamma})_{nm} = \Gamma_p^{(n-m)}\mathbf{I}, \tag{3.152}$$

$$(\mathbb{\Gamma}_{\text{in}})_{nm} = \begin{cases} \Gamma_p^{(n)}\mathbf{I}, & \text{for } n = m, \\ 0, & \text{otherwise}, \end{cases} \tag{3.153}$$

with $(\mathbb{X}_{\text{in}})_n = \mathbf{X}_{\text{in}}$. The unpolarised drift matrix is

$$(\mathbb{\Lambda}_{\text{rel}})_{nm} = \begin{cases} \mathbf{\Lambda}_{\text{rel}}, & \text{for } n = m = 0, \\ 0, & \text{otherwise.} \end{cases} \tag{3.154}$$

We need to see what is the form of the first derivative since this is what governs the dynamics, applying the product rule to differentiate $\mathbf{X}(t)$ we get

$$\frac{d\mathbf{X}(t)}{dt} = \mathbb{V} \cdot \left(i\mathbb{N}\omega_{\text{rf}} e^{i\mathbb{N}\omega_{\text{rf}}t} \mathbb{X}_F + e^{i\mathbb{N}\omega_{\text{rf}}t} \frac{d\mathbb{X}_F}{dt} \right). \tag{3.155}$$

Equating eq. (3.151) and eq. (3.155) and rearranging for $\frac{d\mathbb{X}_F}{dt}$ we get

$$\frac{d\mathbb{X}_F(t)}{dt} = [\tilde{\mathbb{C}} - \mathbb{\Gamma}]\ \mathbb{X}_F + \mathbb{\Gamma}_{\text{in}} \mathbb{X}_{\text{in}} + \mathbb{\Lambda}_{\text{rel}} \mathbb{X}_0, \tag{3.156}$$

where we have defined $\tilde{\mathbb{C}} = \mathbb{C} - i\mathbb{N}\omega_{\text{rf}}$ with the following components

$$\tilde{\mathbb{C}}_{nm} = \begin{cases} \mathbf{C}^{(0)} - in\omega_{\text{rf}}\mathbf{I}, & \text{for } n = mn \\ \mathbf{C}^{(\pm 1)}, & \text{for } m = n \mp 1, \\ 0, & \text{otherwise.} \end{cases} \tag{3.157}$$

Recall the definition for $\mathbf{C}(t) = \mathcal{L}(\mathbf{B}(t)) + \mathcal{R}(\mathbf{B}(t)^T)$, taking this with the zero order term defined in the expression above we can write

$$\mathbf{C}^{(0)} - in\omega_{\text{rf}}\mathbf{I} = \mathcal{L}\left[\mathbf{B}^{(0)} - \frac{in\omega_{\text{rf}}}{2}\mathbf{I}\right] + \mathcal{R}\left[{\mathbf{B}^{(0)}}^T - \frac{in\omega_{\text{rf}}}{2}\mathbf{I}\right], \tag{3.158}$$

which corresponds to an atomic spin resonances at multiples of $\omega_{\text{rf}}/2$ frequencies where ω_{rf} is the frequency of the rf-field. The resonance occurs when $\Omega_{\text{dc}} = \omega_{\text{rf}}/2$. Note that this additional resonance condition is not predicted in the geometric approach that was outlined in section 3.1.

3.2.8 Magnetometer response to external fields (Heisenberg Model)

The magnetometer cycle has two stages, the first stage is the state preparation process where a combination of pumping and repumping laser beams prepare our atomic state to the one given in eq. (3.118), see page 50. With sufficient laser driving using pump/repump beams against the decoherence effects in a given amount of time, the system will reach a steady state. This steady state is a stationary state which can be mathematically expressed as

$$\left.\frac{d\mathbb{X}_F(t)}{dt}\right|_{\text{pump}} = [\tilde{\mathbb{C}} - \mathbb{\Gamma}]\ \mathbb{X}_F + \mathbb{\Gamma}_{\text{in}} \mathbb{X}_{\text{in}} + \mathbb{\Lambda}_{\text{rel}} \mathbb{X}_0 = 0, \tag{3.159}$$

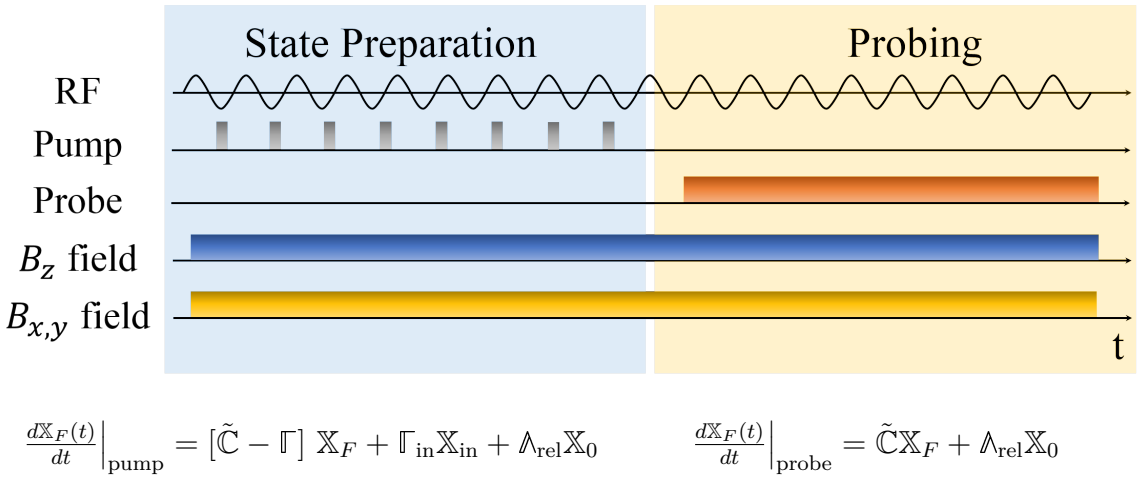

Figure 3.8: Magnetometer sequence. The first stage consists of state preparation process whereby the atoms are dressed by a uniform radio-frequency field and synchronously pumped into a magnetically sensitive state. The static field to match the sensitive field point is ramped simultaneously with the external magnetic fields. The system is driven in such a state until it reaches a steady state. Once the steady state is reached, the pumping is instantly switched off which is then followed by a continuous wave (CW) probe beam which interrogates the state for a given duration, T. The radio-frequency fields as well as the static fields are present as before, and now the state evolves in time. The equations below each section of the OPM cycle correspond to the spin dynamics of the second moment.

which can be solved trivially for $\mathbb{X}_F$ by rearranging the expression above. This gives

$$\mathbb{X}_F = -\left[\tilde{\mathbb{C}} - \mathbb{\Gamma}\right]^{-1}(\mathbb{\Gamma}_{\text{in}}\mathbb{X}_{\text{in}} + \mathbb{\Lambda}_{\text{rel}}\mathbb{X}_0). \tag{3.160}$$

This is the equation of motion during the pumping cycle in steady state conditions. We can see that it depends on the coherent dynamics of the spin-field interaction which is encoded in the matrix $\tilde{\mathbb{C}}$, the pumping cycle contained in expressions $\mathbb{\Gamma}$ and $\mathbb{\Gamma}_{\text{in}}$ and the contribution from the thermal state which depends on the various relaxation mechanisms as well as the coherent and pumping dynamics. The next stage of the magnetometer cycle is the probing stage whereby a far detuned laser beam probes the atomic state. During the probing stage, the pumping is off ($\mathbb{\Gamma} = \mathbb{\Gamma}_{\text{in}} = 0$), and the system evolves freely in time. In this regime, we probe for a short time duration where the atomic dynamics do not reach a steady state, and so the time derivative of the second moment dynamics is no longer zero. Thus, the equation of motion in the probing cycle reads

$$\left.\frac{d\mathbb{X}_F(t)}{dt}\right|_{\text{probe}} = \tilde{\mathbb{C}}\mathbb{X}_F + \mathbb{\Lambda}_{\text{rel}}\mathbb{X}_0. \tag{3.161}$$

Solving this ordinary differential equation by integrating yields

$$\mathbb{X}_F(t) = e^{\tilde{\mathbb{C}}\ t}\ \mathbb{X}_F(0) + \tilde{\mathbb{C}}^{-1}(e^{\tilde{\mathbb{C}}\ t} - \mathbb{I})\ \mathbb{\Lambda}_{\text{rel}}\mathbb{X}_0. \tag{3.162}$$

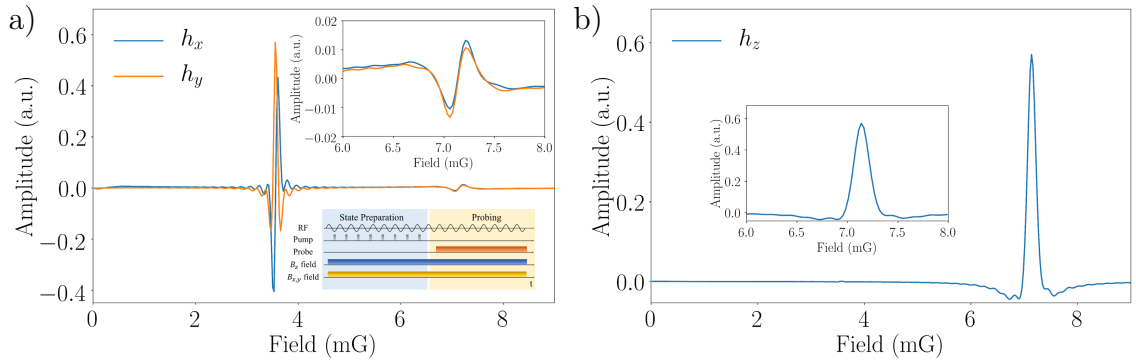

Figure 3.9: a) Theoretical magnetometer response of h_x and h_y as a function of the static field B_z of the first harmonic. The first resonance is the predicted $\Omega_{\rm dc} = \omega_{\rm rf}/2$ resonance. The inset shows the dispersive profiles of the first harmonic which are sensitive to the transverse magnetic fields $B^{\rm ext}_{x,y}$. Here at the bottom of the inset we show the theoretical sequence that is used to produce the theoretical OPM response. b) theoretical magnetometer response of the second harmonic, h_z. Here we obtain a Lorentzian type resonance profile. The inset shows the zoomed in version of the profile. In these theoretical calculations, we truncate our Floquet expansion at $Q = 4$ where Q is the harmonic number, so that the square pumping profile is approximated using terms up to the fourth harmonic which satisfies the minimal harmonic condition for the Floquet expansion to be reliable.

Experimentally the probing happens over a time period T and so the resultant signal measured is averaged over that time period. Our initial state $\mathbb{X}_F(0)$ is equal to the steady state reached during the pump cycle, namely

$$\mathbb{X}_F(0) = -[\tilde{\mathbb{C}} - \mathbb{\Gamma}]^{-1}(\mathbb{\Gamma}_{\rm in}\mathbb{X}_{\rm in} + \mathbb{\Lambda}_{\rm rel}\mathbb{X}_0), \tag{3.163}$$

which we substitute into the solution obtained for the probe cycle

$$\mathbb{X}_F(t) = -e^{\tilde{\mathbb{C}}\ t}\ \left([\tilde{\mathbb{C}} - \mathbb{\Gamma}]^{-1}(\mathbb{\Gamma}_{\rm in}\mathbb{X}_{\rm in} + \mathbb{\Lambda}_{\rm rel}\mathbb{X}_0)\right) + \tilde{\mathbb{C}}^{-1}(e^{\tilde{\mathbb{C}}\ t} - \mathbb{I})\ \mathbb{\Lambda}_{\rm rel}\mathbb{X}_0. \tag{3.164}$$

After probing, the second order moments read

$$\begin{aligned}\mathbb{X}_F^{\rm out} = \frac{1}{T}\int_0^T dt' \mathbb{X}_F(t') = \frac{1}{T}(\tilde{\mathbb{C}})^{-1}\left(e^{\tilde{\mathbb{C}}\ T} - \mathbb{I}\right)\mathbb{X}_F(0) \\ + \frac{1}{T}(\tilde{\mathbb{C}})^{-1}\left[(\tilde{\mathbb{C}})^{-1}\left(e^{\tilde{\mathbb{C}}\ T} - \mathbb{I}\right) - T\right]\mathbb{\Lambda}_{\rm rel}\mathbb{X}_0,\end{aligned} \tag{3.165}$$

where the vector elements of $\mathbb{X}_F^{\text{out}}$ are extracted by recalling that

$$\mathbb{X}_F = \begin{bmatrix} \mathbf{X}^{(-n)} \\ \vdots \\ \mathbf{X}^{(-1)} \\ \mathbf{X}^{(0)} \\ \mathbf{X}^{(1)} \\ \vdots \\ \mathbf{X}^{(n)} \end{bmatrix}, \tag{3.166}$$

with

$$\mathbf{X}(t) = \begin{bmatrix} \left\langle \hat{F}_x(t)\hat{F}_x^T(t) \right\rangle \\ \left\langle \hat{F}_x(t)\hat{F}_y^T(t) \right\rangle \\ \vdots \\ \left\langle \hat{F}_z(t)\hat{F}_z^T(t) \right\rangle \end{bmatrix}, \tag{3.167}$$

such that the resultant ω_{rf} and $2\omega_{\text{rf}}$ quadratures containing h_x, h_y and h_z are given by

$$h_x = \text{Re}\left(\mathbb{X}_F\left(\omega_{\text{rf}}t, \left\langle \hat{F}_x(t)\hat{F}_x^T(t)\right\rangle\right) - \mathbb{X}_F\left(\omega_{\text{rf}}t, \left\langle \hat{F}_y(t)\hat{F}_y^T(t)\right\rangle\right)\right), \tag{3.168}$$

$$h_y = \text{Im}\left(\mathbb{X}_F\left(\omega_{\text{rf}}t, \left\langle \hat{F}_x(t)\hat{F}_x^T(t)\right\rangle\right) - \mathbb{X}_F\left(\omega_{\text{rf}}t, \left\langle \hat{F}_y(t)\hat{F}_y^T(t)\right\rangle\right)\right), \tag{3.169}$$

$$h_y = \text{Re}\left(\mathbb{X}_F\left(2\omega_{\text{rf}}t, \left\langle \hat{F}_x(t)\hat{F}_x^T(t)\right\rangle\right) - \mathbb{X}_F\left(2\omega_{\text{rf}}t, \left\langle \hat{F}_y(t)\hat{F}_y^T(t)\right\rangle\right)\right). \tag{3.170}$$

The characteristic profiles of the magnetometer response as a function of the static field B_z which tunes the magnetometer response are shown in Fig. 3.9 where we have used the sequence of state preparation and probing given in Fig. 3.8. From the figure we can observe that the scan of the longitudinal B_z field reproduces ω_{rf} and $2\omega_{\text{rf}}$ resonance profiles which have a characteristic dispersive and Lorentzian shapes, though the $2\omega_{\text{rf}}$ resonance has additional wings present. We also observe additional structure at $\Omega_{\text{dc}} = \omega_{\text{rf}}/2$ which is not predicted using the geometric model. This resonance, whilst large in the amplitude in the quadrature at ω_{rf} is extremely weak in the quadrature at $2\omega_{\text{rf}}$ which makes it impractical for sensing all three vector components of the field. Moreover, we see additional oscillatory behaviour in between the resonances which are a result of transient effects produced by suddenly switching the pumping beams off and switching the probe on. These oscillations vanish when probing is done during the pump cycle in continuous wave mode, (cw). The model above also shows that the transverse field quadrature profiles h_x and h_y are not perfectly symmetric despite the fact that quantitatively the relaxation and pumping dynamics are symmetric for the transverse field components which is not the case for the longitudinal field B_z. This is shown in Fig. 3.9 a) inset as the dispersive curves do not overlap perfectly.

As in the case of the geometric model, we want to understand the theoretical magnetometer response over small and large external field range set on the sensitive field point where the OPM can detect all three vector field components. We set the longitudinal field to $B_{\text{offs}} = B_{\text{sense}}^{+} = B_{\text{res}} + B_\rho + B_z^{\text{ext}}$ and scan the transverse fields,

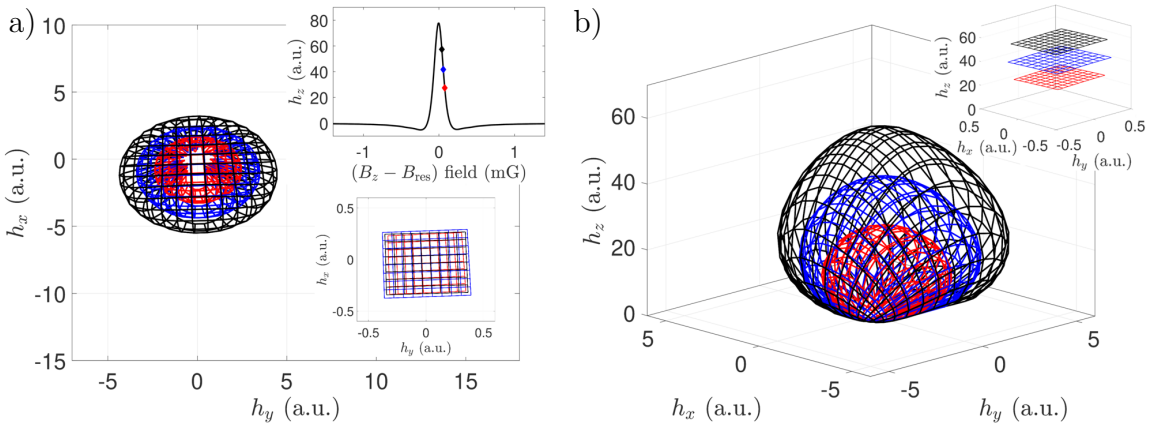

Figure 3.10: Ovoid profiles mapping the full magnetometer response for all 3 field directions. We set the magnetometer to a field sensitive point given by $B_{\text{offs}} = B^{+}_{\text{sense}} = B_{\text{res}} + B_{\rho} + B^{\text{ext}}_{z}$ which are indicated by black, blue and red diamond ticks on in the inset a) of the Lorentzian resonance profile. Each of the colours corresponds to a different B_{offs} point. The transverse fields B_x and B_y are then scanned. The scans are done over a large and small field range where the smaller insets in a) bottom 2D grid and b) top 3D grid show linear OPM response in the presence of small external field perturbation compared to the B_z field whilst the large figures depicting the ovoids in 2D and 3D show the OPM response for large transverse field scans.

Fig. 3.10 shows the OPM response for all three vector components over small and large field scan range. The theoretical state preparation and probing sequence to generate the full OPM response is given in Fig. 3.8. From Fig. 3.10 we can qualitatively infer that the Heisenberg model produces similar behaviour to the geometric model shown in Fig. 3.4 on page 37. Both, the Heisenberg and the geometric models display characteristic ovoid shape in the large field scan regime and the flat plane behaviour in the small external field regime. A key distinguishing feature in the Heisenberg model is the distortion and asymmetry of the ovoid which is not observed in the geometric case. On the scale where the external field perturbation is small, the distortion manifests as field leakage in the transverse field directions i.e. the quadratures h_x and h_y are not orthogonal to each other. When the external fields are large, i.e. $B^{\text{ext}}_{x,y,z} \approx B^{+}_{\text{sense}}$, the ovoid displays asymmetric 3D structure where the h_x and h_y field mapping components have a different response to the same external magnetic fields. This distortion is less prominent for higher radio-frequency dressing fields, ω_{rf}, at the expense of reducing sensitivity of the OPM to transverse fields. The parameter space of the Heisenberg model for the OPM is relatively large and their effects are non-trivial which is the topic of discussion in the following subsection.

3.2.9 OPM parameter space of the Heisenberg Model

As noted in the previous subsection, the description of the OPM response using the Heisenberg formalism gives access to a large number of various physical mechanisms

which influence the spin dynamics of the OPM. This physics-rich parameter space is worth understanding and exploring since it necessarily provides an insight into the effects each parameter has on the system, how sensitive the dynamics are to these effects, and moreover, whether there is some non-trivial coupling mechanisms between the various effects at play. Thus, having a more complete picture of such complex interplay of different phenomena not only allows one to get a better understanding of the behaviour of the system itself, but also provide a way to build such a system to work in the most optimal conditions, which in the context of magnetometry could mean highest sensitivity at the highest bandwidth.

A pictographic summary of this parameter space is shown in Fig. 3.11 on page 62. The parameter space is categorised into three distinct groups which correspond to the three distinct physical processes derived in the formalism of the Heisenberg equation of motion of the second order moments, eq. (3.77) on page 45. These are: coherent spin dynamics, pumping dynamics, and depolarisation due to pumping and collisions/broadening effects. It is noteworthy to consider these effects individually and explore their influence and coupling to other effects.

Radio-frequency field amplitude, Ω_{rf} (Fig. 3.11 b)). As we have shown in the geometric model (see Fig. 3.3 on page 36), the increase in the Ω_{rf} amplitude broadens both the ω_{rf} and $2\omega_{\mathrm{rf}}$ resonance profiles which ultimately reduces the OPM sensitivity in all three field directions, see Fig. 3.12 on page 63. The broadening of the resonance profile also affects the state preparation process. Since the state preparation process happens near resonance at $B_{\mathrm{offs}} = B^{+}_{\mathrm{sense}} = B_{\mathrm{res}} + B_{\rho} + B_z^{\mathrm{ext}}$, the broadening of the resonance and the reduction in sensitivity to all field directions means that the state preparation process is less sensitive to the external perturbing fields. Whilst the behaviour of the quantities like amplitude and FWHM are difficult to infer directly from the equations in the Heisenberg model, the theoretical results show that the figure of merit, characterised by $2\omega_{\mathrm{rf}}$ signal amplitude over the FWHM of the resonance decreases as a function of the rf amplitude.

Frequency of the dressing field, ω_{rf} (Fig. 3.11 c)). The frequency of the dressing field affects the coherent dynamics as well as the pumping. First, the frequency of the dressing field sets out the magnitude of the longitudinal static field B_z to achieve resonance or the sensitive field point, since this is given by $B_{\mathrm{res}} = B_z = \hbar\omega_{\mathrm{rf}}/\mu_B g_F$. Note that this equation is valid for sufficiently small fields where the second order Zeeman shifts can be neglected. In this regime, the static field depends linearly on the dressing frequency. This has several implications. First, the higher the dressing frequency, the higher the static $B_{\mathrm{offs}} = B^{+}_{\mathrm{sense}} = B_{\mathrm{res}} + B_{\rho} + B_z^{\mathrm{ext}}$ field and thus the smaller the relative perturbation of transverse fields. This implies that the coherent spin dynamics will be largely determined by the longitudinal static field and the transverse field effects will play a smaller role. Consequently, the OPM response in the transverse field directions will be reduced. In some cases this may be desirable, e.g. in an unshielded environment where the external fields may be large, in order to operate the OPM on the sensitive point, we may want to be less sensitive to the longitudinal

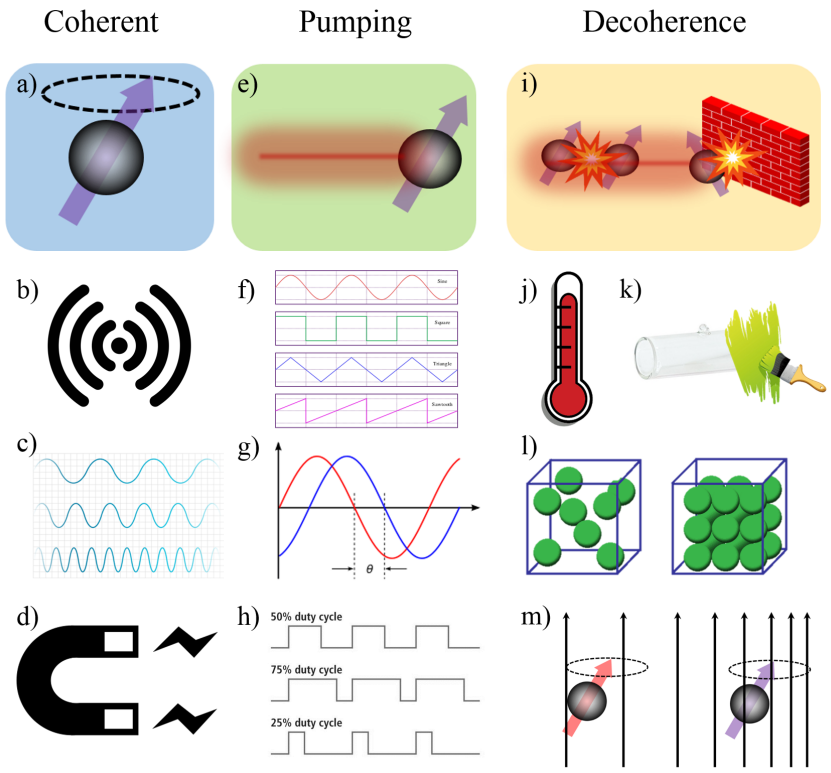

Figure 3.11: Parameter space and its tuning. a) Coherent dynamics of the spin interaction with the magnetic field. b) Amplitude of the radio-frequency dressing field. The larger the amplitude of the rf-field, the broader the OPM dispersive and the resonance profiles are resulting in lower field sensitivity. c) Frequency of the radio-frequency field. Reducing the frequency increases the sensitivity of the OPM to the transverse fields and vice versa. d) External field strength. Broadens the resonance and reduces the sensitivity of the OPM. e) Pumping dynamics. f) Pumping intensity profile. Influences the state preparation dynamics and ultimately influences the OPM sensitivity which depends on how sensitive the state is to external magnetic fields. g) Pumping phase relative to the rf-field phase. Affects the state preparation process where the out of phase pump does not transfer the driven atoms efficiently. h) Pumping duty cycle. In this context if the pumping follows a square intensity profile, the duty cycle again affects the state preparation. i) Depolarisation of the atomic states. j) Temperature of the cell. Increasing this increases the rate of atom-atom, atom-wall collisions and as a result the rate of spin destruction. k) Anti-relaxation coating lifetime. The quality of the coating influences the lifetime of the prepared atomic states due to atom-wall collisions. l) Atomic density. Affects the collision rate as well as increases the signal to noise ratio. The atomic density is temperature dependent. m) Gradient fields. Broaden the atomic resonances and decrease the sensitivity of the OPM due to the fact that atoms see different magnetic fields in different spatial locations and therefore precess at different rates.

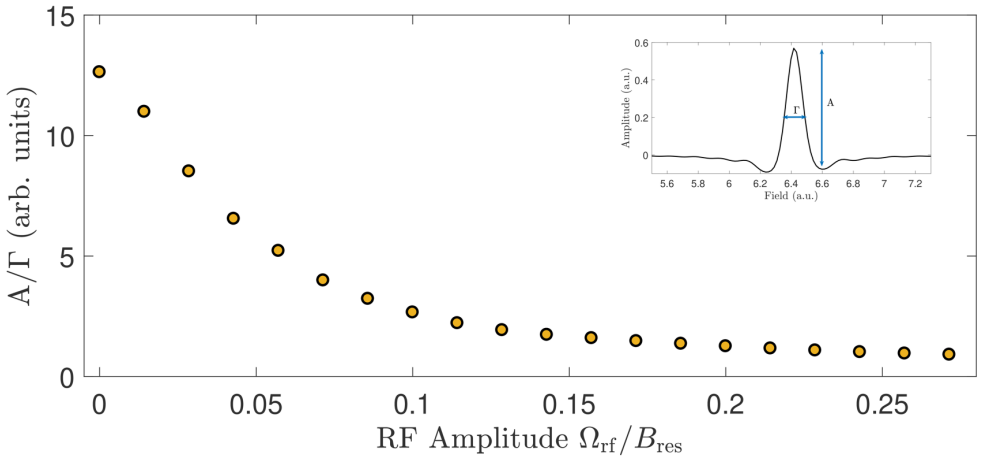

Figure 3.12: $2\omega_{rf}$ resonance profile amplitude and linewidth at FWHM (Figure of Merit, FOM) as a function of the radio-frequency dressing field amplitude Ω_{rf}. The FOM in this case is independent of B_{res}. Here the transverse fields, $B^{ext}_{x,y} \ll B_{res}$.

and transverse fields which would otherwise at low frequency of the dressing field would pose a problem by driving the OPM away from the sensitive field point. Moreover, in some cases, the technical or environmental noise at low dressing frequencies may be large enough to pose a problem when attempting to measure external fields of interest. In our case the magnetic field information is coded into the harmonic components of the dressing field which is then extracted using lock-in detection techniques. As a result, the ability to change the modulation field allows us to move to a low-technical noise region and perform the measurement there. Going to the other extreme of having a low frequency dressing field we immediately encounter the problem of the OPM bandwidth i.e. the range of external magnetic field frequencies we can detect. This also couples to the optical pumping process where the low bandwidth of detection also means that there are fewer cycles of the pumping and they are spaced out by larger time intervals which leave a longer time for atomic collisions to take place resulting in decoherence effects.

External magnetic fields $\Omega^{ext}_{x,y,z}$ (Fig. 3.11 d)). The entire function of the OPM is to detect external magnetic fields. We have already shown the effects of external magnetic fields on the OPM mapping e.g. the ovoid profile in Fig. 3.10 on page 60. If the external transverse fields are large such that the OPM response is no longer linear, the orthogonality of the OPM quadratures is lost and it is no longer possible to distinguish the direction of the field nor the precise magnitude of such field. Moreover, if the external fields are large, transverse and/or longitudinal, then the total effective field $B_{dc} = \sqrt{B_z^2 + B_x^2 + B_y^2} \neq B_{offs} = B^{+}_{sense} = B_{res} + B_\rho + B^{ext}_z$ which drives the OPM away from the sensitive field point which effectively changes the sensitivity of the OPM. Large external field perturbation also affect the state preparation process. Typically, the state preparation process is done on ($B_{offs} = B_{res}$) or near the resonance point ($B_{offs} = B_{res} + B_\rho + B^{ext}_z$) which makes the synchronous pumping process efficient in

transferring the atoms into the mixture $|F = 2, m_F = \pm 2\rangle$ state. This is not the case when external magnetic fields are sufficiently large such that the pumping is no longer done on the sensitive field point which consequently creates a state with a statistical mixture composed of $|F = 2, m_F = \pm 2\rangle$, $|F = 2, m_F = \pm 1\rangle$ and $|F = 2, m_F = 0\rangle$ states which is less sensitive to the external fields when using them to measure the Voigt effect.

Pumping profile $\Gamma_p(t)$ (Fig. 3.11 f)). Here the pumping profile refers to the intensity profile of the pump beam as a function of time (see Fig. 3.11 f)). When the atomic state is dressed with a radio frequency field, the atomic precession of the spins is being actively driven. In the lab frame this atomic precession manifests as a rotation of quantisation axis in time at the frequency of the dressing field, ω_{rf}. This change of quantisation axis in time makes efficient state preparation problematic because the dressed state is time dependent in the lab frame and as a result the dipole transition moment $\langle e(t)| \, q\hat{\mathbf{r}} \, |g(t)\rangle$ is time dependent (depending whether we are in the Schrödinger or the Heisenberg picture). To remedy this, we can switch the pump beam at times such that the dipole transition moment is appropriately aligned, thus ensuring an efficient state transfer, this is known as synchronous optical pumping [47]. The intensity profile of the pump beam as a function of time can therefore influence the magnetically sensitive state that we prepare. For the purposes of maximising the sensitivity of the magnetometer, we want to maximise the efficiency of pumping. The theory of the OPM response contains a pumping term that is time dependent such that it can allow us to compute the spin dynamics and the OPM response for any arbitrary time dependent intensity profile of the pump beam as long as such profile can be trivially decomposed into its constituent Fourier components. For example, for a pumping rate $\Gamma_p(t)$ given by the spectral expansion

$$\Gamma_p(t) = \Gamma_p^{(0)} + \Gamma_p^{(1)} e^{i\omega_{\text{rf}} t} + \Gamma_p^{(-1)} e^{-i\omega_{\text{rf}} t} + \Gamma_p^{(2)} e^{2i\omega_{\text{rf}} t} + \Gamma_p^{(-2)} e^{-2i\omega_{\text{rf}} t} + \cdots , \tag{3.171}$$

the corresponding Fourier components with a duty cycle d, for square, triangular and sawtooth waves read

$$\text{square} = \begin{cases} \Gamma_p^{(0)} = \Gamma_p \; d, \\ \Gamma_p^{(n)} = \Gamma_p^{(-n)} = \frac{\Gamma_p}{n\pi} \sin(n\pi d), \end{cases} \tag{3.172}$$

$$\text{triangular} = \begin{cases} \Gamma_p^{(0)} = \Gamma_p \; d, \\ \Gamma_p^{(n)} = \Gamma_p^{(-n)} = \frac{\Gamma_p}{(n\pi)^2} \sin^2(n\pi d), \end{cases} \tag{3.173}$$

$$\text{sawtooth} = \begin{cases} \Gamma_p^{(0)} = 0, \\ \Gamma_p^{(n)} = \Gamma_p^{(-n)} = \Gamma_p \left(\frac{1}{(n\pi)^2} \sin(n\pi d) - \frac{d}{n\pi} \cos(n\pi d) \right). \end{cases} \tag{3.174}$$

Figure (3.13) shows the OPM response for different pumping profiles with all other parameters being held constant. The square intensity profile generates the best OPM response characterised by high amplitude to linewidth ratio of the dispersive and Lorentzian resonances.

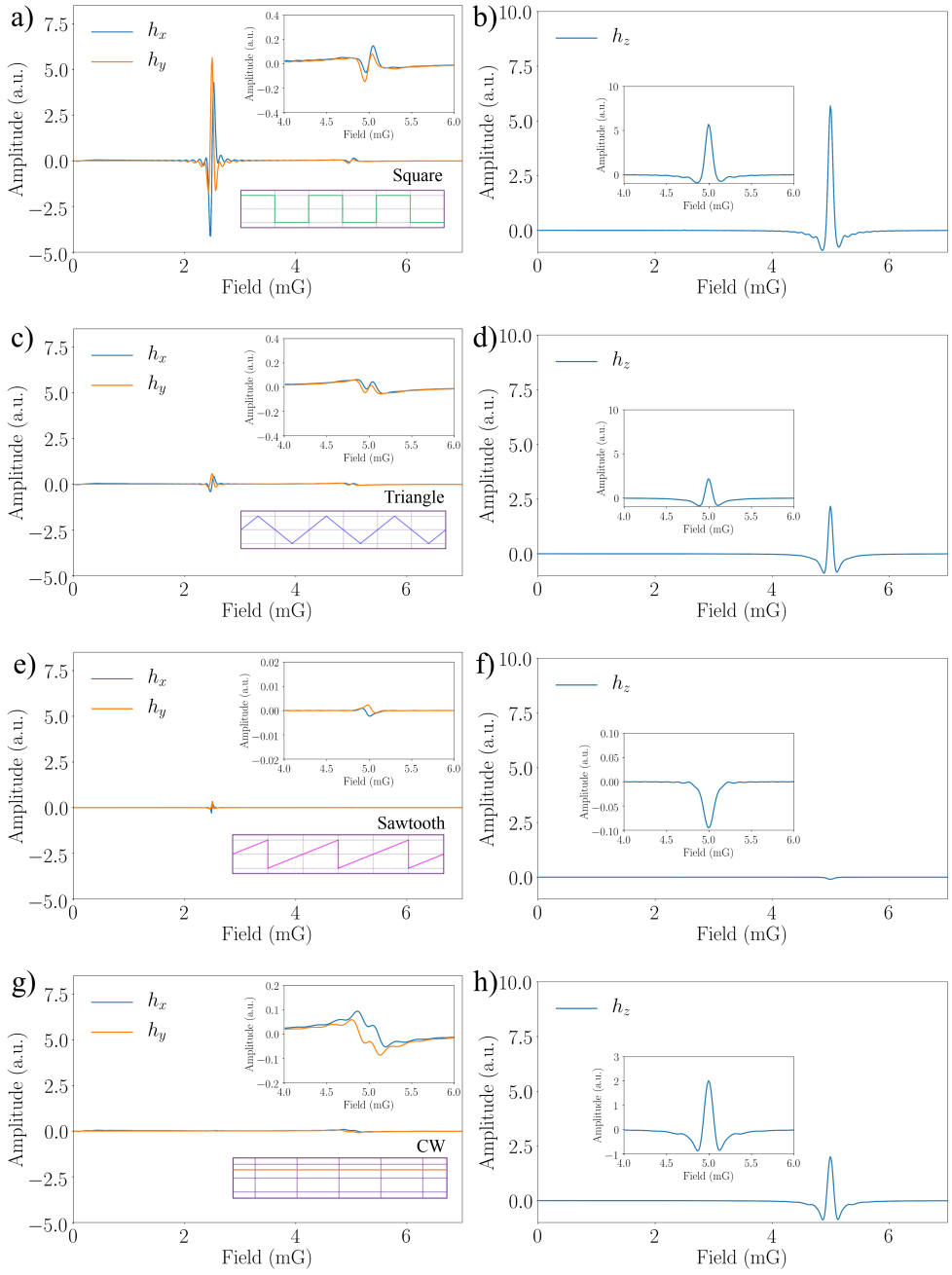

Figure 3.13: Magnetometer response of the ω_{rf} and $2\omega_{\mathrm{rf}}$ profiles as a function of the longitudinal B_z field at different pumping profiles at 10% duty cycle. a-b) Square pumping profile. c-d) Triangular pumping profile. e-f) Sawtooth pumping profile. g-h) Continuous-Wave pumping profile. The small insets show the zoomed-in dispersive and Lorentzian profiles. We see that for the same conditions, the square pumping profile generates the best OPM response which is characterised by the ratio of signal amplitude to field resonance linewidth.

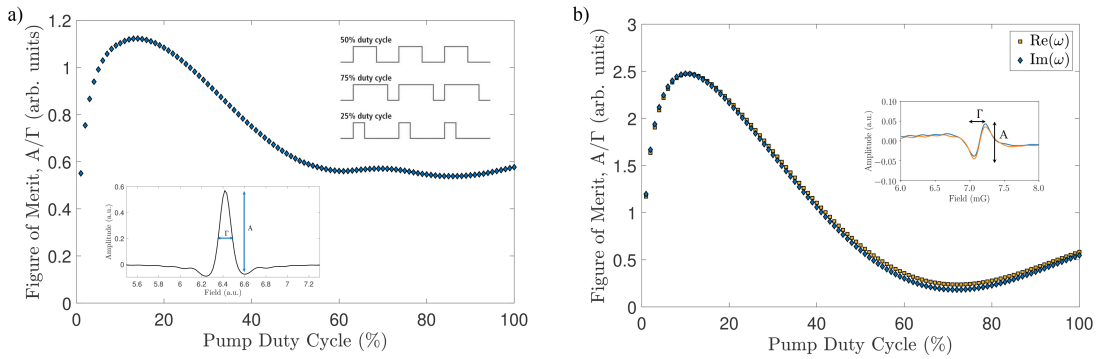

Figure 3.14: Normalised Figure of Merit (FOM) of the a) $2\omega_{\mathrm{rf}}$ and b) ω_{rf} resonance and dispersive profiles as a function of the duty cycle of the pump. Here the FOM is the ratio of the normalised resonance height over the normalised full-width-at-half-maximum (FWHM) of the $2\omega_{\mathrm{rf}}$ and ω_{rf} profiles. The amplitude and the FWHM of the resonance profile changes with the duty cycle of the pump. The optimal point is around 13% pump duty cycle for $2\omega_{\mathrm{rf}}$ quadrature and 10% pump duty cycle for the ω_{rf} quadrature.

Pumping duty cycle, d (Fig. 3.11 h)). The duty cycle in the context of optical pumping refers to the fraction of time the pump beam is switched on relative to the time period of the system. In our case, the time period is given by the frequency of the rf dressing field, $\omega_{\mathrm{rf}} = 2\pi/T$. It has already been discussed that due to the dressing of the atomic states, the dipole transition moment is a time dependent quantity and as a result, in order to achieve an efficient state preparation process we have to carefully engineer the intensity profile of the pump beam. In addition to the general form of the intensity profile, the duty cycle of the pump beam gives an additional degree of freedom to manipulate the state preparation process. This is crucial if we want to produce short pulses of arbitrary intensity profile over a time period where the quantisation axis can be assumed to be constant in time. This, however, comes at a cost, the shorter the pulse, the less power it carries, and as a result the state preparation process may become inefficient as we are not able to saturate the atomic medium. On the other hand, long pulse duration i.e. high duty cycle, will mean that the pump is switched on for a period of time where the quantisation axis has changed appreciably acting as a spin decoherence process, resulting in inefficient state preparation and therefore reduced OPM sensitivity. Therefore, it is possible that the competition between these two effects may produce some optimal duty cycle for which the efficiency of the state preparation process is maximised. Figure (3.14) on page 66 show the effects on OPM sensitivity for all three quadratures as a function of the duty cycle. The theoretical curves predict that there exists an optimal duty cycle in the $10-15\%$ region for the ω_{rf} and $2\omega_{\mathrm{rf}}$ quadratures. For lower duty cycles, the decay rolls off more rapidly which suggests the state preparation is not effective against decoherence due to collisions and other broadening effects. At higher duty cycles the pump is on during times where the quantisation axis is no longer aligned with the

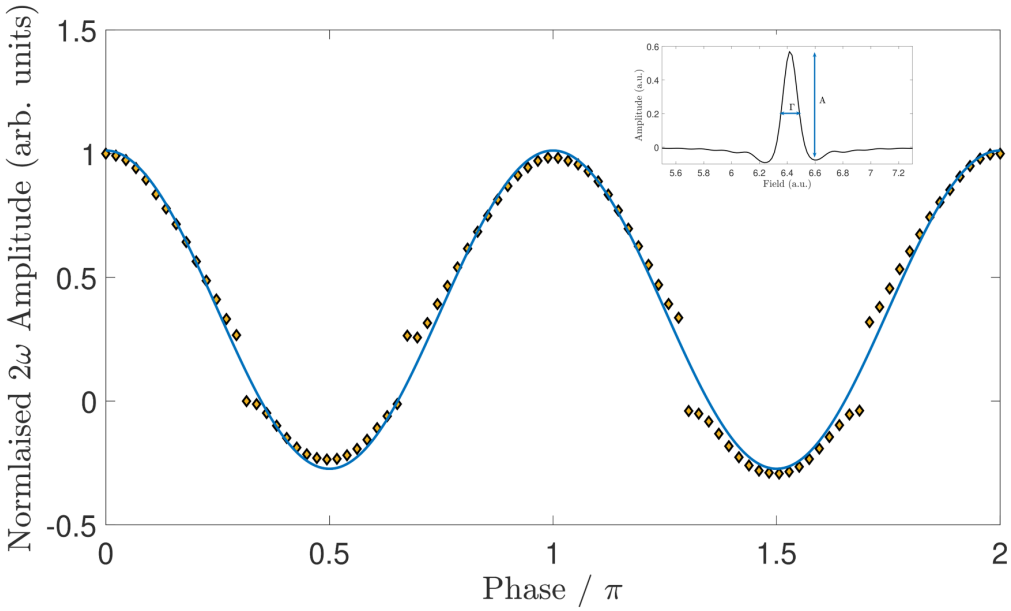

Figure 3.15: Normalised $2\omega_{\mathrm{rf}}$ amplitude as a function of the relative phase between the pumping pulse and radio-frequency dressing field. The pump has a square intensity profile with 10% duty cycle. Here we see the relative phase between the pump and the rf-field changes the amplitude of the OPM response. Same effect (not shown) is observed on the ω_{rf} quadratures. The fitted function has the form $A = A_0 \sin(2\pi\phi + \phi_0) + c$.

polarisation of the pump, as a result, the pumping is not efficient as the atoms are pumped into states that have a lower linear birefringence.

Pumping phase, ϕ (Fig. 3.11 g)). Here pumping phase refers to the relative phase between the radio-frequency dressing field and the pump pulses applied during the state preparation process. The radio frequency field actively drives the atomic precession and so the quantisation axis or the alignment of spin relative to the electric field of the pump beam changes in time. As a result, the state preparation process is influenced by this relative phase. It is therefore imperative to understand how does the relative phase influence the OPM response and whether it is significant. Mathematically, the relative phase between the pump and the rf-field is introduced through the time dependent pumping equation

$$\Gamma_p(t+\phi) = \Gamma_p^{(0)} + \Gamma_p^{(1)} e^{i\omega_{\mathrm{rf}}(t+\phi)} + \Gamma_p^{(-1)} e^{-i\omega_{\mathrm{rf}}(t+\phi)} + \Gamma_p^{(2)} e^{2i\omega_{\mathrm{rf}}(t+\phi)} + \Gamma_p^{(-2)} e^{-2i\omega_{\mathrm{rf}}(t+\phi)} + \cdots , \tag{3.175}$$

the corresponding Fourier components with a duty cycle d, for a square wave read

$$\text{square} = \begin{cases} \Gamma_p^{(0)} & = \Gamma_p \, d, \\ \Gamma_p^{(n)} & = \frac{\Gamma_p}{n\pi} \sin(n\pi d) \left(\cos(n\phi) + i \sin(n\phi)\right), \\ \Gamma_p^{(-n)} & = \frac{\Gamma_p}{n\pi} \sin(n\pi d) \left(\cos(n\phi) - i \sin(n\phi)\right). \end{cases} \tag{3.176}$$

Note that the Fourier coefficients are no longer symmetric around the $n = 0$ index and are complex numbers. Figure (3.15) on page 67 shows the variation of the normalised amplitude of the $2\omega_{\text{rf}}$ resonance as a function of the relative phase between the pump pulses and the rf-field. We note that due to the harmonic truncation in the Floquet space the pump harmonics are truncated, typically around $Q = 4$ where Q is the highest harmonic component. From the figure we observe typical periodic behaviour, however, it's not perfect. One of the reasons due to this is as the phase changes, the characteristic dispersive and Lorentzian profiles of the OPM not only reduce in amplitude, but also become distorted to the point where their characteristic shapes are lost, this makes the amplitude calculations difficult since the profiles have additional features such as ringing in the off-resonance regions. This is reflected in the figure plot where some regions appear to have discontinuities and higher residuals from the ideal sinusoidal fit. Nevertheless, the theoretical results show that the relative phase between the pump and the rf-field have significant effects on the OPM response.

Temperature of the cell, T, atomic density, n_{Rb}, collisions and coating (Fig. 3.11 j), l)). The temperature of the cell affects a number of parameters of the magnetometer. Firstly, some of the ^{87}Rb atoms in the cell are in a gaseous form with an equilibrium vapour density which is a temperature dependent quantity. The equilibrium vapour pressure, n_{Rb} (cm^{-3}) for ^{87}Rb at temperature T is given by [49]

$$n_{\text{Rb}} = \frac{1}{T} 10^{21.866 + A - \frac{B}{T}}, \tag{3.177}$$

where $A = 4.857$ and $B = 4215$K. Recall that the Voigt effect signal is given by

$$\left\langle \hat{S}'_z(t) \right\rangle = g_F^{(2)} S_y n_F \left\langle \hat{F}_x^2(t) - \hat{F}_y^2(t) \right\rangle, \tag{3.178}$$

where n_F is the number of atoms in the prepared mixed state. Thus, increasing the temperature, increases the number of atoms and as a result increases the signal to noise ratio enhancing the sensitivity of the OPM. However, the vapour inside the cell to a good approximation follows Maxwell-Boltzmann statistics. Due to thermal motion of the atoms they occasionally collide and exchange momentum with each other and the walls surrounding them. The rate of the collisions is dependent not only on the density of the atoms, but also the speed at which they are moving. Just like the density, the speed of the atoms is also a temperature dependent quantity. The mean speed $\bar{v}$ of atoms at temperature T and mass m is given by

$$\bar{v} = \sqrt{\frac{8 k_B T}{m}}, \tag{3.179}$$

where k_B is the Boltzmann constant. The collision rate between the ^{87}Rb atoms themselves with a density n_{Rb}, velocity $\bar{v}$ and a collision cross section σ_c is given by

$$\Gamma_{\text{self}} = n_{\text{Rb}} \sigma_c \bar{v}. \tag{3.180}$$

In the case where we have buffer gas of density n', then total collision rate is the sum, namely

$$\Gamma_{\text{self+buffer}} = n_{\text{Rb}} \sigma_c \bar{v} + n' \sigma' \bar{v}', \tag{3.181}$$

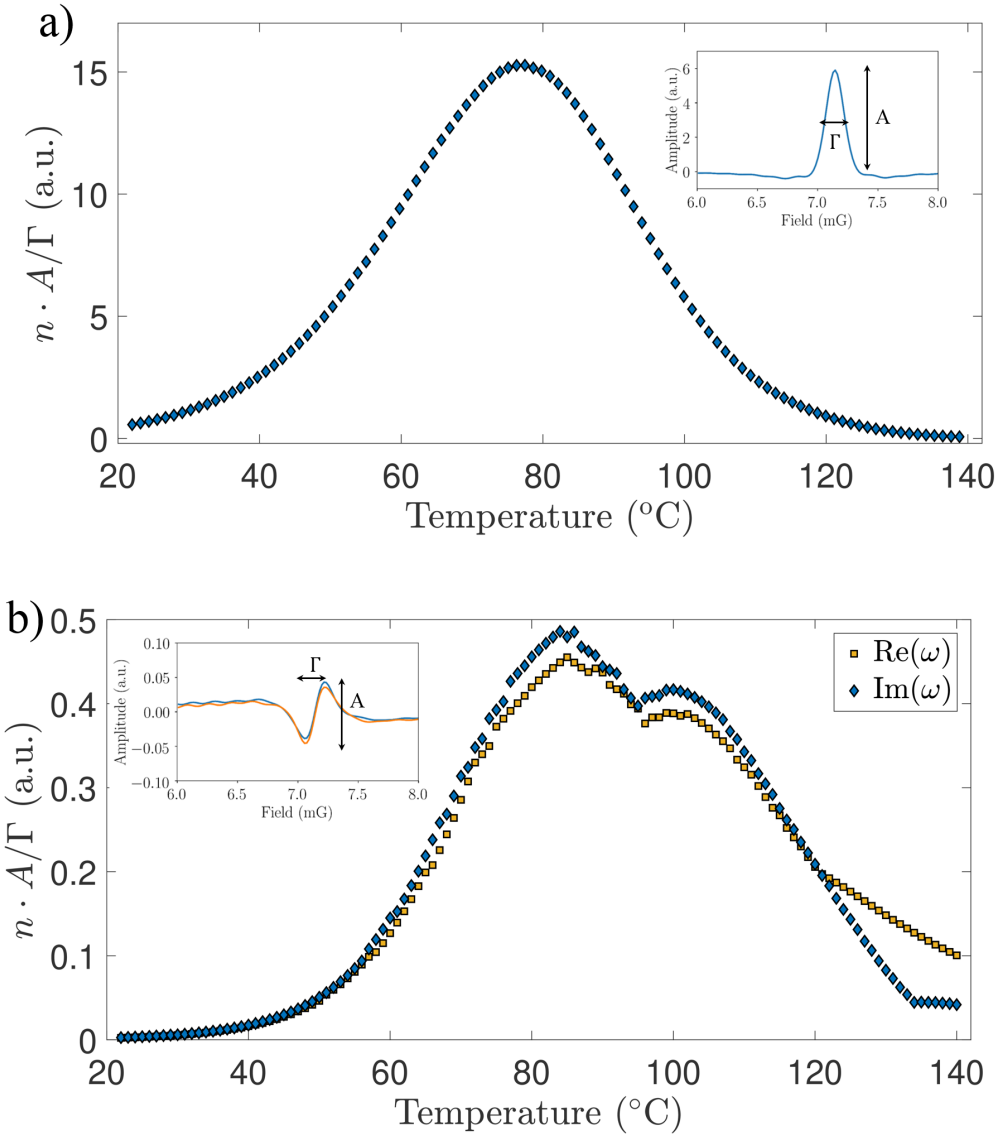

Figure 3.16: Atom number adjusted figure of merit (FOM) of the a) $2\omega_{\mathrm{rf}}$ and b) ω_{rf} resonance and dispersive profiles as a function of the temperature of the cell. Here the FOM is the ratio of the resonance height over the full-width-at-half-maximum (FWHM) of the $2\omega_{\mathrm{rf}}$ and ω_{rf} profiles times the atomic density at a given temperature T. We observe that the competition between the collision rate and the signal strength has an optimum point. This optimum point is different for the ω_{rf} and $2\omega_{\mathrm{rf}}$ quadratures. The most obvious contribution to this difference is down to the difference between the transverse and longitudinal relaxation rates.

where $\bar{v}'$ is the mean speed of the buffer gas, n' is the density of buffer gas and σ' is the collision rate between ^{87}Rb and the buffer gas. In addition, for a spherically shaped

cell with a cross sectional area A_{cell} and a volume V_{cell} the average time between the collisions of the atoms with the cell walls is given by [49]

$$\tau_{\text{wall}} = \frac{4V_{\text{cell}}}{\bar{v}A_{\text{cell}}}, \tag{3.182}$$

such that the rate of collisions between the atoms and the walls is given by

$$\Gamma_{\text{wall}} = \frac{\bar{v}A_{\text{cell}}}{4V_{\text{cell}}} = \frac{A_{\text{cell}}}{4V_{\text{cell}}}\sqrt{\frac{8k_BT}{m}}. \tag{3.183}$$

Here it is apparent that the geometric considerations in designing the cell can reduce or increase the the atom-wall collision rate. Combining the different collisional mechanisms gives

$$\Gamma_{\text{Tot}} = \Gamma_{\text{wall}} + \Gamma_{\text{self}} = \sqrt{\frac{8k_BT}{m}}\left(\frac{1}{T}10^{21.866+A-\frac{B}{T}}\sigma_c + \frac{A_{\text{cell}}}{4V_{\text{cell}}}\right), \tag{3.184}$$

where we have neglected the atomic collisions with the buffer gas atoms since our cells are paraffin coated. The increase in atom number density increases the signal to noise ratio when measuring the Voigt effect, but at the same time there is an increased rate of spin-destruction which depolarises the atoms due to the atom-atom, atom-wall collisions. A natural question to ask is whether this competition results in some optimal temperature point where the OPM sensitivity is maximised i.e. is there a stationary point such that $\partial\left\langle \hat{S}'_z(t,T)\right\rangle/\partial T = 0$? A mere inspection of the equation of motion for $\left\langle \hat{S}'_z(t)\right\rangle$ is not sufficient to make that conclusion (see e.g. eq. 3.124 on page 51), but if we look at the magnetometer response of the $2\omega_{\text{rf}}$ resonance curve which sets the OPM sensitivity by changing the temperature we find that the competition between the collision rate and the signal to noise ratio does indeed produce an optimal point (see Fig. 3.16). Here we have to note that there are several issues with the model as well as the physical interpretation of such optimal point. First of all, the prediction of the optimal point does not take into account of the degradation of the anti-relaxation coating. For example, paraffin melts at around 60-80°C whilst OTS can stand up to 170°C [49]. The quality of such coating will influence the atom-wall spin destruction collision rate and so the optimum point is dependent upon it. Moreover, because of the difference between the transverse and longitudinal relaxation rates, these optimal points may be different for the transverse and longitudinal field sensing directions, as seen in Fig. 3.16 comparing ω_{rf} and $2\omega_{\text{rf}}$ optimal points. This is affected by the geometry of the cell. Finally, the maximum for the figure of merit (A/Γ) is dependent on the magnitude of the transverse fields as well as the rf amplitude, Ω_{rf}, since they affect the state preparation process and therefore the number of atoms, n_F, prepared in the ideal state.

Magnetic field gradients. Atoms in an anti-relaxation coated cell are free to move and through atom-atom, atom-wall collisions end up randomly exploring the entire volume of the cell. If there exists an external magnetic field across the volume of the cell, then the polarised atoms precess around that effective field. Now, if

additionally, a magnetic field gradient is present across the cell due to an external field source inhomogeneity or technical inhomogeneity of the coils or both, then the atoms exploring the volume of the cell will experience different effective fields around which they will precess. Every time a collision occurs, the velocity and the direction of travel of the atom is changed and as a result the field experienced by the atom changes - in effect, the atoms experience magnetic field fluctuations. In the case where Larmor precession frequency, $\Omega_L = \gamma B^+_{\text{sense}} = \gamma(B_{\text{res}} + B_\rho + B_z^{\text{ext}})$, is much faster than the total rate of collisions $\Omega_L R/\bar{v} \gg 1$, then the longitudinal relaxation time Γ_1 due to field gradients is given by [61]

$$\Gamma_1 \sim \left(\frac{\bar{v}\Delta B}{\gamma B^+_{\text{sense}} R}\right)^2 \frac{\bar{v}}{R}, \tag{3.185}$$

where $\Delta B \ll B^+_{\text{sense}}$ is the amplitude of the fluctuating field, R is the size of the cell (for a spherical or cubic cell). In the case where the Larmor precession is slower than the collision rate, $\Omega_L R/\bar{v} \ll 1$ the relaxation due to the field gradients is then given by

$$\Gamma_1 \sim \frac{R}{\bar{v}}(\gamma\Delta B)^2. \tag{3.186}$$

Additionally, the transverse field relaxation rate follows a similar form to the longitudinal relaxation rate in the limit of the Larmor precession being much smaller than the collision rate

$$\Gamma_2 \sim \frac{R}{\bar{v}}(2\gamma\Delta B)^2. \tag{3.187}$$

Now, in all of the stated cases, the relaxation effects due to the gradient fields are not only dependent on the actual magnetic field gradients, but also the mean velocity of the atoms, which in turn depend on the temperature of the cell. In addition, because the radio-frequency dressing field ω_{rf} sets our sensitive field point B^+_{sense}, the longitudinal relaxation rates can exist in different regimes since the Larmor precession frequency and the collision rate product set the longitudinal relaxation scaling laws.

3.2.10 Scope and Limitations of the Heisenberg model

The Heisenberg model outlined in this section allows us to take into account many of the effects that influence the spin dynamics of the OPM ranging from coherent spin dynamics, pumping and decoherence. As a result, it provides us with a solid theoretical framework in understanding and modelling the OPM response using a large parameter space. However, the Heisenberg equation of motion is limited to only being able to provide information of one particular observable relative to the Hamiltonian of the system. The model does not provide any information on how the state populations evolve in time during the pumping and the probing cycles and more importantly, does not take into account that we are dealing with large ensembles of atoms. Moreover, as has been shown, additional complexity arises when attempting to model higher order moments of the observables, where in particular, the form of the decoherence effects take non-trivial forms and require extensive treatment using

the fluctuation-dissipation theorem. Furthermore, the form of the decoherence effects are dependent on the properties of the observables (e.g. commutation relations), and as a result if a different observable is to be measured, a significant amount of effort has to be expended in order to derive the form of such decoherence effects.

The density matrix approach can circumvent some of these problems with an additional advantage that it can provide the information about the state populations in time, as well as their coherences. Moreover, it can be generalised to calculate any observable of any order since the expectation value is simply given by the trace of the product between the density operator and the observable, i.e. $\left\langle \hat{O}^n \right\rangle = \mathrm{Tr}\left[\hat{\rho}\hat{O}^n\right]$ where $n \in \mathbb{Z}$. The density operator approach also allows us to deal with quantum systems which are more general than the ensembles described by a pure state wavefunction. This is a crucial part in the case of the Voigt effect OPM since the input state is a mixed state and cannot be described by a wavefunction. Moreover, the modelling of decoherence and pumping effects take a more simplistic phenomenological approach whereby it is given as the difference between the current state of the ensemble and some input state governed by some rate, i.e. $\Gamma(\hat{\rho} - \hat{\rho}_{\mathrm{in}})$. Finally, the density matrix approach enables the addition of other types of interactions in the system e.g. a microwave or optical fields, which the Heisenberg formalism is unable to cater for. Consequently, this enriches our theoretical toolbox as well as the knowledge and interpretation of the theoretical results. However, the richness and power of the density matrix approach comes at a cost of vastly increasing the size of the vector and matrix spaces which result in a significant increase in computational resources and time required to study the problems.

3.3 Density matrix interpretation of spin dynamics in a rf-dressed field

3.3.1 Liouville-von Neumann equation of motion

An ensemble in a mixed state can be described by a density operator expressed as an outer product of pure states where the coefficients represent probabilities

$$\hat{\rho}(t) = \sum_n p_n \left|\psi_n\right\rangle \left\langle\psi_n\right|, \tag{3.188}$$

where p_n is the probability of the ensemble being in state $|\psi_n\rangle$ after the measurement. For any observable of order n, $\hat{O}^n$ the expectation value using the density operator formalism is given by

$$\left\langle \hat{O}^n \right\rangle = \mathrm{Tr}\left[\hat{\rho}\hat{O}^n\right]. \tag{3.189}$$

Now the state evolution is given by the Schrödinger equation

$$i\hbar\partial_t \left|\psi(t)\right\rangle = \hat{H}\left|\psi(t)\right\rangle. \tag{3.190}$$

Taking the time derivative of eq. (3.188) and substituting into the Schrödinger equation after some algebra yields the Liouville-von Neumann equation of motion which describes the time evolution of the density operator given some Hamiltonian, $\hat{H}$

$$\partial_t \hat{\rho}(t) = \frac{1}{i\hbar}\left[\hat{H}(t), \hat{\rho}(t)\right], \tag{3.191}$$

where $\left[\hat{H}(t), \hat{\rho}(t)\right]$ is a commutator relation. As before, the Hamiltonian of a radio-frequency dressed spin with external fields is given by

$$\hat{H}(t) = (\Omega_{\mathrm{rf}}\cos(\omega_{\mathrm{rf}}t) + \Omega_x^{\mathrm{ext}})\hat{F}_x(t) + \Omega_y^{\mathrm{ext}}\hat{F}_y(t) + (\Omega_{\mathrm{dc}} + \Omega_z^{\mathrm{ext}})\hat{F}_z(t). \tag{3.192}$$

The above describes the coherent dynamics of the spin. To add the pumping and decoherence mechanisms a phenomenological approach is followed whereby the state preparation process consists of two processes namely the pumping dynamics and decoherence due to the pump [53]. These are modelled as positive and negative contributions respectively in the density matrix, whereby active pumping positively contributes to the total rate of change $\Gamma_i\hat{\rho}_i$ with the decoherence rate modelled by $-\Gamma_i\hat{\rho}(t)$. Here $\hat{\rho}_i$ is some ideal state which we pump into. In the scenario where the rate Γ_i may be time dependent, i.e. $\Gamma_i \to \Gamma_i(t)$ (e.g. time dependent pumping profile) the total contribution to the density matrix dynamics due to pumping and pump decoherence takes the following general form

$$\partial_t \hat{\rho}_i(t) = -\Gamma_i(t)\left(\hat{\rho}(t) - \hat{\rho}_i\right). \tag{3.193}$$

In our case, the pumping follows a time dependent profile, $\Gamma_p(t)$ such that it can be spectrally decomposed and we have an input state, $\hat{\rho}_{\mathrm{in}}$, defined in the basis where the measurements takes place. Therefore, the contribution to the density matrix due to pumping dynamics is simply given by

$$\partial_t \hat{\rho}(t)\big|_{\mathrm{pump}} = -\Gamma_p(t)\left(\hat{\rho}(t) - \hat{\rho}_{\mathrm{in}}\right). \tag{3.194}$$

Equivalently, the decoherence effects characterised by the rate Γ_{rel} and the contribution of the thermal state given by (as before), $\hat{\rho}_0$. The contribution to the density operator due to relaxation dynamics is given by

$$\partial_t \hat{\rho}(t)\big|_{\mathrm{rel}} = -\Gamma_{\mathrm{rel}}\left(\hat{\rho}(t) - \hat{\rho}_0\right). \tag{3.195}$$

Combining the coherent, pumping and relaxation terms of the density operator yields the full dynamics

$$\partial_t \hat{\rho}(t) = \underbrace{\frac{1}{i\hbar}\left[\hat{H}(t), \hat{\rho}(t)\right]}_{\text{Coherent Dynamics}} - \underbrace{\Gamma_p(t)\left(\hat{\rho}(t) - \hat{\rho}_{\mathrm{in}}\right)}_{\text{Pumping}} - \underbrace{\Gamma_{\mathrm{rel}}\left(\hat{\rho}(t) - \hat{\rho}_0\right)}_{\text{Decoherence}}. \tag{3.196}$$

However, as encountered previously in section (3.2.6), we cannot solve the equation above trivially, we need to transform it into Liouville space.

3.3.2 Density Matrix in the Liouville Space

Using the same procedure as outlined in detail in Sec. (3.2.6) we transform eq. (3.196) into the Liouville space. First, we define the following super (Liouville) operators

$$\hat{\mathbf{O}}\ \hat{\rho} \rightarrow \mathcal{L}(\hat{\mathbf{O}})\mathbf{X}, \tag{3.197}$$

$$\hat{\rho}\ \hat{\mathbf{O}} \rightarrow \mathcal{R}(\hat{\mathbf{O}})\mathbf{X}. \tag{3.198}$$

Using these results, we can write eq. (3.196) as

$$\frac{d\mathbf{X}(t)}{dt} = \mathbf{C}(t)\mathbf{X}(t) - \Gamma_p(t)\left[\mathbf{X}(t) - \mathbf{X}_{\text{in}}\right] - \Lambda_{\text{rel}}\left[\mathbf{X}(t) - \mathbf{X}_0\right], \tag{3.199}$$

where $\Lambda_p(t)$ and Λ_{rel} are pumping and relaxation constants with

$$\mathbf{C}(t) = \mathcal{L}(\hat{H}(t)) + \mathcal{R}(\hat{H}(t)^T). \tag{3.200}$$

$$\tag{3.201}$$

The density matrix in the Liouville space is written in a vector form is

$$\mathbf{X}(t) = \begin{bmatrix} \rho_{11} \\ \rho_{12} \\ \rho_{13} \\ \vdots \end{bmatrix}. \tag{3.202}$$

As before, we cannot trivially solve the equation above due to the oscillating rf-field as well as the time dependent pumping processes. The pumping and the rf-dressing field have periodicity which satisfies the Floquet theorem. Therefore, the same method will be applied to transform the density operator equation of motion into the Floquet space.

3.3.3 Density Matrix in the Floquet Space

The Liouville-von Neumann equation in the Liouville space is given by

$$\frac{d\mathbf{X}(t)}{dt} = \mathbf{C}(t)\mathbf{X}(t) - \Gamma_p(t)\ \left[\mathbf{X}(t) - \mathbf{X}_{\text{in}}\right] - \Lambda_{\text{rel}}\left[\mathbf{X}(t) - \mathbf{X}_0\right], \tag{3.203}$$

where we can spectrally decompose the coherent dynamics and the pumping into its harmonics, namely, we can write

$$\mathbf{C}(t) = \mathbf{C}^{(0)} + \mathbf{C}^{(1)}\ e^{i\omega_{\text{rf}}t} + \mathbf{C}^{(-1)}\ e^{-i\omega_{\text{rf}}t}, \tag{3.204}$$

and

$$\Gamma_p(t) = \Gamma_p^{(0)} + \Gamma_p^{(1)}e^{i\omega_{\text{rf}}t} + \Gamma_p^{(-1)}e^{-i\omega_{\text{rf}}t} + \Gamma_p^{(2)}e^{2i\omega_{\text{rf}}t} + \Gamma_p^{(-2)}e^{-2i\omega_{\text{rf}}t} + \cdots = \sum_{n=0} \Gamma_p^{(n)}e^{in\omega_{\text{rf}}t}, \tag{3.205}$$

Note that that these operator functions obey periodic properties which satisfy

$$\mathbf{C}(t+T) = \mathbf{C}(t), \tag{3.206}$$

$$\Gamma_p(t+T) = \Gamma_p(t), \tag{3.207}$$

$$\frac{d\mathbf{X}(t+T)}{dt} = \frac{d\mathbf{X}(t)}{dt}. \tag{3.208}$$

We spectrally expand the density operator expression in the Liouville space

$$\mathbf{X}(t) = \mathbf{X}^{(0)}(t) + \mathbf{X}^{(1)}(t)\ e^{i\omega_{\mathrm{rf}}t} + \mathbf{X}^{(-1)}(t)\ e^{-i\omega_{\mathrm{rf}}t} + \mathbf{X}^{(2)}(t)e^{2i\omega_{\mathrm{rf}}t} + \mathbf{X}^{(-2)}(t)\ e^{-2i\omega_{\mathrm{rf}}t} + \cdots, \tag{3.209}$$

and substitute the expressions for $\mathbf{C}(t)$, $\Gamma_p(t)$ and $\mathbf{X}(t)$ into the equation of motion which we generalise to the nth harmonic

$$\begin{aligned}\frac{d\mathbf{X}^{(n)}(t)}{dt} =& \mathbf{C}_n^{(0)}\mathbf{X}^{(n)}(t) + \mathbf{C}^{(1)}\mathbf{X}^{(n-1)}(t) + \mathbf{C}^{(-1)}\mathbf{X}^{(n+1)}(t) - \sum_i \Gamma_p^{(n-i)}\mathbf{X}^{(i)}(t) \\ &+ \Gamma_p^{(n)}\mathbf{X}_{\mathrm{in}} - \Lambda_{\mathrm{rel}}\mathbf{X}^{(n)}(t) + \Lambda_{\mathrm{rel}}\ \mathbf{X}_0\ \delta_{n,0}.\end{aligned} \tag{3.210}$$

As before, we can express the recursive relation given in eq. (3.210) in a more compact form by defining a new linear space. We define a harmonic vector $\mathbb{X}$ such that

$$\mathbb{X} = \begin{bmatrix} \mathbf{X}^{(-n)}e^{-in\omega_{\mathrm{rf}}t} \\ \vdots \\ \mathbf{X}^{(-1)}e^{-i\omega_{\mathrm{rf}}t} \\ \mathbf{X}^{(0)} \\ \mathbf{X}^{(1)}e^{i\omega_{\mathrm{rf}}t} \\ \vdots \\ \mathbf{X}^{(n)}e^{in\omega_{\mathrm{rf}}t} \end{bmatrix}, \tag{3.211}$$

and by defining a matrix $\mathbb{N}$ with matrix elements $\mathbb{N}_{ij} = j\delta_{ij}$ and j spanning for all possible harmonics, the spin operator can be written as

$$\mathbb{X}(t) = e^{i\omega_{\mathrm{rf}}\mathbb{N}t}\mathbb{X}_F, \tag{3.212}$$

where

$$\mathbb{X}_F = \begin{bmatrix} \mathbf{X}^{(-n)} \\ \vdots \\ \mathbf{X}^{(-1)} \\ \mathbf{X}^{(0)} \\ \mathbf{X}^{(1)} \\ \vdots \\ \mathbf{X}^{(n)} \end{bmatrix}. \tag{3.213}$$

If we additionally define a vector $\mathbb{V}$ with $\mathbb{V}_i = 1$ for all i's, the second order moment operator can be written as $\mathbf{X}(t) = \mathbb{V}\cdot\mathbb{X}(t)$. With these definitions we can write the eq. (3.210) in a more compact form

$$\frac{d\mathbf{X}(t)}{dt} = \mathbb{V}\cdot e^{i\mathbb{N}\omega_{\mathrm{rf}}t}\left([\mathbb{C} - \mathbb{\Gamma}_T]\ \mathbb{X}_F + \mathbb{\Gamma}_{\mathrm{in}}\mathbb{X}_{\mathrm{in}} + \mathbb{\Lambda}_{\mathrm{rel}}\mathbb{X}_0\right), \tag{3.214}$$

where the pump matrix term reads

$$(\mathbb{\Gamma}_T)_{nm} = \Gamma_p^{(n-m)}\mathbf{I} + \Lambda_{\text{rel}}\mathbf{I}, \tag{3.215}$$

$$(\mathbb{\Gamma}_{\text{in}})_{nm} = \begin{cases} \Gamma_p^{(n)}\mathbf{I}, & \text{for } n = m, \\ 0, & \text{otherwise}, \end{cases} \tag{3.216}$$

with $(\mathbb{X}_{\text{in}})_n = \mathbf{X}_{\text{in}}$. The unpolarised drift matrix is

$$(\mathbb{\Lambda}_{\text{rel}})_{nm} = \begin{cases} \Lambda_{\text{rel}}\mathbf{I}, & \text{for } n = m = 0, \\ 0 & \text{otherwise}. \end{cases} \tag{3.217}$$

The first derivative governs the dynamics, applying the product rule to differentiate $\mathbf{X}(t)$ we get

$$\frac{d\mathbf{X}(t)}{dt} = \mathbb{V} \cdot \left(i\mathbb{N}\omega_{\text{rf}} e^{i\mathbb{N}\omega_{\text{rf}}t}\mathbb{X}_F + e^{i\mathbb{N}\omega_{\text{rf}}t}\frac{d\mathbb{X}_F}{dt} \right). \tag{3.218}$$

Equating eq. (3.214) and eq. (3.218) and rearranging for $\frac{d\mathbb{X}_F}{dt}$ we get

$$\frac{d\mathbb{X}_F(t)}{dt} = [\tilde{\mathbb{C}} - \mathbb{\Gamma}_T]\ \mathbb{X}_F + \mathbb{\Gamma}_{\text{in}}\mathbb{X}_{\text{in}} + \mathbb{\Lambda}_{\text{rel}}\mathbb{X}_0, \tag{3.219}$$

where we have defined $\tilde{\mathbb{C}} = \mathbb{C} - i\mathbb{N}\omega_{\text{rf}}$ with the following components

$$\tilde{\mathbb{C}}_{nm} = \begin{cases} \mathbf{C}^{(0)} - in\omega_{\text{rf}}\mathbf{I}, & \text{for } n = m, \\ \mathbf{C}^{(\pm 1)}, & \text{for } m = n \mp 1, \\ 0 & \text{otherwise}. \end{cases} \tag{3.220}$$

Recall the definition for $\mathbf{C}(t) = \mathcal{L}(\hat{H}(t)) + \mathcal{R}(\hat{H}^T(t))$, taking this with the zero order term defined in the expression above we can write

$$\mathbf{C}^{(0)} - in\omega_{\text{rf}}\mathbf{I} = \mathcal{L}\left[\hat{H}^{(0)} - \frac{in\omega_{\text{rf}}}{2}\mathbf{I}\right] + \mathcal{R}\left[\hat{H}^{(0)^T} - \frac{in\omega_{\text{rf}}}{2}\mathbf{I}\right], \tag{3.221}$$

which gives rise to the same atomic spin resonances at multiples of $\omega_{\text{rf}}/2$ frequencies where ω_{rf} is the frequency of the rf-field as in the case of the Heisenberg model. The resonance occurs when $\Omega_{\text{dc}} = \omega_{\text{rf}}/2$.

3.3.4 State space using density operator approach

So far, in the analysis of the spin dynamics using the density operator approach we have not specified the form of the input states $\hat{\rho}_{\text{in}}$ and $\hat{\rho}_0$. In the previous sections, where we have used the Heisenberg approach to model the second order spin dynamics we have only considered a single manifold of the ^{87}Rb ground state i.e. $F = 2$ of the $5^2S_{1/2}$ ground state. This made the definitions of the states trivial to compute. However, the model does not say anything about the state evolution. This becomes

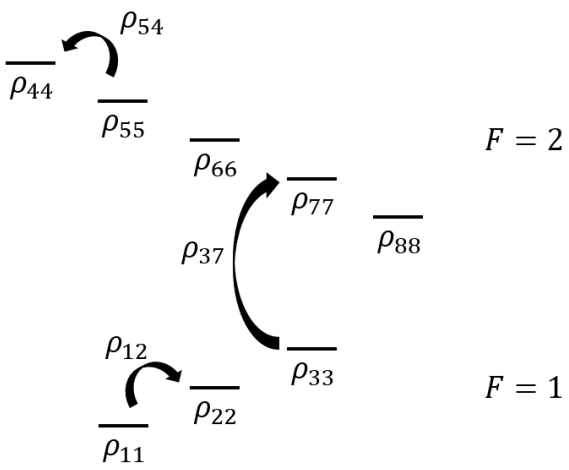

Figure 3.17: Density elements and their relations within the $F = 1 + F = 2$ manifold.

crucially important if we want to perform microwave spectroscopy which couples the $F = 1 \rightarrow F = 2$ manifolds. Since the performance of the OPM depends heavily on how well we prepare our magnetically sensitive states, microwave spectroscopy enables us to probe the system and assess the efficacy of this state preparation process. Moreover, having control over the various parameters in the Hamiltonian we can in principle partially probe the state both, theoretically and experimentally which allows us to understand the consequent evolution of the state.

We begin by defining the density operator for the complete $F = 1 + F = 2$ manifold of the ^{87}Rb ground state

$$\hat{\rho} = \begin{bmatrix} \rho_{11} & \rho_{12} & \rho_{13} & \rho_{14} & \rho_{15} & \rho_{16} & \rho_{17} & \rho_{18} \\ \rho_{21} & \rho_{22} & \rho_{23} & \rho_{24} & \rho_{25} & \rho_{26} & \rho_{27} & \rho_{28} \\ \rho_{31} & \rho_{32} & \rho_{33} & \rho_{34} & \rho_{35} & \rho_{36} & \rho_{37} & \rho_{38} \\ \rho_{41} & \rho_{42} & \rho_{43} & \rho_{44} & \rho_{45} & \rho_{46} & \rho_{47} & \rho_{48} \\ \rho_{51} & \rho_{52} & \rho_{53} & \rho_{54} & \rho_{55} & \rho_{56} & \rho_{57} & \rho_{58} \\ \rho_{61} & \rho_{62} & \rho_{63} & \rho_{64} & \rho_{65} & \rho_{66} & \rho_{67} & \rho_{68} \\ \rho_{71} & \rho_{72} & \rho_{73} & \rho_{74} & \rho_{75} & \rho_{76} & \rho_{77} & \rho_{78} \\ \rho_{81} & \rho_{82} & \rho_{83} & \rho_{84} & \rho_{85} & \rho_{86} & \rho_{87} & \rho_{88} \end{bmatrix}, \tag{3.222}$$

where the relations between the energy levels are depicted in Fig. 3.17. Now the spin operators (in the z-basis) for the complete manifold are given by the

$$\hat{F}_i^{\text{Full}} = \begin{bmatrix} \hat{F}_i^{F=1} & 0 \\ 0 & \hat{F}_i^{F=2} \end{bmatrix}, \tag{3.223}$$

where for example, the $\hat{F}_x^{\text{Full}}$ operator is given by (see Appendix B.6.1 on page 187 for the full description of other spin operators)

$$\hat{F}_x^{\text{Full}} = \begin{bmatrix} 0 & \frac{1}{2}\sqrt{2} & 0 & 0 & 0 & 0 & 0 & 0 \\ \frac{1}{2}\sqrt{2} & 0 & \frac{1}{2}\sqrt{2} & 0 & 0 & 0 & 0 & 0 \\ 0 & \frac{1}{2}\sqrt{2} & 0 & 0 & 0 & 0 & 0 & 0 \\ 0 & 0 & 0 & 0 & 1 & 0 & 0 & 0 \\ 0 & 0 & 0 & 1 & 0 & \sqrt{\frac{3}{2}} & 0 & 0 \\ 0 & 0 & 0 & 0 & \sqrt{\frac{3}{2}} & 0 & \sqrt{\frac{3}{2}} & 0 \\ 0 & 0 & 0 & 0 & 0 & \sqrt{\frac{3}{2}} & 0 & 1 \\ 0 & 0 & 0 & 0 & 0 & 0 & 1 & 0 \end{bmatrix}. \tag{3.224}$$

The definition of our input state in the x-basis corresponds to an equal statistical mixture of $|F = 2, m_F = \pm 2\rangle$, such that the density input state takes the form

$$\hat{\rho}_{\text{in}}^x = \begin{bmatrix} 0 & 0 & 0 & 0 & 0 & 0 & 0 & 0 \\ 0 & 0 & 0 & 0 & 0 & 0 & 0 & 0 \\ 0 & 0 & 0 & 0 & 0 & 0 & 0 & 0 \\ 0 & 0 & 0 & \frac{1}{2} & 0 & 0 & 0 & 0 \\ 0 & 0 & 0 & 0 & 0 & 0 & 0 & 0 \\ 0 & 0 & 0 & 0 & 0 & 0 & 0 & 0 \\ 0 & 0 & 0 & 0 & 0 & 0 & 0 & 0 \\ 0 & 0 & 0 & 0 & 0 & 0 & 0 & \frac{1}{2} \end{bmatrix}, \tag{3.225}$$

where, after applying a unitary transformation to transform the state in z-basis where the measurement takes place, the state takes the form

$$\hat{\rho}_{\text{in}}^z = \hat{U}^\dagger \hat{\rho}_{\text{in}}^x \hat{U} = \begin{bmatrix} 0 & 0 & 0 & 0 & 0 & 0 & 0 & 0 \\ 0 & 0 & 0 & 0 & 0 & 0 & 0 & 0 \\ 0 & 0 & 0 & 0 & 0 & 0 & 0 & 0 \\ 0 & 0 & 0 & \frac{1}{16} & 0 & \frac{3}{16}\sqrt{\frac{2}{3}} & 0 & \frac{1}{16} \\ 0 & 0 & 0 & 0 & \frac{1}{4} & 0 & \frac{1}{4} & 0 \\ 0 & 0 & 0 & \frac{3}{16}\sqrt{\frac{2}{3}} & 0 & \frac{3}{8} & 0 & \frac{3}{16}\sqrt{\frac{2}{3}} \\ 0 & 0 & 0 & 0 & \frac{1}{4} & 0 & \frac{1}{4} & 0 \\ 0 & 0 & 0 & \frac{1}{16} & 0 & \frac{3}{16}\sqrt{\frac{2}{3}} & 0 & \frac{1}{16} \end{bmatrix}, \tag{3.226}$$

where $\hat{U}$ is computed using eq. (3.120) on page 50. The thermal state is simply given by

$$\hat{\rho}_0 = \frac{1}{8}\mathbb{I}_{8\times 8}, \tag{3.227}$$

where $\mathbb{I}_{8\times 8}$ is a 8×8 identity matrix. As before, the Voigt effect is given by eq. (3.32) on page 34. Using the density operator approach, the Voigt effect can the be expressed

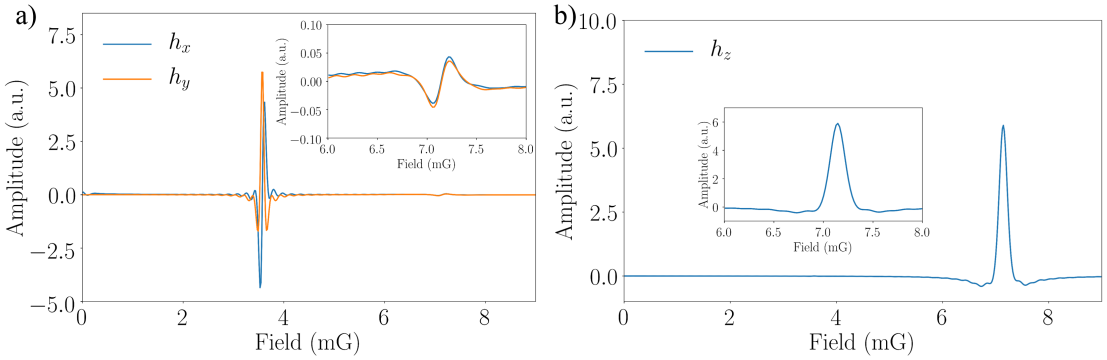

Figure 3.18: Magnetometer response as a function of longitudinal magnetic field B_z using the density operator approach. The sequence, is the same as outlined in sec. (3.2.8) where the state preparation is done using synchronous pumping using square pulses followed by a cw probing.

in terms of the coherences, namely

$$\left\langle \hat{S}'_z(t) \right\rangle^{F=1} = g^{(2)}_{F=1} S_y n_F \, \mathrm{Tr}^{F=1}\left[\left((\hat{F}^{\mathrm{Full}}_x)^2 - (\hat{F}^{\mathrm{Full}}_y)^2\right)\hat{\rho}\right] = g^{(2)}_{F=1} S_y n_F \left(\rho_{13} + \rho_{31}\right), \tag{3.228}$$

$$\begin{aligned}\left\langle \hat{S}'_z(t) \right\rangle^{F=2} &= g^{(2)}_{F=2} S_y n_F \, \mathrm{Tr}^{F=2}\left[\left((\hat{F}^{\mathrm{Full}}_x)^2 - (\hat{F}^{\mathrm{Full}}_y)^2\right)\hat{\rho}\right] \\ &= g^{(2)}_{F=2} S_y n_F \left(\sqrt{6}\rho_{46} + \sqrt{6}\rho_{64} + \sqrt{6}\rho_{68} + \sqrt{6}\rho_{86} + 3\rho_{57} + 3\rho_{75}\right), \end{aligned} \tag{3.229}$$

where we have traced over $F = 1$ and $F = 2$ manifolds to show their contributions individually.

3.3.5 Magnetometer response to external fields (Density Matrix Model)

The procedure to derive the OPM response in the pump and probe regions are equivalent to the Heisenberg model section. We thus proceed by simply stating the solutions to the pump and probe sequences. For the pump, the steady state solution is

$$\mathbb{X}^{\mathrm{pump}}_F = -\left[\tilde{\mathbb{C}} - \mathbb{\Gamma}_T\right]^{-1}(\mathbb{\Gamma}_{\mathrm{in}}\mathbb{X}_{\mathrm{in}} + \mathbb{\Lambda}_{\mathrm{rel}}\mathbb{X}_0). \tag{3.230}$$

During the probe, the pumping is off, and the state evolves freely in time. We average the OPM response over a few cycles, giving

$$\mathbb{X}^{\mathrm{probe}}_F = \frac{1}{T}(\tilde{\mathbb{C}}')^{-1}\left(e^{\tilde{\mathbb{C}}' \, T} - \mathbb{I}\right)\mathbb{X}^{\mathrm{pump}}_F + \frac{1}{T}(\tilde{\mathbb{C}}')^{-1}\left[(\tilde{\mathbb{C}}')^{-1}\left(e^{\tilde{\mathbb{C}}' \, T} - \mathbb{I}\right) - T\right]\mathbb{\Lambda}_{\mathrm{rel}}\mathbb{X}_0. \tag{3.231}$$

where $\tilde{\mathbb{C}}' = \tilde{\mathbb{C}} - \mathbb{\Lambda}_{\mathrm{rel}}$. The OPM response as a function of longitudinal B_z field is depicted in Fig. 3.18. As can be observed from the figure the density operator theory approach

provides the same qualitative response when compared to the Heisenberg model depicted in Fig. 3.9 on page 58. Whilst the density operator approach contains complete information about the system such as the populations and coherences compared to the Heisenberg model, this, however, comes at the expense of having a larger state space which is computationally more intense. For example, using the Heisenberg approach, the Liouville-Floquet space results in a square matrix dimension $(2F+1)^2 \times (2Q+1)$ whilst for the density matrix approach $((2F_1+1)+(2F_2+1))^2 \times (2Q+1)$, where $F_{1,2}$ are the manifolds of the hyperfine states and Q is the harmonic cut-off frequency index $n\omega$, $-Q \leq n \leq Q$ for the Floquet approximation. The equations of motion derived in both the Heisenberg model and the Density matrix model are equivalent. Thus, the theoretical results for the density operator based on various OPM parameters which were shown in the Heisenberg model will not be repeated. Instead, the focus will shift towards the theoretical investigation of the microwave spectroscopy in the context of the Voigt effect. The motivation for this (which will become more obvious in the coming sections) is due to a number of reasons. First, due to the complexity of state preparation process in the rf-dressed atomic state picture, it is not trivial to infer that our input state is a statistical mixture of $|F=2, m_F=\pm 2\rangle$ states. We want to be able to assess the efficiency of this state preparation process and understand how the parameter space affects it. Moreover, in this work, the Voigt effect measures the square difference of the angular momentum operators which we can relate to the angular momentum probability surfaces. The knowledge of the angular momentum probability surfaces allows one to reconstruct partial density matrix. This allows us to discriminate between the different states that can be generated during the process of optical pumping. This is extremely useful because the microwave spectrum of the state allows us to assess what is the prepared state before the measurement (probing) takes place.

3.3.6 Angular Momentum Probability Surfaces

The density matrix can be visualised graphically by transforming it into an angular momentum probability surface [38, 63]. In our case, the density matrix is expressed in terms of the Zeeman sublevels of the hyperfine manifold with a total angular momentum F, where the diagonal elements of the density matrix represent state populations of each sub-level and the off-diagonal elements are coherences which represent correlations between any two given states within the manifold. The probability of measuring the state being in a hyperfine sublevel m is given by $\rho_{m,m} = \langle F, m \,|\, \hat{\rho} \,|\, F, m\rangle$. We can express the probability of finding the system in an m sublevel along the (θ, ϕ) direction using the following relation [38]

$$\rho_F(\theta,\phi) = \langle F, m \,|\, \hat{\rho} \,|\, F, m\rangle = \sum_{m,m'} \left(D^{(F)}_{m,F}\right)^* (\phi,\theta,0)\hat{\rho}_{m,m'} D^{(F)}_{m',F}(\phi,\theta,0), \tag{3.232}$$

where $D^{(F)}_{m',m}(\phi,\theta,0)$ are the Wigner D-functions which are given by

$$D^{(F)}_{m',m}(\phi,\theta,0) = e^{-i\phi m'} d^{(F)}_{m',m}(\theta), \tag{3.233}$$

and the general form of $d^{(F)}_{m',m}(\theta)$ is given by

$$d^{(F)}_{m',m}(\theta) = \sum_k (-1)^{k-m+m'} \frac{\sqrt{(F+m)!(F-m)!(F+m')!(F-m')!}}{(F+m-k)!k!(F-k-m')!(k-m+m')!} \times \cos\left(\frac{\theta}{2}\right)^{2F-2k+m-m'} \sin\left(\frac{\theta}{2}\right)^{2k-m+m'}, \tag{3.234}$$

such that for and $F = 2$ manifold where our state is prepared, the matrix $d^{(F=2)}_{m',m}(\theta)$ reads (see Appendix B.6.2 on page 189 for a detailed calculation)

$$d^{(2)}_{m',m}(\theta) = \begin{bmatrix} c^4_{\theta/2} & -2c^3_{\theta/2}s_{\theta/2} & \sqrt{6}c^2_{\theta/2}s^2_{\theta/2} & -2c_{\theta/2}s^3_{\theta/2} & s^4_{\theta/2} \\ 2c^3_{\theta/2}s_{\theta/2} & 4c^4_{\theta/2} - 3c^2_{\theta/2} & (\sqrt{6}c_{\theta/2} - 2\sqrt{6}c^3_{\theta/2})s_{\theta/2} & -4c^4_{\theta/2} + 3c^2_{\theta/2} & -2c^3_{\theta/2}s_{\theta/2} \\ \sqrt{6}c^2_{\theta/2}s^2_{\theta/2} & (2\sqrt{6}c^3_{\theta/2} - \sqrt{6}c_{\theta/2})s_{\theta/2} & 6c^4_{\theta/2} - 6c^2_{\theta/2} + 1 & (\sqrt{6}c_{\theta/2} - 2\sqrt{6}c^3_{\theta/2})s_{\theta/2} & \sqrt{6}c^2_{\theta/2}s^2_{\theta/2} \\ 2c_{\theta/2}s^3_{\theta/2} & 3s^2_{\theta/2} - 4s^4_{\theta/2} & (2\sqrt{6}c^3_{\theta/2} - \sqrt{6}c_{\theta/2})s_{\theta/2} & 4c^4_{\theta/2} - 3c^2_{\theta/2} & -2c^3_{\theta/2}s_{\theta/2} \\ 0 & 2s^3_{\theta/2}c_{\theta/2} & \sqrt{6}c^2_{\theta/2}s^2_{\theta/2} & 2c^3_{\theta/2}s_{\theta/2} & c^4_{\theta/2} \end{bmatrix}, \tag{3.235}$$

where $c^n_{\theta/2} = \cos^n(\theta/2)$ etc. The Wigner functions describe rotations of a state written in the basis of the angular momentum eigenstates. We can use these relations to plot the probability surfaces for our input state which is an equal statistical mixture of $|F = 2, m_F = \pm 2\rangle$. In the rotated frame in the x-basis density operator has the form

$$\hat{\rho}^x_{\text{in}} = \begin{bmatrix} \frac{1}{2} & 0 & 0 & 0 & 0 \\ 0 & 0 & 0 & 0 & 0 \\ 0 & 0 & 0 & 0 & 0 \\ 0 & 0 & 0 & 0 & 0 \\ 0 & 0 & 0 & 0 & \frac{1}{2} \end{bmatrix}, \tag{3.236}$$

where, using eq. (3.232) the probability surface matrix $\rho_F(\theta, \phi)$ is given by

$$\rho^x_F(\theta,\phi) = \langle F = 2, m \,|\, \hat{\rho}^x_{\text{in}} \,|\, F = 2, m\rangle = \sum_{m,m'} \left(D^{(F)}_{m,F}\right)^* (\phi,\theta,0)\hat{\rho}_{m,m'} D^{(F)}_{m',F}(\phi,\theta,0), \tag{3.237}$$

$$\rho^x_F(\theta,\phi) = \frac{1}{2}\sin^8\left(\frac{1}{2}\theta\right) + \frac{1}{2}\cos^8\left(\frac{1}{2}\theta\right). \tag{3.238}$$

For a qualitative comparison, a state in the same basis with the following density matrix

$$\hat{\rho} = \frac{1}{3}\begin{bmatrix} 0 & 0 & 0 & 0 & 0 \\ 0 & 1 & 0 & 0 & 0 \\ 0 & 0 & 1 & 0 & 0 \\ 0 & 0 & 0 & 1 & 0 \\ 0 & 0 & 0 & 0 & 0 \end{bmatrix}, \tag{3.239}$$

has the following probability surface

$$\rho_F(\theta,\phi) = -\frac{2}{3}\cos^8\left(\frac{1}{2}\theta\right) + \frac{4}{3}\cos^6\left(\frac{1}{2}\theta\right) - 2\cos^4\left(\frac{1}{2}\theta\right) + \frac{4}{3}\cos^2\left(\frac{1}{2}\theta\right), \tag{3.240}$$

on the other hand, a thermal state, given by

$$\hat{\rho}_{\text{th}} = \frac{1}{5}\begin{bmatrix} 1 & 0 & 0 & 0 & 0 \\ 0 & 1 & 0 & 0 & 0 \\ 0 & 0 & 1 & 0 & 0 \\ 0 & 0 & 0 & 1 & 0 \\ 0 & 0 & 0 & 0 & 1 \end{bmatrix}, \tag{3.241}$$

where we note the fact that the thermal state has the same form regardless in which basis we work in. The probability surface is given by

$$\rho_F^{\text{th}}(\theta, \phi) = \frac{1}{5}. \tag{3.242}$$

To visualise the surfaces, we convert from the spherical polar coordinates to Cartesian coordinates using

$$x = \rho_F \sin(\theta)\cos(\phi), \tag{3.243}$$
$$y = \rho_F \sin(\theta)\sin(\phi), \tag{3.244}$$
$$z = \rho_F \cos(\theta), \tag{3.245}$$

where ρ_F is the radius of our probability surface calculated in the expressions above and $0 \leq \theta \leq \pi$, $0 \leq \phi \leq 2\pi$. Figure 3.19 on page 83 shows surface plots for each calculated state. As can be seen, the topology of the surface can tell whether the state is polarised or not, the degree of this polarisation and whether there exists a preferential axis for the polarisation. These symmetry properties can be further utilised to infer the properties of the density operator. More, rigorously

Theorem 1. *There exists a one-to-one mapping between the density matrix defined for the manifold of Zeeman sublevels of a state with a total angular momentum F and the corresponding angular momentum probability surface, $\rho_F(\theta, \phi)$ [38, 62].*

For example, the thermal state has no preferred axis or direction, which means that any form of rotation of the probability surface will have no effect - the only matrix form that satisfies this property is the identity matrix, which means that the density matrix must have only diagonal elements. On the other hand, the mixed state $|F = 2, m_F = \pm 2\rangle$ in the x-basis, Fig. 3.19 a), has a preferred axis of symmetry which is the quantisation axis. This makes it easy to infer the state of polarisation and the rough distribution of the populations. Moreover, the peanut shaped probability surface has a preferred axis of symmetry, but no preferred direction. This is known as an aligned state. In contrast to the mixed state surface, the pure state depicted in b), not only has a preferred symmetry axis, but also a direction that coincides with it, this is known as a polarised state. The polarisation, alignment and symmetry properties of the state determine the optical anisotropies the states can have [38, 62]. For instance, an aligned state can have properties where the interaction between light polarisation and the state result in linear birefringence effects. This occurs when the interactions between vertically and horizontally decomposed light polarisations with

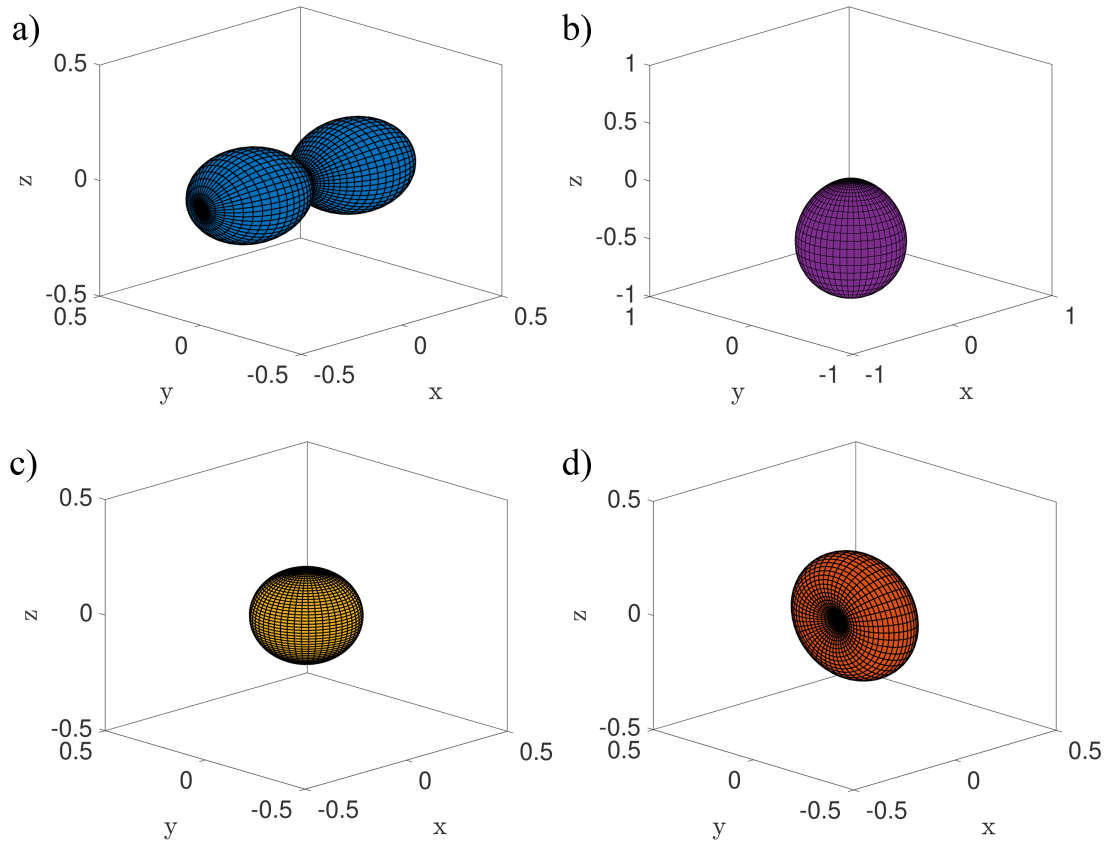

Figure 3.19: a) Angular momentum surface of the $\hat{\rho}^x_{\text{in}}$, $|F = 2, m_F = \pm 2\rangle$ state expressed in the x-basis. b) Angular momentum surface of the $|F = 2, m_F = -2\rangle$ state expressed in the z-basis. c) Angular momentum surface of the thermal state, $\hat{\rho}_{\text{th}}$. d) Angular momentum surface of the state in the x-basis which is given by the probability surface in eq. (3.240).

the atoms is different. Meanwhile, for a polarised state, the light-atom interactions result in no linear birefringence, but instead, circular birefringence i.e. the difference in light interaction with the atoms between the $\sigma^{\pm}$ components.

The theoretical OPM response in the context of the density operator approach contains information about the state populations as well as the coherences between them. In the model, we assume that the input state is given by $\hat{\rho}^x_{\text{in}}$ which then evolves in time and is affected by various parameters such as pumping, decoherence as well as longitudinal field setpoint, B^+_{sense}, which governs the overall OPM sensitivity. It is therefore instructive to understand how our ideal input state is affected and modified during the pump and probe cycles. During the pumping stage, the OPM dynamics

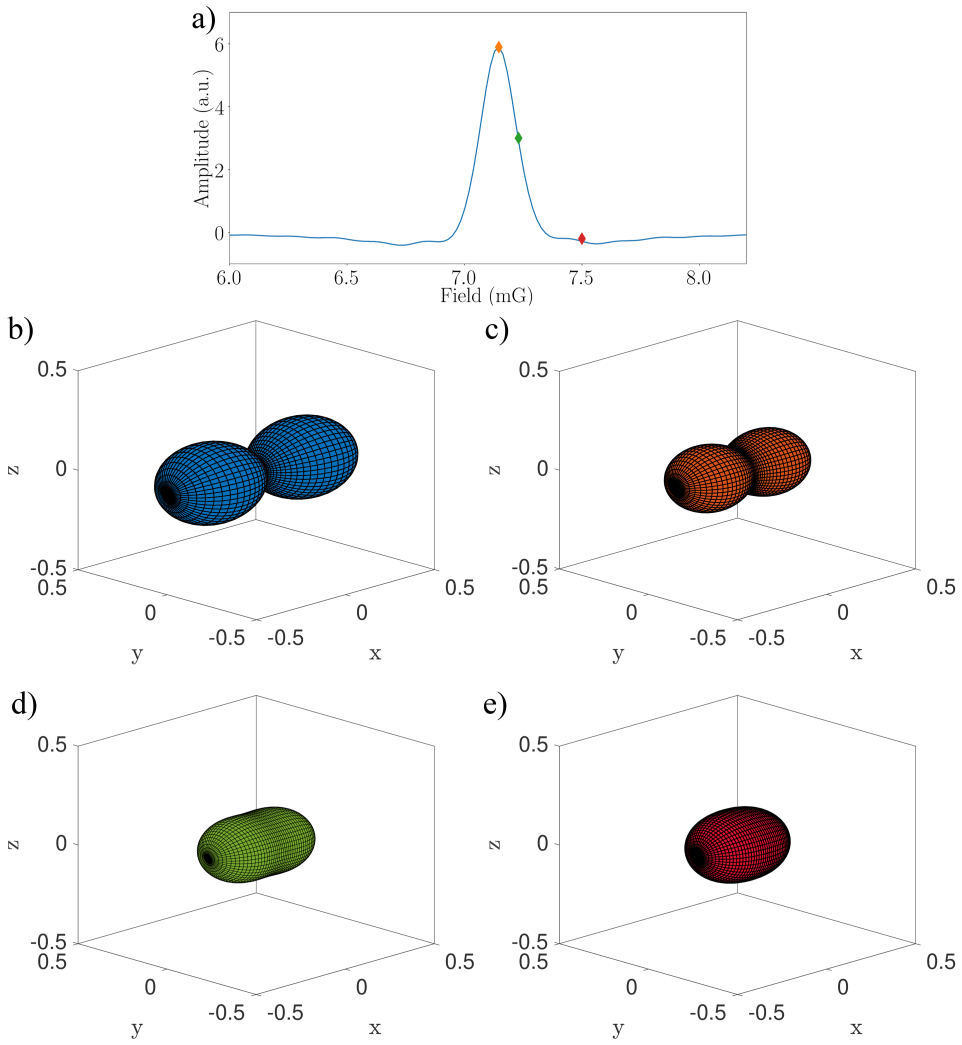

Figure 3.20: a) $2\omega_{\mathrm{rf}}$ resonance indicating the different field points where density matrix of the zeroth harmonic is obtained and its corresponding probability surface calculated. The colours of the points match the colours of the surfaces. b) Angular momentum surface of the mixed $|F = 2, m_F = \pm 2\rangle$ input state expressed in the x-basis. This is the initial state before OPM dynamics are taken into account. c) Angular momentum probability surface of the mixed $|F = 2, m_F = \pm 2\rangle$ input state on the $2\omega_{\mathrm{rf}}$ resonance, $B_{\mathrm{offs}} = B_{\mathrm{res}} = \hbar\omega_{\mathrm{rf}}/\mu_B g_F$. d) Angular momentum surface of the same state on the sensitive point, $B_{\mathrm{offs}} = B^{+}_{\mathrm{sense}} = B_{\mathrm{res}} + B_{\rho}$. e) Probability surface when the field, B_{offs} is off resonance. All states are shown here in the x-basis and in steady state conditions during the pumping cycle.

reach steady state conditions characterised by

$$\mathbb{X}_F^{\mathrm{pump}} = -\left[\tilde{\mathbb{C}} - \mathbb{\Gamma}_T\right]^{-1}(\mathbb{\Gamma}_{\mathrm{in}}\mathbb{X}_{\mathrm{in}} + \mathbb{\Lambda}_{\mathrm{rel}}\mathbb{X}_0), \tag{3.246}$$

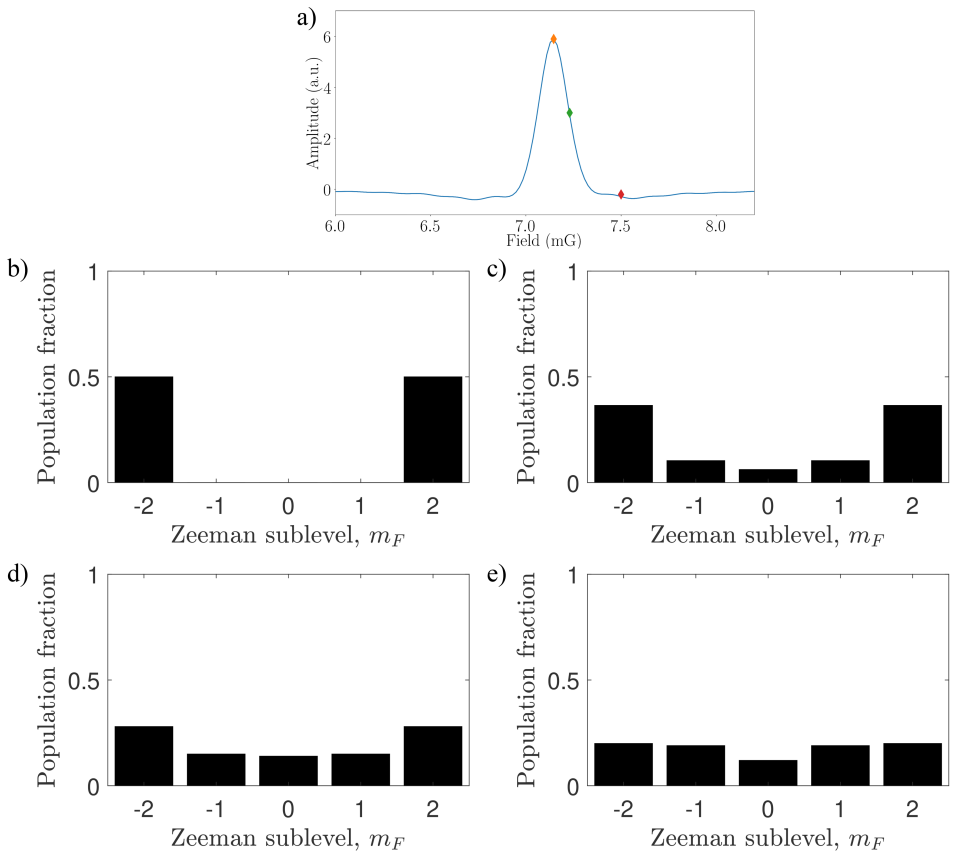

Figure 3.21: a) $2\omega_{\mathrm{rf}}$ resonance indicating the different field points where density matrix of the zeroth harmonic is obtained and its corresponding populations plotted. b) Populations of the mixed $|F = 2, m_F = \pm 2\rangle$ input state expressed in the x-basis. This is the initial state before OPM dynamics are taken into account. c) Populations of the mixed $|F = 2, m_F = \pm 2\rangle$ input state on the $2\omega_{\mathrm{rf}}$ resonance, $B_{\mathrm{offs}} = B_{\mathrm{res}} = \hbar\omega_{\mathrm{rf}}/\mu_B g_F$. d) Populations of the same state on the sensitive point, $B_{\mathrm{offs}} = B^{+}_{\mathrm{sense}} = B_{\mathrm{res}} + B_\rho$. e) Populations where B_{offs} is off resonance.

where the quantity, $\mathbb{X}_F^{\mathrm{pump}}$ contains our density matrix in vector form. The sensitivity of the OPM for all three vector field directions is dependent on the longitudinal offset field, B_{offs}. We look at three limiting cases where the longitudinal field is set on resonance, i.e. $B_{\mathrm{offs}} = \hbar\omega_{\mathrm{rf}}/\mu_B g_F$, sensitive field point, $B_{\mathrm{offs}} = B^{+}_{\mathrm{sense}} = B_{\mathrm{res}} + B_\rho$, and far off resonance. Fig. 3.20 on page 84 shows the corresponding angular momentum probability surfaces starting with the initial input state given by $\hat{\rho}^{x}_{\mathrm{in}}$. The surfaces are extracted by taking the density matrix of the zeroth harmonic. From the figure one can observe that when the state preparation occurs on resonance, the key characteristics of the probability surface are preserved, though the state populations in stretched states, $|F = 2, m_F = \pm 2\rangle$, decrease to 36.5% from 50%, the $|F = 2, m_F = \pm 1\rangle$ states acquire 10.4% with the clock state $|F = 2, m_F = 0\rangle$ having a population of 6.2%,

see Fig. 3.21 on page 85. Further down the resonance on the sensitive field point, $B_{\text{offs}} = B^{+}_{\text{sense}} = B_{\text{res}} + B_{\rho}$, the state is deformed further almost completely losing the characteristic peanut shape. The population distribution in the stretched states is further reduced to 28%, the $|F = 2, m_F = \pm 1\rangle$ states acquire 15% with the remaining 14% population residing in the clock state. Finally, in the off-resonance limit, the state has populations close to the thermal state distribution, as evidenced by having a nearly spherical probability distribution. These results show that efficient state preparation is heavily dependent on whether the longitudinal static field matches the resonance condition set by the frequency of the rf-dressing field. In the case where the OPM is operated as a vector magnetometer, the longitudinal field setpoint degrades the optimally chosen state due to the pumping process becoming less efficient, thus compromising the sensitivity of the OPM. The density operator approach coupled with the angular momentum probability surface formalism gives a much deeper insight into the fundamental state dynamics which is unavailable in the Heisenberg formalism outlined in the previous sections.

The next step involves exploring the state evolution during the probing cycle. The time evolution of the density operator in the probe region is given by

$$\mathbb{X}_F^{\text{probe}}(t) = -e^{\tilde{\mathbb{C}}' \, t} \left([\tilde{\mathbb{C}} - \mathbb{\Gamma}_T]^{-1} (\mathbb{\Gamma}_{\text{in}} \mathbb{X}_{\text{in}} + \mathbb{\Lambda}_{\text{rel}} \mathbb{X}_0) \right) + \tilde{\mathbb{C}}'^{-1} (e^{\tilde{\mathbb{C}}' \, t} - \mathbb{I}) \, \mathbb{\Lambda}_{\text{rel}} \mathbb{X}_0. \quad (3.247)$$

Varying the time t after which we probe the state and looking at the corresponding populations allows us to track the time evolution of the state, this is depicted in Fig. 3.22 on page 87. Once again we consider cases where the probing times relative to the relaxation lifetime are given by $T \ll 1/\Gamma_{\text{rel}}$, $T \approx 1/\Gamma_{\text{rel}}$ and $T \gg 1/\Gamma_{\text{rel}}$. Where Γ_{rel} is the relaxation time. The evolution of the state is performed on the sensitive field point, $B_{\text{offs}} = B^{+}_{\text{sense}} = B_{\text{res}} + B_{\rho}$. Here the input state takes the form of the one depicted in Fig. 3.20 a). The time evolution of the states at the zeroth harmonic is depicted in Fig. 3.22. As can be seen from the figure, probing the system shortly after the pump cycle where the relaxation has not had time to dominate the dynamics, the state looks almost identical to the input state obtained during the pump cycle. As the time for the evolution increases, the state begins to lose its features as the state populations begin to redistribute. In the limit where the evolution is much longer than the relaxation time, the state converges to a thermal state, which is characterised by a perfect spherically symmetric surface.

The various symmetry properties of the angular momentum probability surfaces depend on the chosen states which in turn depend on the angular momentum quantum numbers. The symmetry properties of such states can tells us whether the state is aligned or oriented and what kind of light-matter interactions will be dominant. Geometrically, it is possible to express the probability surfaces in terms of linear combinations of spherical harmonic functions, $Y_{m,l}(\theta, \phi)$. As a result, because the density operator is related to the angular momentum probability surface, it is possible to spectrally decompose the density operator into components that correspond to the coefficients of the spherical harmonic functions, $Y_{m,l}(\theta, \phi)$. Mathematically, the

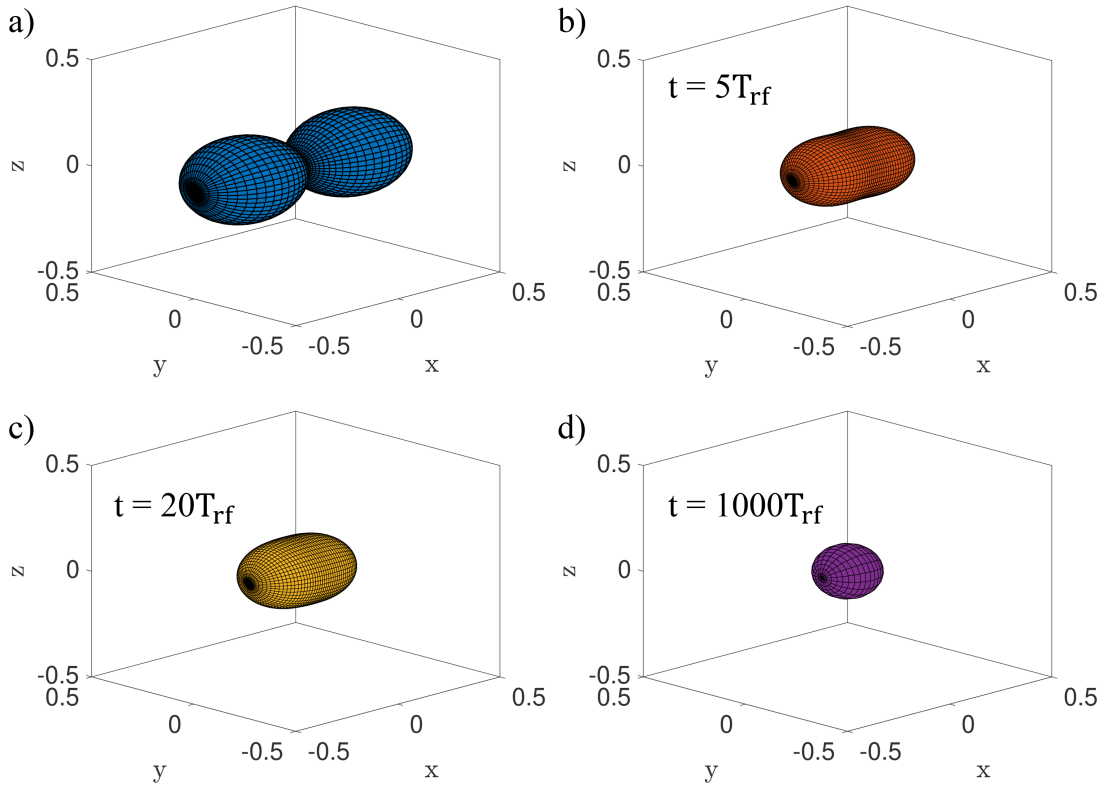

Figure 3.22: a) For reference; input state before pump/probe evolution takes place. b) Angular momentum surface of the mixed $|F = 2, m_F = \pm 2\rangle$ input state expressed in the x-basis after pumping and then evolved for 5 rf-cycles in the probe region. c) Same as in the previous plot, but the probe is now extended to 20 rf-cycle duration. d) state after 1000 rf-cycle duration. Here $T = 2\pi/\omega_{\mathrm{rf}}$. The plots containing time evolution are obtained from the density matrix of the zeroth harmonic.

density operator can be decomposed into the following [38, 63]

$$\rho = \sum_{\kappa=0}^{2F} \sum_{q=-\kappa}^{\kappa} \rho^{\kappa q} T_q^{\kappa}, \tag{3.248}$$

where the quantity $\rho^{\kappa q}$ is known as the polarisation moment. The matrix element of the polarisation operator, T_q^{κ} is given by

$$T_q^{\kappa} = (-1)^{F-m} \langle F\ m'\ F, -m \,|\, \kappa\ q \rangle, \tag{3.249}$$

where the quantities in $\langle F\ m'\ F, -m \,|\, \kappa\ q \rangle$ are the corresponding Clebsch-Gordan coefficients calculated using the Wigner-3j symbols. If we have the form of the density operator, ρ, we can find the polarisation moments by taking the trace

$$\rho_q^{\kappa} = \mathrm{Tr}\left[\rho T_q^{\kappa}\right] = \sum_{m,m'} (-1)^{F-m'} \langle F\ m\ F, -m' \,|\, \kappa q \rangle\, \rho_{m',m}, \tag{3.250}$$

where $\rho_{m,m'}$ is the density operator element. Using the equation above, we can directly compute the general form of spectral decomposition for each polarisation moment for $F = 2$ state (see Appendix B.6.3 on page 191 for detailed calculation). For the case where we consider our input state $\hat{\rho}^x_{\text{in}}$ expressed in the x-basis (see eq. (3.236) on page 81 and Fig. 3.22 a) on page 87), the only non-zero spectral components, ρ^κ_q, are

$$\hat{\rho}^x_{\text{in}} \to \rho^\kappa_q = \sum_{m,m'} (-1)^{F-m'} \langle F\ m\ F, -m' \,|\, \kappa q \rangle \rho_{m',m} = \begin{cases} \rho^0_0 & = \frac{1}{\sqrt{5}}, \\ \rho^2_0 & = \sqrt{\frac{2}{7}}, \\ \rho^4_0 & = \frac{1}{\sqrt{70}}. \end{cases} \tag{3.251}$$

For the particular state considered here, we have contributions from the monopole moment, ρ^0, quadrupole moment, ρ^2, and hexadecapole moment, ρ^4. The even power contributions indicate that the state is an aligned state. Odd powers would indicate an oriented state. In general, polarisation moments taking the form $\rho^\kappa_{q=0}$ describe polarisation along the quantisation axis or the longitudinal polarisation. Conversely, if $\rho^\kappa_{q\neq 0} \neq 0$, then we have contributions from the coherences and the state has transverse polarisation. The polarisation moments, ρ^κ_q, combined with the spherical harmonics functions, $Y_{m,l}(\theta, \phi)$, can be used to compute the angular momentum probability surfaces using the following relation [62, 63]

$$\rho_F(\theta, \phi) = \sqrt{\frac{4\pi}{2F+1}} \sum_{\kappa=0}^{2F} \sum_{q=-\kappa}^{\kappa} \langle F\ F\ \kappa\ 0 \,|\, F\ F \rangle \rho^{\kappa q} Y_{\kappa q}(\theta, \phi), \tag{3.252}$$

where $\langle F\ F\ \kappa\ 0 \,|\, F\ F \rangle \rho^{\kappa q}$ are Clebsch-Gordan coefficients in the Wigner-3j symbol form. Using the coefficients calculated above for the $\hat{\rho}^x_{\text{in}}$ state, the angular momentum probability surface is (see Appendix B.6.3 on page 191 for detailed calculation)

$$\rho_F(\theta, \phi) = \frac{1}{16} + \frac{3}{8}\cos^2(\theta) + \frac{1}{16}\cos^4(\theta), \tag{3.253}$$

which looks different to the probability surface derived for the same state in eq. (3.238) on page 81. Upon inspection and the use of De Moivre's theorem, $(\cos(\theta) + i\sin(\theta))^n = \cos(n\theta) + i\sin(n\theta)$ it is found that the two expressions given by eqns. (3.238) and (3.253) are equivalent, as they should be. The spherical harmonic decomposition of the angular momentum probability surface allows us to see which polarisation moments contribute to the overall structure of the desired state and how much of a contribution they produce. For example, the decomposition of the $\hat{\rho}^x_{\text{in}}$ state into its constituent spherical harmonics is shown in Fig. 3.23 on page 89. From the decomposition and the coefficients, $\rho^{\kappa q}$, we observe that the two largest contributions are from the monopole moment, ρ^0, and the quadrupole moment, ρ^2. The monopole moment, ρ^0, represents the population of the density operator divided by $\sqrt{2F+1}$, and so the spherical component, $Y_{0,0}(\theta, \phi)$, is always present in the decomposition. The higher moments of the decomposition further describe the distribution of the corresponding populations. In the case of the measurements of the Voigt effect, it is more instructive to transform the state into the basis z-basis along which we set our static field B_z. The density matrix given in eq. (3.226) used to describe our input

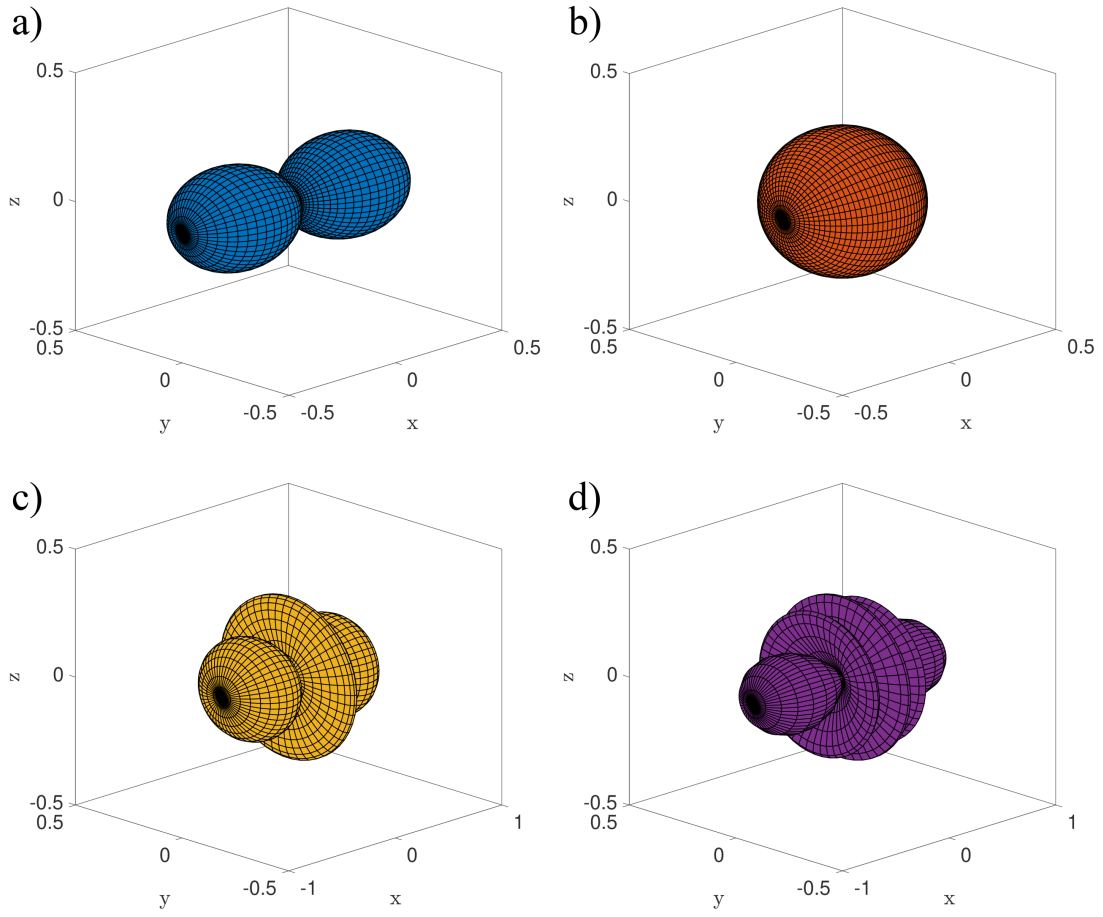

Figure 3.23: a) For reference; input state before pump/probe evolution takes place. b) Spherical harmonic, $Y_{0,0}(\theta,\phi)$. c) Spherical harmonic, $Y_{2,0}(\theta,\phi)$. d) Spherical harmonic, $Y_{4,0}(\theta,\phi)$. Note here that the spherical harmonics are not prescaled. To compute the ρ_F we multiply each harmonic shown here by its corresponding $\rho^{\kappa q}$ moment coefficient and take the sum. Note that the states c) and d) are not physical.

state in the z-basis contains coherences. The coherences are the quantities probed in the experiment. If we constrain ourselves to the $F = 2$ manifold, the general form of the density matrix is given by

$$\hat{\rho} = \begin{bmatrix} \rho_{11} & \rho_{12} & \rho_{13} & \rho_{14} & \rho_{15} \\ \rho_{21} & \rho_{22} & \rho_{23} & \rho_{24} & \rho_{25} \\ \rho_{31} & \rho_{32} & \rho_{33} & \rho_{34} & \rho_{35} \\ \rho_{41} & \rho_{42} & \rho_{43} & \rho_{44} & \rho_{45} \\ \rho_{51} & \rho_{52} & \rho_{53} & \rho_{54} & \rho_{55} \end{bmatrix}. \tag{3.254}$$

Thus, the corresponding matrix elements that contribute to the Voigt effect are given

by

$$\begin{aligned}\left\langle \hat{S}'_z(t)\right\rangle^{F=2} &= g^{(2)}_{F=2} S_y n_F \,\mathrm{Tr}\left[\left((\hat{F}_x^{\mathrm{F}=2})^2 - (\hat{F}_y^{\mathrm{F}=2})^2\right)\hat{\rho}\right] \\ &= g^{(2)}_{F=2} S_y n_F \left(\sqrt{6}\rho_{13} + \sqrt{6}\rho_{31} + \sqrt{6}\rho_{35} + \sqrt{6}\rho_{53} + 3\rho_{24} + 3\rho_{42}\right). \quad (3.255)\end{aligned}$$

Using the general result for the decomposition of the density matrix into polarisation moments, $\rho^{\kappa q}$, for the $F = 2$ manifold, calculated in the Appendix B.6.3 on page 191, the moments which contribute to the Voigt effect signal are

$$\left\langle \hat{S}'_z(t)\right\rangle \propto \sum_{\kappa,q} \rho^{\kappa}_{q} = \begin{cases}\rho^2_{\pm 2}, \\ \rho^3_{\pm 2}, \\ \rho^4_{\pm 2}.\end{cases} \quad (3.256)$$

Taking our input state in the z-basis

$$\hat{\rho}^z_{\mathrm{in}} = \hat{U}^\dagger \hat{\rho}^x_{\mathrm{in}} \hat{U} = \begin{bmatrix} \frac{1}{16} & 0 & \frac{3}{16}\sqrt{\frac{2}{3}} & 0 & \frac{1}{16} \\ 0 & \frac{1}{4} & 0 & \frac{1}{4} & 0 \\ \frac{3}{16}\sqrt{\frac{2}{3}} & 0 & \frac{3}{8} & 0 & \frac{3}{16}\sqrt{\frac{2}{3}} \\ 0 & \frac{1}{4} & 0 & \frac{1}{4} & 0 \\ \frac{1}{16} & 0 & \frac{3}{16}\sqrt{\frac{2}{3}} & 0 & \frac{1}{16} \end{bmatrix}, \quad (3.257)$$

and using multipole decomposition gives the following non-zero multipole moments

$$\hat{\rho}^z_{\mathrm{in}} \to \rho^{\kappa}_{q} = \sum_{m,m'} (-1)^{F-m'} \left\langle F\ m\ F, -m' \,|\, \kappa q\right\rangle \rho_{m',m} = \begin{cases}\rho^0_0 &= \frac{1}{\sqrt{5}}, \\ \rho^2_0 &= -\frac{1}{\sqrt{14}}, \\ \rho^2_{\pm 2} &= \frac{1}{2}\sqrt{\frac{3}{7}}, \\ \rho^4_0 &= \frac{1}{\sqrt{70}}\frac{3}{8}, \\ \rho^4_{\pm 2} &= -\frac{1}{8\sqrt{7}}, \\ \rho^4_{\pm 4} &= \frac{1}{16}.\end{cases} \quad (3.258)$$

We see that the state in the z-basis contains multipole moments which are also contained in the Voigt effect signal, $\left\langle \hat{S}'_z(t)\right\rangle$. However, we also observe a significant portion of the multipole moments in the input state which are redundant in relation to the Voigt effect signal. The only contributions to the Voigt effect signal using the state $\hat{\rho}^z_{\mathrm{in}}$ come from the $\rho^2_{\pm 2}$ and $\rho^4_{\pm 2}$ components. Knowing which of the multipole moments contribute to the measured signal, it is possible to construct an ansatz form of the density matrix which would allow to maximise the response of the quantity of interest by using the multipole moments to derive the density matrix

$$\rho_{m'm} = \sum_{\kappa=0}^{2F} \sum_{q=-\kappa}^{\kappa} (-1)^{F-m'} \left\langle F\ m\ F, -m' \,|\, \kappa q\right\rangle \rho^{\kappa}_{q}. \quad (3.259)$$

If the system is prepared in some state, we would like to know what that state is and quantify it. Direct optical probing addresses the entire ground state $F = 2$ manifold

and therefore it is difficult to discriminate between the differently prepared states. However, if we use an additional field to couple the low energy levels, i.e. $F = 1$ and $F = 2$ manifolds by means of a microwave field, then we can appreciably change the population levels of the prepared state which would be sensitive to the optical probing - this is because the populations contributing to the signal would be changed thus changing the signal level. In our case, during the state preparation process the $F = 1$ manifold is empty (or almost empty) due to pumping and repumping, the application of a microwave field allows us then to infer the state of the system in the $F = 2$ manifold by removing the populations from it. However, because the atoms are dressed using a radio-frequency field, the spectrum can be somewhat more complicated (due to the rf-field coupling between each hyperfine m_F sublevels) which makes it less trivial to infer the distribution of the Zeeman populations in the $F = 2$ manifold. The density operator model outlined above allows us to incorporate the microwave field and calculate the theoretical response which we can compare to the experimental results and thus partially deconstruct our density matrix. The microwave interaction Hamiltonian and the OPM response is outlined in the next subsection.

3.3.7 Interaction Hamiltonian with a Microwave Field

The interaction Hamiltonian between the atom in an electronic ground state and a microwave field $\mathbf{B}_{\mathrm{MW}}(t)$ is given by [64]

$$\hat{H}_{\mathrm{MW}}(t) = \frac{\mu_B}{\hbar}\left(g_I\hat{\mathbf{I}} + g_J\hat{\mathbf{J}}\right)\cdot\mathbf{B}_{\mathrm{MW}}(t), \tag{3.260}$$

where

$$g_J = g_L\frac{J(J+1)+L(L+1)-S(S+1)}{2J(J+1)} + g_S\frac{J(J+1)+S(S+1)-L(L+1)}{2J(J+1)}. \tag{3.261}$$

In the ^{87}Rb ground state $^2S_{1/2}$, $L = 0$, hence $\hat{\mathbf{J}} = \hat{\mathbf{L}} + \hat{\mathbf{S}} = \hat{\mathbf{S}}$. Moreover, $g_I \ll g_J$ and for the purposes of the MW spectrum we can neglect the contribution from the nuclear term, $\hat{\mathbf{I}}$. Thus, the microwave interaction Hamiltonian reduces to

$$\hat{H}_{\mathrm{MW}}(t) = \frac{\mu_B}{\hbar}g_s\hat{\mathbf{S}}\cdot\mathbf{B}_{\mathrm{MW}}(t), \tag{3.262}$$

where $g_s \approx 2$. We want to find the form of the operator $\hat{\mathbf{S}}$ which induces the transitions in our ground state from $F = 1$ to $F = 2$. First, we note that the states that we have been dealing with to compute $\hat{\rho}_{\mathrm{in}}$ etc., are expressed in the $|F, m_F\rangle$ basis which we cannot use to compute $\hat{\mathbf{S}}$ because the basis is different. The total angular momentum state $|F, m_F\rangle$ can be expressed as a combination of product states $|S, m_S\rangle\,|I, m_I\rangle$, namely [38]

$$|F, m_F\rangle = \sum_{m_S}\sum_{m_I}\langle S, m_S, I, m_I \,|\, F, m_F\rangle\,|S, m_S\rangle\,|I, m_I\rangle\,, \tag{3.263}$$

where $\langle S, m_S, I, m_I \,|\, F, m_F\rangle$ are the Clebsch-Gordan coefficients, given by

$$C^F_{m_I,m_S} = \langle I, S, m_I, m_S \,|\, F, m_F\rangle = (-1)^{-I+S-m_F}(2F+1)\begin{pmatrix} I & S & F \\ m_I & m_S & -m_F\end{pmatrix}, \tag{3.264}$$

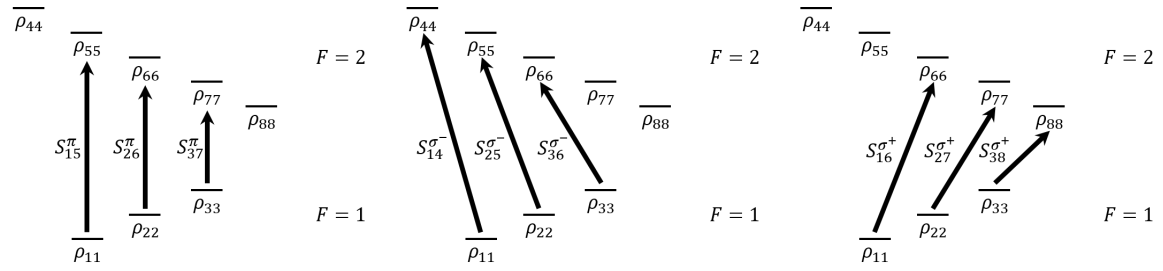

Figure 3.24: Microwave transitions for π, σ^- and σ^+ polarisations of $F = 1 \to F = 2$ hyperfine manifold.

where the 2×3 matrix represents the Wigner-3j symbols. The detailed calculations of the states are given in the Appendix B.6.4 on page 194. In this new basis, we can now define the interaction between the microwave field $\mathbf{B}_{\mathrm{MW}}(t)$ and the spin operator $\hat{\mathbf{S}}$. First, the microwave radiation produces fields that have π and $\sigma^{\pm}$ polarisations. The interaction between the fields and the spin drive the transitions to the various levels as depicted in Fig. 3.24. We can consequently decompose the interaction between the fields and the spin into its separate components

$$\hat{H}_{\mathrm{MW}}(t) = \Omega_{\pi}(t)\hat{S}_{\pi} + \Omega_{\sigma^+}(t)\hat{S}_{\sigma^+} + \Omega_{\sigma^-}(t)\hat{S}_{\sigma^-}, \tag{3.265}$$

where $\Omega_i(t) = \mu_B g_s/\hbar B_i(t)$. The matrix elements for the spin operators can be computed in two ways. The first method involves using the basis states $|S, m_S\rangle |I, m_I\rangle$ and computing the matrix elements for each allowed transition depicted in Fig. 3.24. The matrix element reads

$$S^k_{ij} = \left\langle i \middle| \hat{S}_k \middle| j \right\rangle. \tag{3.266}$$

The second method involves computing the magnetic dipole transition moment elements for π, σ^- and σ^+-transitions respectively (see Appendix B.6.5 on page 198 for a full calculation) [64]

$$\begin{aligned} S^{\pi} &= \left\langle F+1, m_F \middle| \hat{S}_{\pi} \middle| F, m_F \right\rangle = \\ &= (-1)^{F+m_F-1}\sqrt{\frac{2I(I+1)}{2I+1}} \begin{pmatrix} F+1 & 1 & F \\ -m_F & 0 & m_F \end{pmatrix}, \end{aligned} \tag{3.267}$$

$$\begin{aligned} S^{\sigma^-} &= \left\langle F+1, m_F-1 \middle| \hat{S}_{\sigma^-} \middle| F, m_F \right\rangle = \\ &= (-1)^{F+m_F}\sqrt{\frac{4I(I+1)}{2I+1}} \begin{pmatrix} F+1 & 1 & F \\ -(m_F-1) & -1 & m_F \end{pmatrix}, \end{aligned} \tag{3.268}$$

$$\begin{aligned} S^{\sigma^+} &= \left\langle F+1, m_F+1 \middle| \hat{S}_{\sigma^+} \middle| F, m_F \right\rangle = \\ &= -(-1)^{F-m_F}\sqrt{\frac{4I(I+1)}{2I+1}} \begin{pmatrix} F+1 & 1 & F \\ -(m_F+1) & 1 & m_F \end{pmatrix}, \end{aligned} \tag{3.269}$$

which for example, the $\hat{S}_\pi$ operator takes the form

$$\hat{S}_\pi = \begin{bmatrix} 0 & 0 & 0 & 0 & \frac{\sqrt{3}}{4} & 0 & 0 & 0 \\ 0 & 0 & 0 & 0 & 0 & \frac{1}{2} & 0 & 0 \\ 0 & 0 & 0 & 0 & 0 & 0 & \frac{\sqrt{3}}{4} & 0 \\ 0 & 0 & 0 & 0 & 0 & 0 & 0 & 0 \\ \frac{\sqrt{3}}{4} & 0 & 0 & 0 & 0 & 0 & 0 & 0 \\ 0 & \frac{1}{2} & 0 & 0 & 0 & 0 & 0 & 0 \\ 0 & 0 & \frac{\sqrt{3}}{4} & 0 & 0 & 0 & 0 & 0 \\ 0 & 0 & 0 & 0 & 0 & 0 & 0 & 0 \end{bmatrix}. \tag{3.270}$$

We further note that the hyperfine splitting energy between $F = 1 \rightarrow F = 2$ levels is Δ. This gives the bare atom Hamiltonian for the hyperfine state [48, 64]

$$\hat{H}_{\text{Atom}} = \frac{A}{\hbar^2}\hat{\mathbf{I}} \cdot \hat{\mathbf{J}} = -\sum_{i,j} \Delta \left|i\right\rangle \left\langle j\right| \delta_{ij}, \tag{3.271}$$

where A is the hyperfine structure constant and δ_{ij} is the Kronecker delta. In our case, the bare atom Hamiltonian in the rotated frame matrix reads

$$\hat{H}_{\text{Atom}} = \begin{bmatrix} 0 & 0 & 0 & 0 & 0 & 0 & 0 & 0 \\ 0 & 0 & 0 & 0 & 0 & 0 & 0 & 0 \\ 0 & 0 & 0 & 0 & 0 & 0 & 0 & 0 \\ 0 & 0 & 0 & -\Delta & 0 & 0 & 0 & 0 \\ 0 & 0 & 0 & 0 & -\Delta & 0 & 0 & 0 \\ 0 & 0 & 0 & 0 & 0 & -\Delta & 0 & 0 \\ 0 & 0 & 0 & 0 & 0 & 0 & -\Delta & 0 \\ 0 & 0 & 0 & 0 & 0 & 0 & 0 & -\Delta \end{bmatrix}, \tag{3.272}$$

where Δ corresponds here to the detuning from the resonance of the hyperfine clock transition $|F = 1, m_F = 0\rangle \rightarrow |F = 2, m_F = 0\rangle$. The interaction between the magnetic field and the hyperfine sublevels is given as before

$$\hat{H}_{\text{B}}(t) = (\Omega_{\text{rf}} \cos(\omega_{\text{rf}} t) + \Omega_x^{\text{ext}})\hat{F}_x(t) + \Omega_y^{\text{ext}}\hat{F}_y(t) + (\Omega_{\text{dc}} + \Omega_z^{\text{ext}})\hat{F}_z(t). \tag{3.273}$$

Thus, combining the two, we obtain the interaction between the atomic energy levels and the external magnetic and microwave fields

$$\hat{H}_{\text{Total}} = \hat{H}_{\text{Atom}} + \hat{H}_{\text{MW}}(t) + \hat{H}_{\text{B}}(t). \tag{3.274}$$

After transforming the Hamiltonian into the rotated frame and applying the rotating wave approximation, (RWA), the time dependence of the $\hat{H}_{\text{MW}}$ vanishes since the MW frequency is much higher than the hyperfine Zeeman splitting set by the static and the rf-fields. Thus, the only time dependence remains in the $\hat{H}_{\text{B}}(t)$, where as in previous sections we have applied the Floquet expansion. Due to the simplified form of the MW Hamiltonian after the RWA, the Liouville and Floquet space produce the same

equations of motion with an additional term added to the DC (zero order) component. Namely, the equation of motion reads

$$\frac{d\mathbb{X}_F(t)}{dt} =[\tilde{\mathbb{C}} - \mathbb{\Gamma}_T]\ \mathbb{X}_F + \mathbb{\Gamma}_{\text{in}}\mathbb{X}_{\text{in}} + \mathbb{\Lambda}_{\text{rel}}\mathbb{X}_0, \tag{3.275}$$

where as before we have

$$\tilde{\mathbb{C}}_{nm} = \begin{cases} \mathbf{C}^{(0)} - in\omega_{\text{rf}}\mathbf{I}, & \text{for } n = m, \\ \mathbf{C}^{(\pm 1)}, & \text{for } m = n \mp 1, \\ 0, & \text{otherwise}, \end{cases} \tag{3.276}$$

but in this case, the definition of $\mathbf{C}^{(0)}$ contains the microwave field and bare atomic Hamiltonians when the microwave field is applied

$$\begin{aligned} \mathbf{C}^{(0)}_{\text{MW}} - in\omega_{\text{rf}}\mathbf{I} = \mathcal{L}&\left[\hat{H}^{(0)}_{\text{B}} + \hat{H}_{\text{Atom}} + \hat{H}_{\text{MW}} - \frac{in\omega_{\text{rf}}}{2}\mathbf{I}\right] \\ &+ \mathcal{R}\left[\hat{H}^{(0)^T}_{\text{B}} + \hat{H}^T_{\text{Atom}} + \hat{H}^T_{\text{MW}} - \frac{in\omega_{\text{rf}}}{2}\mathbf{I}\right]. \end{aligned} \tag{3.277}$$

When the microwave field is off, the coherent spin dynamics are simply given by

$$\begin{aligned} \mathbf{C}^{(0)} - in\omega_{\text{rf}}\mathbf{I} = \mathcal{L}&\left[\hat{H}^{(0)}_{\text{B}} - \frac{in\omega_{\text{rf}}}{2}\mathbf{I}\right] \\ &+ \mathcal{R}\left[\hat{H}^{(0)^T}_{\text{B}} - \frac{in\omega_{\text{rf}}}{2}\mathbf{I}\right]. \end{aligned} \tag{3.278}$$

3.3.8 Magnetometer response to CW Microwave Fields (Density Matrix Model)

The magnetometer microwave spectrum has three stages, synchronous pumping, microwave pulse and the probe pulse, these are shown schematically in Fig. 3.25 on page 95. Each sequence is characterised by the following equation of motion

$$\frac{d\mathbb{X}_F(t)}{dt} = \begin{cases} [\tilde{\mathbb{C}} - \mathbb{\Gamma}_T]\ \mathbb{X}_F + \mathbb{\Gamma}_{\text{in}}\mathbb{X}_{\text{in}} + \mathbb{\Lambda}_{\text{rel}}\mathbb{X}_0, & \text{Pump Cycle}, \\ [\tilde{\mathbb{C}}_{\text{MW}} - \mathbb{\Lambda}_{\text{rel}}]\ \mathbb{X}_F + \mathbb{\Lambda}_{\text{rel}}\mathbb{X}_0, & \text{MW Cycle}, \\ [\tilde{\mathbb{C}} - \mathbb{\Lambda}_{\text{rel}}]\ \mathbb{X}_F + \mathbb{\Lambda}_{\text{rel}}\mathbb{X}_0, & \text{Probe Cycle}. \end{cases} \tag{3.279}$$

During the pumping stage, as before, a steady state is reached. This is given by

$$\mathbb{X}_F^{\text{Pump}} = -\,[\tilde{\mathbb{C}} - \mathbb{\Gamma}_T]^{-1}(\mathbb{\Gamma}_{\text{in}}\mathbb{X}_{\text{in}} + \mathbb{\Lambda}_{\text{rel}}\mathbb{X}_0). \tag{3.280}$$

After reaching the steady state, the pump pulse is switched off, which is immediately followed by an application of a microwave pule. During microwave cycle, the system evolves freely which is described by the following equation of motion

$$\left.\frac{d\mathbb{X}_F(t)}{dt}\right|_{\text{MW}} = [\tilde{\mathbb{C}}_{\text{MW}} - \mathbb{\Lambda}_{\text{rel}}]\ \mathbb{X}_F + \mathbb{\Lambda}_{\text{rel}}\mathbb{X}_0. \tag{3.281}$$

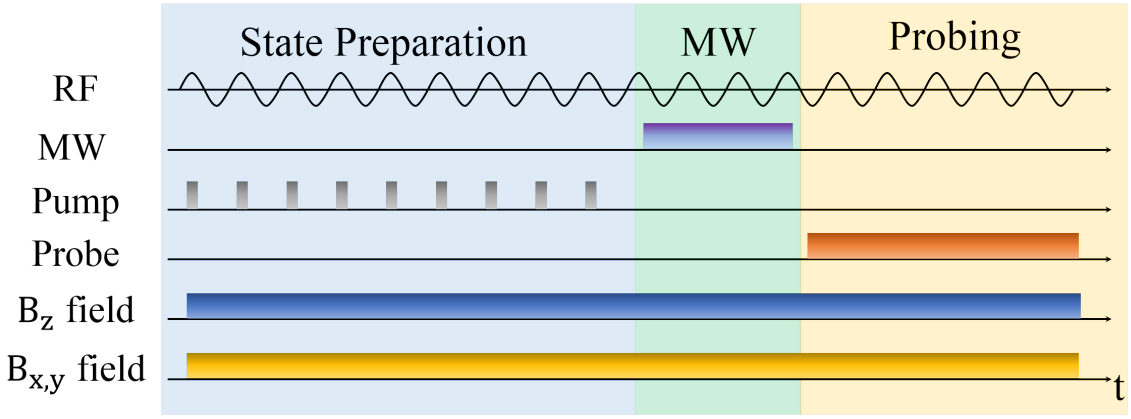

Figure 3.25: Sequence to produce the MW spectroscopy.

Integrating the equation above allows us to compute the evolution of the density matrix after time, t, namely

$$\mathbb{X}_F^{\mathrm{MW}}(t) = e^{(\tilde{\mathbb{C}}_{\mathrm{MW}}-\mathbb{\Lambda}_{\mathrm{rel}})t}\mathbb{X}_F^{\mathrm{Pump}} + (\tilde{\mathbb{C}}_{\mathrm{MW}}-\mathbb{\Lambda}_{\mathrm{rel}})^{-1}(e^{(\tilde{\mathbb{C}}_{\mathrm{MW}}-\mathbb{\Lambda}_{\mathrm{rel}})t}-\mathbb{I})\mathbb{\Lambda}_{\mathrm{rel}}\mathbb{X}_0. \tag{3.282}$$

If the microwave is on for an integer number of rf cycles $t_{\mathrm{MW}} = n/\omega_{\mathrm{rf}}$, then the state at a later time is simply

$$\mathbb{X}_F^{\mathrm{MW}}(t_{\mathrm{MW}}) = e^{(\tilde{\mathbb{C}}_{\mathrm{MW}}-\mathbb{\Lambda}_{\mathrm{rel}})t_{\mathrm{MW}}}\mathbb{X}_F^{\mathrm{Pump}}+(\tilde{\mathbb{C}}_{\mathrm{MW}}-\mathbb{\Lambda}_{\mathrm{rel}})^{-1}(e^{(\tilde{\mathbb{C}}_{\mathrm{MW}}-\mathbb{\Lambda}_{\mathrm{rel}})t_{\mathrm{MW}}}-\mathbb{I})\mathbb{\Lambda}_{\mathrm{rel}}\mathbb{X}_0. \tag{3.283}$$

After the microwave pulse, a probe pulse is applied for a given time duration t_{Probe}. During the probing, the equation of motion reads

$$\left.\frac{d\mathbb{X}_F(t)}{dt}\right|_{\mathrm{Probe}} = [\tilde{\mathbb{C}}-\mathbb{\Lambda}_{\mathrm{rel}}]\ \mathbb{X}_F + \mathbb{\Lambda}_{\mathrm{rel}}\mathbb{X}_0, \tag{3.284}$$

which has a solution

$$\mathbb{X}_F^{\mathrm{Probe}}(t) = e^{(\tilde{\mathbb{C}}-\mathbb{\Lambda}_{\mathrm{rel}})t}\mathbb{X}_F^{\mathrm{MW}}(t_{\mathrm{MW}}) + (\tilde{\mathbb{C}}-\mathbb{\Lambda}_{\mathrm{rel}})^{-1}(e^{(\tilde{\mathbb{C}}-\mathbb{\Lambda}_{\mathrm{rel}})t}-\mathbb{I})\mathbb{\Lambda}_{\mathrm{rel}}\mathbb{X}_0. \tag{3.285}$$

The total signal is recovered by taking the average of the solution by integrating over some number of rf cycles. This gives the following output response

$$\begin{aligned}\mathbb{X}_{\mathrm{out}}^{\mathrm{Probe}} = \frac{1}{T}\int_0^T \mathbb{X}_F^{\mathrm{Probe}}(t)dt = \frac{1}{T}(\tilde{\mathbb{C}}-\mathbb{\Lambda}_{\mathrm{rel}})^{-1}\left(e^{(\tilde{\mathbb{C}}-\mathbb{\Lambda}_{\mathrm{rel}})T}-\mathbb{I}\right)\mathbb{X}_F^{\mathrm{MW}}(t_{\mathrm{MW}})+ \\ + \frac{1}{T}(\tilde{\mathbb{C}}-\mathbb{\Lambda}_{\mathrm{rel}})^{-1}\left((\tilde{\mathbb{C}}-\mathbb{\Lambda}_{\mathrm{rel}})^{-1}\left(e^{(\tilde{\mathbb{C}}-\mathbb{\Lambda}_{\mathrm{rel}})T}-\mathbb{I}\right)-T\right)\mathbb{\Lambda}_{\mathrm{rel}}\mathbb{X}_0,\end{aligned} \tag{3.286}$$

where as before, the quadrature responses $h_{x,y,z}$ are extracted according to eqns. (3.170-3.170) on page 59. The microwave radiation provides additional coupling between the hyperfine states corresponding to coherences in the density matrix which contain important information about the correlations between any two given populations. The

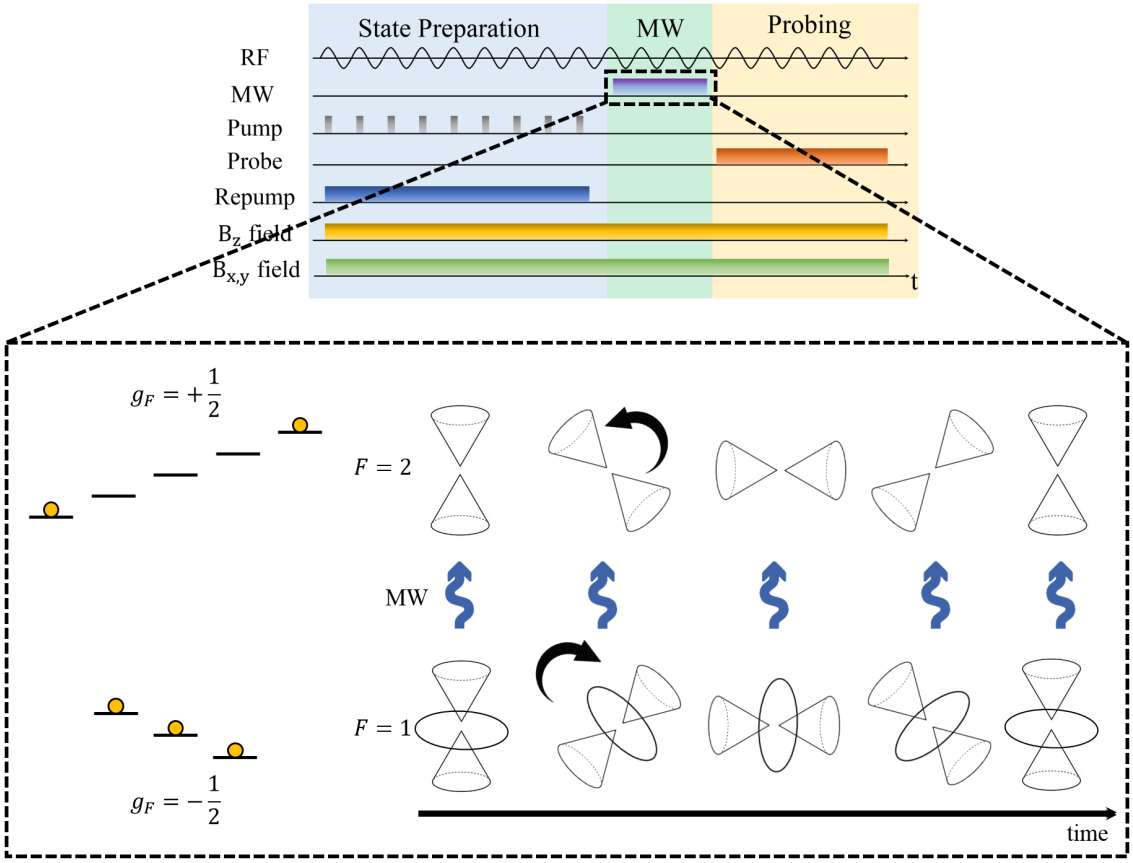

Figure 3.26: Illustration of the microwave coupling of the ground state manifolds in the continuous-wave (CW) model. Here the states in each manifold rotate in opposite directions due to the different g_F-factors. The microwave radiation transfers the state populations between the two energy levels at different cone orientations during the evolution.

picture is made more complicated by the fact that our atomic spins are dressed with a radio-frequency field which additionally couples the hyperfine sublevels, see Fig. 3.26 for a schematic illustration. If the mw-field is turned on all the time, then the evolution of the mw-field and the state is averaged, i.e. different relative orientations between the cones end up contributing to the overall spectrum. The coupling of the mw-field from one manifold to the other probes the orientation of those two cones relative to each other as the mw-field frequency is continuously scanned. This allows the probing of all the possible transitions and a big forest of lines is observed because each cone orientation is probed. In fact, the standard selection rules are no longer valid and with the rotating cones, transitions between $|F = 1, m_F = -1\rangle$ and $|F = 2 m_F = 2\rangle$ are possible giving rise to many transitions some of which are degenerate. As a result, the microwave spectrum can no longer be interpreted trivially since the the combination of a microwave and radio-frequency photons give rise to two-photon transitions enabling the coupling between any two given states [64]. Typically, for a microwave field

composed of $\sigma^{\pm}-$ and $\pi-$ polarisations applied to $F = 1 \rightarrow F = 2$ in a presence of an external magnetic field, there are a total of 9 possible microwave transitions three of which have the same transition energy (see Fig. 3.24 on page 92). This results in 7 distinct resonance peaks in the undressed microwave spectrum when the microwave field frequency is scanned (assuming a thermal state in each manifold). The transitions are known as group transitions. For example, in the undressed microwave spectrum ($\Omega_{\text{rf}} = 0$), if there is a thermally distributed population in the Zeeman sublevels in $F = 2$ manifold, all 7 groups can be observed due to the microwave transitions. If the state is polarised, e.g. we have a stretched state, then only that group will be observed. And in our case, if an equal mixture $|F = 2, m_F = \pm 2\rangle$ is prepared, then the two extreme groups can be observed. Therefore, probing the hyperfine manifolds using microwave radiation can be useful in probing the state populations and assessing the efficacy of the state preparation process. Unfortunately, this picture is complicated in our scheme because the presence of the radio-frequency photons causes additional coupling between hyperfine levels which results in extra transitions within the Zeeman sublevels. This gives rise to structure within each of the microwave transition groups making the interpretation about the populations of the Zeeman sublevels difficult. However, our density matrix model contains complete information about the populations of the system as well as the coherences, this information coupled with the theoretically computed microwave spectrum using the Voigt effect can be used as a reference point when interpreting such spectra in an experimental setting in similar working conditions.

We have already looked at the effects on the state preparation process and probing and their influence on the observed state through the angular momentum probability surface formalism as well as the Heisenberg model. However, whilst it is important to investigate such effects theoretically, ideally, we would like to bridge the gap between the theory and the experiment in order to make our theory falsifiable. Our magnetometer response curves outlined in sections (3.1), (3.2) and (3.3) provide us with a varying degree of predictability which is experimentally testable. However, the models so far have not given us tools to probe the fundamental building block of our system which is our state or the density matrix. The reason why this is important is that not only do we gain understanding of how well we prepare our state, but also how the state evolves in time and decoheres which are important processes for sensitive measurements. Moreover, it may provide the motivation and additional tools for a more robust state preparation process or the ability to prepare exotic states which may yield higher sensitivity to the external field and are better protected against decoherence effects.

The microwave spectrum is obtained by computing the theoretical OPM response given in equation (3.286). Figs. 3.27 and 3.28 show the computed spectrum of the $\text{Re}(m_2)$ demodulated signal amplitude for $F = 2$ and $F = 1$ manifolds respectively. Here the input state used is shown as a probability surface in Fig. 3.20 c) on page 84 corresponding to a sate prepared on resonance $B_z = B_{\text{res}}$. In the model we assume that the field strength contribution for each polarisation is equivalent, i.e. $\Omega_{\pi}(t) = \Omega_{\sigma^{\pm}}(t)$. The dressed microwave spectrum provides a unique fingerprint of the probed system

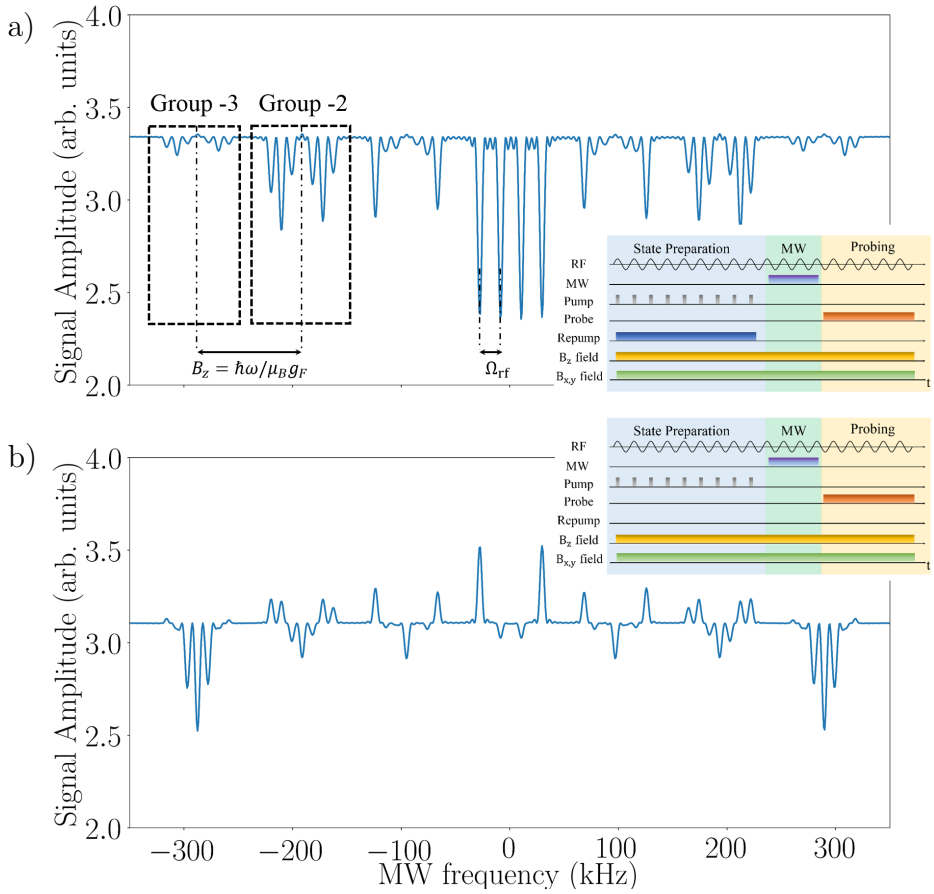

Figure 3.27: Theoretically computed microwave spectrum of $\mathrm{Re}(m_2) = h_z$ quadrature response in a pump-microwave-probe type sequence at $\omega_{\mathrm{rf}} = 2\pi \times 90$ kHz dressing frequency. The static field is set on resonance, $B_z = B_{\mathrm{res}}$. The state is prepared until a steady state is reached, given by eq. (3.280), then a CW MW pulse is applied for 20-rf cycles followed by a probe. The $F = 1$ state is empty to a good approximation. a) Dressed microwave spectrum probing $F = 2$ manifold with pump and repump on. b) Dressed microwave spectrum probing $F = 2$ manifold with pump on and repump off. Here the MW frequency refers to frequency detuning from $|F = 1, m_F = 0\rangle \rightarrow |F = 2, m_F = 0\rangle$ clock state transition. Here the MW frequency refers to frequency detuning from $|F = 1, m_F = 0\rangle \rightarrow |F = 2, m_F = 0\rangle$ clock state transition.

which is dependent on its quantum state. In the case where the two microwave coupled manifolds both posses non-zero populations and therefore non-zero density matrices, the resultant microwave spectra result in further complexity. In the case where only one manifold is empty, the microwave coupling removes/adds the population (depending on which manifold is probed) resulting in an increase/decrease of the measured linear birefringence. Here in Fig. 3.27 a) the ground state $F = 2$ manifold contains most of the population while the $F = 1$ manifold is basically empty. As a result, the coupling of

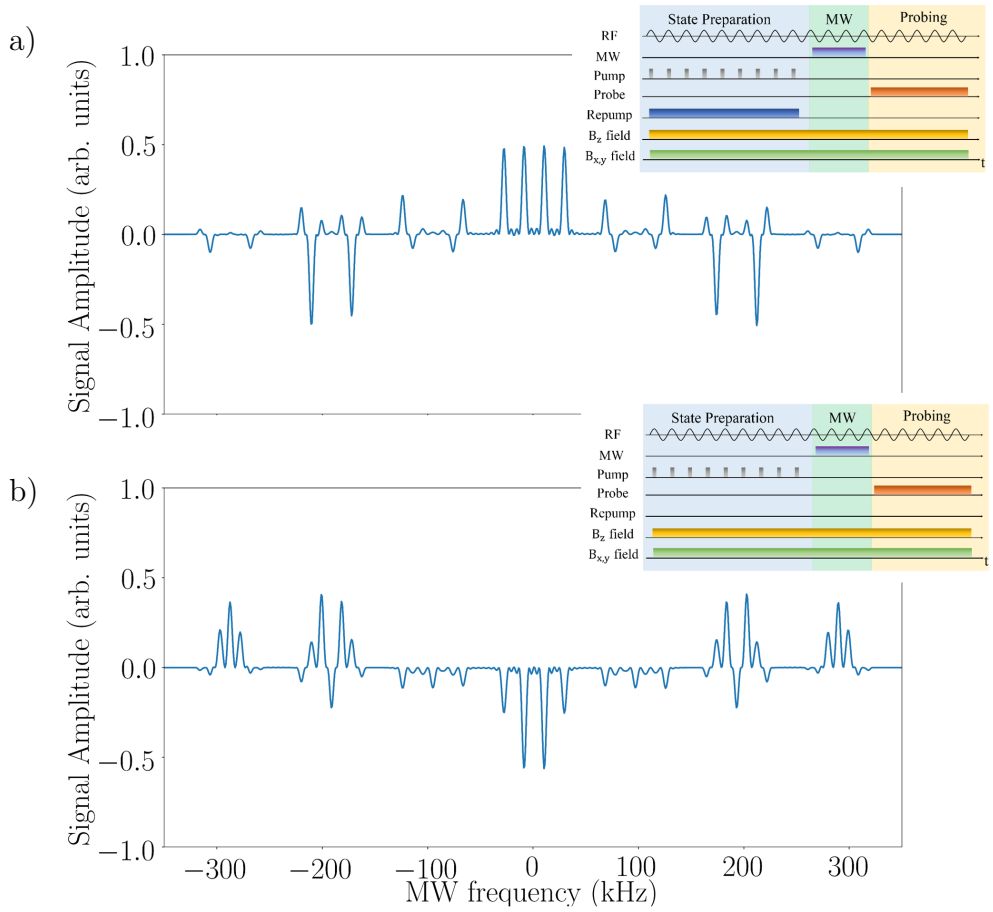

Figure 3.28: Theoretically computed microwave spectrum of $\mathrm{Re}(m_2) = h_z$ quadrature response in a pump-microwave-probe type sequence at $\omega_{\mathrm{rf}} = 2\pi \times 90$ kHz dressing frequency. The static field is set on resonance, $B_z = B_{\mathrm{res}}$. The state is prepared until a steady state is reached, given by eq. (3.280), then a CW MW pulse is applied for 20-rf cycles followed by a probe. a) Dressed microwave spectrum probing $F = 1$ manifold with pump and repump on. b) Dressed microwave spectrum probing $F = 1$ manifold with pump on and repump off. Here the MW frequency refers to frequency detuning from $|F = 1, m_F = 0\rangle \rightarrow |F = 2, m_F = 0\rangle$ clock state transition.

the microwave field between the two energy levels results in a removal of the population from the $F = 2$ manifold and adding it to the $F = 1$ manifold - this manifests as a decrease in the Voigt effect signal amplitude when the probing is done on the $F = 2$ level. This is not the case if both of the manifolds contain non-zero populations, here the microwave coupling transfers some of the populations from one manifold to the other, which are then further redistributed by the radio-frequency photons. This results in peaks or troughs depending on whether the population of the probed energy level is increased or decreased respectively. The theoretical microwave spectra computed in the figures convey unique fingerprints of the prepared states and can be used as an

indicator to infer the characteristics of the prepared state. It is important to note some additional features of these theoretical spectra. The spacing between each group is determined by the static field B_z, in our case $B_z = \Delta_{\text{group}} = \hbar\omega_{\text{rf}}/\mu_B g_F$. In addition, within each group, the spacing between the subgroup peaks is given by the strength of the rf-field $\Omega_{\text{rf}} = \Delta_{\text{subgroup}}$. The spectroscopic features of the peaks depend both on the static and rf-fields which are coupled to fundamental properties of the atomic spin and their respective constants. This can be used to obtain absolute field values for both the static and rf-fields which provides a method for absolute ac and dc field calibrations.

The measured Voigt effect signal only provides a limited number of density matrix elements, and so the microwave spectra computed for the particular state may not be unique. However, it may be a good starting point to infer some of the properties of the state, especially if the theoretical results which allow us to extract the full density matrix can be used in conjunction with the experimentally obtained spectra. The clear drawback of the dressed microwave spectroscopy is that it's not easy to interpret in what state the system is without the full knowledge of the density operator (to infer the populations) as well as the comparison to the experimentally obtained dressed spectrum. This complexity is largely down to the fact that within the microwave pulse cycle, the quantisation axis of the system changes in time due to the rf-dressing field. This issue was encountered already with the state preparation cycle, whereby to circumvent this problem, the pump was pulsed in phase with the rf-field at some small duty cycle such that the effective quantisation axis for each pulse points in the same direction. The microwave field can also be pulsed such that the quantisation axis relative to the electric and magnetic fields of the mw-pulse is constant. This will remove significant complexity from the microwave spectrum and allow for an easier interpretation of the results.

3.3.9 Magnetometer response to pulsed Microwave Fields (Density Matrix Model)

In order to understand the microwave spectra in pulsed conditions, we need to first compute the Liouville-von Neumann equation in the pulsed conditions of the mw-field. We begin with the microwave Hamiltonian

$$\hat{H}_{\text{MW}}(t) = \Omega_{\pi}(t)\hat{S}_{\pi} + \Omega_{\sigma^+}(t)\hat{S}_{\sigma^+} + \Omega_{\sigma^-}(t)\hat{S}_{\sigma^-} = \sum_k \Omega_k(t)\hat{S}_k, \tag{3.287}$$

where $\Omega_k(t) = \mu_B g_s/\hbar B_k(t)$. In this case, the microwave field is pulsed in the same way as the pump pulse. As a result, the microwave field can be spectrally decomposed to the following

$$\Omega_k(t+\phi) = \Omega_k^{(0)} + \Omega_k^{(1)} e^{i\omega_{\text{rf}}(t+\phi)} + \Omega_k^{(-1)} e^{-i\omega_{\text{rf}}(t+\phi)} + \Omega_k^{(2)} e^{2i\omega_{\text{rf}}(t+\phi)} + \Omega_k^{(-2)} e^{-2i\omega_{\text{rf}}(t+\phi)} + \cdots, \tag{3.288}$$

where the index k corresponds to the polarisation of the mw-field i.e. $k = 1, 2, 3 \rightarrow \pi, \sigma^{\pm}$ and ϕ is the phase relative to the rf-field. In the case of a square pulse with a

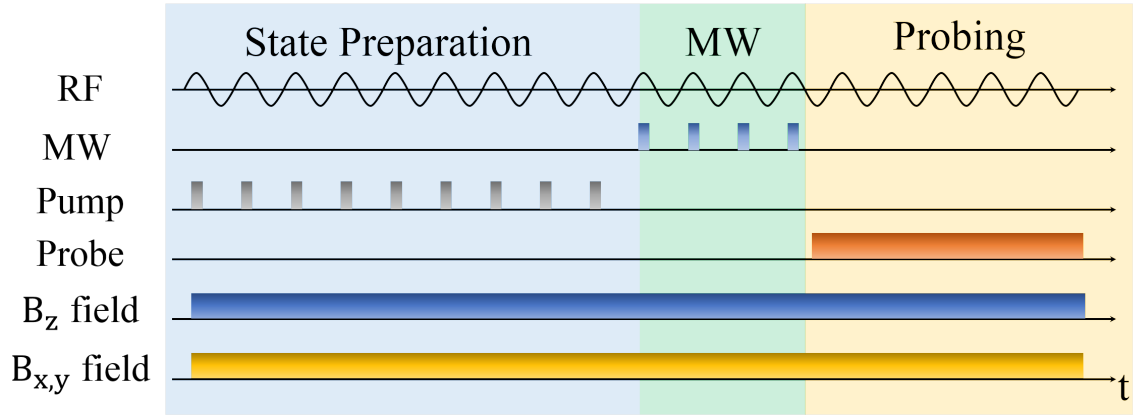

Figure 3.29: Sequence to produce the pulsed MW spectroscopy.

duty cycle d, the spectral components read

$$\Omega_i^{(0)} = \Omega_i \; d, \tag{3.289}$$

$$\Omega_i^{(n)} = \frac{\Omega_i}{n\pi} \sin(n\pi d) e^{in\phi}, \quad n \in \mathbb{Z}_{>0}, \tag{3.290}$$

$$\Omega_i^{(-n)} = \frac{\Omega_i}{n\pi} \sin(n\pi d) e^{-in\phi}, \quad n \in \mathbb{Z}_{>0}. \tag{3.291}$$

The full equation of motion in the Liouville space reads

$$\frac{d\mathbf{X}(t)}{dt} = \underbrace{\mathbf{C}(t)\mathbf{X}(t)}_{H_B + H_{\text{Atom}}} + \underbrace{\left(\sum_k \Omega_k(t)\mathbf{\Pi}_k\right)\mathbf{X}(t)}_{\text{Pulsed } H_{\text{MW}}} - \underbrace{\Gamma_p(t)\;[\mathbf{X}(t) - \mathbf{X}_{\text{in}}]}_{\text{Pumping}} - \underbrace{\Lambda_{\text{rel}}\,[\mathbf{X}(t) - \mathbf{X}_0]}_{\text{Decoherence}}, \tag{3.292}$$

where the $\mathbf{\Pi}_k$ terms are the microwave Hamiltonian operators in the Liouville space. The n$^{\text{th}}$ harmonic term of the equation of motion above is given by

$$\begin{aligned}\frac{d\mathbf{X}^{(n)}(t)}{dt} =& \mathbf{C}_n^{(0)}\mathbf{X}^{(n)}(t) + \mathbf{C}^{(1)}\mathbf{X}^{(n-1)}(t) + \mathbf{C}^{(-1)}\mathbf{X}^{(n+1)}(t) \\ &+ \left(\sum_k \sum_i \Omega_k^{(n-i)}(t)\mathbf{\Pi}_k\mathbf{X}^{(i)}(t)\right) - \sum_i \Gamma_p^{(n-i)}\mathbf{X}^{(i)}(t) \\ &+ \Gamma_p^{(n)}\mathbf{X}_{\text{in}} - \Lambda_{\text{rel}}\mathbf{X}^{(n)}(t) + \Lambda_{\text{rel}}\;\mathbf{X}_0\;\delta_{n,0}.\end{aligned} \tag{3.293}$$

Using the same recipe as before to convert the expression above into Floquet space we obtain

$$\frac{d\mathbb{X}_F(t)}{dt} = [\tilde{\mathbb{C}} + \sum_k \mathbb{\Omega}_k \mathbb{\Pi}_k - \mathbb{\Gamma}_T]\;\mathbb{X}_F + \mathbb{\Gamma}_{\text{in}}\mathbb{X}_{\text{in}} + \mathbb{\Lambda}_{\text{rel}}\mathbb{X}_0, \tag{3.294}$$

where

$$(\mathbb{\Omega}_k)_{nm} = \Omega_k^{(n-m)}\mathbf{I}, \tag{3.295}$$

$$\tilde{\mathbb{\Pi}}_{nm} = \mathbf{\Pi}, \text{for } n = m, \tag{3.296}$$

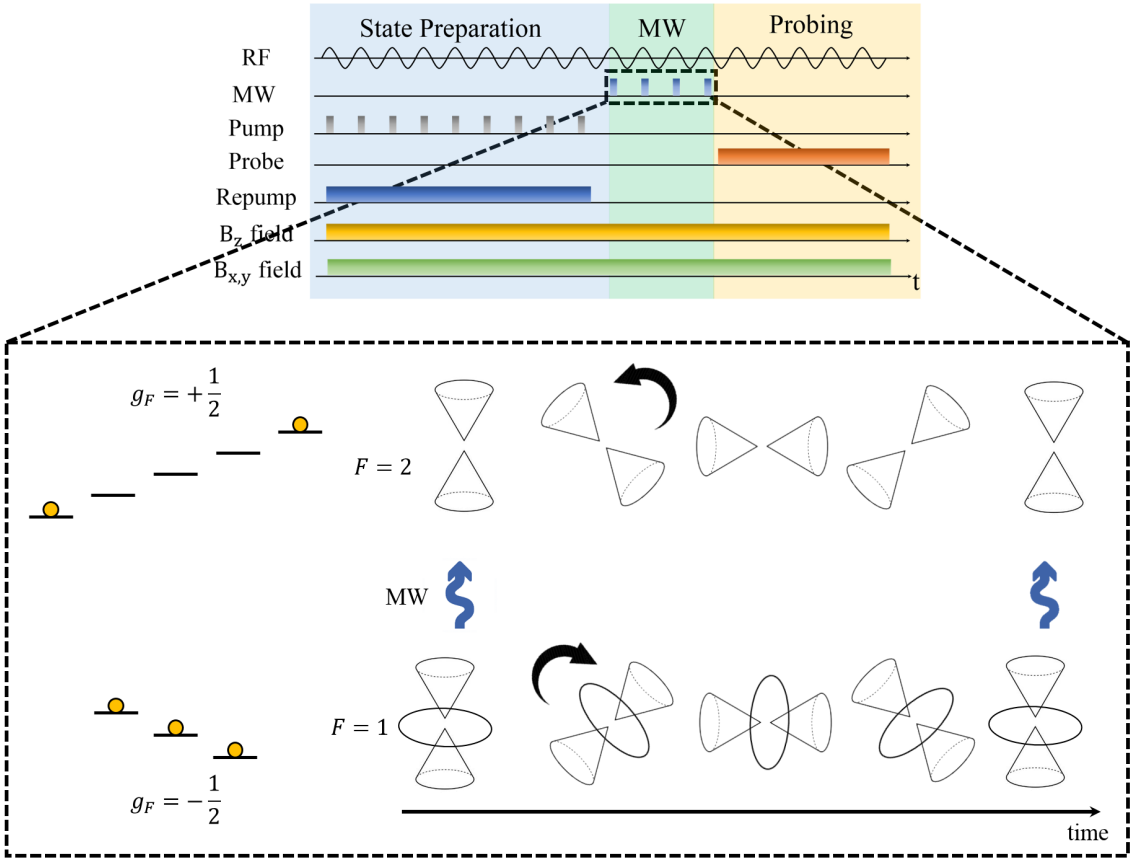

Figure 3.30: Illustration of the microwave coupling of the ground state manifolds during stroboscopic microwave probing. Here the states in each manifold are probed only at a specific time which means that the population transfer between the two levels happens only at a certain orientation between the two cones.

and as before

$$\tilde{\mathbb{C}}_{nm} = \begin{cases} \mathbf{C}^{(0)} - in\omega_{\mathrm{rf}}\mathbf{I}, & \text{for } n = m, \\ \mathbf{C}^{(\pm 1)}, & \text{for } m = n \mp 1, \\ 0, & \text{otherwise}, \end{cases} \tag{3.297}$$

but in this case, the definition of $\mathbf{C}^{(0)}$ contains the microwave field and bare atomic Hamiltonians when the microwave field is applied and the pulsed microwave field is separated

$$\begin{aligned} \mathbf{C}^{(0)}_{\mathrm{MW}} - in\omega_{\mathrm{rf}}\mathbf{I} = \mathcal{L}\left[\hat{H}^{(0)}_{\mathrm{B}} + \hat{H}_{\mathrm{Atom}} - \frac{in\omega_{\mathrm{rf}}}{2}\mathbf{I}\right] \\ + \mathcal{R}\left[\hat{H}^{(0)T}_{\mathrm{B}} + \hat{H}^{T}_{\mathrm{Atom}} - \frac{in\omega_{\mathrm{rf}}}{2}\mathbf{I}\right], \end{aligned} \tag{3.298}$$

where as before the microwave sequence has three stages described in the previous section 3.3.8 on page 94.

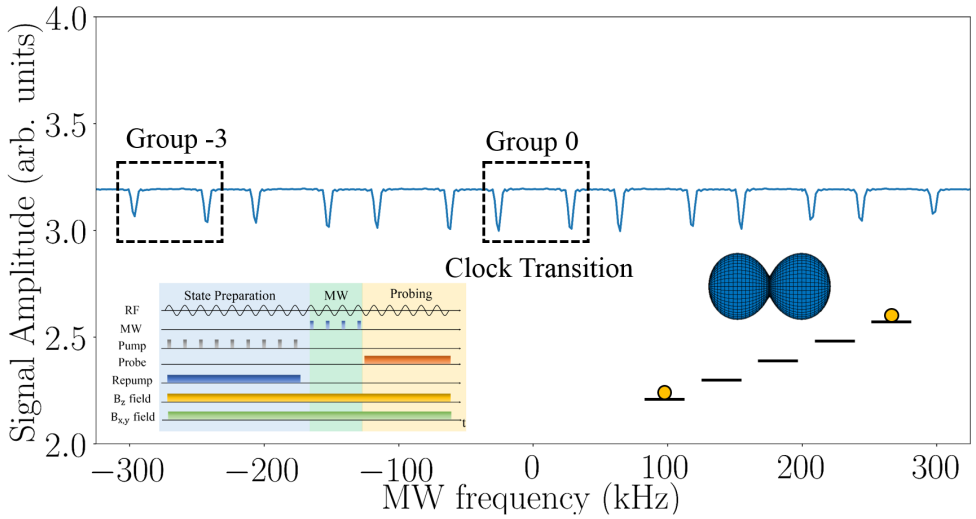

Figure 3.31: Theoretically computed stroboscopic microwave spectrum of $\mathrm{Re}(m_2) = h_z$ quadrature response in a pump-microwave-probe type sequence at $\omega_{\mathrm{rf}} = 2\pi \times 90$ kHz dressing frequency. The static field is set on resonance, $B_z = B_{\mathrm{res}}$. The state is prepared until a steady state is reached, given by eq. (3.280), then a square microwave pulse in phase with the rf-field is applied for 20-rf cycles followed by a probe. Dressed microwave spectrum probing $F = 2$ manifold with pump on and repump on. Here the MW frequency refers to frequency detuning from $|F = 1, m_F = 0\rangle \rightarrow |F = 2, m_F = 0\rangle$ clock state transition.

The mw spectrum measurement by pulsing the mw field is stroboscopic. This means that we probe the states at a certain time in their evolution as they precess around the static and rf-fields, see Fig. 3.30. As a result, when the mw field is pulsed and its frequency scanned, only a certain part of the cone configuration is probed and so the spectrum acquires only the bare spectrum shape, or rather, the spectrum is obtained based on a single orientation of the cones. Imagine this as a certain effective angle between the cones that happens at a certain time window and each pulse probes only at that specific cone orientation - this is stroboscopic probing. The bare spectrum for a short mw pulse reveals the information of relative population sizes for each state. Therefore, by playing with pump frequency, polarisation and the repump laser one wants to make sure that the bare spectrum yields populations which are in the extremes - implying that most of the atoms are prepared in the stretched states, see Fig. 3.31 for results. The theoretical calculations show that when the system is prepared in an equal statistical mixture of the stretched states and then is probed stroboscopically using mw radiation in phase with the dressing rf-field, the state populations appear as the two extrema peaks in the dressed microwave spectrum repeated over the 7 groups. The repeated pattern arises as a consequence of the train of square mw pulses. This is because the Fourier transform of a a train of square

pulses, produces a train of pulses in frequency space. In a fully undressed scenario, such a state would produce the same features, but only in the two extreme groups. As a result, this stroboscopic microwave probing can be used as a smoking gun to infer the prepared state and its corresponding population levels. In addition, if the phase of the microwave pulse is changed, then we end up probing different orientations during the state evolution. If we probe the spectra at different rf-phases and then add them, this would yield the mw spectrum when the mw is in cw mode.

Chapter 4

Experimental Apparatus

This chapter outlines and discusses the experimental apparatus, its intricacies and sequence of operation to run the magnetometer. In the first few sections the discussion centres around laser light preparation, stabilisation and control and give an overview of the shielded setup and its optics. The discussion is then followed by the experimental requirements for magnetic field generation and stabilisation in the unshielded environments with a particular emphasis on generating uniform field coils, their performance as well as the necessary electronics required to drive such a coil system. The chapter is concluded with data acquisition and signal processing in the context of magnetometry, focusing on experimental sequence procedures and how that influences signal characteristics and magnetometer bandwidth.

4.1 Laser Optics and Magnetic Shield System

Laser Locking. The laser system depicted in Fig. 4.1 is housed on a vibrationally insensitive table consisting of three frequency stabilised diode lasers, pump, repump and probe. The pump and repump lasers are used for state preparation of the magnetically sensitive states whilst the probe laser is used for the measurement of the Voigt effect which allows us to infer information about the local magnetic field. The pump laser is a commercial Toptica DL Pro whilst the repump and probe lasers are home built DFB and cat-eye laser designs respectively (see Appendix C.1 for a detailed description, characterisation and schematics of the cat-eye laser). The pump and repump lasers are locked using an error signal derived from Doppler-free-saturated-absorption spectroscopy [65–67]. The error signal is generated by modulating the laser current at high frequency (typically <100 kHz) and detecting the corresponding response via lock-in detection, see Fig. 4.2. The error signal is fed to a piezo driver to stabilise the laser onto the atomic line. We lock the pump on the $F = 2 \rightarrow F' = 1$ transition of the D1 line and the repump on the $F = 1 \rightarrow F' = 2$ transition of the D2.

The probe laser is locked in a master-slave setup where the pump acts as the master. The locking point for the probe beam is typically set at -550 MHz red detuned from the $F = 2 \rightarrow F' = 1$ of the D1 line. The locking error signal is generated via detection of the frequency beat signal between the pump and the probe in a Mach-Zehnder type interferometer configuration [68]. A fast photodetector beat signal is split into two equal parts where one half of the beat signal is passed through a delay line. This causes a phase shift between the two beams which is dependent on the path-length difference ΔL and the beat frequency, f,

$$\phi = \frac{2\pi f \Delta L}{c}. \tag{4.1}$$

In the ideal case, the corresponding interference fringes have the following intensity profile

$$I = I_0 \left(1 - \cos\phi\right). \tag{4.2}$$

The path-length difference, ΔL is fixed and determines the fringe spacing of the beat signal. In our case, we choose this to be 50 MHz between successive peaks or troughs. Inside the coaxial cable, the speed of light is roughly $v_{\text{light}} = 2/3c$, the spacing between the fringes is then simply given by $\Delta f = (2/3)c/\Delta L$. Figure 4.2 on page 108 illustrates the layout of the master-slave Mach-Zehnder type lock. The beat lock method is advantageous over the atomic reference lock method because it is not constrained by the inherent spacing and distribution of the spectroscopic features. This provides great flexibility in tuning the laser over a large frequency range. This is important to us because we want to find an optimal value of the probe detuning which maximises the signal strength of the measured Voigt effect. However, the disadvantage of this method lies in the fact that the stability of the lock is dependent on how robust and stable the master laser is. If the master lasers is unlocked so will the slave laser be, and moreover, if the master lock has inherent frequency noise, then this frequency noise may be translated in the beat signal adding additional noise to the slave frequency stability.

Pulse Generation. The magnetometer operation typically consists of the state preparation and probing stages, which occur in succession. A key requirement for this is to be able to generate well timed laser pulses of arbitrary duration and phase relative to our radio-frequency dressing field. This is important because as the theory calculations outlined in sec. 3.2.9 suggest that phase, duty cycle, pulse profile as well as duration of the probing influence the OPM response. We use acousto-optical-modulators (AOMs) to produce the pulses. Within the shortest experimental time scale, which are of the order of 1 rf cycle (e.g. 200 μs at 5 kHz rf and 11 μs at 90 kHz rf), we can trivially generate < 1 μs pulses with fractional rise and fall times of the power and typical delays of $\approx 1\mu$s which can be easily corrected through software/hardware adjustments. The rise and fall times of the AOMs depend on the switching electronics as well as the beam waist.

Fibres and Polarisation. The light is coupled into polarisation maintaining single

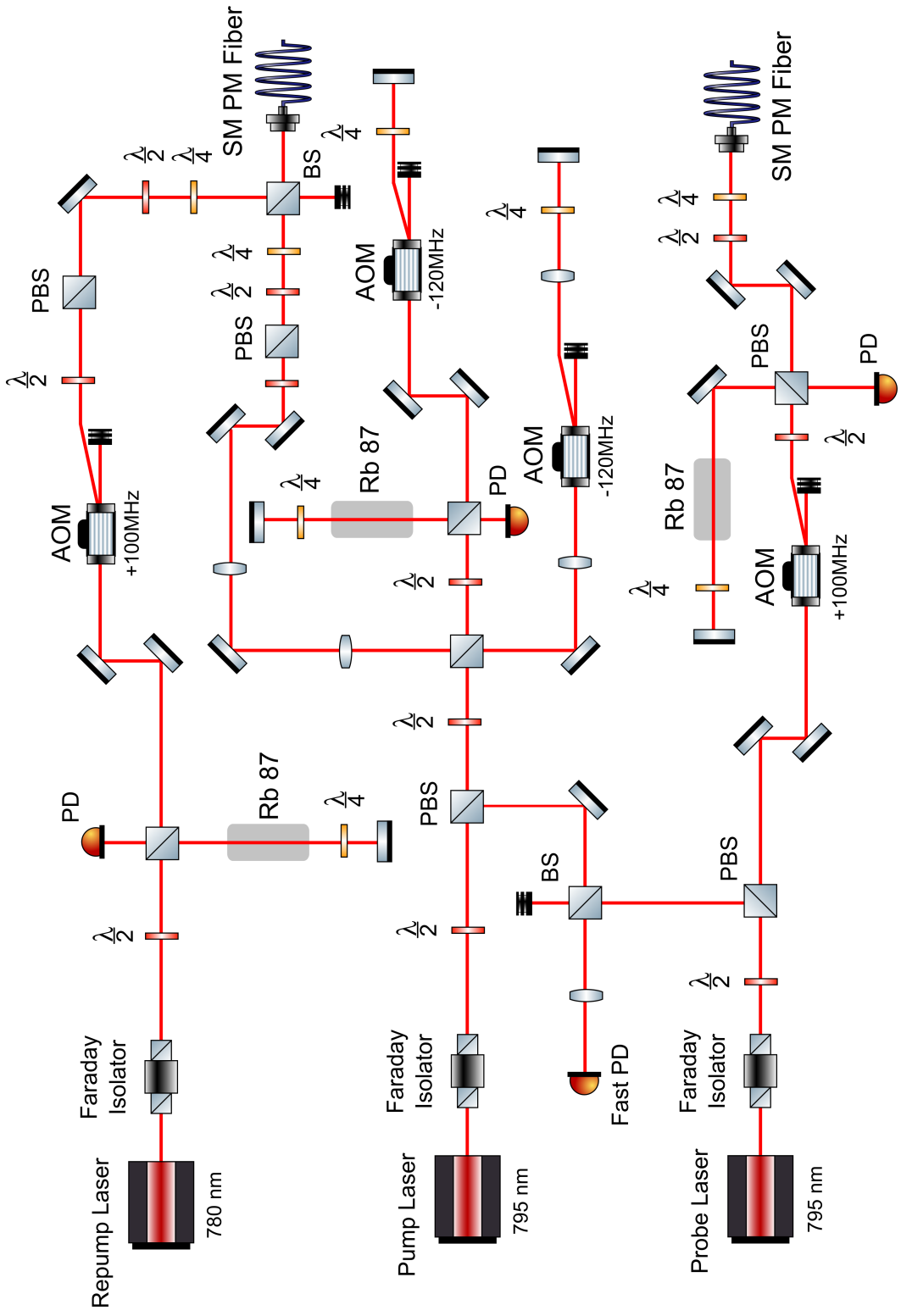

Figure 4.1: Schematic layout of the laser table setup.

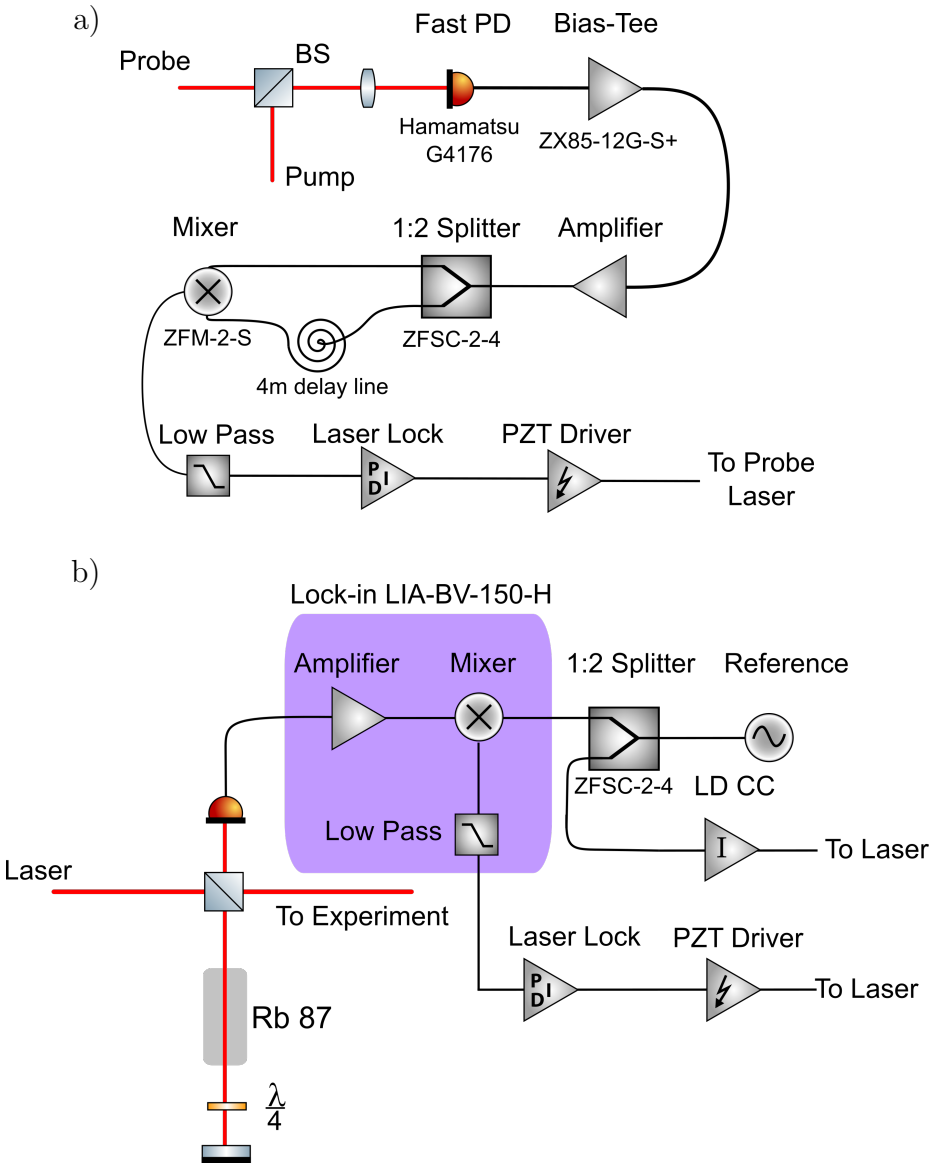

Figure 4.2: a) Mach-Zehnder type beat lock schematic layout. With the exception of the fast photodiode, the electronic components with ID numbers are from Minicircuits. The delay line is a simple 50 Ω BNC coaxial cable. b) Doppler-free-saturated absorption locking schematic. Here the lock-in amplifier is a commercial device with the rest of the electronics being home built. The LD CC is the laser diode current controller.

mode fibres (Thorlabs P3-780PM-FC) with a experimentally measured polarisation extinction ratio of between 55-60 dB. We check this with a polarisation analyser (Thorlabs PAX5710IR1-T) by mechanically and thermally stressing the fibre and looking at the corresponding polarisation change on the Poincaré sphere. The pump and repump light is combined over a beam splitter and is coupled into the same fibre. This ensures a good spatial overlap between the two laser sources for the state preparation process. The clear disadvantage of this approach is the loss of 50% of the

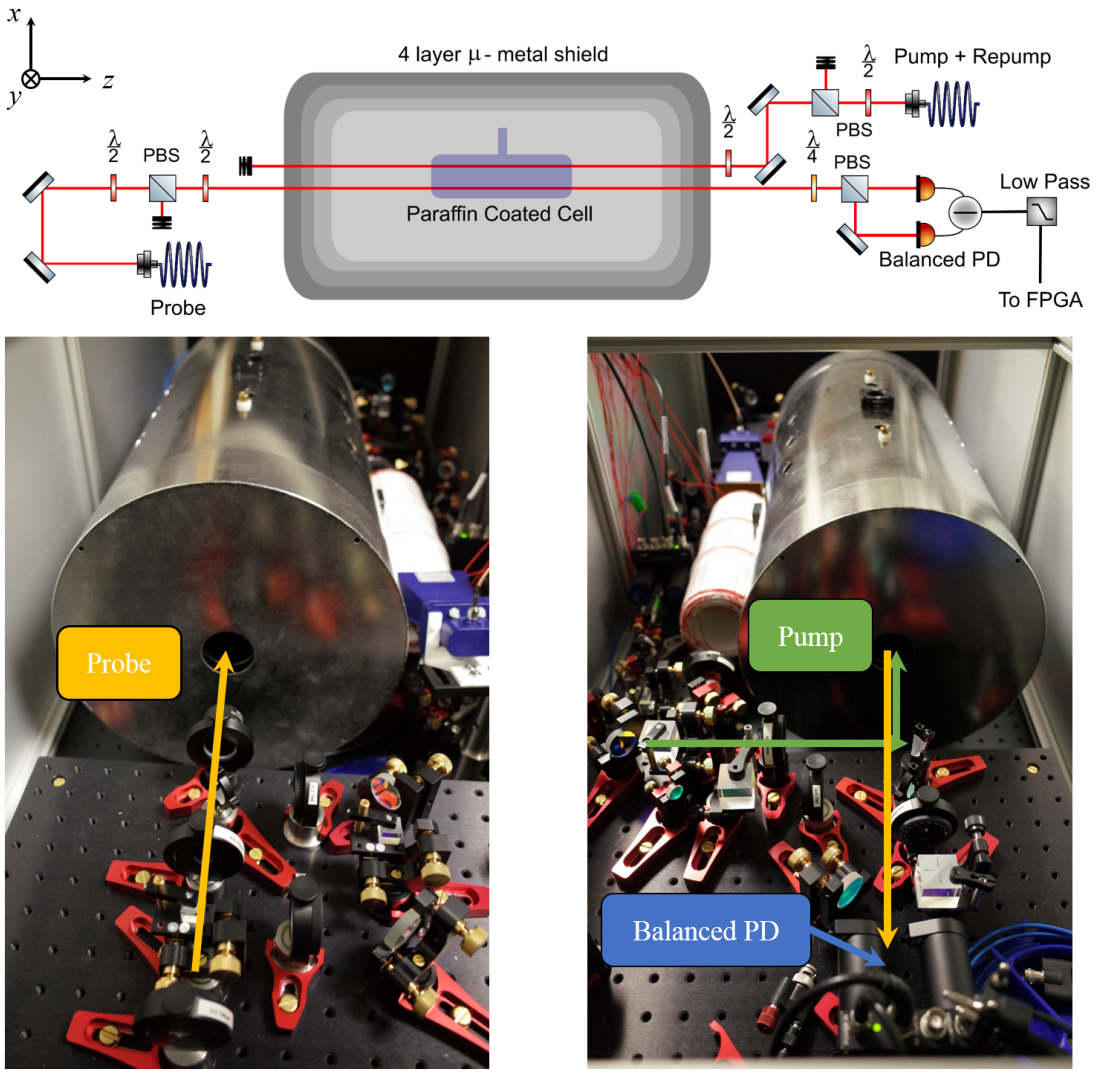

Figure 4.3: Schematic and experimental layout of the μ-metal chamber optics.

power in each beam. With additional beam shaping, the typical light power coupling efficiency into the fibres is around 70%.

μ-metal shield table and the cell. After light conditioning on the main optical table, we then send it through fibres to a separate vibrationally isolated table with non-magnetic optomechanics where the 4 layer μ-metal shield (Twinleaf MS-2) houses our paraffin coated cell (from Precision Glass Blowing), see Fig. 4.3. The shield has precision coils which we drive with our home built low noise Hall-Librecht-Durfee current drivers [77, 78]. The cell has a diameter $d = 26$ mm and length $l = 106$ mm, is anti-reflection coated and enriched with ^{87}Rb with a density of approximately 10^{10} atoms per cubic cm at room temperature (see eq. (2.82) on page 22). When the shield is first opened to place the cell, the innermost μ-metal shield acquires some remnant

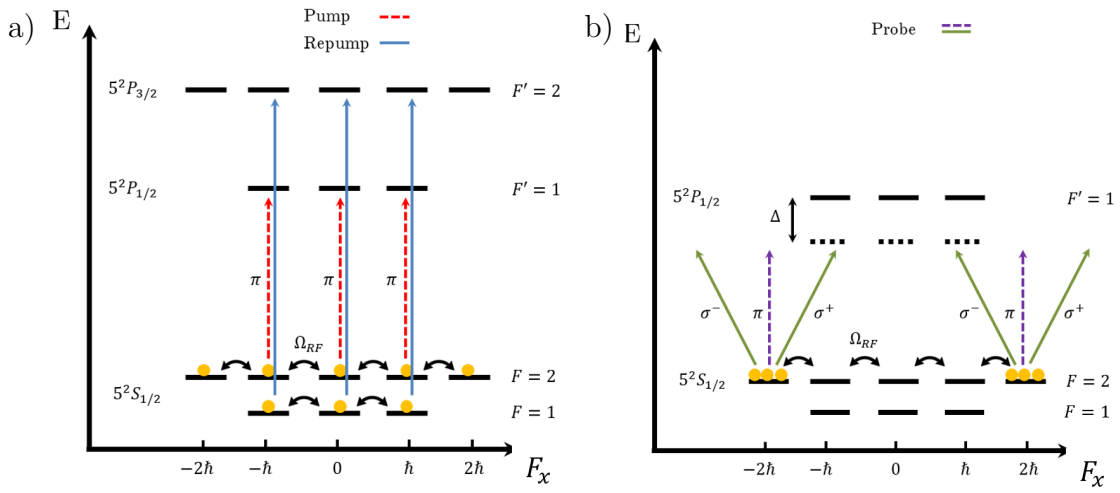

Figure 4.4: a) Laser pulses during the state preparation process. The pump and repump beams are linearly polarised with respect to the rf-field in the x-axis. The dashed red line represents the fact that the pump beam is pulsed whilst the solid blue line of the repump indicates a cw mode b) Red detuned probe laser addressing the prepared atomic state. Here the probe is at 45° to the x-axis.

magnetisation due the Earth's field. This acquired remanent magnetisation may not be uniform across the shield and therefore may introduce magnetic field gradients inside which may be difficult to compensate for despite having gradient field coils. To remedy this, we de-Gauss the innermost shield by applying a linearly decaying sinusoidal wave through the de-Gaussing coils with a start current amplitude of 20 A and frequency of 10 Hz. The frequency of the current is kept constant during the de-Gaussing process. The decay time from 20 A max amplitude to 0 A takes around 100 s. The de-Gaussing procedure is done with the shield covers on. Overtime, because of the constantly changing magnetic fields inside the shield (though small), the innermost layer acquires some residual magnetisation due to hysteresis. The de-Gaussing procedure is mainly useful for removing the residual DC fields present inside the shield [69].

Light characteristics. From Fig. 4.3, the pump/repump beam counter-propagates relative to the probe beam along the z-axis. This is for ease of use of gaining enough optical access without needing to overlap pump/repump with the probe over a beam splitter further reducing the power. As a result, the pump/repump beam is at a slight angle relative to the probe beam as well as the longitudinal B_z field. This introduces some distortion in the OPM response profile because the pump/repump and/or the probe beams are not perfectly aligned with the quantisation axis (this is discussed in detail in the following chapter). For state preparation, the pump and repump beams share the same Gaussian intensity profile with 7.3 mm diameter ($1/e^2$) and 2.2 mW/cm^2 and 1.6 mW/cm^2 peak intensity, respectively with linear polarisation

along the x-axis and address $F = 2 \rightarrow F' = 1$ of the D1 line and $F = 1 \rightarrow F' = 2$ of the D2 line respectively, see Fig. 4.4. The probe beam has a Gaussian profile of 3.4 mm diameter ($1/e^2$) and 2.6 mW/cm^2 peak intensity and linear polarization set to 45° with respect to the rf field and off-resonantly addresses $F = 2 \rightarrow F' = 1$ transition of the D1 line.

4.2 Magnetic Field Control (Unshielded Environment)

4.2.1 Field Coils

One of the challenges in operating magnetometry experiments in magnetically unshielded environments is the presence of external magnetic fields originating from various sources, be it the Earth's magnetic field, ferromagnetic mechanical components such as screws or power supplies, to name just a few. These magnetic field sources typically produce a combination of uniform and gradient magnetic fields, which can also vary in time. This becomes a problem if the magnetic field has to be carefully controlled and compensated in order to create optimal working conditions for magnetometry experiments. Our magnetometer setup requires a single-axis optical access and therefore a cylindrical coil geometry is a suitable choice for magnetic field control and compensation. The two most widely used cylindrical geometries for uniform field generation in the longitudinal and transverse directions are the solenoidal and $\cos\theta$ coil geometries respectively [81–83]. For a solenoid, of n number of turns and length, L, the helical current carrying wire distribution is given by the following parametric equations

$$x = R\cos(n\theta), \tag{4.3}$$
$$y = R\sin(n\theta), \tag{4.4}$$
$$z = L, \tag{4.5}$$

where θ is the polar angle in cylindrical polar coordinates. Using this geometry, the total field generated by a finite length solenoid can be calculated using the Biot-Savart law

$$\mathbf{B}(\mathbf{r}) = \frac{\mu_0 I}{4\pi}\int_C \frac{d\mathbf{l}\times\mathbf{r}'}{|\mathbf{r}'|^3}, \tag{4.6}$$

which we compute numerically [80]. We use problems with known analytical solutions to confirm the validity of the numerical field calculations of Biot-Savart law. To generate uniform transverse fields, including a uniform radio-frequency field we use the cosθ geometry. The distribution of current sources and sinks for a $\cos\theta$ coil is given by (see Fig. 4.5)

$$x_n = R\cos\theta_n, \tag{4.7}$$
$$y_n = R\bar{y}_n, \tag{4.8}$$
$$z = L, \tag{4.9}$$

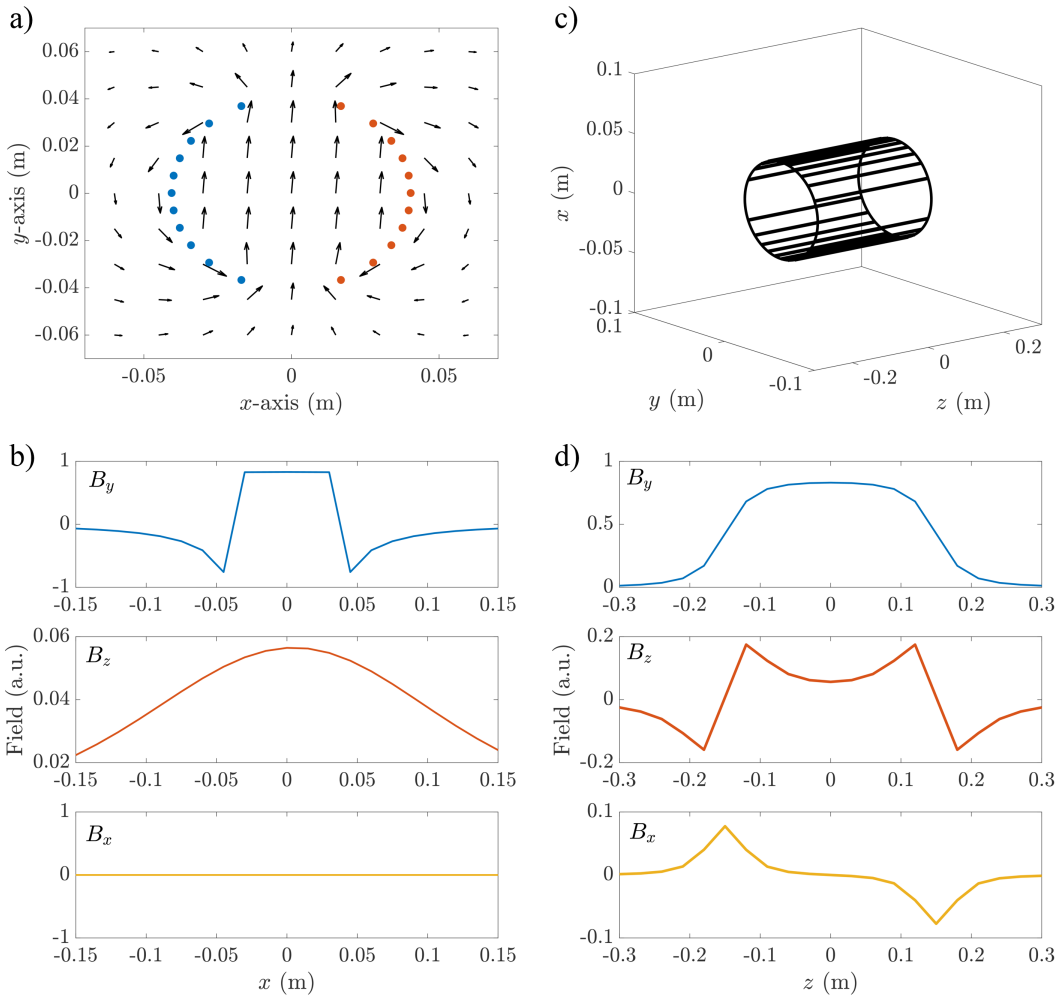

Figure 4.5: Biot-Savart field simulation of $\cos\theta$ coil for the y-field. a) vector field distribution cross-section at the centre of the coil. The blue and red dots represent the negative and positive current flow and distribution. b) Field profile along x-axis of the coil at $(y = 0, z = 0)$. c) 3D plot of the coil profile including the saddle. d) Field distribution along the z-axis of the coil from the $(x = 0, y = 0)$ coordinate point. Due to the saddles as the wire returns over the arc of the shell, additional fields are generated causing inhomogeneities in the field profile.

where R is the radius of the coil. The expression for $\bar{y}_n$ is given by

$$\bar{y}_n^{\text{odd}} = -\left(1 - \frac{1}{2}\Delta y^{\text{odd}}\right) + n\Delta y^{\text{odd}}, \tag{4.10}$$

$$\bar{y}_n^{\text{even}} = -\left(1 - \Delta y^{\text{even}}\right) + n\Delta y^{\text{even}}, \tag{4.11}$$

where $\Delta y^{\text{odd}} = 2/N$ and $\Delta y^{\text{even}} = 2/(N+1)$ with N being the number of source-sink

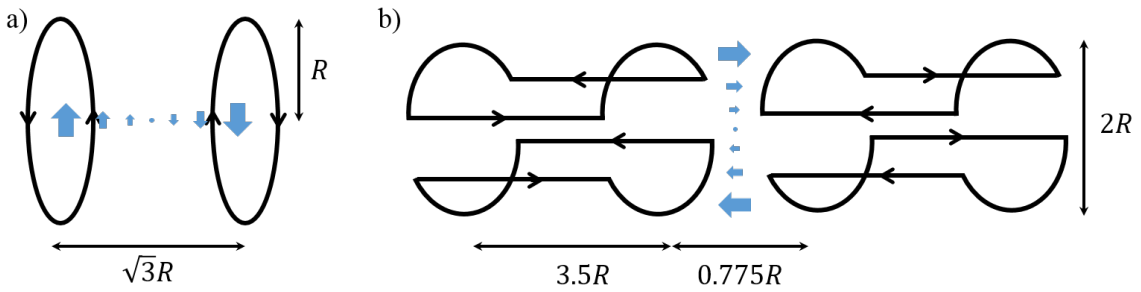

Figure 4.6: a) Maxwell gradient field coil generates a linear field gradient $\partial B_z/\partial z$. b) Golay gradient field coil generates a linear field gradient $\partial B_z/\partial x$ and $\partial B_z/\partial y$ depending on the orientation [84]. The blue arrows indicate the field variation along the axis.

pairs. The angle is given by

$$\theta_n = \sin^{-1}(\bar{y}_n). \tag{4.12}$$

Note that for $\cos\theta$ geometry, the vertical spacing between each successive conductors is the same. In practice, the $\cos\theta$ geometry is not simply made of finite straight wires, but contains additional saddle geometries as a result of the wire being distributed around a cylinder. The saddle arc depends on the nth position of the current carrying wire defined by the following parametric equations

$$\phi_n = \pi - |2\theta_n|, \tag{4.13}$$
$$-\phi_n/2 \leq \theta_n \leq \phi_n/2, \tag{4.14}$$
$$x_n = R\cos\theta_n, \tag{4.15}$$
$$y_n = R\sin\theta_n, \tag{4.16}$$

which introduce additional field non-uniformities. The field profiles generated by the $\cos\theta$ coil are shown in Fig. 4.5. For the compensation of linear gradients, we use a combination of Golay and Maxwell coils. The corresponding geometries for the Golay and Maxwell Coils are shown in Fig. 4.7. With the Maxwell and Golay coils it is possible to compensate linear gradient fields in the x, y and z directions with respect to the B_z field.

The coils are are designed using CAD software[1] and then wire wound on a 3D printed shell which contains trenches outlining the current distribution. We use a standard commercial 3D printer[2] utilising Polylactic acid (PLA) plastic as the material for printing. The cylindrical coil geometries of each coil allow for nested design making the entire structure compact. Table 4.1 on page 115 summarises each coil layer and its function.

The home made $\cos\theta$ coils have a typical radius $r \approx 40$ mm with length $l = 300$ mm

[1]Solidworks
[2]Ultimaker 2+ Extended

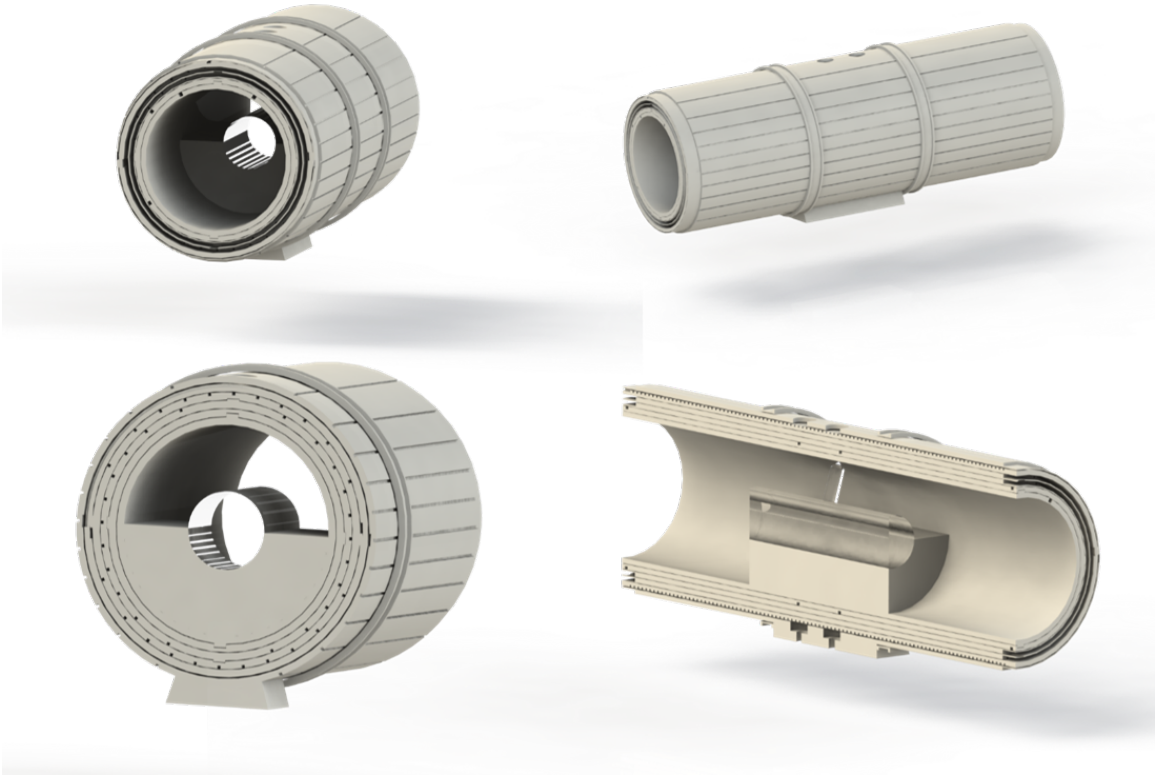

Figure 4.7: Full Coil Assembly based on the layer structure given in Table 4.1. For each layer there are linear grooves which automatically align the coil axes when the coils are nested. The bottom rendered pictures depict the cross sections of the coils along the optical axis and perpendicular to it.

and a typical number of 11 pairs of current carrying wires. The resistances and inductances of our coils are of the order of $R \approx 2\ \Omega$ and $L \approx 30\ \mu$H respectively with the current-to-field conversion of ≈ 0.8 G/A. Our solenoid has $N \approx 100$ turns with a resistance $R \approx 7\ \Omega$ and an inductance $L \approx 0.3\ \mu$H. The field to current conversion for the solenoid is ≈ 4 G/A. Because the range of field frequencies in the experiment are well below $\ll 1$ MHz, the wavelength of the rf-field is much larger than the features of the coils, it is not necessary to consider finite size effects, which would otherwise become important at higher frequencies.

In the simulations, the typical field uniformities for both the $\cos\theta$ and solenoid coils are around $\leq 0.1\%$ in the x-y plane and $\approx 1\%$ along the z-axis of symmetry within the dimensions of the cell, i.e. diameter of the cell $d = 26$ mm in the x-y plane and length $l = 106$ mm along the z-axis. We investigated the effects on the field uniformity as a result of the deviations from the ideal track geometry. This was simulated by introducing a random Gaussian distributed deviation from the ideal point of the order of $\sigma = \pm 1$ mm for each finite element point and computing the

resultant field profile. The simulations indicate that the field uniformity degrades by approximately a factor of 2 across all directions. The 3D printer tolerances are of similar order. The field homogeneity of the coils can be further increased by increasing the coil length and reducing the diameter. The former dimensional change has a stronger effect on the field homogeneity due to finite length effects. However, due to the limitations of our 3D printer, longer length coils would mean that the printing assembly would have to be broken up further into smaller parts increasing alignment imperfections and potentially spoiling the homogeneity.

Table 4.1: Composite field coil system

Layer	Coil	Function
1	Golay 1 coil	$\partial B_z/\partial x$
2	Golay 2 coil	$\partial B_z/\partial y$
3	$\cos\theta$ x coil	DC, uniform field x
4	$\cos\theta$ y coil	DC, uniform field y
5	Solenoid z coil	DC, uniform field z
6	$\cos\theta$ x coil	rf-dressing field x
7	Maxwell coil	$\partial B_z/\partial z$

4.2.2 PID Stabilised bi-polar current source

As was discussed at the beginning of this section, the environment contains many external sources of magnetic fields which can vary on a day to day basis. Having constructed a system of coils with the capability to generate uniform magnetic fields as well as cancel out the various inhomogeneities, the next step involves constructing a current driver capable of supplying the the proposed coil system.

Our bipolar current source is based on Class B Amplifier which is also known as a push-pull amplifier, see Fig. 4.8 [85]. It consists of two complementary transistors with matching characteristics except their polarity, one being PNP whilst the other NPN. Both transistors have the same input signal at their gates. When the voltage signal input at the base of the transistor is sufficient to satisfy the gate threshold voltage, then current flows from the emitter to the collector (PNP) which ultimately passes through the coils. In this case, the current flow is proportional to the gate voltage as well as the resistance of the coils. Note that the gate voltage for the other transistor (NPN) will have the opposite sign and as a result no current will flow from its corresponding emitter to the collector. A problem arises when the input voltage signal is smaller than the minimum gate voltage required for the transistor to emit - i.e. no current flows from either of the transistors despite the voltage being non-zero. This region is known as the zero-crossover distortion. It can be remedied by biasing the gates of the transistors with diodes causing a voltage drop equivalent to the minimum voltage required to activate the transistors. This results in a class AB-type push-pull

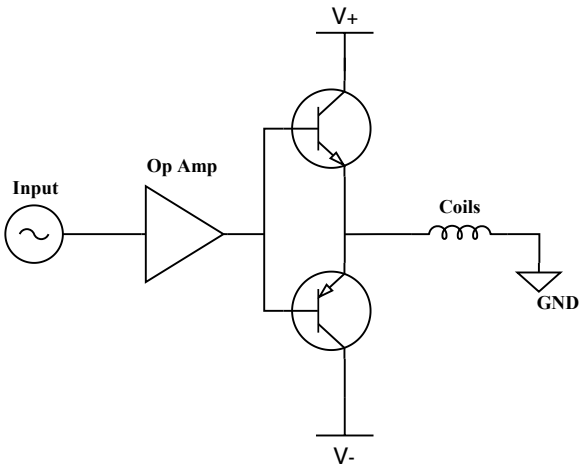

Figure 4.8: Class B type push-pull circuit topology used for our bipolar current source.

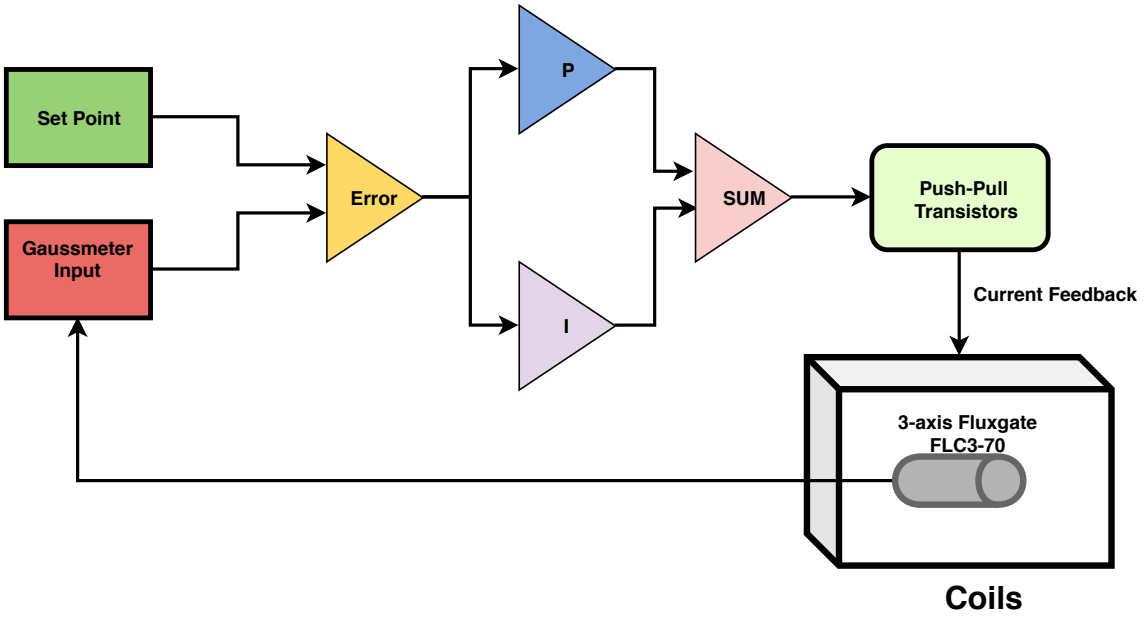

Figure 4.9: Flow diagram decpiting our home made PI-stabilised Class B type bipolar current source with fluxgate sensor and the coils.

current amplifier.

The design of our home made PI stabilised bipolar current source consists of three major functional components, see Fig. 4.9. The first is the proportional-integral part which computes the error signal by taking the difference between the set-point field

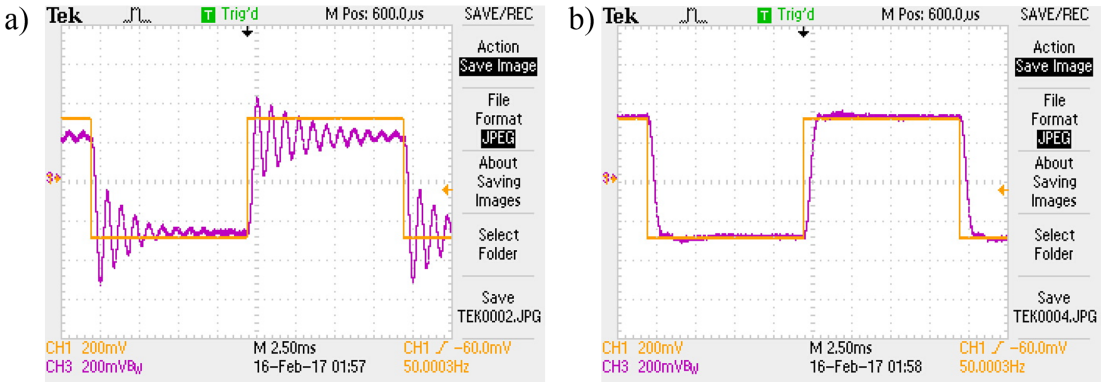

Figure 4.10: Tuning of PI source using the Ziegler-Nichols method. a) Only the proportional gain is non zero. As the gain is increased, the system begins to oscillate at its natural resonance frequency. This allows us to derive the time period $T_{\max}$ for the integral gain as well as scale the proportional gain. b) Optimised proportional and integral gains in effect. We no longer see any oscillations and no overshoot. The yellow square wave is the setpoint reference which is running at 50 Hz.

value and the actual field measured by a commercial fluxgate magnetometer[3] inside the coil assembly. The error signal is then split into a proportional and integral parts of the circuit which computes the correction signal which is then sent to the push-pull transistors. The push-pull transistors then output the current which is sent to the coils to produce the desired field.

To optimise noise cancellation and stabilisation, the PI loop is tuned heuristically using the Ziegler-Nicholls method [86]. The procedure is as follows; the setpoint is chosen to be a time varying square wave at 50 Hz. Initially, the integral gain (assume no differential part of the PID loop is present) is set to zero. The proportional gain K_p is then tuned from zero to $K_{\max}$ where the output begins to oscillate at a constant frequency and amplitude. From this we calculate the period of oscillation $T_{\max}$. Then, according to the Ziegler-Nichols method, the proportional and integral gains in terms of the maximum proportional gain and the corresponding time period of the oscillation frequency of the system are given by

$$K_p = \frac{9}{20} K_{\max}, \tag{4.17}$$

$$K_i = \frac{K_p}{T_{\max}}. \tag{4.18}$$

The different stages of PI tuning are depicted in Fig. 4.10 with the noise performance comparison between PI regulated and unregulated field compensation given in Fig. 4.11, as measured by the in-loop fluxgate. With PI regulation, the noise floor

[3]Stefan-Mayer 3-axis Magnetic Field Sensor FLC3-70

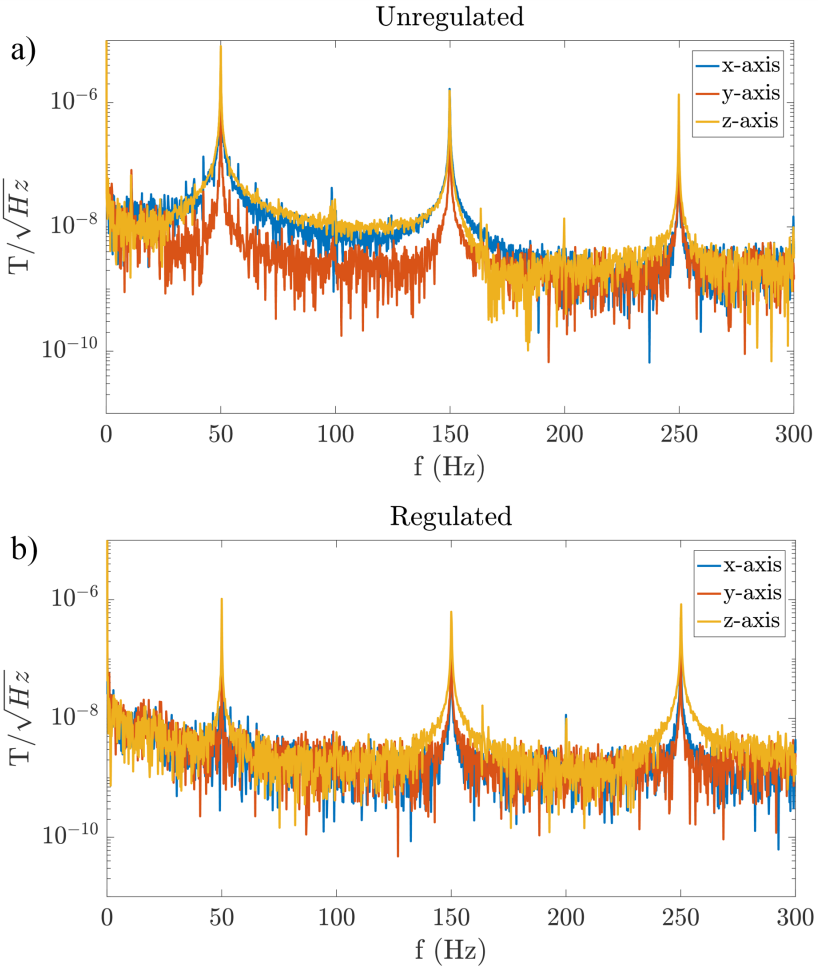

Figure 4.11: a) Fluxgate environmental noise without PI stabilisation b) Fluxgate environmental noise with PI stabilisation. Here the fluxgate is a 3-axis Stefan-Mayer Instruments FLC3-70.

(excluding the harmonic components) is reduced by approximately a factor of 4 in the range 2 Hz $\leq f \leq$ 250 Hz, the 50 Hz harmonic is reduced by nearly an order of magnitude with the additional 150 Hz and 250 Hz harmonics reduced by a factor of 5 and a factor of 2 respectively. The noise floor of the fluxgate magnetometer used in this frequency range is 0.12 nT/$\sqrt{\text{Hz}}$ which is more than order of magnitude lower than the environmental noise, therefore we can ignore the contribution from the fluxgate noise added to the PI servo loop when actively compensating the field.

To achieve a higher level noise suppression of the ac line noise due to the 50 Hz and its harmonics a phase sensitive feed-forward could be added to the existing PI loop. An added feature to further minimise the noise of PI loop and the bipolar current sources would be to include a battery powered supply. We have implemented

this only in an unshielded environment and observed a marginal improvement. An additional feature which would potentially improve the PI performance would be a software-enabled PI loop. This not only provides a flexible way to tune the PI parameters, but also removes a significant amount of thermal drifting which can affect the gain constants for the P and I components of the loop as well as the value of the field setpoint. Moreover, there exists a number of software library packages (e.g. Arduino PID Library) which offer self-tuning capabilities.

4.3 Data Acquisition and Digital Signal Processing

4.3.1 Signal Detection, Processing and Bandwidth

Balanced Homodyne Detection. The Voigt rotation signal, which contains information about external magnetic fields is detected using a method of balanced homodyne detection. Balanced homodyne detection refers to a technique where an incident beam (signal) with a well defined frequency and phase is split into two equal components which are read by two photodetectors, the resultant signals are then subtracted or added electronically, depending on the application. If the beam (signal) has properties (e.g light polarisation) that interact differently with the medium (e.g. the atomic medium), the phase information, as well as the signal strength for those components may change and will result in an imbalance in the subtracted signals providing the information about the interaction in terms of the amplitude and the phase. Typically, no interaction results in a differential (subtracted) signal equal to zero and any fluctuation due to interactions will introduce an imbalance manifesting in a positive or negative differential signal output. In our case, since we measure the linear birefringence of our Stokes' vectors, our linearly polarised beam set to 45° relative to the x-axis produces a balanced signal with a differential output equal to zero. This is assuming the medium is not pumped, i.e. the atoms are in a thermal state, and the probe beam is far detuned to remove any light-matter interactions. However, atoms pumped to our aligned state with a radio-frequency dressing field induce a modulated linear birefringence at ω_{rf} and $2\omega_{\mathrm{rf}}$ frequencies and as a result, the light-matter interaction results in our probe light acquiring elliptical polarisation modulated at ω_{rf} and $2\omega_{\mathrm{rf}}$ frequencies. Using a quarter-wave plate this ellipticity can be decomposed into linear polarisation components which are further spatially split into vertical and horizontal polarisation components by a polarising beam splitter. The corresponding light is then incident on our balanced photodetector[4]. Figure 4.3 on page 109 illustrates the optics setup used to measure the Voigt effect. The advantage of balanced homodyne detection is that it has a high common mode noise rejection which allows to suppress intensity and polarisation fluctuations in the probe laser and other sources of noise. Moreover, since our homodyne signals are modulated at rf-harmonics the important field information is encoded within them. This allows us

[4]Thorlabs PDB210A/M

to implement phase-sensitive lock-in detection to further remove additional sources of noise.

Signal Processing. The detected Voigt effect signal on the balanced photodetector is given by

$$U(t) = g_{\rm el}\left\langle \hat{S}'_z(t)\right\rangle = g_{\rm el} g_F^{(2)} S_y n_F \left\langle \hat{F}_x^2(t) - \hat{F}_y^2(t)\right\rangle, \tag{4.19}$$

where $g_{\rm el}$ is the electronic gain of the photodetector. Experimentally, $U(t)$ has voltage, [V] dimensions. The signal is low-pass filtered with a cut-off frequency of 400 kHz at 3 dB to prevent aliasing from the analog input from a Field-Programmable-Gate-Array (FPGA)[5] running at sampling rate of 800 kHz. The detected signal carries field information at $\omega_{\rm rf}$ and $2\omega_{\rm rf}$ frequencies. We demodulate the raw balanced signal digitally at those frequencies. The complex demodulated signal amplitudes m_k for $\omega_{\rm rf}$ and $2\omega_{\rm rf}$ ($k = 1,\ 2$) are given by

$$m_k = \int_{t_1}^{t_2} e^{(-ik\omega_{\rm rf}-\gamma)t} U(t)dt \Big/ \sqrt{\int_{t_1}^{t_2} e^{-2\gamma t}dt} = \sqrt{\frac{2\gamma}{1-e^{-2\gamma T_p}}} \int_{t_1}^{t_2} e^{(-ik\omega_{\rm rf}-\gamma)t} U(t)dt, \tag{4.20}$$

where γ is the atomic decay, which is due to collisions and other decoherence mechanisms. Here, t_1 and t_2 are the interval times of the probe pulse with $T_p = t_2 - t_1$. For small external magnetic fields

$$m_1 \sim B_x^{\rm ext} + iB_y^{\rm ext}, \tag{4.21}$$

$$m_2 \sim B_z^{\rm ext}, \tag{4.22}$$

see equations (3.43)-(3.45) on page 37 for comparison. The demodulated signal amplitudes, m_k have units [V$\sqrt{\rm s}$]. With a proper digital phase adjustment, the real and imaginary parts of m_1 can be related to the measured external field components $B_x^{\rm ext}$ and $B_y^{\rm ext}$ whilst the real part of the m_2 component is related to the longitudinal field measurement $B_z^{\rm ext}$. The response functions m_k are directly associated with the dispersive and Lorentzian profiles when the longitudinal field B_z is scanned.

Theoretical OPM Bandwidth. The OPM sequence consists of state preparation and probing which have a square pulse profile. This sequence is repeated at some rate f_s which depends on various OPM parameters such as the pump/probe powers, coherence time of the cell etc. With each discrete probe pulse of duration T_p we acquire a signal $U(t)$ with the corresponding mode amplitude m_k. Running this sequence for n_s cycles at a rate f_s gives the total sampling time $T_s = n_s/f_s$ and frequency resolution $\Delta f = f_s/n_s$ with the $i^{\rm th}$ component of demodulated signal amplitude, m_i. The total demodulated signal amplitude reads

$$m_{\rm Tot} = \frac{1}{T_s f_s} \sum_i^{T_s f_s} m_i, \tag{4.23}$$

[5]National Instruments PCIe-7852

where

$$m_i = \frac{1}{\sqrt{T_p}} \int_{t_i}^{t_i+T_p} U(t)dt. \tag{4.24}$$

The quantity m_{Tot} contains the time trace of the demodulated signal amplitudes which contain the external field information. Typically, to evaluate the OPM performance we are interested in computing the power spectral density (PSD). This gives us the power distribution over the frequency components that make up the signal. Using the definition of the demodulated signal amplitudes the PSD is given by

$$\left\langle m_{\text{Tot}}^2 \right\rangle = \frac{S_{UU}}{T_s f_s} = \frac{S_{mm}}{T_s}, \tag{4.25}$$

where we have used the fact that

$$\langle U(t)U(t')\rangle = S_{UU}\delta(t-t'). \tag{4.26}$$

In other words, decreasing the total sampling time T_s increases the noise level of the demodulated mode amplitudes. However, the picture is not complete. The finite probe pulse time as well as the atomic signal decay within the probing region can further limit the magnetometer bandwidth which should be considered in detail. Theoretically, the rf-driven atomic precession in an external magnetic field results in the modulation of the linear birefringence of light, which is dominated by the first and second harmonics of the modulation frequency, ω_{rf}. With the atomic decay, and multiple pump/probe cycles, the i^{th} signal can be described by the following relation (see Fig. 4.12 for illustration)

$$U_i(t) = g_{\text{el}} e^{-\gamma(t-iT_s)} H(T_p - t + iT_s) H(t - iT_s) \mathcal{V}(\omega_{\text{rf}}, 2\omega_{\text{rf}}), \tag{4.27}$$

where $H(t)$ is the Heaviside step function, T_s is the sampling period and T_p is the probing time period. The definition of the Heaviside step function is given by

$$H(t) = \begin{cases} 0, & \text{for } t < 0, \\ 1, & \text{for } t \geq 0. \end{cases} \tag{4.28}$$

The sampling frequency is affected by the duration of the state preparation and probing stages. The pumping time, i.e. the minimum time to fully pump the atomic medium to an aligned state is dependent on the pump power, rf-dressing frequency as well as the coherence lifetime of the cell. The probing time T_p is affected by the probe power, detuning and also the coherence lifetime of the cell. Here, $\mathcal{V}(\omega_{\text{rf}}, 2\omega_{\text{rf}}) \sim \left\langle \hat{F}_x^2(t) - \hat{F}_y^2(t) \right\rangle$. We can model the envelope of the signal decay, $U_{\text{env}}(t)$, within the probing region using the following function

$$U_{\text{env}}(t) = g_{\text{el}} e^{-\gamma t} H(T_p - t) H(t). \tag{4.29}$$

Because of the decaying atomic signal as well as finite sampling time, the OPM response gain function has a frequency as well as the decay rate, γ, dependent profile.

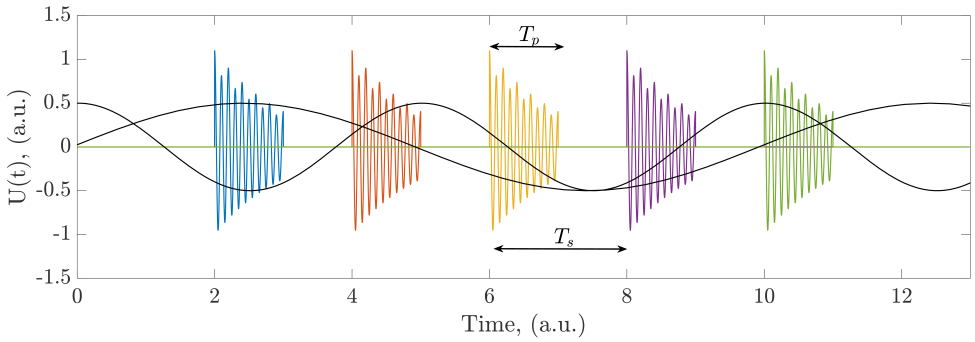

Figure 4.12: Probe pulse sequence. Here the probe of duration T_p is pulsed at a rate of $f_s = 1/T_s$ - which is our sampling frequency which approximately determines the magnetometer bandwidth $\Delta B = f_s/2$. Here the probe pulse signals oscillate at ω_{rf} and $2\omega_{\text{rf}}$ frequencies and the black sinusoidal traces represent the external magnetic fields and their sampling by the probe pulses which are seen as regions of overlapping. The gaps between the probe pulses corresponding to $T_s - T_p$ are the pumping stages where the Voigt effect is not measured. The black sinusoidal waves represent how the external magnetic field source of various frequencies are sampled by the probe beam via the Voigt effect. The signal is averaged over the probe time T_p.

The decay rate represents the coherence lifetime of the cell which is dependent on various parameters discussed in sec. (3.2.9). The normalised gain profile can be found by taking the Fourier transform of the envelope function $U_{\text{env}}(t)$ and computing the normalised amplitude response as a function of frequency

$$\Pi(\omega) = \sqrt{|U_{\text{env}}(\omega)|^2} = \sqrt{\frac{\gamma^2}{\gamma^2+\omega^2}\frac{\cosh(T_p\gamma)-\cos(\omega T_p)}{(\cosh(T_p\gamma)-1)}}, \tag{4.30}$$

where we have explicitly assumed that the decay $\gamma > 0$. The gain correction function, $\Pi(\omega)$ is dimensionless as its normalised to unity. Hence, the decay and square probe time adjusted field noise spectrum is given by

$$\mathcal{N}_{\text{field}}(\omega) = \frac{g_{\text{el}}}{\Pi(\omega)}\sqrt{\langle m^2_{\text{Tot}}(\omega)\rangle}, \tag{4.31}$$

where $\mathcal{N}_{\text{field}}(\omega)$ has units $\text{V}\sqrt{\text{s}}/\sqrt{\text{Hz}}$. To convert to field units we use the voltage-to-field calibration which in the linear OPM regime is a constant and has units $\text{V}\sqrt{\text{s}}/\text{T}$, where [T] are the field units in Tesla. The field noise spectrum in field units $\text{T}/\sqrt{\text{Hz}}$ is then given by

$$\mathcal{N}_{\text{field}}(\omega) = \frac{g_{\text{cal}}g_{\text{el}}}{\Pi(\omega)}\sqrt{\langle m^2_{\text{Tot}}(\omega)\rangle}. \tag{4.32}$$

4.3.2 Experimental Sequence

Hardware intricacies and experimental sequence generation. The hardware architecture consists of four levels, see Fig. 4.13. The first level consists of experimental

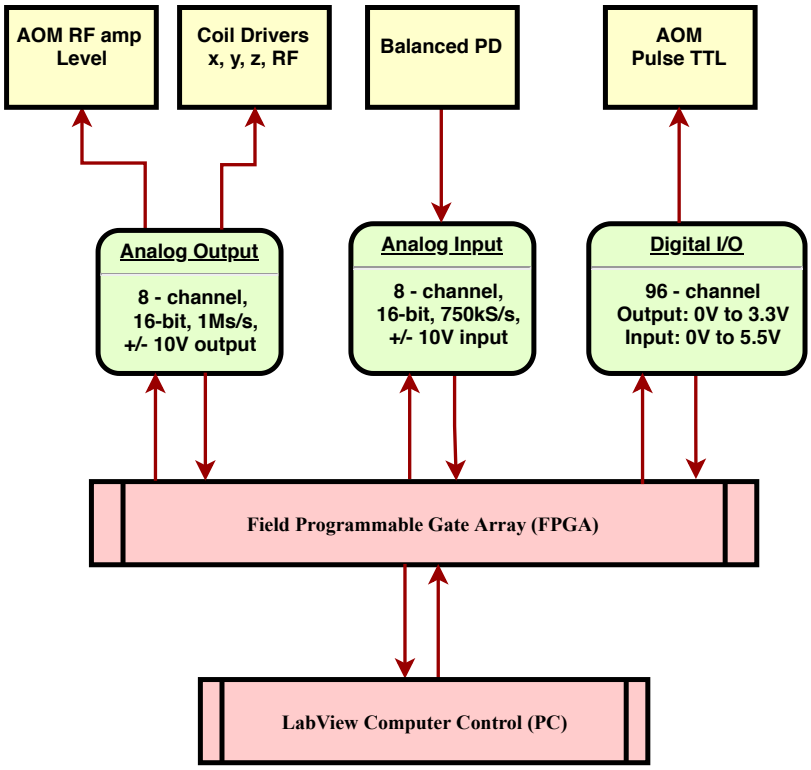

Figure 4.13: Functional block diagram showing the basic layout of the computer control hardware and its interface with the experimental apparatus.

computer control software which is based on LabView visual programming language. It has a dual functionality. It sends instructions to the field programmable gate array (FPGA) in order to control the experimental equipment to produce the necessary sequence of laser pulses and magnetic fields as well as analyse the retrieved data from the FPGA to visualise and estimate the magnetometer response. The data analysis involves taking the raw balanced photodetector signal, digitally demodulating it and computing the corresponding OPM mode amplitudes, m_k. The second level consists of the FPGA. In our experiments we use National Instruments PCIe-7852 which provides digital as well as analog input and output channels to control our hardware. The final level consists of the peripheral hardware equipment that directly influences the magnetic field and laser light properties to control the magnetometer response as well as measure it.

OPM Sequence. As has been outlined in the theoretical section, the OPM sequence consists of two stages in our typical magnetometer sequence (where we have excluded the additional microwave stage). The cycle begins with a state preparation sequence consisting of synchronous optical pumping and cw repump beams with the dressing and other magnetic fields ramped immediately. We typically use a train of pump pulses at 10% duty cycle and in phase with a uniform 5 kHz rf-field of $\leq$0.1 mG near resonant with B_z static field. The typical state preparation process in our setup

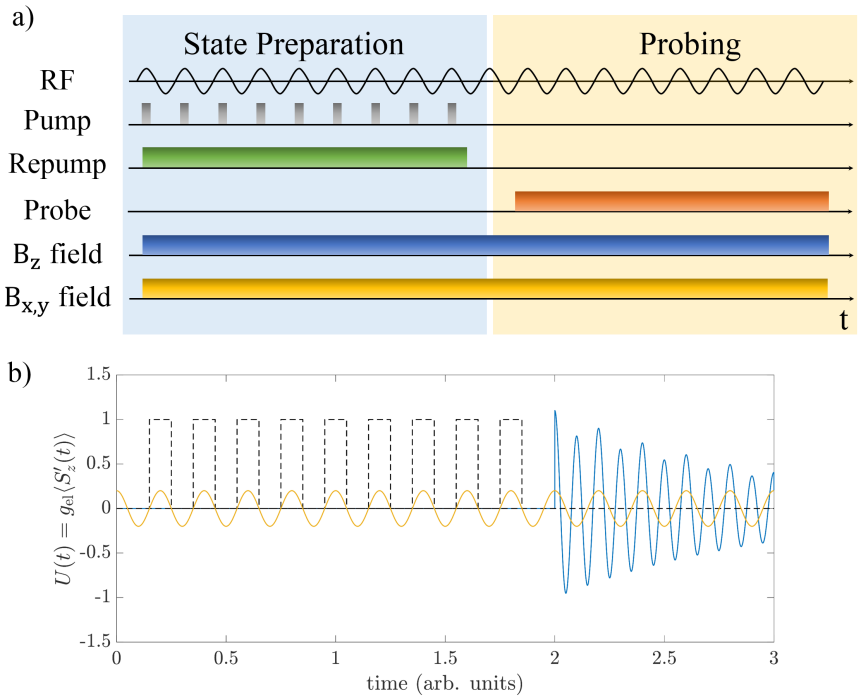

Figure 4.14: a) Experimental sequence diagram consisting of two stages involving the state preparation process and probing. The control magnetic fields as well as the radio-frequency field are ramped instantaneously. The laser pulses have square time profiles. The typical state preparation procedure takes 5 ms with the probing stage lasting 3 ms. b) theoretical plot of the balanced PD signal for the two stages of the OPM cycle. Here the yellow curve represents the oscillating rf-dressing field, the dashed black pulses represent the pump pulses and the blue decaying signal represents the Voigt rotation.

lasts 5 ms and is primarily limited by the coherence time of the cell. This results in an approximately incoherent mixture of $|F = 2, m_F = \pm 2\rangle$. After this stage, the pump/repump beams are switched off which is then followed immediately by a cw probe pulse for 3 ms. The rf as well as the static fields remain constant, see Fig. 4.14. The entire sequence is then repeated again at a rate f_s which is our sampling frequency. The probe pulse allows us to extract the mode field amplitudes, m_k, which contain the vector information of the external magnetic fields.

OPM Resonance Profiles. The theoretical models outlined in Chapter 3 allowed us to compute the OPM response as a function of the longitudinal magnetic field B_z which produce characteristic dispersive and Lorentzian profiles. To obtain these profiles experimentally, we generate the OPM sequence described above and shown in Fig. 4.14. For each pulse sequence, we change the B_z field whilst keeping all other parameters constant and extract the corresponding mode field amplitudes, m_k from the ω_{rf} and $2\omega_{\text{rf}}$ field quadratures. The mode field amplitudes are then

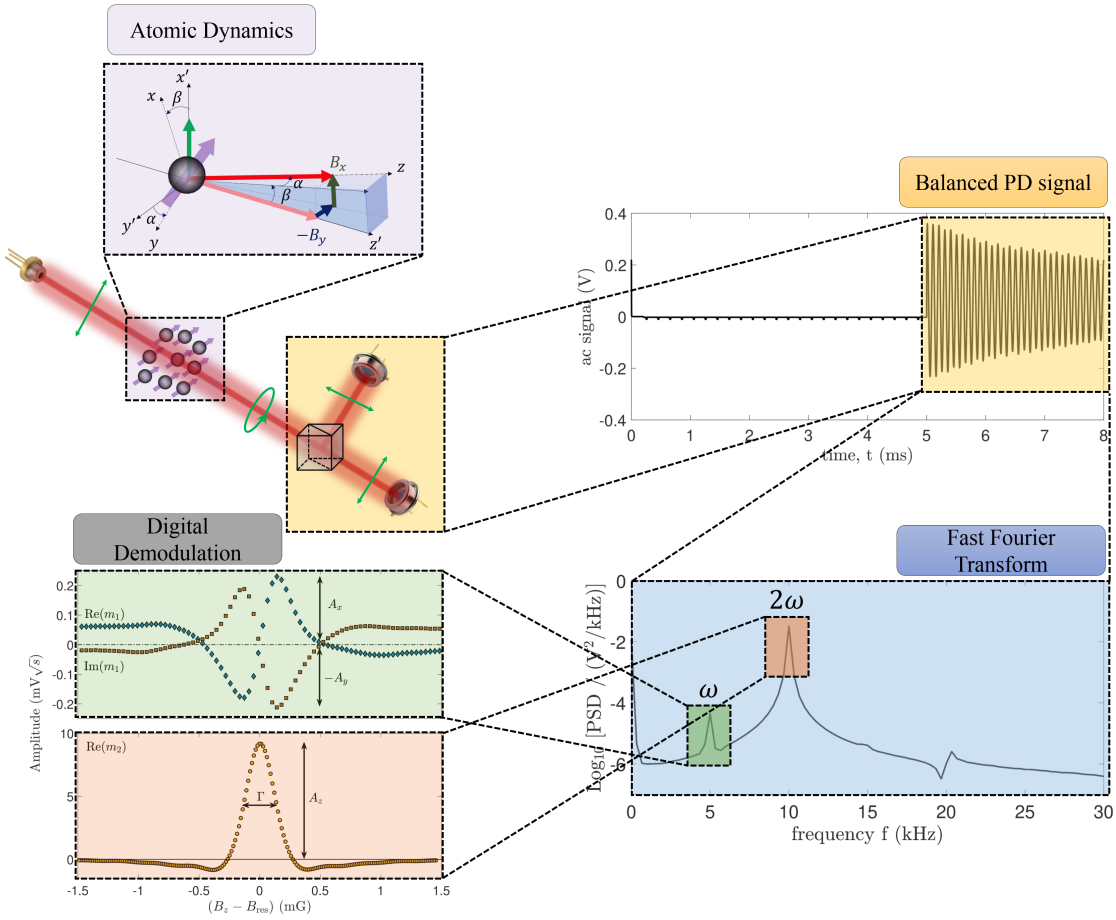

Figure 4.15: Diagram depicting how the spin-field interaction is used to measure magnetic fields. The spin-field interaction and the subsequent light-spin interaction induces linear birefringence which results in the linearly polarised beam acquiring ellipticity which is modulated at ω_{rf} and $2\omega_{\mathrm{rf}}$ frequencies. The balanced photo detector signal is then decomposed spectrally by taking its Fourier transform. The amplitudes of the quadratures at those frequencies correspond to external magnetic fields and are then digitally demodulated. The dispersive and Lorentzian profiles are obtained when the longitudinal magnetic field is scanned.

plotted against the B_z field, see Fig. 4.15 for details. The OPM response expressed in terms of the mode field amplitudes, m_k, as a function of the B_z field is a starting point in optimising signal strength of the magnetometer. In general, the narrower the resonances, and the larger the amplitude of those resonances, the more sensitive we are to the external fields. Moreover, the OPM response to the longitudinal B_z field gives us a good starting point in comparing our theory to the experiment.

Demodulation Phase adjustment. The dispersive and Lorentzian resonance profiles characterised by the extracted mode field amplitudes m_k as a function of the

B_z field are obtained by digital demodulation. Like any lock-in detection, it requires careful phase adjustment relative to the phase of our referenced local oscillator (rf-field) in order to make sure that we can extract the correct field quadratures corresponding to external fields. First, we make sure that the external transverse fields are zero, such that we measure $m_1 = 0 + i0$ for the transverse field quadrature. We then scan the longitudinal B_z field and measure the corresponding m_2 mode amplitude response and adjust the phase digitally until we obtain a Lorentzian profile, see Fig. 4.15. For the phase adjustment in the transverse field directions we set the longitudinal field on the sensitive point, $B_z = B_{\text{res}} + B_\rho$, and scan the transverse fields over a small range such that the OPM response of the m_1 amplitudes is linear. If only one transverse field is scanned, then the corresponding m_1 quadrature response should be observed only in the real or imaginary part (depending on which transverse field is scanned). If the phase for the m_1 mode amplitude is not properly adjusted, then the OPM response for the transverse fields will be seen in both m_1 quadratures to varying proportion. Hence, the phase is adjusted until the response is detected only in the corresponding quadrature related to that external field. This is only the case for small external fields.

OPM Calibration. The magnetometer response to external magnetic fields is measured via the light-matter interaction where the polarisation of the probe beam acquires ellipticity which depends on the external magnetic field. This ellipticity is detected on a balanced photodetector where the photon flux is converted to a photo-current giving rise to a voltage when measured on a photodector. This is not very useful if we want to extract the actual field information in field units, e.g. Gauss or Tesla. We want to find a way to convert the measured voltage signals into magnetic field units. Our magnetometer relies on dressing the atoms using an rf-field oscillating at frequency ω_{rf}. If there are no transverse fields present, then the maximal magnetometer response at $2\omega_{\text{rf}}$ amplitude is given by

$$B_z = B_{\text{res}} = \frac{\hbar\omega_{\text{rf}}}{\mu_B|g_F|}. \tag{4.33}$$

In other words, the characteristic Lorentzian resonance profile has a maximum when the resonance field condition, B_{res} is met. To make sure that there are no transverse fields present, we monitor the presence of ω_{rf} frequency quadrature and adjust the transverse fields such that it is zero when the B_z field is scanned. The coil current drivers are voltage controlled by the FPGA which have a linear voltage to current conversion [V/A]. The magnetic field generated by uniform field coils is linearly proportional to the current running across them, [A/T]. Hence, by varying the dressing frequency ω_{rf} and measuring the location of the maximum peak for a given field setpoint in terms of the voltage, gives us the voltage to field conversion for the $2\omega_{\text{rf}}$ quadrature which for small external fields corresponds to mapping of the B_z^{ext} field. The calibration of the transverse fields follows a similar method. If one of the transverse fields is present in addition to the longitudinal magnetic field B_z, then the new resonance condition of the $2\omega_{\text{rf}}$ Lorentzian profile is given by

$$B_{\text{res}} = \sqrt{B_z^2 + B_{x,y}^2} = \frac{\hbar\omega_{\text{rf}}}{\mu_B|g_F|}. \tag{4.34}$$

To determine the voltage to field calibration for B_x and B_y quadratures, we set the external transverse field to some value and scan the B_z field to obtain the OPM response of the $2\omega_{\mathrm{rf}}$ Lorentzian profile. Because of the presence of the transverse field the new location of the resonance as a function of the B_z occur at a lower value of the B_z. From the previous calibration of the B_z field we can easily determine what that field is, which allows us to calculate the remaining field contribution from the transverse field direction, B_x and B_y. Since we know the voltage set point for the transverse field, we can relate this to the calculated value. By varying the transverse field as a function of voltage, and calculating the remainder field by locating the new $2\omega_{\mathrm{rf}}$ resonance location, we can obtain the voltage to field calibration for the transverse fields. The advantage of using this magnetic field calibration is that it does not require additional external field sensors. Nevertheless, to confirm the reliability of the calibration, we use a commercial 3-axis fluxgate magnetometer (FLC3-70) and scan the external magnetic fields using our coil drivers to confirm our calibration.

Chapter 5

Results and Discussion

This chapter outlines and discusses the main experimental results obtained for the Voigt magnetometer in both unshielded and shielded environments. The two sections of this chapter explore the general characteristics of the Voigt effect magnetometry, touching upon typical raw Voigt effect signals, the demodulated response quadratures which contain the 3D field information, field sensitivity as a function of various experimental parameters such as probe power, detuning, temperature of the cell etc. Where possible, we attempt to compare our theoretical results with experimental observations.

5.1 Unshielded Operation

Historically, the experiment was started in an unshielded environment due to the fact it was not clear at the time whether Voigt effect magnetometry would even be possible. As a result, the constructed setup including the laser system and experimental control were a lot more pragmatic and simpler compared to the shielded setup outlined in the experimental chapter section. Nevertheless, the core principles of pump-probe sequence, signal demodulation as well as field control remained the same. Consequently, due to a variety of experimental imperfections and our inexperience in this field the results obtained in the unshielded environment were far from perfect, but were more than sufficient to convince us to build a magnetically shielded setup. In the following we discuss major results of the unshielded magnetometer setup.

5.1.1 Voigt effect signal and quadrature responses

Based on the experimental setup and sequence procedures outlined in the Experimental Apparatus chapter (see page 109 for example) the raw balanced Voigt effect signals with the corresponding power spectral density of the trace are shown in Fig. 5.1. Here

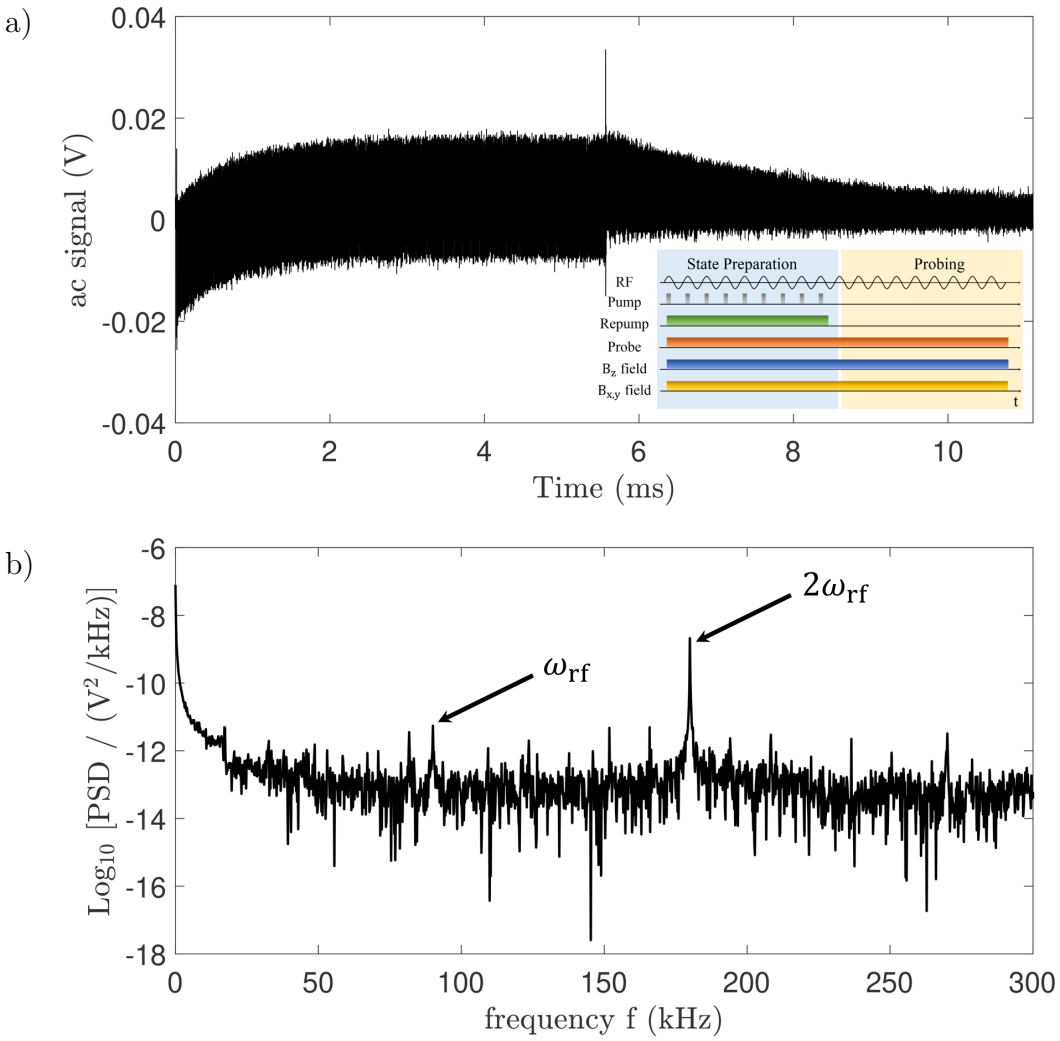

Figure 5.1: Typical experimental signals. a) Raw balanced signal of the Voigt rotation. The state preparation occurs within the first 6 ms of the cycle followed by a 5 ms probing pulse. The trace is obtained where $B_z \approx B_{\text{res}}$. b) Single-sided, power spectral density (psd) of the amplified signal during the probe pulse. Atomic signals arise at ω_{rf} and $2\omega_{\text{rf}}$, where $\omega_{\text{rf}} = 2\pi \times 90$ kHz is the dressing frequency of the rf-field. Here we see a strong signal $2\omega_{\text{rf}}$ and a comparatively weak ω_{rf} response due to the fact that the trace is taken on resonance. Here the synchronous pumping is at 14% duty cycle and the probe has -400 MHz detuning from the $F = 2 \rightarrow F' = 1$ transition on the D1 line.

a $\omega_{\text{rf}} = 2\pi \times 90$ kHz radio-frequency field is used to dress the atoms with an rf-field amplitude $\Omega_{\text{rf}} \approx 2$ mG. The choice of the dressing frequency is large enough to avoid environmental low frequency magnetic field noise whilst also being comparatively small such that second order Zeeman shifts can be neglected. As can be seen from

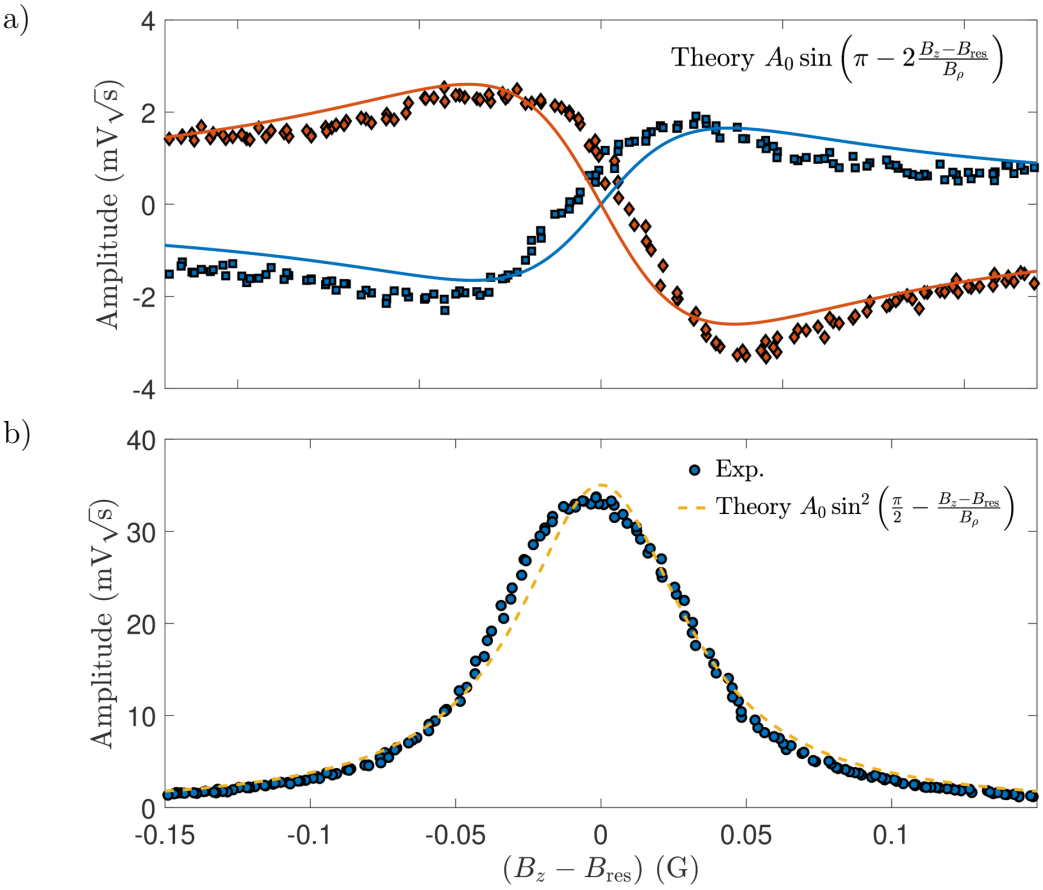

Figure 5.2: Experimental magnetometer response in the unshielded environment. Panels a) to b) show the three relevant quadratures of the mode amplitudes m_1 and m_2, i.e. responses at frequencies $\omega_{\rm rf}$ and $2\omega_{\rm rf}$, for a scan of the longitudinal field B_z across the rf resonance. Here, non-zero transverse fields $B_x^{\rm ext}$ and $B_y^{\rm ext}$ are kept constant. The mode amplitudes, extracted according to eq. (4.20) on page 120, follow the predicted behaviour, see eqns. (3.39-3.41) on page 36.

the figure, the pumping to steady state takes roughly 3 ms with the $1/e$ decay time being $\approx$ 2 ms. The mechanisms affecting the time to reach a steady state as well as the signal decay time are numerous. The presence of field gradients, collisions, probe induced signal decay etc., all negatively contribute to the state preparation and signal decay. Unlike in the shielded setup, the unshielded setup had optomechanics that possessed ferromagnetic properties, e.g. screws, mirror mounts etc., along with many power supplies and other electronic modules in the close vicinity of the OPM. The gradient fields across the cell, some of which were time dependent, were found to be a dominant source of noise in these experiments. The Voigt rotation spectrum is taken on Larmor resonance with the transverse fields around zero. The power spectral density of the probing window (indicated in the figure) reveals a presence of a strong

$2\omega_{\mathrm{rf}}$ resonance with a small ω_{rf} resonance. As we can see in the spectrum, there exist other noise frequencies with amplitudes similar to that of the ω_{rf} resonance which are of nuisance since they may be influencing the atomic spin dynamics acting as additional rf-dressing fields.

If we scan the longitudinal B_z field around the Larmor resonance whilst simultaneously demodulating the signals at ω_{rf} and $2\omega_{\mathrm{rf}}$ frequencies we obtain the signal amplitudes m_k which are proportional to the external magnetic fields, see Fig. 5.2 and Fig. 4.15 on page 125 for diagrammatic illustration of the process. The demodulated signal amplitudes have dispersive and Lorentzian resonance profiles, which are consistent with the profiles predicted by our geometric, Heisenberg and density matrix models (see pages 35, 58, 79 for reference). However, there are qualitative differences in the fact that our experimentally obtained Lorentzian resonance profile does not posses wings present in the Heisenberg and density matrix models whilst it agrees well with the geometric model. This is due to the fact that the dispersive and resonance profiles were obtained with the probe being applied across the state preparation and probing sequences. In this case the probe provides additional pumping affecting the state preparation in the off-resonant regime thus affecting the birefringence of the medium.

In the next subsection we investigate magnetometer response by varying various experimental parameters. The motivation behind this was to optimise for performance as well as test the predictions of our models.

5.1.2 Magnetometer characterisation in the unshielded environment

Probe Power and Detuning. The parameter space of the magnetometer is vast, and as a result, our initial rationale was to focus on a select few parameters that would allow us to optimise the performance i.e. high signal to noise ratio. Since the Voigt effect signal is obtained through dispersive light-matter interaction, the signal is directly affected by the probe power and detuning from the atomic transition. The performance is evaluated by setting the longitudinal static field to $B_{\mathrm{offs}} = B^{+}_{\mathrm{sense}} = B_{\mathrm{res}} + B_{\rho}$ which maximises the sensitivity of all three quadratures and applying a small linear field ramp ($\approx \pm 0.01$ G) for each quadrature sequentially for a given probe power and detuning (see page 122 for details on the sequence). For small linear field ramps, the corresponding OPM response is linear which yields an OPM quadrature response m_k as a function of the external field. The gradient $\Delta m_k / \Delta B_k$ yields the OPM sensitivity, with larger values indicating higher sensitivity to external fields. Fig. 5.3 shows the results for all three quadratures. Here we observe that increasing the probe power decreases the signal scale factor. A major contributing effect to this is that increasing optical powers increases the light scattering rate, and so the probe begins to act as a pump with increased absorption rates affecting the off-resonance light-matter interaction. From the figure, we also observe that the signal strength increases with

a)

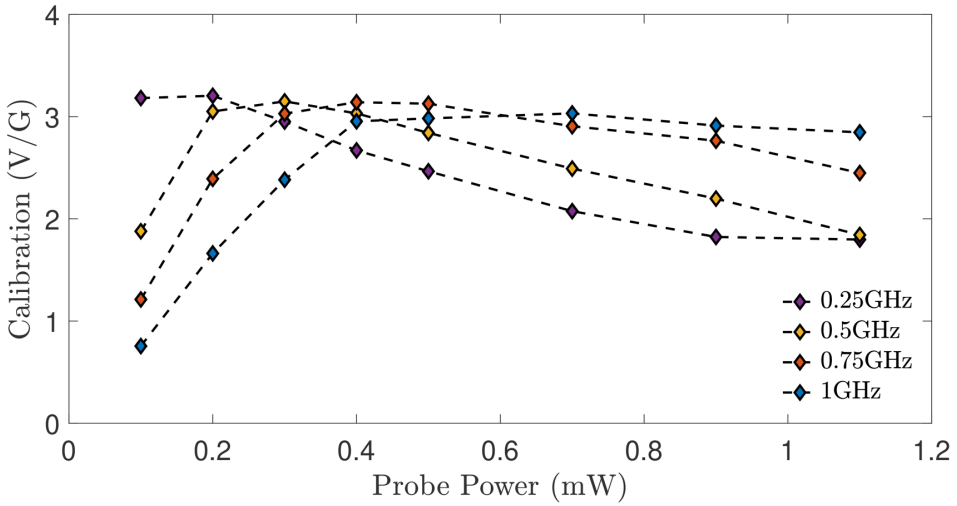

b)

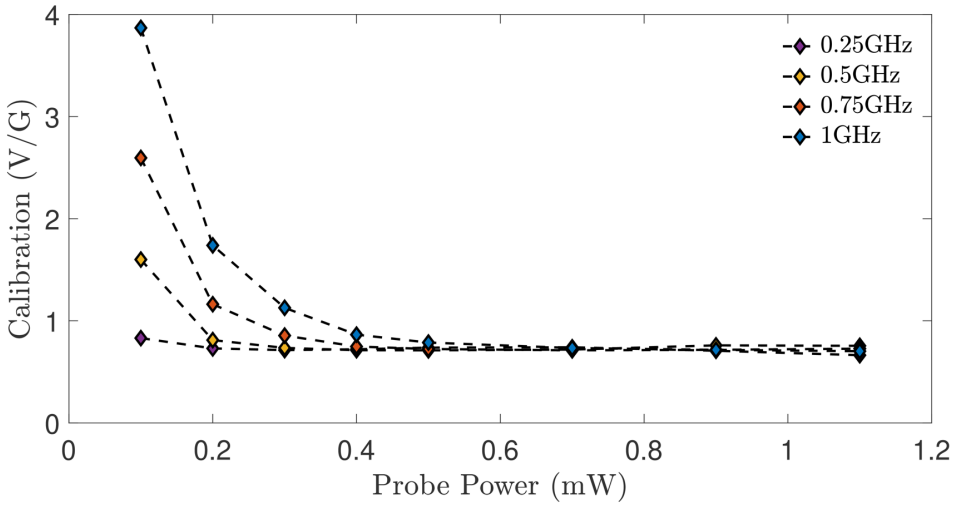

Figure 5.3: Field sensitivity as a function of probe detuning and power. a) field sensitivity at ω_{rf} corresponding to $\mathrm{Im}(m_1) \propto h_y$ mode amplitude. b) field sensitivity at $2\omega_{\mathrm{rf}}$ corresponding to $\mathrm{Re}(m_2) \propto h_z$ mode amplitude.

increasing probe detuning getting close to the atomic resonance. Unfortunately, due to the limitations of our initial setup, we were not able to explore the interaction as a function of the detuning further (this is explored in greater detail in the Shielded section).

Radio-frequency amplitude. The effects of the amplitude of the radio frequency field on the linewidth were also investigated. In the geometric model, the linewidth of the $2\omega_{\mathrm{rf}}$ Lorentzian is described by an envelope given by

$$h_z \propto \sin^2(\theta) = \sin^2\left(\frac{\pi}{2} - \tan^{-1}\frac{B_{\mathrm{dc}} - B_{\mathrm{res}}}{B_\rho}\right). \tag{5.1}$$

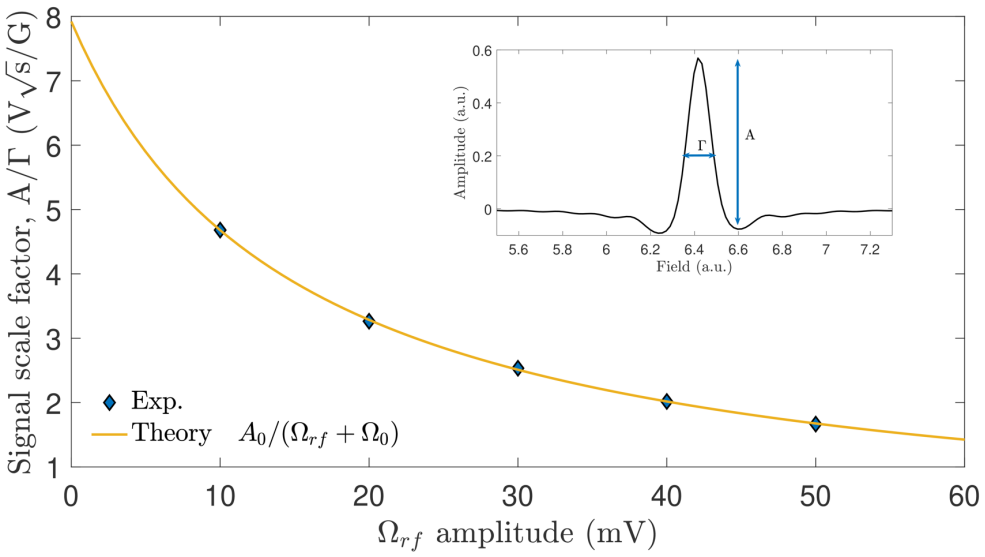

Figure 5.4: Signal scale factor of the $2\omega_{\mathrm{rf}}$ quadrature corresponding to m_z demodulated field signal scale factor. The signal scale factor is a quantity that should be maximised as it is proportional to the magnetometer's sensitivity to the external magnetic fields. The mV amplitude range corresponds to mG range field amplitude.

From this, increasing the rf-amplitude will linearly increase the linewidth of the ω_{rf} and $2\omega_{\mathrm{rf}}$ dispersive and resonance curves. This has the consequence of reducing the sensitivity of the quadratures for increasing rf-field driving amplitude. However, in some cases increasing the dressing field amplitude may be required where the environmental field noise in the system begins to dominate. Fig. 5.4 shows signal scale factor of the $2\omega_{\mathrm{rf}}$ quadrature corresponding to m_z demodulated field signal scale factor as a function of the amplitude of rf-dressing field. As can be seen, the signal scale factor has a $1/\Omega_{\mathrm{rf}}$ dependence predicted by both the geometric and Heisenberg models (see pages 36 and 63 for comparison).

Synchronous Pumping. The spin precession of our OPM is actively driven by a radio-frequency dressing field. As a result of this, the quantisation axis in the lab frame is rotating in time. This makes efficient state preparation with continuous wave (cw) light problematic because during the rf-cycle, the precessing atoms have a changing quantisation axis, and as a result the cw pumping results in an inefficient state preparation, with few atoms ending up in the desired state that is useful for Voigt magnetometry. Consequently, this can significantly affect the signal strength and the OPM sensitivity. To remedy this issue, the pumping light is synchronously pumped at the rf-field frequency and in phase with the rf-field [47]. The state preparation process also involves having a repump beam to repopulate the atoms from the $F = 1$ ground state. Here pulsing the repump synchronously is not necessary since its purpose is to transfer the atoms back to the $F = 2$ ground state which is then redistributed by the

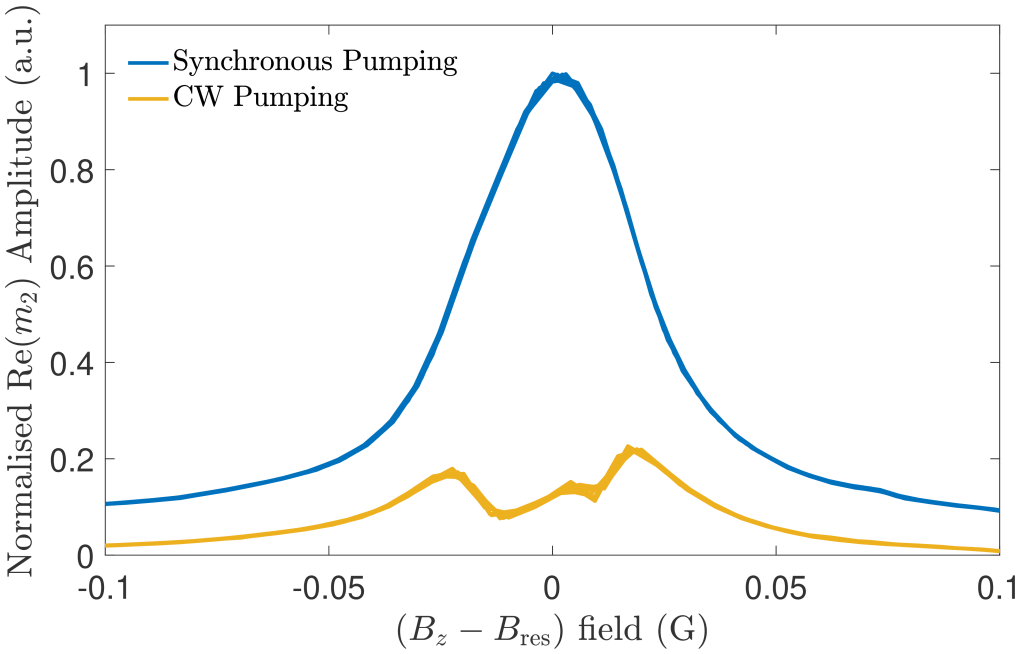

Figure 5.5: Re(m_2)$\propto h_z$ resonance profile as a function of B_z field in different cw and synchronous pumping conditions. Here the synchronous pumping method reproduces the expected Lorentzian profile whilst cw pumping results in significant distortion in the OPM response with a greatly reduced amplitude.

pump. A comparison between cw pumped and synchronously pumped $2\omega_{\mathrm{rf}}$ profiles is shown in Fig. 5.5. As can be seen from the figure, the cw resonance profile has an irregular shape and is of low amplitude compared to the profile obtained using synchronous pumping. Here the synchronous pumping is done at 90 kHz and ≈14% duty cycle and in phase with the rf-field. The duty cycle, as well as the relative phase to the rf influence the ω_{rf} and $2\omega_{\mathrm{rf}}$ profiles. This will be discussed in more detail in the Shielded results section.

Temperature and Vapour density. A common practice to increase signal strength in experiments with hot vapours is to heat the cell thus increasing the vapour density. As discussed in the theory section (see e.g. page 69) whilst increasing the temperature does indeed increase the atomic density and the signal strength, it also increases the atomic collision rate which results in depolarisation and ultimately signal loss, hence there is a trade-off. We looked into these effects by heating the cell with hot air (to avoid ac/dc generated magnetic fields due to Joule heating), and measuring the corresponding increase in signal amplitude of the Re(m_2) quadrature, see Fig. 5.6. The data shows that increasing the temperature and thus, the atomic density can improve the signal amplitude by over a factor of 2. However, passed the 40°C mark, the signal saturates and does not increase in strength for an increase in vapour density.

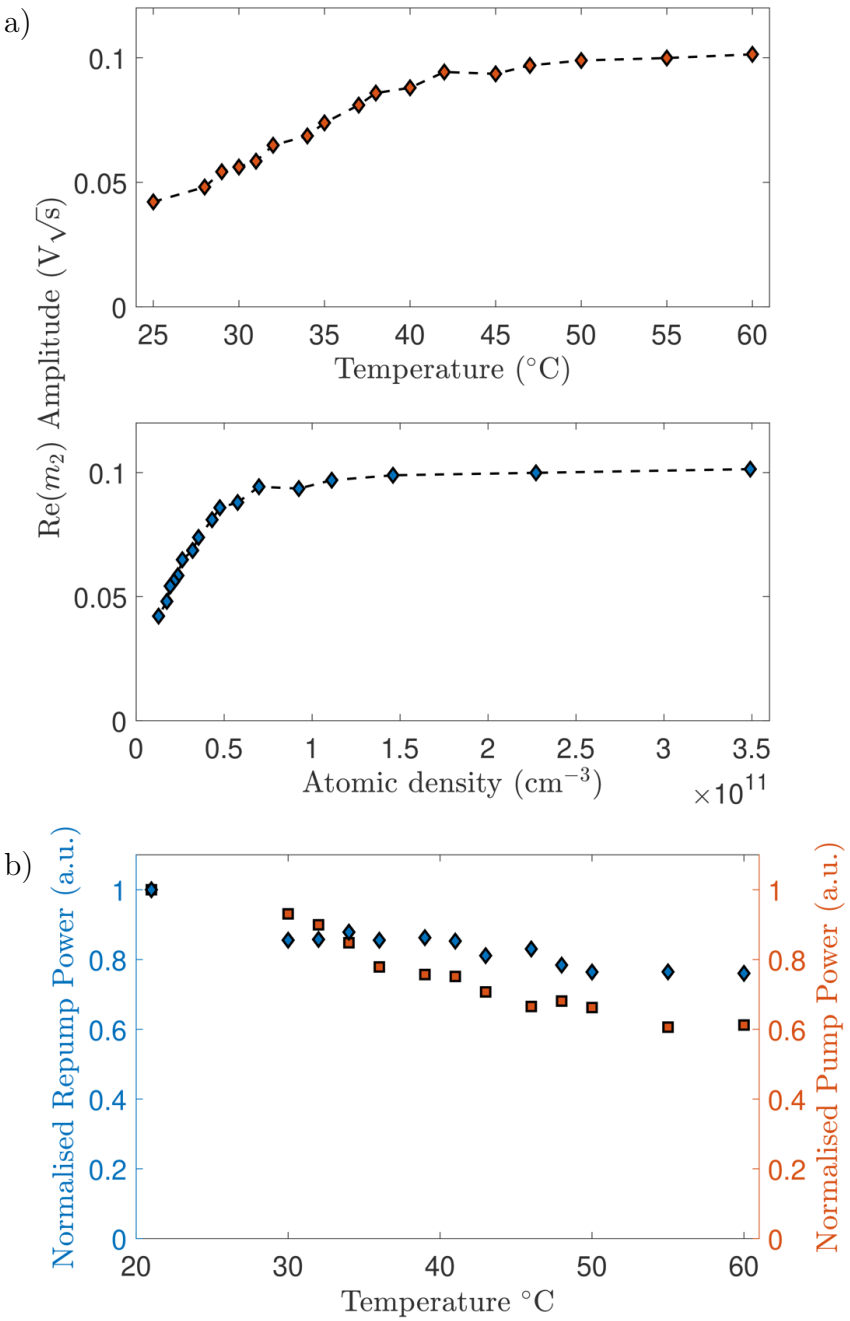

Figure 5.6: a) Re(m_2)$\propto h_z$ amplitude as a function of temperature/atomic density. b) Normalised transmitted cell pump/repump power as a function of temperature of the cell.

Unfortunately, due to the fact that paraffin begins to melt around 60°C we were not able to explore the effects on the signal strength beyond that point. Furthermore,

there may be a number of additional reasons which may be limiting the improvement of the signal strength. As already mentioned, the effect of increasing the temperature results in an increased rate of collisions and the consequent increase in the rate of spin destruction. Additionally, the increase in temperature increases the atomic velocities, which in turn increase the relaxation rate due to the gradient fields, (see the discussion of the gradient fields on page 71). However, the temperature change in our experiment is small which means that the contribution of these effects is small. Another effect that should be considered is the change in the optical density as a function of temperature which is due to an increase in atomic density. Given that our pump/repump beams are on resonance, the increase in optical density would result in the beam attenuation across the medium, especially because our cell is long ($l = 106$ mm). As a result, the increase in atomic density would not necessarily result in an increase of signal strength because the pump/repump beams do not have a sufficient power to pump all of the atoms. Indeed, monitoring the transmitted output power of the pump and repump beams at the output as a function of the temperature of the cell shows significant effects of absorption, see Fig. 5.6 b) on page 135. To address this, a counter-propagating pump/repump beams could be used to pump the medium more efficiently or indeed a shorter cell.

5.1.3 3D Vector Mapping and Noise

3D Vector Mapping. The theoretical models outlined in Chapter 2 predict what the response of the magnetometer should be to external magnetic fields. In all cases, but to a varying qualitative degree, the models suggest that the OPM response follows an approximate ovoid shape in the large external field range, i.e. $B_x^{\text{ext}} = B_y^{\text{ext}} \sim B_{\text{sense}}^{+}$ (see pages 37 and 60 for reference). Recall that in the geometric model, the demodulated atomic response of each quadrature maps the field according to

$$h_x = \text{Re}(h_1) = \frac{1}{4}(3 - \cos 2\beta) \sin 2\alpha \sin 2\theta, \tag{5.2}$$

$$h_y = \text{Im}(h_1) = \frac{1}{2} \cos\alpha \sin 2\beta \sin 2\theta, \tag{5.3}$$

$$h_z = \text{Re}(h_2) = -\frac{1}{4}\left((3 - \cos 2\beta)\cos^2\alpha + 2\cos 2\beta\right)\sin^2\theta, \tag{5.4}$$

where

$$\alpha = \arctan\left(\frac{-B_y^{\text{ext}}}{B_z'^{\text{ext}}}\cos(\beta)\right), \tag{5.5}$$

$$\beta = \arctan\left(\frac{B_x^{\text{ext}}}{B_z'^{\text{ext}}}\right). \tag{5.6}$$

To obtain the magnetometer vector response, we set the longitudinal field $B_z'^{\text{ext}} = B_{\text{sense}}^{+} + B_z^{\text{ext}} = B_{\text{res}} + B_\rho + B_z^{\text{ext}}$ and scan the transverse fields B_x^{ext} and B_y^{ext} sequentially with a linear field ramp and demodulate the corresponding signal quadratures $m_k \propto g_{\text{el}} h_k$. Fig 5.7 shows the results at $\omega_{\text{rf}} = 2\pi \times 90$ kHz dressing frequency. From

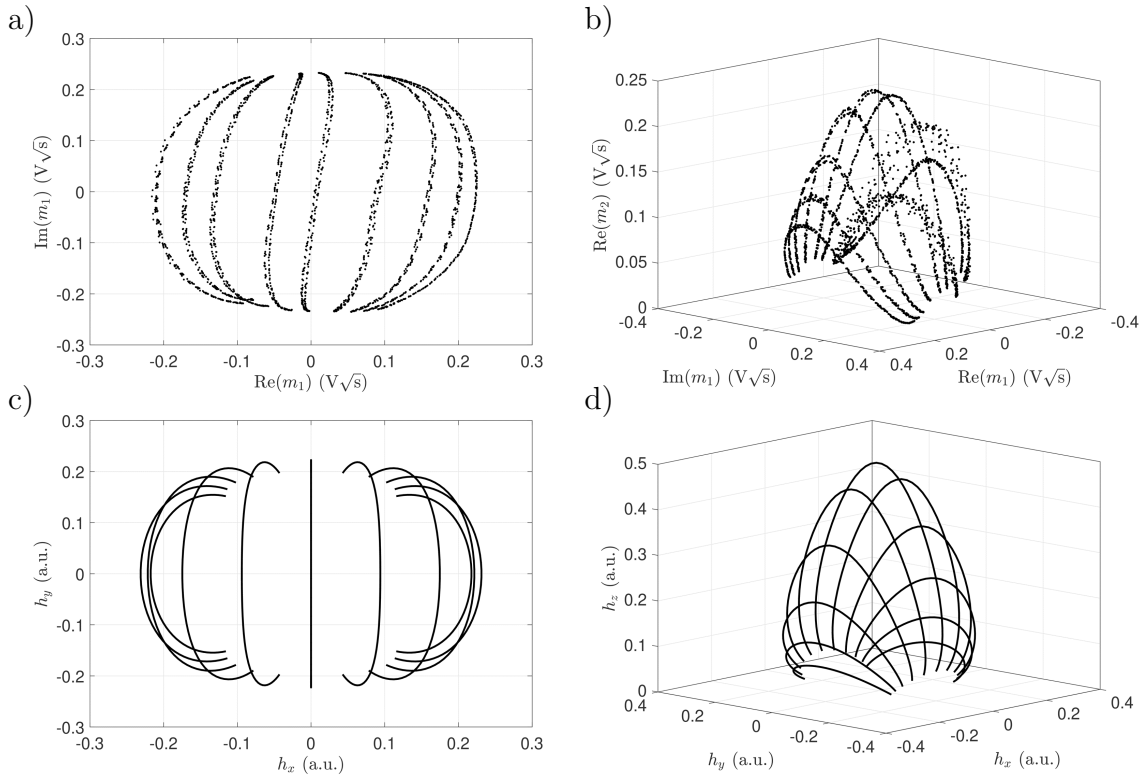

Figure 5.7: Atomic response to external magnetic fields. Here a) shows the experimental transverse field quadrature response at ω_{rf} frequency as a function of transverse fields B_x, B_y and constant B_z. b) Shows full 3D experimental response of the mode amplitudes m_1 and m_2. c) and d) is the theoretical response calculated according to the theory based on the geometric model equations (3.43)-(3.45) on page 37. The additional noise apparent in some of the lines are due to the fact that the repump laser was temporarily out of lock affecting the state preparation process.

the figure, we can observe that the experimental results in the unshielded case confirm our theoretical predictions of the ovoid response. The slight distortion of the 2D ovoid characterised by tilted lines are most likely due to imperfect demodulation phase adjustment between the transverse field quadratures resulting in imperfect quadrature orthogonality. Moreover, the ovoid profile does not appear to possess the same level of asymmetry/distortion as predicted by the Heisenberg model (see page 60 for plot details). This is due to the fact that the distortion effects on the ovoid shape have a much stronger influence for lower rf-dressing fields as well as rf-amplitudes (e.g. unshielded experimental rf-dressing field is at $\omega_{\text{rf}} = 2\pi \times 90$ kHz with $\Omega_{\text{rf}} = 10$ mG whilst in the simulation we have $\omega_{\text{rf}} = 2\pi \times 5$ kHz with $\Omega_{\text{rf}} = 0.25$ mG). This can be explained more intuitively using the geometric model; the effective field angles α and β, which map the transverse fields, are much larger for low rf-dressing frequencies because the Larmor resonance field and furthermore the sensitive field point B^{+}_{snese} depend on the rf-dressing frequency. As a result, any geometric beam misalignment

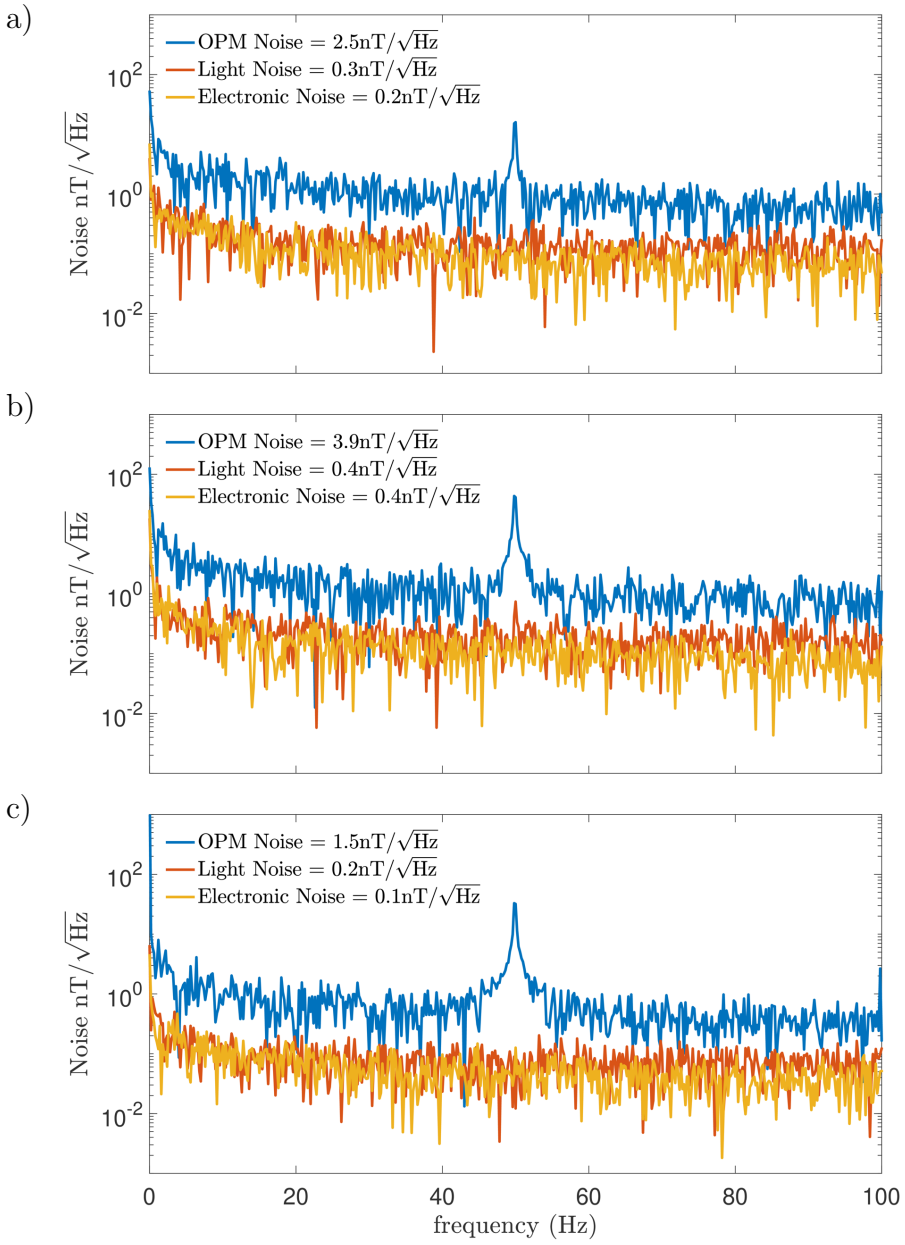

Figure 5.8: OPM Noise at room temperature 21°C with 90 kHz radio-frequency dressing. The noise estimate is done in the range 1−45 Hz. a) and b) convey the noise spectrum of the transverse field quadratures B_x and B_y respectively. c) measures the noise of the longitudinal direction corresponding to the B_z field. In all cases the atomic noise is above the shot noise and electronic noise limit. The light noise is obtained by detuning the laser well off-resonance ($\Delta > 10$ GHz) and measuring the corresponding demodulated signals. For the electronic noise, the noise is obtained by additionally blocking the probe light incident upon the balanced photodetector.

may result in larger imperfections in field mapping manifesting into field leakage and non-linear distortion in the field mapping. In both cases, the scanned field range is the same, and as can be seen from the figure, the transverse field quadratures have a near identical field response indicating similar field sensitivity. The magnitude of the field response in the B_z field quadrature also has the same range of response.

Unshielded Noise Performance. Measuring noise is one of the key performance indicators of the magnetometer. To perform the noise measurements we detune the static B_z field to $B_z = B^{+}_{\text{sense}}$, which optimises the magnetometer sensitivity for all three components. We then adjust the transverse fields such that the first harmonic signal vanishes. Based on the field calibrations described on page 126, we record field equivalent signal noise for the three field components. To measure the light noise, we block the pump and repump light and detune the probe beam such that no Voigt rotation is observed. We then measure the corresponding mode amplitudes m_k for the same duration and sampling frequency. The electronic noise is measured by further blocking the probe beam and recording the mode amplitude response. The noise amplitude spectrum is then computed according to eq. (4.32) (see page 122). However, in the unshielded case the probing happens across both the state preparation and probing regions, see Fig. 5.1 on page 129 for the sequence layout, this complicates the interpretation of the magnetometer bandwidth as well as the gain profile of the mode amplitude response function outlined on page 122. For all three quadratures, the noise level is around $\sim \text{nT}/\sqrt{\text{Hz}}$ in the range if $1-45$ Hz.

There are several limitations in OPM noise performance. First, the environmental noise, manifesting in gradient fields and other time dependent field phenomena not only affects the state preparation process, but also broadens the resonances of the OPM in the probe region - this ultimately reduces the overall sensitivity. In addition, because of the inherent environmental noise at the rf frequencies and a significant 1/f noise at low frequencies, the choice of the dressing field frequency had to be sufficiently large. This negatively impacts the sensitivity to transverse fields, because the geometric tilt of the quantisation axis as a result of external transverse fields becomes smaller and consequently, more difficult to measure. Note that due to the fact that the field control is PI regulated using an external fluxgate sensor, we may be inadvertently adding noise into the system. This is because the fluxgate has it's own noise floor which is fed into the servo loop of the PI regulated bipolar current source which then converts it into the field noise. As a result, this poses a limit on the level of field stabilisation and ultimately affects the OPM noise performance.

A way to improve the noise performance is to increase the temperature of the cell thus increasing the signal to noise ratio; however, as it has been shown in the previous section, there are temperature induced saturation effects which do not result in a significant improvement in the sensitivity. Due to a variety of technical reasons, it was not possible to explore the OPM parameter space well enough in order to really probe and understand the OPM response, let alone optimise it. More importantly, the various sources of noise and experimental imperfections, make it difficult in interpreting

the results and comparing them to the theory models, since a significant portion of the noise cannot be compensated for. In addition, due to the simplicity of the initial experimental setup, the precise control of various OPM parameters was not possible, e.g. pump duty cycle and phase, probe and pump pulse shaping and timing, OPM bandwidth control, to name just a few. This lack of control further hampered the degree to which we could experimentally test our theories (see Fig. 3.11 on page 62 for the OPM parameter space). As a result, these were major driving factors in motivating us to build a shielded OPM setup.

5.1.4 Dressed State Microwave Spectroscopy

In the ideal case, the theoretical magnetometer response outlined in Chapter 3 is produced using an equal statistic mixture of $|F = 2, m_F = \pm 2\rangle$ states which during the pumping and probing cycles is modified by the various physical processes such as the rf and static fields, collisions and other broadening mechanisms responsible for the decoherence of the state. These effects and their influence on the spin dynamics and the quantum state can be understood using the density matrix, which contains complete information about the quantum state. However, quantifying the prepared quantum state experimentally is difficult. As we saw in Chapter 3, subsection 3.3.8 on page 94 the coupling of a microwave field between the two hyperfine ground state levels enables the probing of the quantum state via the measurement of the Voigt effect. Scanning the frequency of the microwave field yields a microwave spectrum with features that are dependent upon the prepared state (see Fig. 3.27 on page 98 and onwards for the theoretical microwave spectra in different conditions). In this picture we explicitly assume that one of the ground states are empty, yielding a zero density matrix for $F = 1$ manifold. This becomes more complicated when the two hyperfine ground states are populated where the density matrices for each manifold are non-zero. Here the microwave field couples two different states making the interpretation of the resultant microwave spectrum even more difficult.

The experimental techniques and conditions used to produce the microwave spectra of the magnetometer follow the methods described in the Experimental chapter with a few additional modifications. There exists an extra step in the OPM sequence after the state preparation process where a microwave pulse is produced for a certain period typically for a millisecond duration followed by the probing sequence. The microwave field is generated by a home made dipole antenna resonant at the 6.834 GHz frequency to match the hyperfine ground state splitting of the $F = 1 \rightarrow F = 2$ transition. The dipole antenna is aligned along the z-direction coinciding with the direction of the static B_z field that is used to set the Larmor resonance. The radiating elements of the antenna are perpendicular to the rf-dressing field such that the corresponding magnetic field produced by the antenna is parallel to the x-axis with the electric field oscillating along the y-axis. The polarisation of the microwave field is composed of $\pi-$ and $\sigma^{\pm}-$ polarisations. The antenna is placed at a distance of < 1 cm from the cell to maximise the strength of the driving field. The static field is set on Larmor resonance $B_z = B_{\text{res}}$ to maximise the microwave signal strength. This is also the point

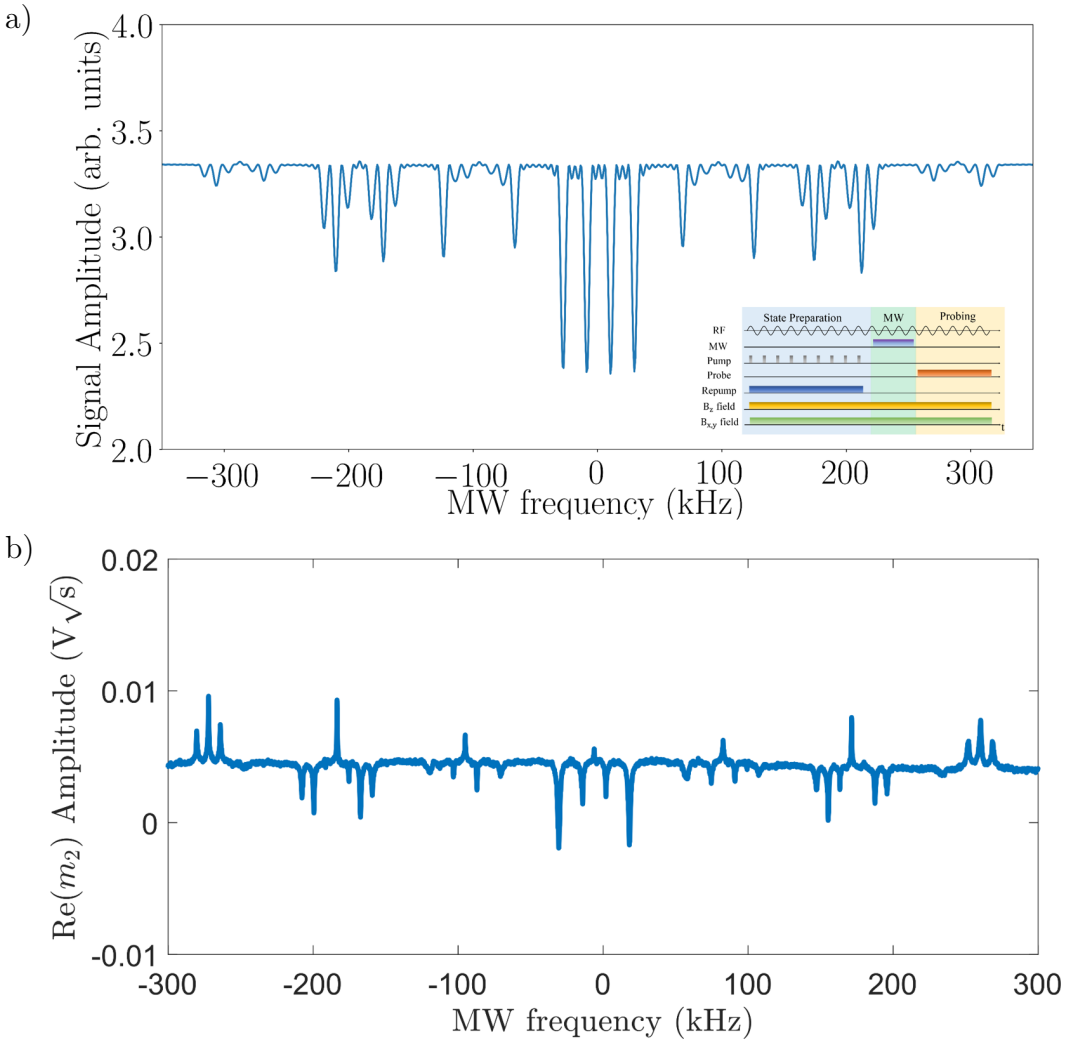

Figure 5.9: a) Theoretical, and b) experimental, dressed microwave spectra at $\omega_{\mathrm{rf}} =$ 90 kHz dressing frequency, on resonance $B_z = B_{\mathrm{res}}$, with synchronous pumping, cw repump and mw measuring the Voigt effect at Re(m_2) quadrature. The probe addresses $F = 2 \rightarrow F' = 1$ transition with a detuning of $\Delta \approx -500$ MHz. Here the MW frequency refers to the MW frequency detuning from the clock transition $|F = 1, m_F = 0\rangle \rightarrow |F = 2, m_F = 0\rangle$.

where theoretically the prepared state is close to the ideal input state, see Fig. 3.20 on page 84 for reference. The microwave field is then scanned and the corresponding Voigt effect of the demodulated mode amplitude Re(m_2) measured. Figs. 5.9, 5.10 5.11 and 5.12 show the results of microwave spectra in different state preparation and probing conditions.

From the experimental microwave spectra we observe that to a good approxima-

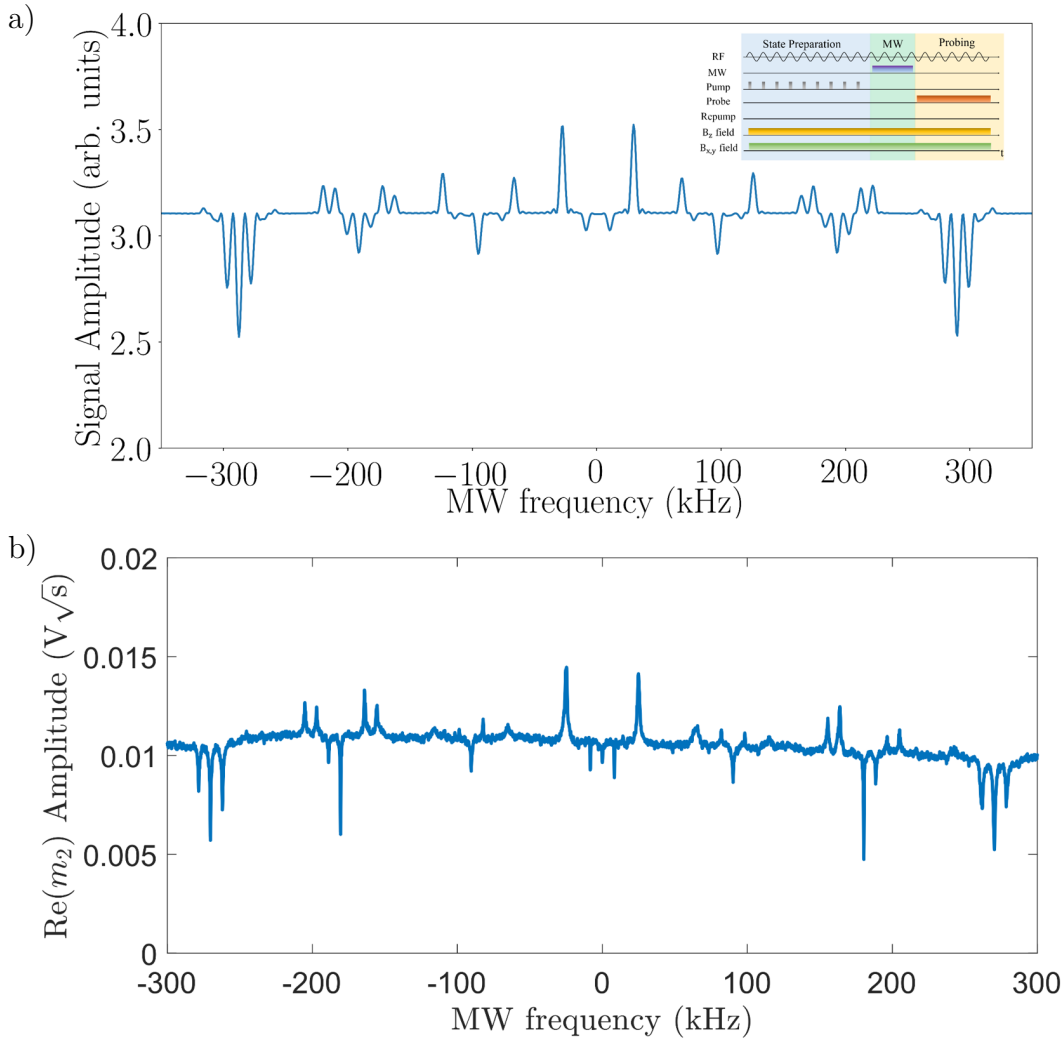

Figure 5.10: a) Theoretical, and b) experimental, dressed microwave spectra at $\omega_{\mathrm{rf}} = 2\pi \times 90$ kHz dressing frequency, on resonance $B_z = B_{\mathrm{res}}$, with synchronous pumping, repump off and cw mw measuring the Voigt effect at Re(m_2) quadrature. The probe addresses $F = 2 \rightarrow F' = 1$ transition with a detuning of $\Delta \approx -500$ MHz. Here the MW frequency refers to the MW frequency detuning from the clock transition $|F = 1, m_F = 0\rangle \rightarrow |F = 2, m_F = 0\rangle$.

tion, the addition of the repump beam inverts the peaks/troughs of the microwave spectra when compared to the mw-spectrum without the repumping beam. The absence of the repump beam, results in a thermal distribution of populations of the Zeeman sublevels in the $F = 1$ manifold containing a ≈50-75% fraction of the total population. Probing the $F = 2$ manifold to obtain the mw spectrum and comparing it to the theoretical spectra we find a good qualitative agreement between the spectra with repump beam off reproducing key spectral features. However, the microwave

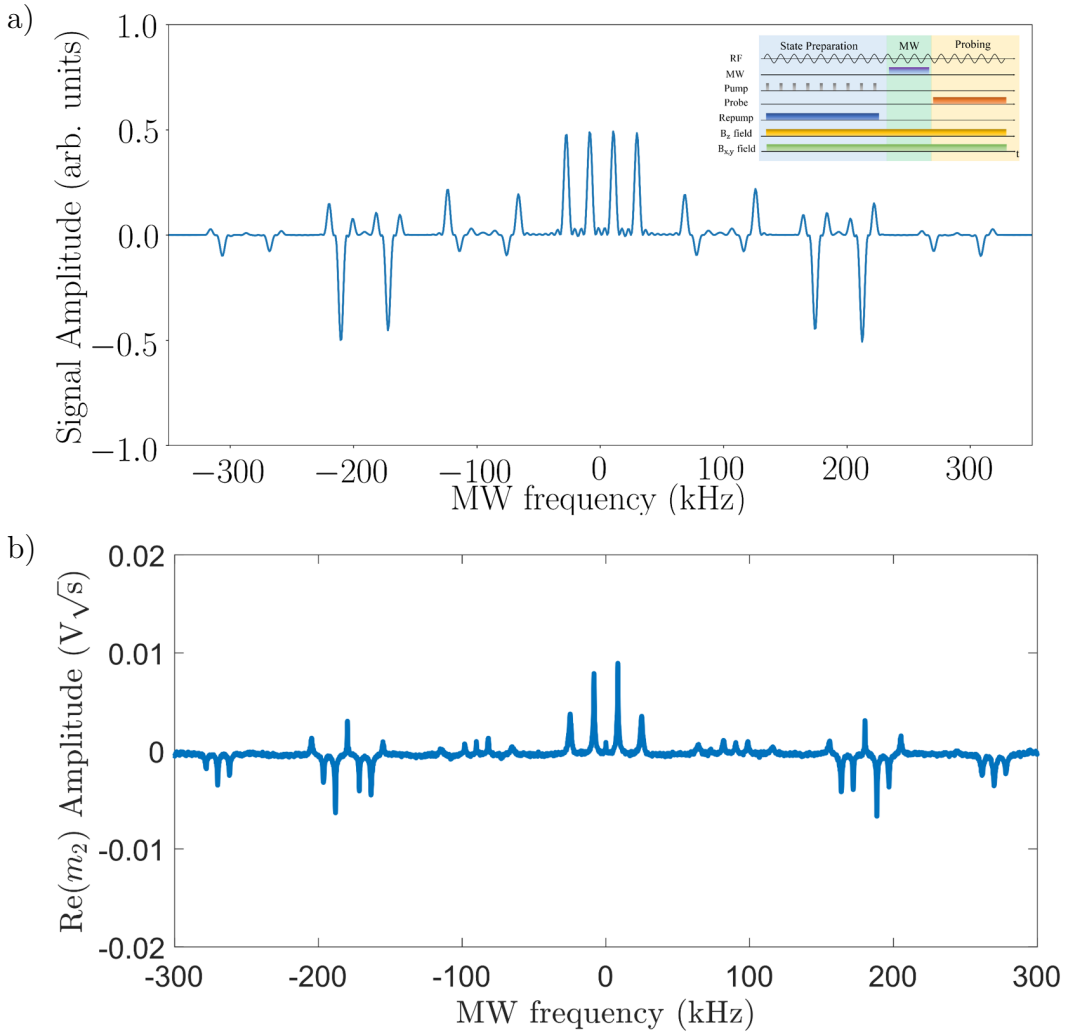

Figure 5.11: a) Theoretical, and b) experimental, dressed microwave spectra at $\omega_{\text{rf}} = 2\pi \times 90$ kHz dressing frequency, on resonance $B_z = B_{\text{res}}$, with synchronous pumping, cw repump and mw measuring the Voigt effect at Re(m_2) quadrature. The probe addresses $F = 1 \rightarrow F' = 1$ transition with a detuning of $\Delta \approx -500$ MHz. Here note that the Voigt effect signal amplitude is centered around zero, this is because the ground state $F = 1$ is in a thermal state which has no linear birefringence. Here the MW frequency refers to the MW frequency detuning from the clock transition $|F = 1, m_F = 0\rangle \rightarrow |F = 2, m_F = 0\rangle$.

spectra obtained with the repump on don't share many spectroscopic features. One of the reasons to explain this discrepancy is that the theoretically-computed state after the pumping sequence differs from the steady state reached during the experimental pump cycle. In addition, the appearance of peaks and troughs in the experimental microwave spectra with the repump on suggests that perhaps the repump is not

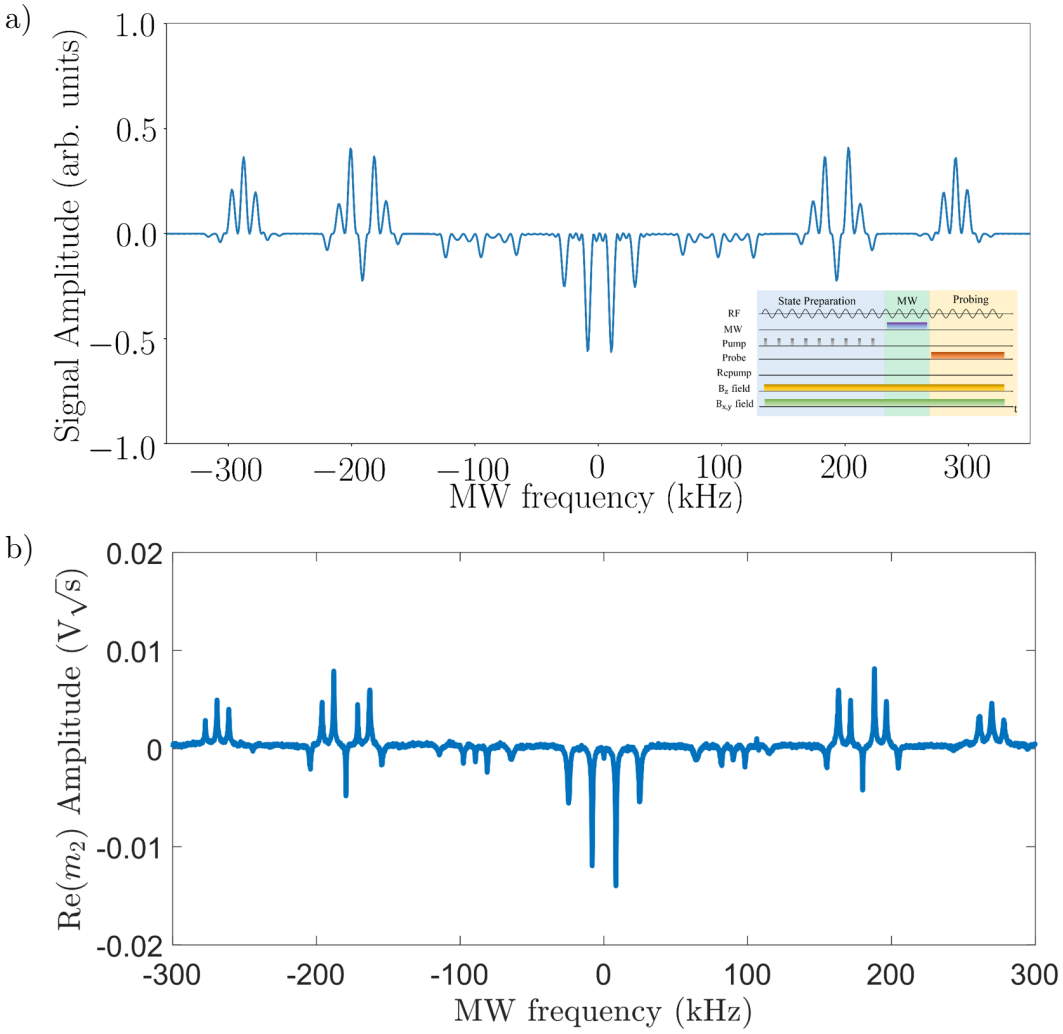

Figure 5.12: a) Theoretical, and b) experimental, dressed microwave spectra at $\omega_{\mathrm{rf}} = 2\pi \times 90$ kHz dressing frequency, on resonance $B_z = B_{\mathrm{res}}$, with synchronous pumping, repump off and cw mw measuring the Voigt effect at $\mathrm{Re}(m_2)$ quadrature. The probe addresses $F = 1 \rightarrow F' = 1$ transition with a detuning of $\Delta \approx -500$ MHz. Here note that the Voigt effect signal amplitude is centered around zero, this is because the ground state $F = 1$ is in a thermal state which has no linear birefringence. Here the MW frequency refers to the MW frequency detuning from the clock transition $|F = 1, m_F = 0\rangle \rightarrow |F = 2, m_F = 0\rangle$.

efficient enough to depopulate the ground state $F = 1$ manifold which means that some of the populations in the $F = 2$ manifold increase.

Fig. 5.13 shows the result of pulsed microwave spectrum probing the $F = 2$ ground state manifold of the $\mathrm{Re}(m_2)$ quadrature of the Voigt effect. Here the microwave field

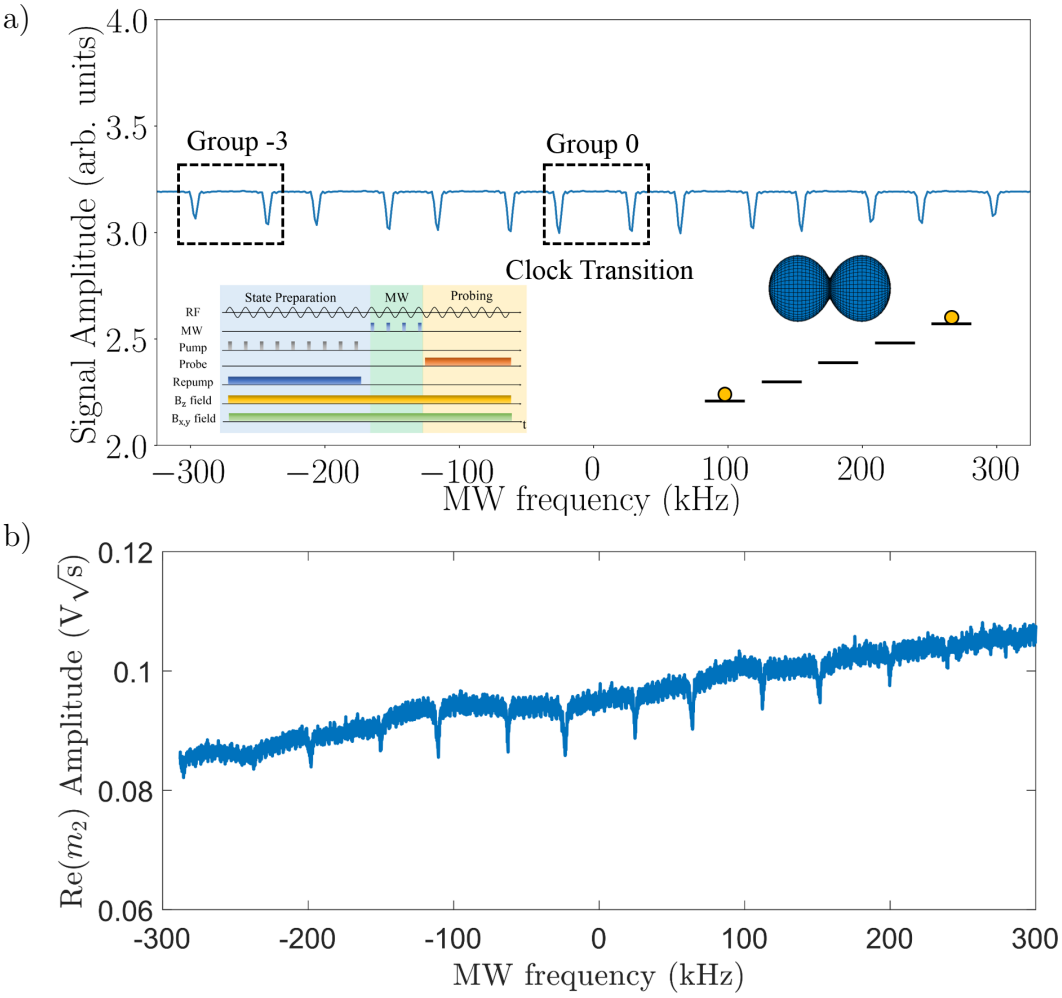

Figure 5.13: a) Theoretical, and b) experimental, dressed microwave spectra at $\omega_{\mathrm{rf}} = 2\pi \times 90$ kHz dressing frequency, on resonance $B_z = B_{\mathrm{res}}$, with synchronous pumping, cw repump and synchronously pulsed mw with 10% duty cycle and in phase with the rf-dressing field measuring the Voigt effect at Re(m_2) quadrature. The probe addresses $F = 2 \rightarrow F' = 1$ transition with a detuning of $\Delta \approx -500$ MHz. Here the MW frequency refers to the MW frequency detuning from the clock transition $|F = 1, m_F = 0\rangle \rightarrow |F = 2, m_F = 0\rangle$.

is pulsed with the same duty cycle of 10% and in phase with the radio-frequency dressing field. Here the experimental stroboscopic microwave spectrum shows only two peaks per group, which lie on the two extreme edges. This is consistent with the theoretical calculations indicating that the majority of the populations reside in the Zeeman sublevels of the $|F = 2, m_F = \pm 2\rangle$ mixed state thus confirming that our state preparation process works. This methodology can be extended to the radio-frequency dressed Faraday measurements to map the state population profile.

The theoretical and experimental results presented on the dressed microwave spectra are far from complete and require significant future work. Firstly, we have not explored what happens to the mw spectra when the state is prepared on the sensitive field point $B_z = B^+_{\text{sense}}$ where the OPM acts as a full vector magnetometer. The density matrix analysis in Fig. 3.21 on page 85 suggests that a significant proportion of the total population reside in the $|F = 2, m_F = 0, \pm 1\rangle$ sublevels. In addition, we talked about how the mw-spectrum could be used to track the evolution of the state by obtaining the microwave spectra by probing the system at different times. The presence of external sources of noise in the unshielded setup are of nuisance and are responsible for a variety of broadening mechanisms which affect the state preparation process, decoherence etc. Dressed microwave spectroscopy in magnetically shielded conditions would provide a cleaner and more controlled environment improving the quality of the results.

5.2 Shielded Operation

The experimental results obtained in the unshielded magnetometer setup have confirmed our main hypothesis of being able to measure three dimensional vector fields with a single-beam axis geometry via radio-frequency dressed linear birefringence of the atomic medium. However, many questions remained unanswered regarding its characteristics as a function of its vast parameter space and crucially the noise performance. These reasons provided great impetus to build and develop a new magnetometer setup with a flexible and robust laser system with precise and high resolution pulse timing control and data acquisition hardware in a low magnetic field noise environment. The key advantage of the magnetically shielded setup is that it enables the creation of a comparatively noise-free system where the various limitations and scope of the magnetometer performance could be understood. This allowed us to test our theoretical models as well as optimise the sensitivity of the OPM. For further reference of the shielded system, refer to Chapter 4.

5.2.1 Voigt effect signal and quadrature responses

The experimental setup and sequence procedures to measure the Voigt effect were outlined in the Experimental Apparatus chapter (see page 109 for example). The raw balanced Voigt effect signals with the corresponding power spectral density of the trace are shown in Fig. 5.14. Here a 5 kHz radio-frequency field is used to dress the atoms with an rf-field amplitude of $\lessapprox$0.1 mG. The choice of the dressing frequency is small compared to the unshielded setup such that the field sensitivity in the transverse field directions are maximised. The dressing field effects will be discussed in the follow-up sections. As can be seen from the figure, the raw atomic signal decays due to a finite state lifetime. In the shielded case, this is predominantly limited by the atom-atom and atom-wall collisions as well as the absorption induced decay of the probe beam. In our case, the limiting factor on the cell lifetime is dominated by the exchange of

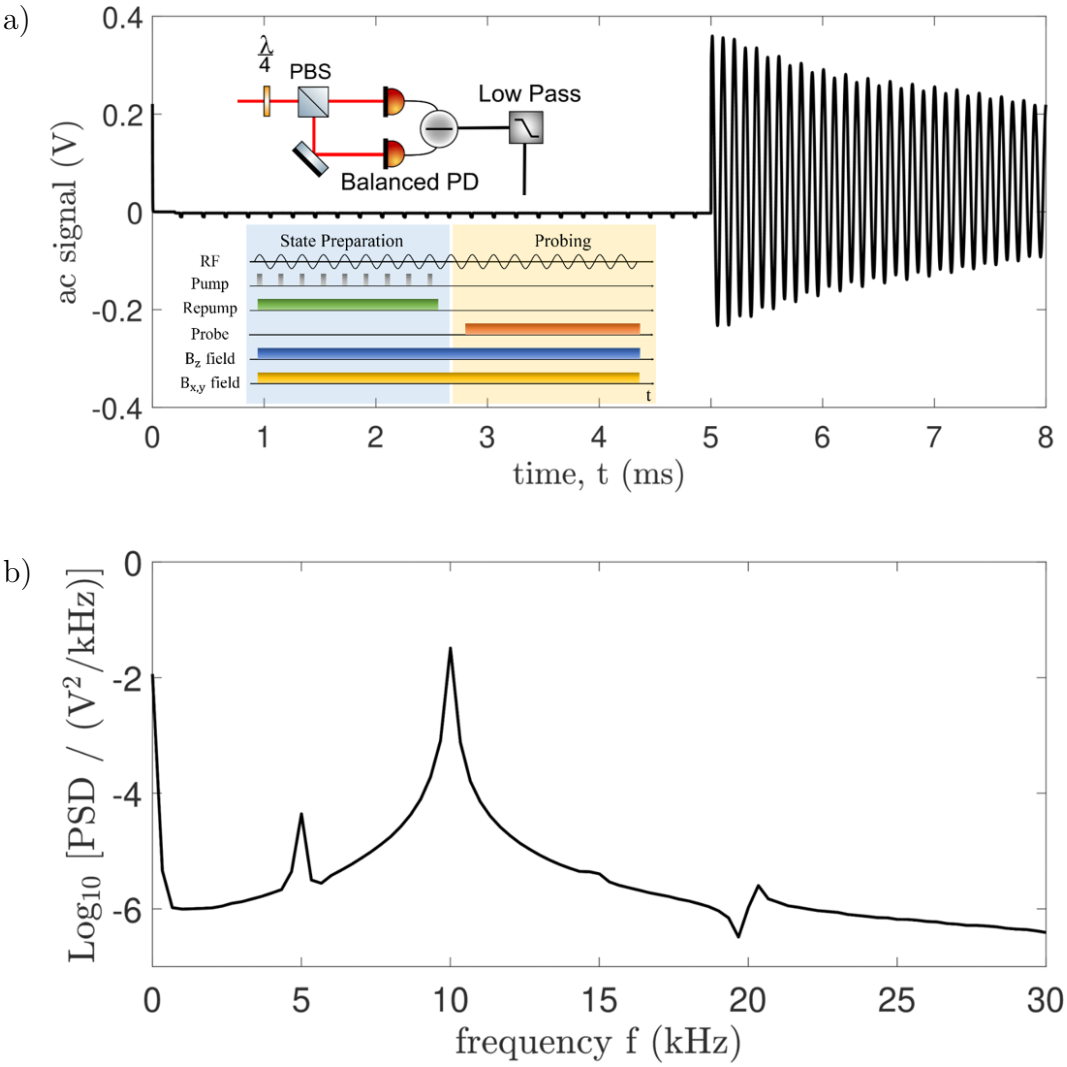

Figure 5.14: Typical experimental signals. a) Raw balanced signal of the Voigt rotation. The state preparation occurs within the first 5 ms of the cycle followed immediately by a 3 ms probing pulse. b) Single-sided, power spectral density (psd) of the amplified signal during the probe pulse. Atomic signals arise at ω_{rf} and $2\omega_{\mathrm{rf}}$. Weak harmonics at $3\omega_{\mathrm{rf}}$ and $4\omega_{\mathrm{rf}}$ can also be observed, which may arise due to non-linear magneto-optical effects [88] and non-linearities in the electronic detection path.

atoms between the main body of the cell and the stem with the Rb reservoir. A longer L-shaped stem with a capillary or a lockable stem mechanism would in principle increase the finite state lifetime by restricting the exchange between the pump and the unpumped atoms [87]. Due to the fact that the atomic exchange is the dominant factor of the cell lifetime, it is difficult to assess the quality of the anti-relaxation coating.

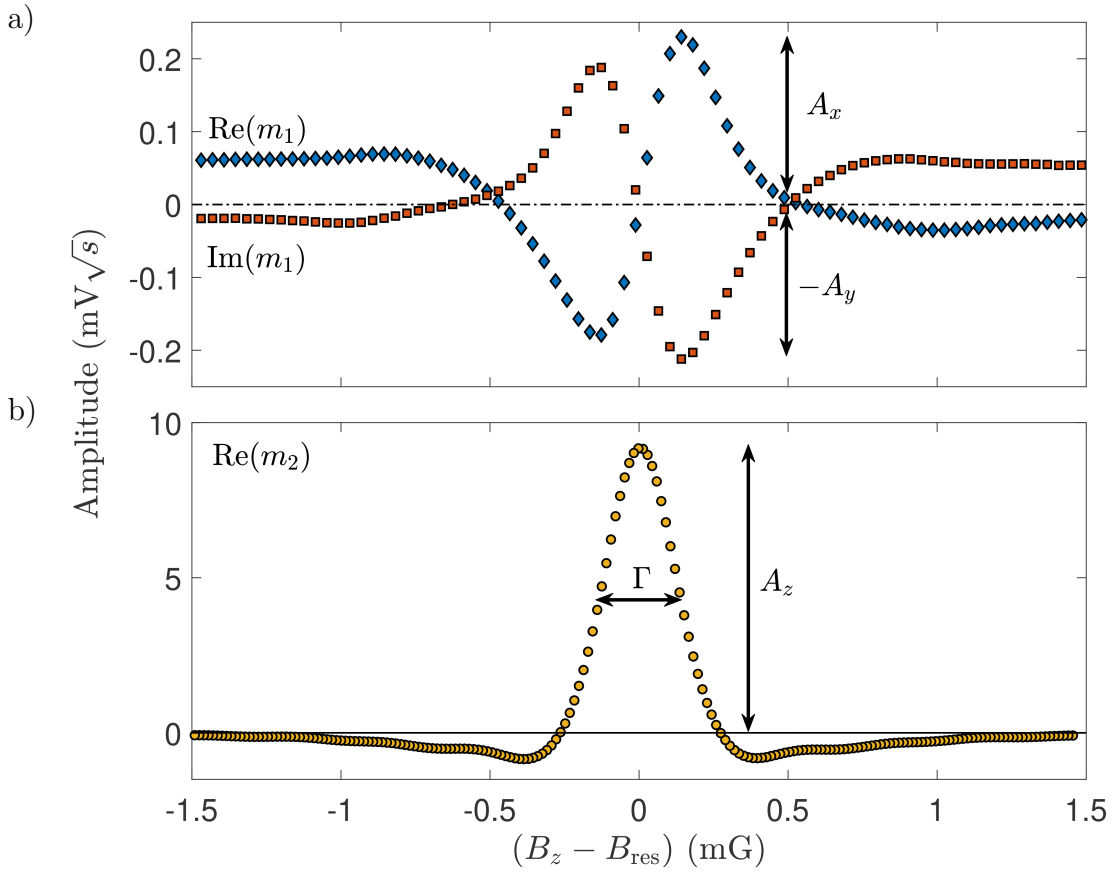

Figure 5.15: Experimental magnetometer response. Panels a) to b) show the three relevant quadratures of the mode amplitudes m_1 and m_2, i.e. responses at frequencies ω_{rf} and $2\omega_{\mathrm{rf}}$, for a scan of the longitudinal field B_z across the rf resonance. Here, non-zero transverse fields B_x and B_y are kept constant. The mode amplitudes, extracted according to Eq. (4.20) on page 120, follow the predicted behaviour, see Eq. (3.32) on page 34.

The Voigt rotation spectrum is taken near Larmor resonance with the transverse fields around zero. The power spectral density of the probing window (indicated in the figure) reveals a presence of a strong $2\omega_{\mathrm{rf}}$ resonance with a small ω_{rf} resonance. These code the external field information. As we can see in the spectrum, there exist additional harmonic frequencies of the dressing field at $3\omega_{\mathrm{rf}}$ and $4\omega_{\mathrm{rf}}$. A number of physical processes may be contributing to the existence of these harmonics, such as electronic non-linearities in the signal detection, additional non-linear magneto-optical effects as well as non-adiabatic ramp-up/down of the pumping and probing beams during the state preparation and probing stages, respectively [88]. The latter effects have impulse response profiles which increase the probability of higher harmonic excitation in the atomic dynamics.

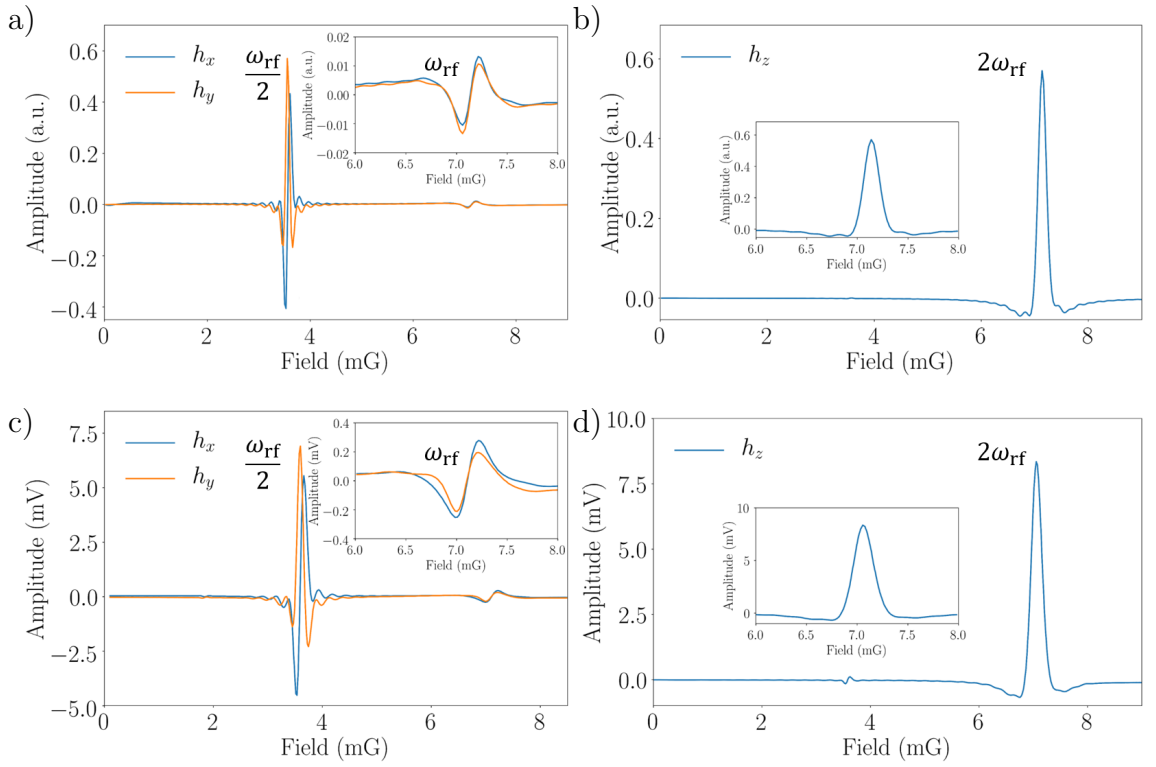

Figure 5.16: Theoretical and Experimental behaviour of the h_x, h_y and h_z quadratures as a function of the static B_z field. Here, a) and b) are the theoretical simulations compared to the experimental results obtained in c) and d). The pumping follows a square intensity profile with a 10% duty cycle at 5 kHz rf-dressing frequency in both the theoretical and experimental traces. After the system reaches a steady state in the pumping region, we switch the pump off and then probe the system as a function of static field B_z. The small insets show a more detailed structure of the h_x, h_y and h_z dispersive and Lorentzian quadrature responses as well as the experimental and theoretical sequences of state preparation and probing. Here the theory is based on the Heisenberg model approach outlined on page 58.

As before, if we scan the longitudinal B_z field around the Larmor resonance whilst simultaneously demodulating the signals at ω_{rf} and $2\omega_{rf}$ frequencies we obtain the signal amplitudes m_k which are proportional to the external magnetic fields, see Fig. 5.15. The demodulated signal amplitudes have dispersive and Lorentzian resonance profiles, which are consistent with the profiles predicted by our, Heisenberg and density matrix models (see pages 58, 79 for reference). From the figure we observe that experimentally obtained Lorentzian resonance profile posses wings that are consistent with the predictions given by the Heisenberg and the density matrix models. The geometric model does not predict magneto-optical resonance effects beyond the Larmor resonance. This is in contrast to the Heisenberg and density matrix models which show there are additional resonance phenomena predicted at $\omega_{rf}/2$ frequency field

value. This was investigated by sweeping the longitudinal magnetic field B_z from 0 to past the ω_{rf} resonance field and observing the demodulated response of each quadrature, see Fig. 5.16. As can be seen from the figure, the experimental OPM response agrees well with the theory. The $\omega_{\mathrm{rf}}/2$ response appears to be significantly larger in the ω_{rf} quadrature response than in $2\omega_{\mathrm{rf}}$ as well as the responses occurring at ω_{rf}. Unfortunately, the $\omega_{\mathrm{rf}}/2$ resonances are not of practical use for 3D vector magnetometry as they do not show the same linear response observed in the resonances at ω_{rf}. Both the experimental and theoretical results show ringing effects in the off-resonant regime. The ringing arises as a consequence of a fast switch-off/on (non-adiabatic) of the pump and the probe pulses, which become prominent closer to the resonances. The ringing vanishes when the probing is done in cw mode i.e. across the state preparation and probing regions.

5.2.2 Magnetometer characterisation in the shielded environment

Effects of RF power. The strength of the dressing field, which actively drives the atomic precession, has been predicted to decrease the signal scale factor as a function of increasing rf-field amplitude, see Fig. 3.12 on page 63. In the unshielded case the results showed that increasing the rf-field amplitude decreased the signal scale factor, consistent with the predictions. Fig. 5.17 shows the results in the shielded scenario. As can be seen from the figures, the general trend is that increasing the rf-amplitude, decreases the signal scale factor of the OPM in all field quadratures. This is due to the fact that the $2\omega_{\mathrm{rf}}$ resonance broadens reducing in amplitude and increasing in linewidth which results in a reduced sensitivity to the external fields. We also, see that there exists a maximum in the ω_{rf} field quadratures which is not coincident with the $2\omega_{\mathrm{rf}}$ resonance behaviour. In fact, in the experiments, as the rf-amplitude tends to a zero value, the dispersive profiles at ω_{rf} lose their characteristic dispersive shape and no longer map the transverse field information. This does not appear to be the case for the $2\omega_{\mathrm{rf}}$ resonance. There also appears to be a difference in the sensitivity of ω_{rf} quadratures. The most likely reason for this difference is the external offset fields present in the chamber. Typically, additional transverse fields are applied such that the demodulated field amplitudes are $m_{x,y} \approx 0$ on the sensitive field point B^{+}_{sense}. However, geometric misalignment between the probe and the rf-field can change the sensitivity between the quadratures where one quadrature readings become more sensitive than the other.

Effects of Pump Duty Cycle and Phase. As was shown by the results in the unshielded section, the state preparation process plays a crucial role in enabling sensitive magnetic field measurements. The train of pump pulses with a well defined duty cycle and phase relative to the rf-field affect the efficiency of optical pumping. The theoretical results considering these effects obtained on pages 66−67 predict a global maximum in sensitivity with a monotonically decaying profile as a function of duty cycle, while the relative phase harmonically modulates the amplitude of the

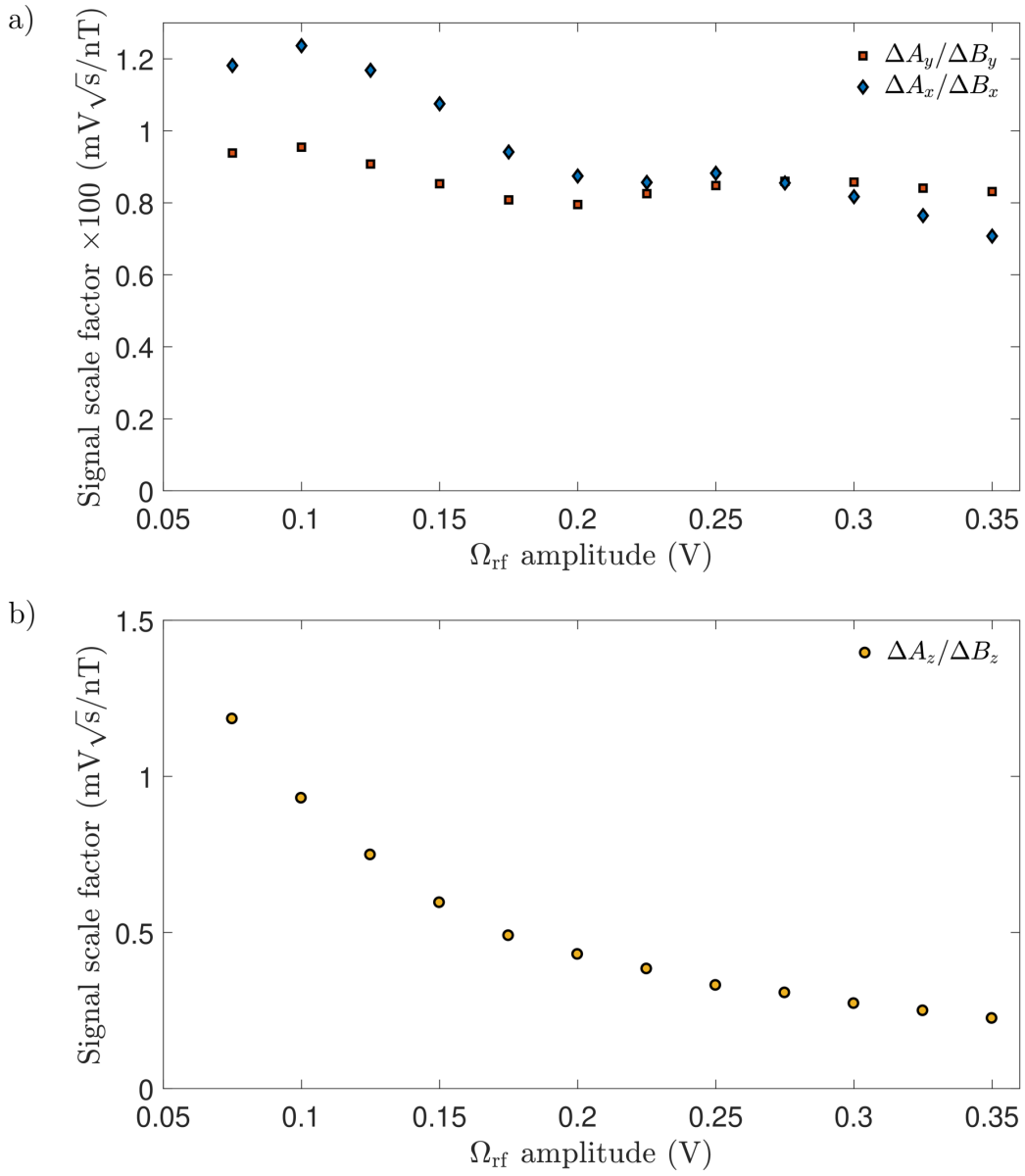

Figure 5.17: a) Signal scale factor of the ω_{rf} quadratures corresponding to m_x and m_y demodulated field signal scale factors. b) Signal scale factor of the $2\omega_{\mathrm{rf}}$ quadrature corresponding to m_z demodulated field signal scale factor. The signal scale factor is a quantity that should be maximised as it is proportional to the magnetometer's sensitivity to the external magnetic fields. Here the results are obtained at 5 kHz dressing frequency on the sensitive field point $B^{+}_{\mathrm{sense}} = B_{\mathrm{res}} + B_{\rho}$.

signal. The effects on the linewidth as a function of pump phase were only investigated qualitatively since the phase affects the overall profile of the dispersive and Lorentzian curves rendering it impossible to extract their linewidths. Nevertheless, where it is

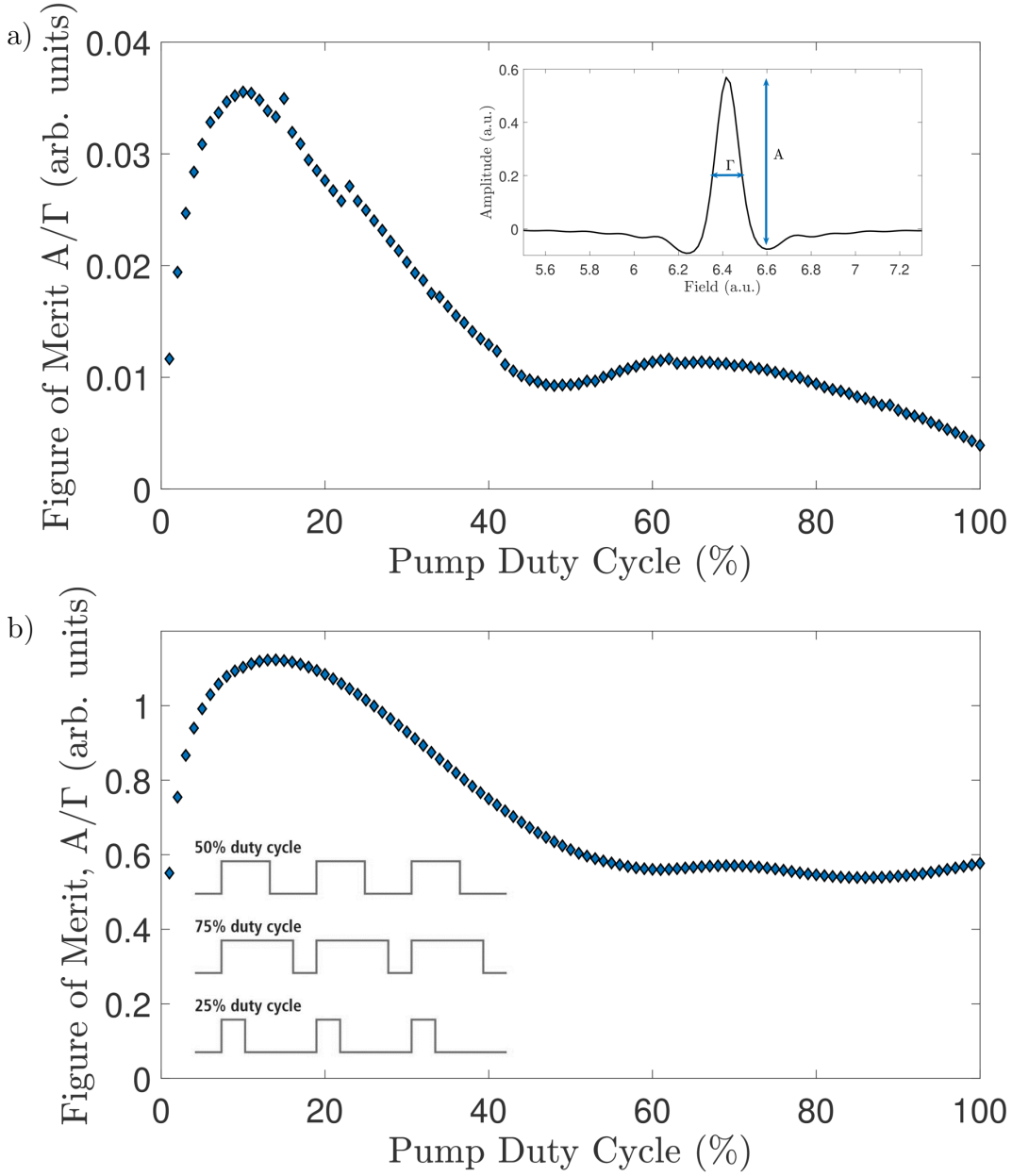

Figure 5.18: a) Experimental figure of merit of the Re(m_2) quadrature as a function of the pump duty cycle. The data shows a global peak at around 9% duty cycle with monotonically decreasing sensitivity and then a temporary revival. The pump pulses have a frequency ω_{rf} and are in phase with the rf-dressing field. Here the discontinuities in the data are due to the fact that they were taken over a long time period where thermal drifts begin to play a role in the fibre/AOM coupling etc. Here the results are obtained at 5 kHz dressing frequency. b) Theoretical figure of merit based on the Heisenberg model.

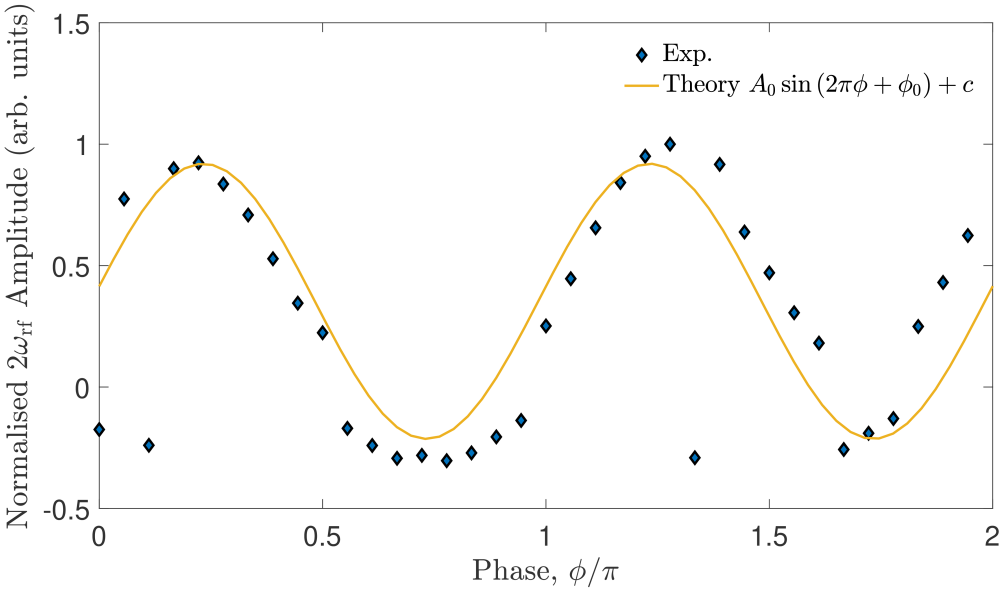

Figure 5.19: Normalised Re(m_2) amplitude as a function of the relative phase between the pump pulses and the rf-dressing field. Here we observe periodic behaviour consistent with the theoretical model. Here the results are obtained at 5 kHz dressing frequency.

possible to do the calculation, the linewidths of the dispersive and resonance curves increase with the increasing the phase difference and follows a harmonic profile consistent with the period observed in the amplitude vs phase results. The experimental results depicting the scale factor and amplitude response as a function of the pump duty cycle and phase respectively are shown in Figs. 5.18 and 5.19. Unfortunately, it was not possible to test the effects of different intensity profiles (e.g. triangular and sawtooth pump pulse trains) on the magnetometer response due to hardware limitations. As can be seen from the experimental results and the theoretical calculation on pages 66−67, the model is effective in describing the behaviour observed in the experiments. As can be seen from the figures, higher pump duty cycles and out of phase pumping reduce the magnetometer sensitivity and are not practical if sensitivity is an important factor. Moreover, the reduced sensitivity implies that the state we are pumping into is not an equal statistical mixture of the $|F = 2, m_F \pm 2\rangle$ states. An obvious technical drawback of synchronous pumping technique is the fact that most of the laser power is wasted due to a low duty cycle. One of the limitations of our theoretical models is that they do not take into account of pumping/probing effects of a Doppler broadened medium during the spin dynamics, which may result in non-trivial pumping mechanisms due to velocity-class-dependent pumping. Whilst these effects were considered in the light-matter interaction section, their effects were decoupled from the atomic spin dynamics. These simplifying assumptions may help explain some of the differences seen between the experimental data and the theory. However, an additional complexity arises due to the fact that we have a thermally broadened medium rendering more detailed and accurate calculations tricky to accomplish.

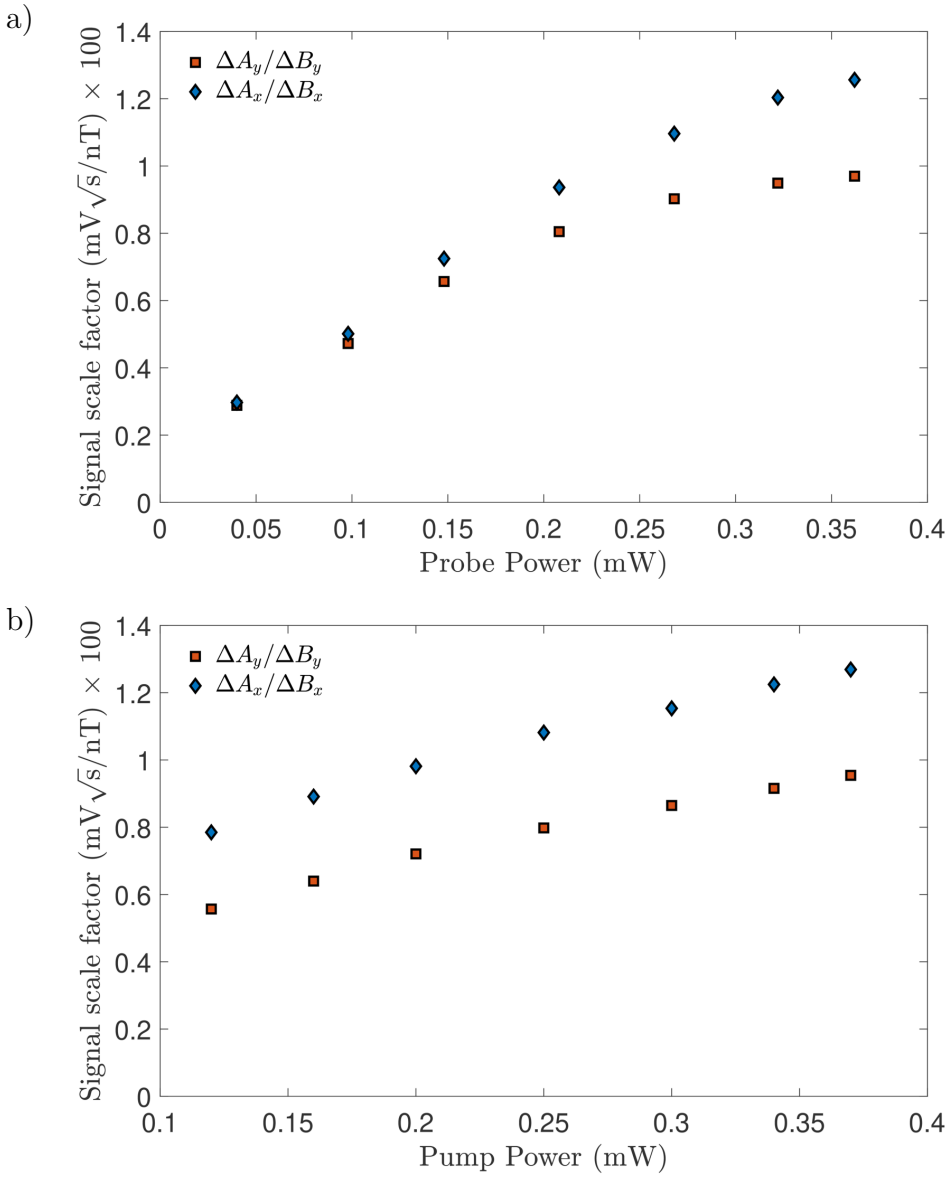

Figure 5.20: Signal scale factors as a function of optical powers for ω_{rf} quadratures. a) Signal scale factors $\Delta A_y/\Delta B_y$ and $\Delta A_x/\Delta B_x$ as a function of probe power. b) Signal scale factors $\Delta A_y/\Delta B_y$ and $\Delta A_x/\Delta B_x$ as a function of pump power. Here the results are obtained at 5 kHz dressing frequency on the sensitive field point $B^{+}_{\text{sense}} = B_{\text{res}} + B_{\rho}$.

Effects of Optical Power and Detuning. As mentioned already, our theoretical models do not take into account the various light-matter interaction effects such as power and detuning when modelling the magnetometer response. This is largely complicated by the fact that we have a Doppler-broadened medium. Nevertheless, it was still highly instructive to understand the effects of light power and detuning on

the magnetometer response qualitatively. Figs. 5.20 and 5.21 show the signal scale factors as a function of pump and probe powers for all three quadratures. Increasing the probe power increases both the ω_{rf} and $2\omega_{\mathrm{rf}}$ quadrature signal scale factors where at higher powers we observe potential saturation effects due to the fact that higher probing power increases the light scattering rate, which begins to have pumping effects affecting the state and consequently reducing the signal strength. Increasing the pump power for a fixed probe and repump power and detuning also increases the signal scale factor in all quadratures, however, it also begins to show saturation effects at higher powers. It is highly probable, that the major feature limiting the increase in signal strength scale factor is down to the rate of exchange of unpumped atoms between the cold finger and the cell. Additionally, the rate of atom-atom and atom-wall collisions will contribute towards the spin destruction processes, further affecting the final steady state during the pump cycle.

In our experiments the pump and repump beams have intensities $I \approx I_{\mathrm{sat}}$, where the pump/repump diameters are of the order of the size of the cell's diameter. This means that the pumping volume is near its maximum. Due to the free exchange between the unmpumped atoms in the cold finger and the body of the cell, it is not possible here to assess the quality of the anti-relaxation coating and its contribution to the spin destruction due to atom-wall collisions. The variation of the signal scale factor as a function of the repump power (not shown) is much less strong (due to a lower branching ratio of the optical transition from the excited states to $F = 1$ during the pump cycle); however, the absence of the repump reduces the signal scale factor by approximately a factor of 2 over the duration of the state preparation process. Experimentally, the pump and repump frequencies were generated using separate laser sources that were then coupled into the same polarisation maintaining fibre. As a result of this scheme, 50% of pump and repump powers were lost due to a non-polarising-beam-splitter which was used to combine the two beams. An easier and more practical solution would be to use a sideband-suppressed EOM to generate the repump from the pump beam [90]. Since the repump does not require much power, it would not only simplify the laser system, but also the make it more practical for miniaturisation purposes.

The light-matter interaction describing the Voigt effect assumes a far detuned probe where the effects of absorption can be ignored. The strength of this interaction is still dependent on the detuning from the atomic resonance which is given by the tensor polarisabilities (see page 14 for reference). The tensor polarisabilities predict the signal scaling as a function of the probe detuning, however, they do not take into account of the effects of Doppler broadening nor the absorption and light retardation effects. These become dominant for probe detunings close to the atomic optical resonance, but can be ignored for detuning $\Delta > \Gamma_D$, where Γ_D is the width of the Doppler valley. As a result it becomes difficult to know a priori for which choice of detuning the signal scale factor (or sensitivity) will be maximised, and whether the signal scale factors will all be equally maximised for the same detuning in the first place. Fig. 5.22 shows the results of the quadrature signal scale factors as a function of the probe detuning. The probe is scanned in steps of 50 MHz over nearly a 3 GHz

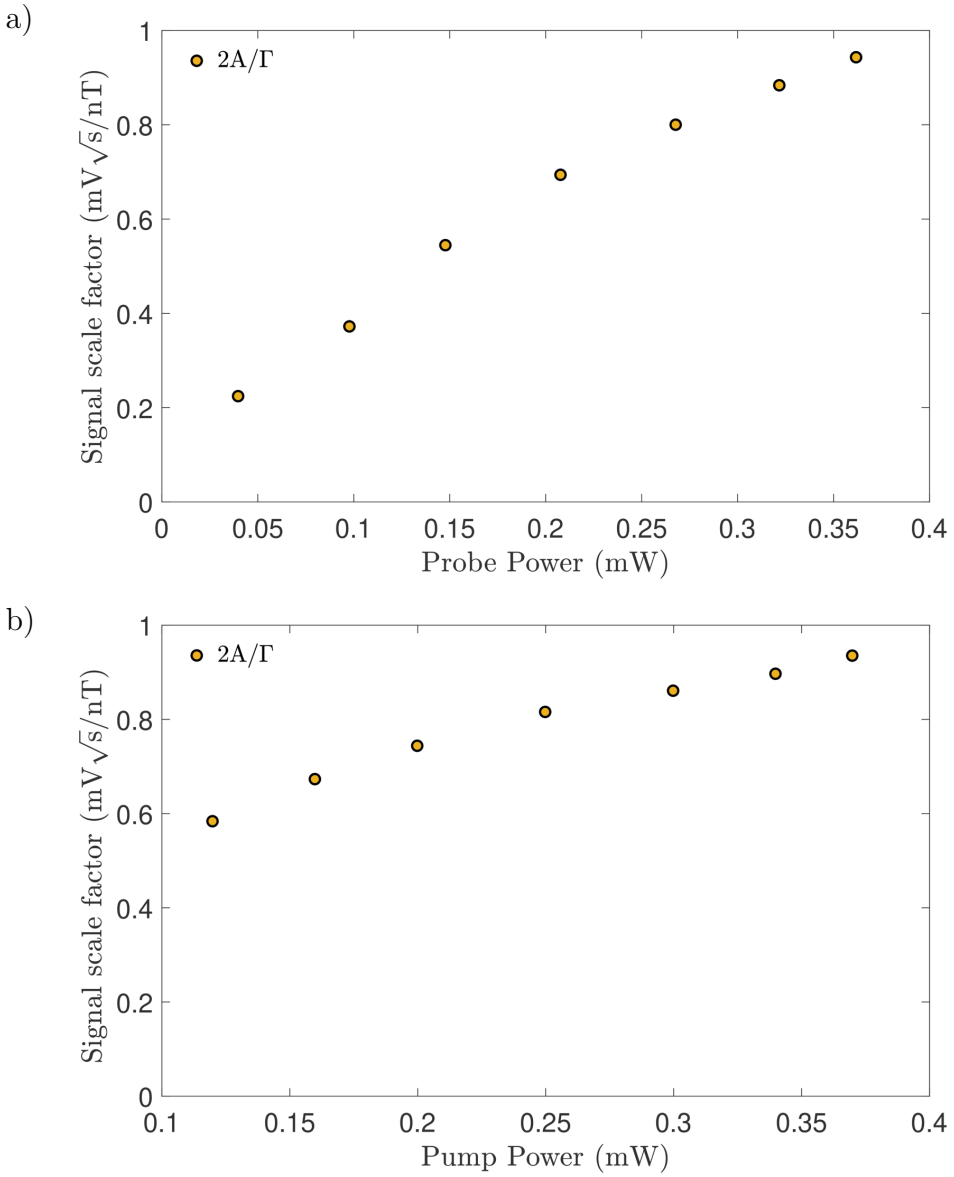

Figure 5.21: Signal scale factors as a function of optical powers for $2\omega_{\mathrm{rf}}$ quadratures. a) Signal scale factor of $\mathrm{Re}(m_2)$ as a function of probe power. b) Signal scale factor of $\mathrm{Re}(m_2)$ as a function of pump power. In all cases we observe that increasing optical power increases the signal scale factor which begins to saturate. Here the results are obtained at 5 kHz dressing frequency on the sensitive field point $B^{+}_{\mathrm{sense}} = B_{\mathrm{res}} + B_{\rho}$.

range and the resultant signal scale factors are obtained by scanning the longitudinal and transverse fields when the longitudinal field is set on the sensitive field point, B^{+}_{sense}. The results in the figure show that the signal scale factors are maximised for probe detuning values roughly being ± 550 MHz red/blue detuned from $|F = 2\rangle \rightarrow |F' = 1\rangle$

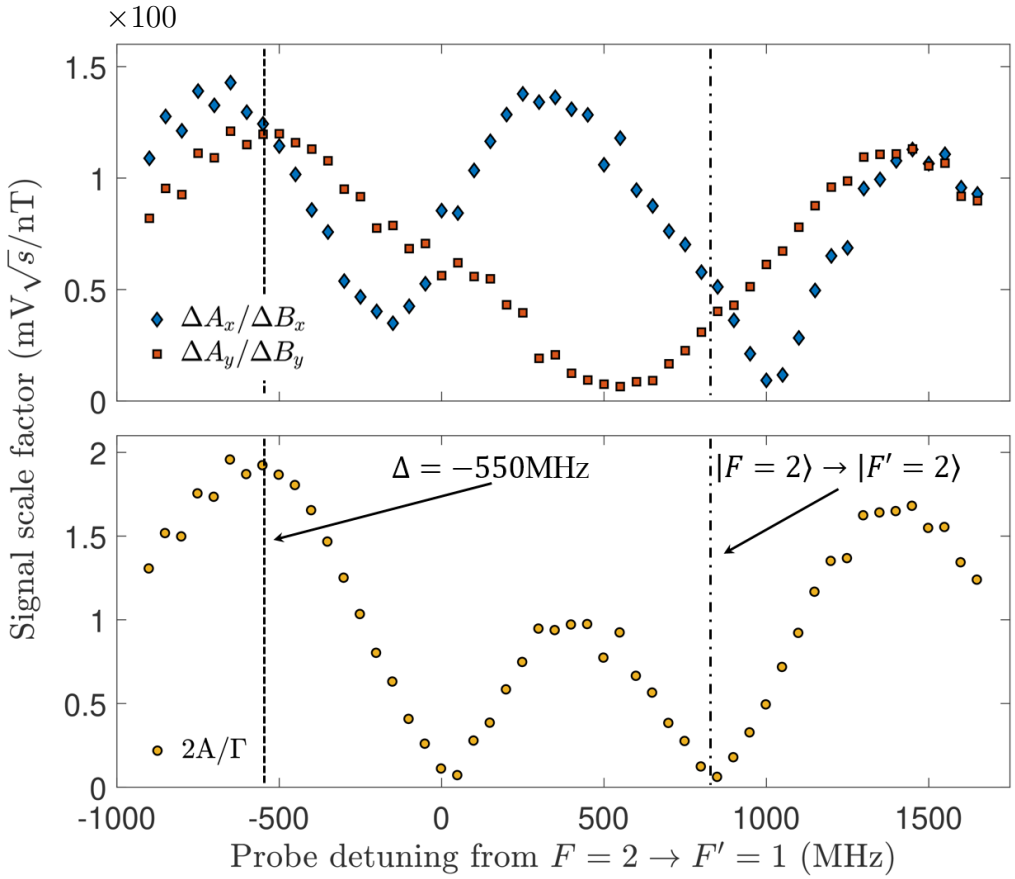

Figure 5.22: Experimental estimates for the three signal scale factors as a function of probe detuning. For the longitudinal field, this is the slope of the $2\omega_{\mathrm{rf}}$ resonance profile, estimated as $2A/\Gamma$. Near the chosen probe detuning of -550 MHz (dashed lines), all scale factors are close to maximal, and the first order responses to orthogonal external fields are orthogonal. Here the results are obtained at 5 kHz dressing frequency on the sensitive field point $B^{+}_{\mathrm{sense}} = B_{\mathrm{res}} + B_{\rho}$. The dash-dotted line indicates the $|F = 2\rangle \rightarrow |F' = 2\rangle$ transition for reference.

and $|F = 2\rangle \rightarrow |F' = 2\rangle$ transitions respectively with the former giving a slightly higher sensitivity. The signal scale factors reach minimal values on resonance to the atomic transitions. This is expected since the probe experiences significant absorption at detuning $\Delta \approx 0$, which begins to dominate the phase shifts introduced by the ac Stark effect and our theoretical model is no longer valid in effectively describing the physics. Moreover, as the detuning approaches the resonance transitions, i.e. $\Delta_{1,2} \rightarrow 0$ the field mapping to quadratures becomes no longer orthogonal, and as a result, a significant amount of field leakage is observed. Consequently, the magnetometer is no longer capable of mapping vector information. Coupled to this, the characteristic dispersive and Lorentzian profiles of the OPM as a function of the longitudinal B_z

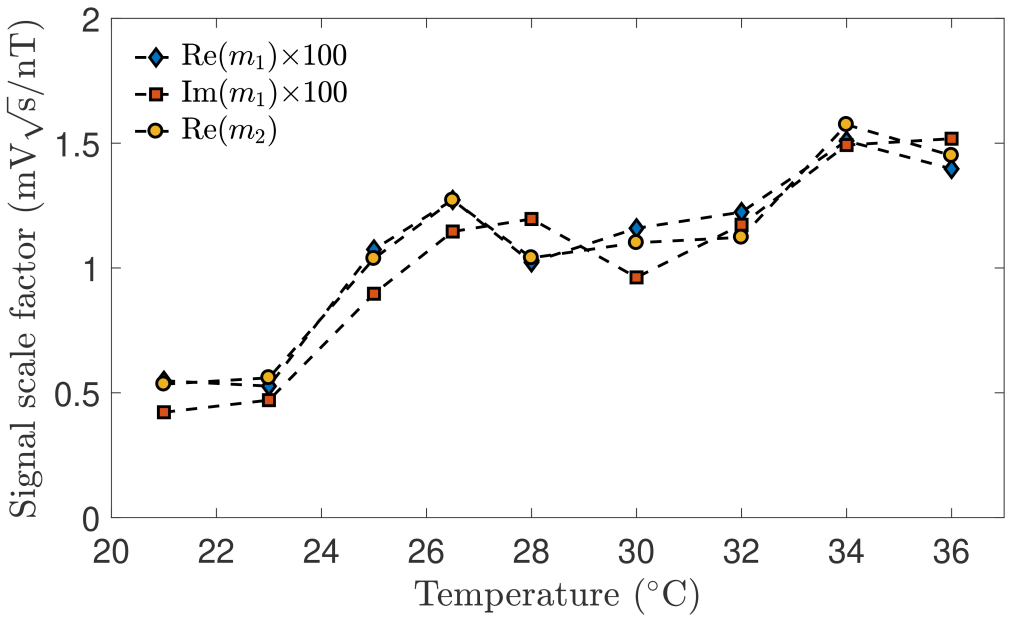

Figure 5.23: Signal scale factor as a function of the cell body temperature. The transverse field quadrature signal scale factors are multiplied by a factor of ×100 to put the signals on the same plot scale. The signal scale factors show a general positive correlation with respect to the cell body temperature. Here the results are obtained at 5 kHz dressing frequency on the sensitive field point $B^{+}_{\text{sense}} = B_{\text{res}} + B_{\rho}$.

field become highly distorted and no longer follow the theoretically predicted shapes, primarily due to the fact that the probe begins to act as a pump, redistributing the prepared state. Interestingly, we observe that the quadrature signal scale factors in phase with the rf-field, i.e. $\Delta A_x/\Delta B_x$ and $2A/\Gamma$ follow the same trend as a function of the probe's detuning whilst the out of phase quadrature signal scale factor $\Delta A_y/\Delta B_y$ does not. Recall that the equation describing the Voigt effect in the off resonance regime is given by

$$\left\langle \hat{S}_z^{\text{out}} \right\rangle = g_F^{(2)} S_y n_F \left\langle \hat{F}_x^2 - \hat{F}_y^2 \right\rangle, \tag{5.7}$$

where we have let

$$g_F^{(k)} = \frac{2g^2 \alpha_F^{(k)}}{c\hbar^{k+1}}, \tag{5.8}$$

which clearly indicates the the entire Voigt effect signal distributed over harmonics ω_{rf} and $2\omega_{\text{rf}}$ should scale identically with the detuning given by the tensor polarisability. However, as observed in Fig. 5.22, this is not the case for the out of phase quadrature, Im(m_1). In order to explain this, it is possible that the out of phase quadrature component acquires an additional detuning dependent factor which was not considered in the tensor polarisability component. The origin of this factor would arise as a consequence of the rf-dressing field which introduces in-phase and out-of-phase detuning dependent component in the dipole transition moment.

Temperature effects. The temperature effects on the signal scale factors were further investigated in the shielded conditions. Fig. 5.23 shows the results for all three quadratures. The heating of the cell was achieved by means of Joule heating using high-resistance, coated wire wrapped around the cell. After the cell reached thermal equilibrium, the heater would be switched off and the measurement taken. This is a suboptimal experimental situation since the cell begins to cool down during the measurement, which takes roughly 16 s. This made the measurements at higher temperatures unreliable due to a temperature gradient between the cell and the surrounding environment. According to eq. (5.7), the Voigt effect signal amplitude should scale linearly with the atomic density, whilst we see this in the unshielded environment data at low densities (see Fig. 5.6 on page 135) we do not see a clear linear relationship in the shielded case in Fig. 5.23. The stem of our relaxation coated cell, where most of the ^{87}Rb is kept, is very short and straight making the exchange of the unpumped atoms between the stem and the main cell body a very significant process as the temperature increases. This negatively impacts the contribution to the overall increase in signal to noise ratio because an increasingly large fraction of unpumped atoms begins to interact with the probe. To remedy this, a longer and L-shaped stem with a capillary would be a possible solution to this issue.

5.2.3 3D vector mapping and characterisation

A key feature of the Voigt magnetometer is its capability of mapping all three vector components of the magnetic field. The 3D vector response is achieved when the longitudinal magnetic field is set to $B_z = B_{\text{res}} + B_\rho$ which corresponds to the steepest slope of the $\text{Re}(m_2)$ resonance and maximum amplitudes of the $\text{Re}(m_1)$ and $\text{Im}(m_1)$ dispersive profiles. We map the magnetometer response at the sensitive field point by linearly scanning the transverse and longitudinal fields sequentially and measure the corresponding quadrature responses, see Fig. 5.24. As can be seen from the figure, for large external fields ($B^{\text{ext}}_{x,y,z} \approx B^{+}_{\text{sense}}$), the OPM response generates a characteristic ovoid shape consistent with the qualitative predictions given by both the Geometric and Heisenberg models (see pages 37 and 60 for reference). The full ovoid profiles display asymmetric distortion and offsets from $m_1^{x,y} = 0$ point. The origin of the distortion and offset are suspected to arise as a consequence of geometric misalignment of the pump/probe beams relative to the rf and longitudinal static fields. We confirm this by introducing misalignment through pump/probe beam steering and observing the corresponding ovoid profile. Larger misalignment causes larger distortion of the field mapping. Increasing the dressing frequency of the rf-field reduces these distortion effects in the transverse field directions. This is due to the fact that effective geometric field angles $\alpha, \beta \approx B_{y,x}/B^{+}_{\text{sense}}$ become smaller due to a larger B^{+}_{sense} field required for sensitive field operation resulting in reduced sensitivity to misalignment. Unfortunately, increasing the rf-field frequency inadvertently decreases the OPM sensitivity to transverse fields while the sensitivity to the longitudinal field remains unchanged. The sensing range of the longitudinal field is dependent upon the resonance linewidth and can be extended by increasing the rf-field amplitude at the expense of reducing its

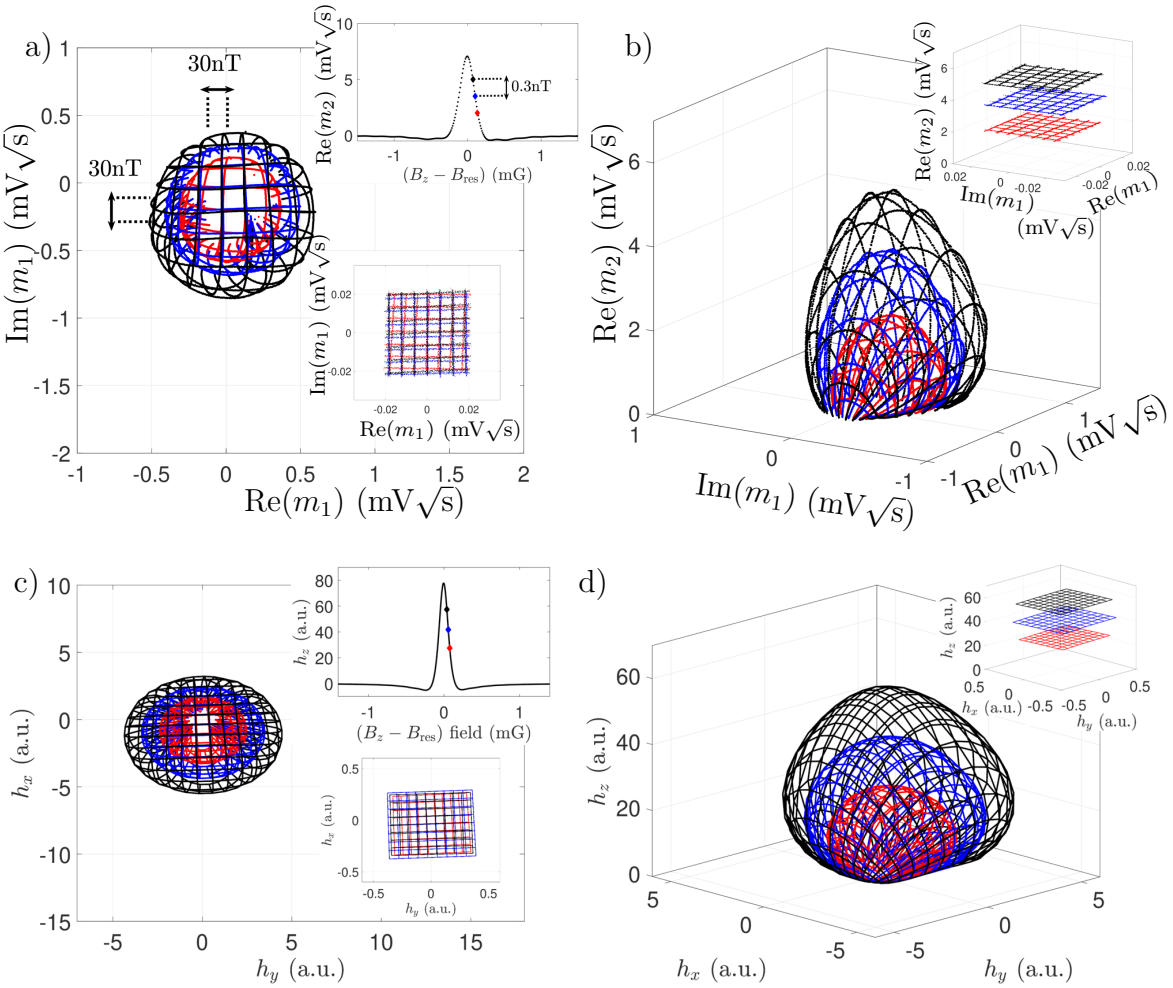

Figure 5.24: Mapping of the OPM response to external fields at 5 kHz radio frequency dressing. a) Quadratures of the first harmonic signal as a function of raster scanned transverse fields $B_{x,y}$ ranging over $\approx \pm 180$ nT for constant B_z. Each colour represents a different B_z field ranging over $\approx \pm 0.3$ nT. The top inset shows the location of the B_z field with respect to the resonant signal at $2\omega_{\mathrm{rf}}$. b) Inclusion of the second harmonic signal produces oviforms in the three-dimensional representation and demonstrates the full vector mapping. The behaviour in the linear regime for small field perturbations is shown in the insets. We attribute deviations from the ideal profiles to geometric misalignment between the pump/probe beams and static and rf fields. The asymmetric distortion increases for lower bias fields, consistent with imperfect orthogonality between static field coils and their alignment with the direction of the probe beam. c) and d) are theoretically calculated ovoid profiles at 5 kHz dressing frequency.

sensitivity. For small external fields, $B_{x,y,z} \ll B^{+}_{\mathrm{sense}}$, the OPM response is linear to the applied field. Here the three calibration values can be used to convert the demodulated signal amplitudes m_k ($\mathrm{mV}\sqrt{\mathrm{s}}$) to fields m_k (T). In principle, the linear field response and the range of the OPM can be extended further by placing it in a closed loop system.

Characterisation of the Ovoid. The OPM ovoid appearance, its shape and, size convey important information about the magnetometer's response to external magnetic fields. We have already explored some of the parameters affecting the sensitivity of the magnetometer (e.g. see Figs. 5.17, 5.18, 5.20, 5.21 and 5.22); however, these effects are only valid for small external fields, $B_{x,y,z} \ll B^{+}_{\text{sense}}$. Furthermore, the theoretical models described in this work do not take into account of the more detailed effects of light matter interaction such as detuning, power, optical transitions etc., which as has been shown in the previous section have significant effects. To this end, the motivation was to explore some of the parameter space and establish qualitative relationships between the parameters and observables, and where possible, compare them to the theoretical predictions. The parameters explored were the dressing field frequency and its amplitude, probe power and the optical transitions of the pump beam. These parameters one of the major contributors to the field sensitivity. Fig. 5.25 shows the results.

The rf-field dressing frequency tunes the static field resonance point $B_{\text{res}} = \hbar\omega_{\text{rf}}/\mu_B g_F$ which further influences the operational field setpoint where the magnetometer is sensitive to all three field directions, $B^{+}_{\text{sense}} = B_{\text{res}} + B_\rho$. Increasing this frequency, reduces the field sensitivity to transverse field directions whilst keeping the longitudinal field sensitivity constant. As a result, for the same range of fields, the OPM ovoid should shrink in the x-y field sensing plane. This is consistent with the observations, see Fig. 5.25 a). For increasing rf-dressing field frequency, the ovoid begins to shrink in the x-y plane. There is some variation in the z-field peak point of the OPM's ovoid responses which are possibly due to imprecise B^{+}_{sense} setpoint. The rf-dressing frequency gives the freedom to precisely tune the field sensitivity to transverse fields enabling high dynamic range operation. The dynamic range is further extended for the longitudinal, z-field, where the sensitivity is tuned with the rf-field amplitude, see Fig. 5.25 b). Here increasing the rf-field amplitude increases the volume of the ovoid affecting the sensitivity in the longitudinal as well as transverse field directions. Here the picture is somewhat more complicated because the rf-field amplitude increases the peak amplitudes of the dispersive and Lorentzian resonance profiles of the m_k quadratures and simultaneously broadens the linewidths of the response functions.

We have already seen that the state preparation process which is primarily dominated by the pumping beam has a strong effect on the sensitivity of the OPM as a function of the duty cycle, phase and optical power. However, we have not considered how the choice of optical transitions of the pump would affect the sensitivity of the OPM. Fig. 5.25 c) shows the results. The pumping from $F = 2 \rightarrow F' = 1$ using π-polarised light yields a larger volume ovoid compared to $F = 2 \rightarrow F' = 2$ optical transition. This is due to the fact that the Clebsch-Gordan coefficients for $F = 2 \rightarrow F' = 1$ are larger compared to the $F = 2 \rightarrow F' = 2$ transitions making the pumping more efficient. Moreover, the branching ratios of the decay from $F' = 2 \rightarrow F = 1$ are larger compared to $F' = 1 \rightarrow F = 1$, further enhancing the efficiency of the pumping. In the regime where the OPM response is linear to external fields, the field sensitivity was observed to scale approximately linearly for low probe

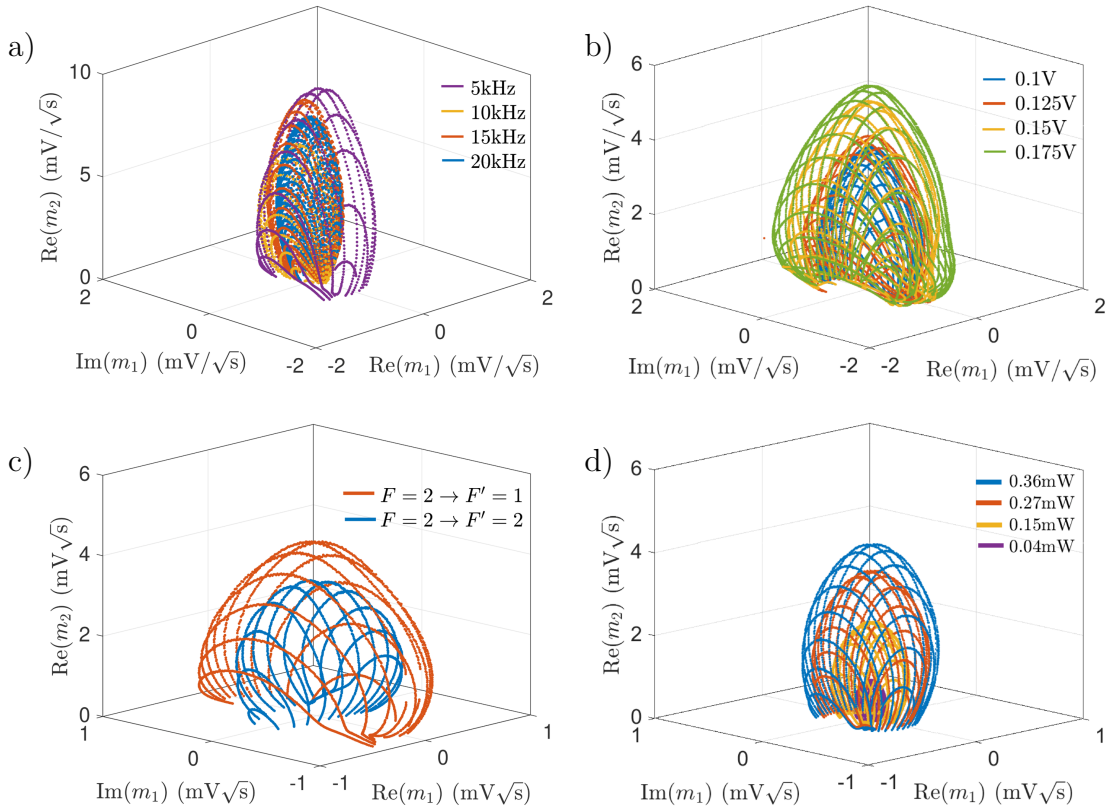

Figure 5.25: a) ovoid profiles at different rf-field frequencies. Increasing the rf-field frequency reduces sensitivity to transverse fields whilst keeping the longitudinal field sensitivity unchanged. b) ovoid profiles at different rf-field amplitudes. Increasing the rf-amplitude increases the volume of the egg for all three quadratures. c) ovoid field profiles for different optical transitions of the pump which for $F = 2 \rightarrow F' = 1$ pump results in an equal statistical mixture of $|F = 2, m_F = \pm 2\rangle$ and for $F = 2 \rightarrow F' = 2$ pump results in a preparation of $|F = 2, m_F = 0\rangle$ state. d) ovoid profile at different probe powers.

powers and then saturate at higher powers. For a full field scan range, the ovoid response has a similar response, where the increase in probe power increases the overall volume of the ovoid in all three quadratures indicating higher field sensitivity for the same field range, see Fig. 5.25 d).

Evidently, the parameter space explored in this section is far from complete. We have not considered the effects of pump/repump power, repump optical transitions, probe detuning to name just a few. However, these effects were largely explored in the linear field regime where the OPM sensitivity can be characterised by a signal scale factor which corresponds to the figure of merit that we are trying to optimise when the OPM

is operated on the sensitive field point B^{+}_{sense}.

5.2.4 Noise performance and characterisation

To perform the noise measurements we detune the static B_z field to $B_z = B^{+}_{\text{sense}}$, which optimises the magnetometer sensitivity for all three components. We then adjust the transverse fields such that the first harmonic signal vanishes, i.e. the noise measurements are done near the apex of the middle (blue) ovoid in Fig. 5.24 b). Based on the field calibrations described on page 126, we record field equivalent signal noise for the three field components over ≈ 16 s (2048 cycles at 125 Hz). Here the sampling frequency refers to the rate at which the state preparation and probing pulses are pulsed at (see Fig. 4.12 on page 122 for illustration). To measure the light noise, we block the light for the state preparation process and detune the probe beam such that no Voigt rotation is observed. We typically switch the magnetic fields off as well as the rf-dressing field. We then measure the corresponding mode amplitudes m_k for the same duration and sampling frequency. The electronic noise is measured by further blocking the probe beam and recording the mode amplitude response. The noise amplitude spectrum is then computed according to eq. (4.32) (see page 122). Fig. 5.26 shows the spectral noise performance for the two quadratures at ω_{rf} and the in-phase quadrature at $2\omega_{\text{rf}}$.

At 5 kHz rf dressing frequency and a temperature of 36°C, the magnetometer operates with an average noise level of ≈ 2.2 pT/$\sqrt{\text{Hz}}$ for the transverse fields over the range of 10-62.5 Hz, dominated by photon shot noise. Longitudinal fields can be measured with a sensitivity of 0.4 pT/$\sqrt{\text{Hz}}$. The noise floor of our 4-layer μ-metal shield is $\approx$11 fT/$\sqrt{\text{Hz}}$ in the 1-100 Hz frequency band [89]. As was discussed in the previous section, the dominant constraint on the noise level is the short coherence time of the cell ($\tau \approx 2$ ms) which is limited by the quality of the paraffin coating and the exchange of the atoms between the main cell body and the stem with the Rb reservoir. Typically, paraffin or OTS coated cells have coherence times ranging from 30 ms to 300 ms [91, 92]. Longer coherence time would improve the field sensitivity of the OPM due to a larger fraction of atoms remaining in the field sensitive state. In addition, higher quality paraffin coating would also shorten the pump/repump pulse time needed to (re-)prepare the stretched states, allowing for increased cycle rate and thus higher bandwidth as well as higher duty cycle and thus reduced aliasing of magnetic field noise. The bandwidth of the OPM could further be increased by significantly shortening the pumping cycle by using a nano-second pulsed laser as a pump with high peak power [30]. A pulse duration of typically 150 ns with a peak power of $\approx$10 W and a 20 GHz spectral bandwidth would allow to significantly shorten the state preparation process. The spectrally broad laser would also act as a repump, which would allow us to further simplify the laser system. In our case, the 5 ms of pumping time would be reduced to ≈ 1 μs which would leave us with 3 ms of probing extended the OPM bandwidth to $\approx$160 Hz.

Recall that the mode amplitudes are acquired by demodulating a decaying windowed

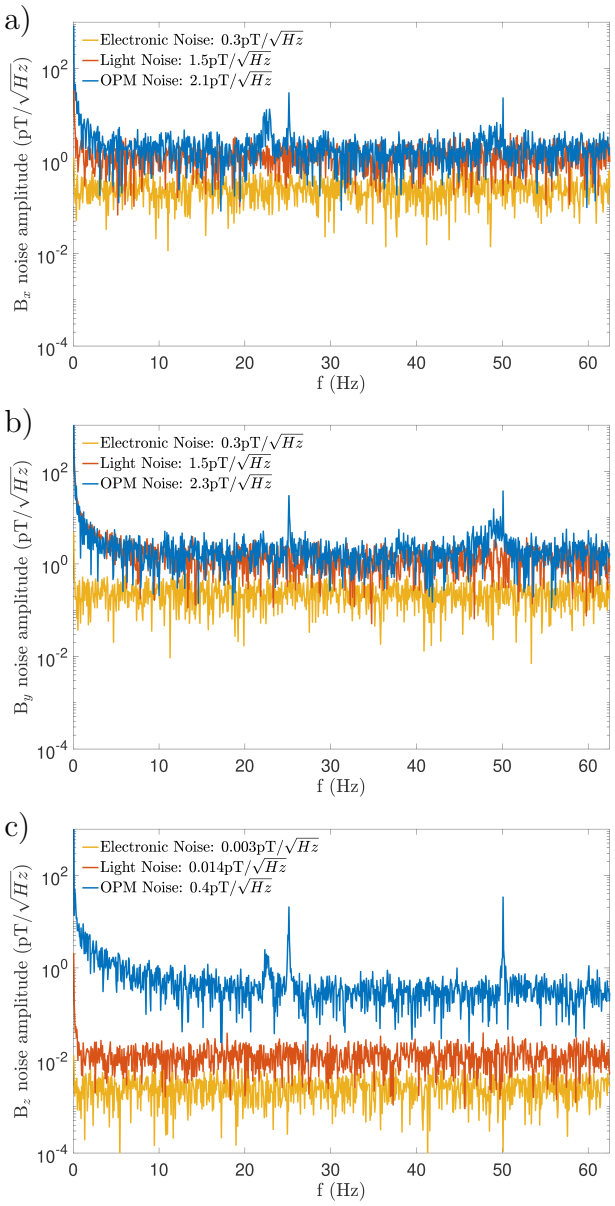

Figure 5.26: OPM noise at 36°C vapour cell temperature in a shielded environment at 5 kHz radio frequency dressing. Noise floor values are estimated for the range 10 Hz - 62.5 Hz. Panels a) and b) show noise performance for the two orthogonal transverse fields. The light noise in one of the signal quadratures shows phase-locked, low-frequency fluctuations of cross talk between the rf generation and detection paths. Panel c) shows the noise performance for the longitudinal field component. The light noise levels (photon shot noise) are obtained with a far-detuned probe laser and disabled pump/repump lasers. The electronic noise is recorded without probe light and no rf field present. The calibration of field equivalent noise amplitudes includes an $\approx 5\%$-drop of the low-pass frequency response function, which is predominantly determined by the mode function entering eq. (4.20) on page 120.

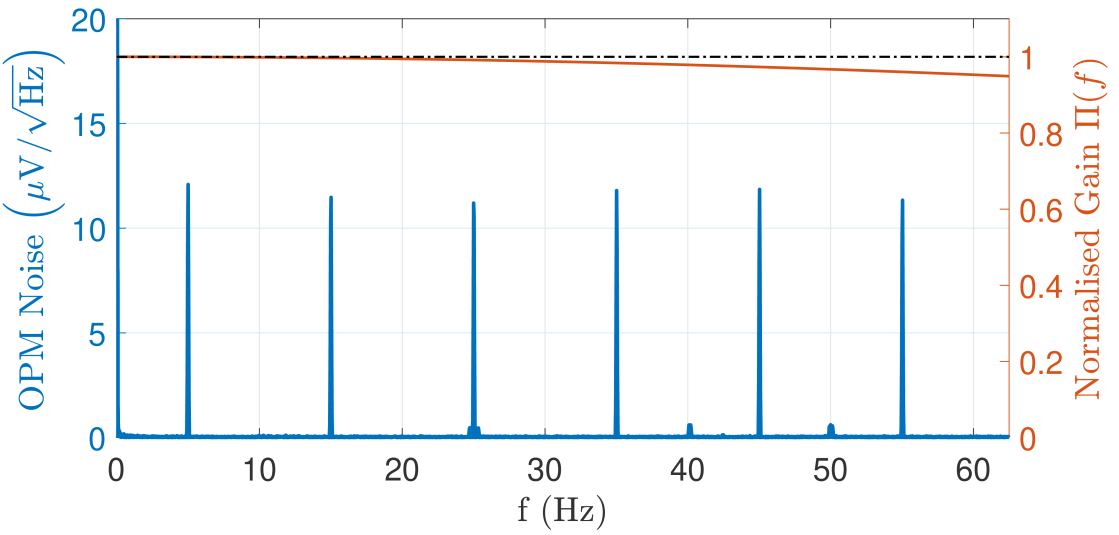

Figure 5.27: OPM noise response with an external control signal in blue. Here the same amplitude sinusoidal wave in blue is injected into the x-coil and the corresponding OPM noise spectrum is taken for the quadrature at different driving frequencies of the control field. The right hand side axis models the gain profile due to a finite probe window in addition to the signal decay. The red line is the theoretical gain given by eq. (5.10) as a function of frequency. The decay time of the signal is $1/\gamma \approx 2$ ms with the probing time $T_p = 3$ ms.

probe signal which takes the following form

$$U_{\text{env}}(t) = g_{\text{el}} e^{-\gamma t} H(T_p - t) H(t). \tag{5.9}$$

This introduces a frequency dependent gain on the signal model amplitudes (see page 122 for additional details) given by

$$\Pi(\omega) = \sqrt{|U_{\text{env}}(\omega)|^2} = \sqrt{\frac{\gamma^2}{\gamma^2 + \omega^2} \frac{\cosh(T_p\gamma) - \cos(\omega T_p)}{(\cosh(T_p\gamma) - 1)}}, \tag{5.10}$$

where T_p is the probing time and $1/\gamma$ is the 1/e signal decay time constant. These two constants affect the bandwidth of the magnetometer by acting as a low-pass filter function. The longer the probing time, T_p, and the shorter the coherence lifetime $1/\gamma$, the bigger the roll-off of the gain at higher frequencies. Fig. 5.27 shows the OPM noise response at difference frequencies of the same amplitude control signal. With the probe time of $T_p = 3$ ms and the 1/e decay time $1/\gamma \approx 2$ ms, the gain drops by 5% given by the $\Pi(\omega)$. At higher frequencies, the inductance of the coils needs to be considered when a constant amplitude signal is fed since the impedance as well as inductance of the circuit is in general complex and frequency dependent. In our case, the coil inductance is in $\approx \mu$H range and its effects can be neglected from control signal frequencies in the 10^2 Hz range.

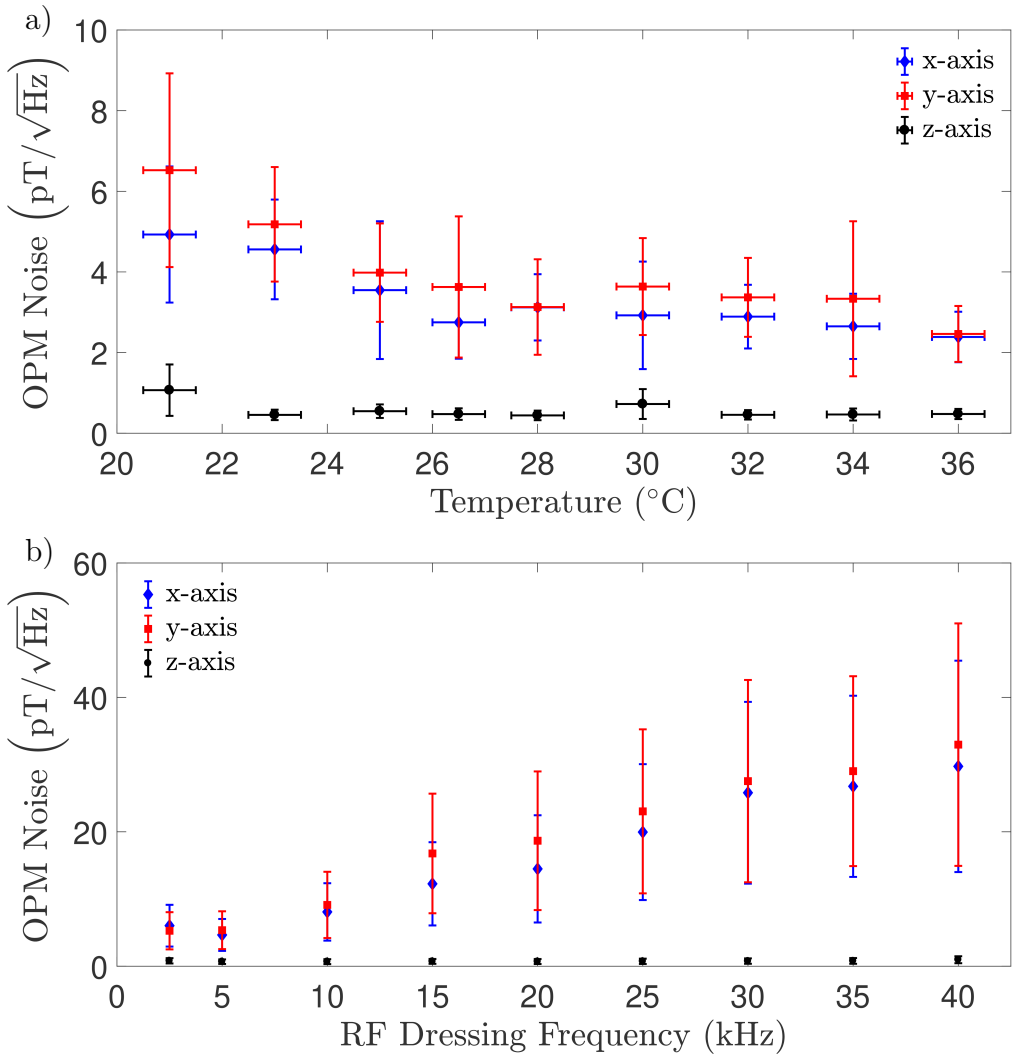

Figure 5.28: Dependencies of the noise performance. a) OPM noise as a function of the vapour cell temperature. b) OPM noise as a function of radio frequency of the dressing field.

Increasing the temperature of the cell thus increasing the atomic density increases the signal scale factors which correspond to the sensitivity of the OPM. However, as it is shown in Fig. 5.28 a), the signal-to-noise-ratio saturates already at temperatures of approximately 32°C for the transverse fields and at even lower temperatures for the longitudinal fields. Initially, increasing signal amplitudes lead to better sensitivity, especially for the transverse fields where the signals are closer to photon shot noise. However, additional atomic processes such as resonance broadening limit the performance at higher temperature where the figure of merit saturates. A similar saturation effect using paraffin coated cells was previously observed in ref. [93], where higher atomic concentrations lead to an increase of the collisional and surface relaxation rates, depolarising the prepared state.

As was previously shown, the sensitivity of the OPM to transverse fields does not only depend on the shape of the resonance, but also on the chosen dressing frequency because the corresponding signals arise from the geometric rotation of the static field. The rotation angle and consequently the signal strength increases for smaller offset fields, see eqs. (3.43) and (3.44) on page 37. The resulting linear dependence of sensitivity on dressing frequency is shown in Fig. 5.28 b). Over the range of 40 kHz to 2.5 kHz the transverse field noise performance varies by a factor of four. This strategy is limited by the linewidth of the rf resonance and other factors such as the required precision of alignment increased susceptibility to magnetic field gradients distorting the oviform mapping as well as the pump cycle duration and the coherence lifetime of the cell.

The vector field sensitivity of the OPM is of similar order of magnitude in all three directions. This makes the OPM practical for 3D vector measurements. Moreover, the sensitivity for z and x-y quadratures can be tuned appropriately to match the field conditions.

Chapter 6

Conclusion and Future Work

In this work we have presented theoretical and experimental results of a novel Voigt-effect-based three-dimensional vector magnetometer. Our scheme requires only a single optical axis geometry for both the state preparation and probing making this sensor architecture ideal for miniaturisation. A key advantage of our magnetometer is the radio-frequency dressing field which encodes the external magnetic field information into its first and second harmonic components. This allows us to extract external field information via lock-in detection techniques removing significant sources of technical noise.

The theoretical models outlined in this thesis have been successful in aiding our understanding of the magnetometer in the experimental setting and feeding back to our efforts in optimising its performance. In addition, the proposed models are capable of taking into account a large parameter space with an extensive dynamical range of values as well as the ability to include arbitrary time-dependent profiles (e.g. pumping) and ancillary interaction effects (e.g. microwave field) combined with a full description of the atomic state using the density matrix approach. The combination of latter two approaches have been instrumental in understanding the state preparation process through dressed microwave spectroscopy paving the way towards realising methods of partial quantum state tomography.

Throughout this work we have encountered a number of theoretical and experimental challenges, which have put a limit on our current understanding of this new type of magnetometer. Theoretically, one of the major limitations in our work has been the absence of a complete description of pump-probe light matter interaction in a Doppler-broadened medium and its impact on the spin dynamics. This may be considered to be unnecessary since our light-matter interaction model used to derive the Voigt-effect is only valid in the far-off resonant regime, where the Doppler effect of thermal atoms can be neglected to a good approximation. A major portion of the

encountered limitations in this work have stemmed largely from the experimental end of things. It is possible that one of the major limiting factors of OPM noise performance are the anti-relaxation coating as well as the cold finger geometry. However, the results to support this hypothesis need further investigation to be conclusive and will form a part of the future work.

With some of the limitations outlined in the previous paragraph, there is a clear and significant number of directions both theoretical and experimental which are worthy to be pursued in continuation of developing this new class of Voigt effect based magnetometers. From the theoretical end of things, a full treatment using the density matrix approach to add the light-matter interaction due to pumping and probing in the off-resonant limit. This would provide a better picture of pump/probe interaction with the spin dynamics and allow us to investigate and understand theoretically the fundamental noise limits. Moreover, this would open the opportunity to study the theoretical performance of the OPM with squeezed light and non-classical quantum states (e.g. using a superposition of $|F = 2, m_F = \pm 2\rangle$ instead of a statistical mixture). Finally, the addition of a microwave field provides us with an extra degree of control where the states can be manipulated and probed.

Experimentally, there is a lot of room for improvement as well as new windows of opportunity to explore. On a basic technical level, the major limitation in our OPM performance has been the cell. Obtaining a properly designed cold finger to minimise exchange of the unpumped atoms with the main cell body as well as having long coherence time with good paraffin coating may allow us to bring the OPM to the $\mathrm{fT}/\sqrt{\mathrm{Hz}}$ noise range. Due to the variability in the quality of the paraffin coated cells [94], it may be more conducive to switch to buffer gas cells. This would also allow us to compare the OPM performance in buffer type against anti-relaxation coated cells.

The limitations of the coherence time of the cell as well as the efficiency of the synchronous pumping are currently setting limits to the bandwidth of the OPM. To improve these a couple of alternative pumping methods could be considered. A pulsed laser with high peak power could be used which would almost completely eliminate the pumping time in relation to the probing. To further increase the sensitivity of the OPM a low finesse cavity or Herriott-type mirrors could be placed around the magnetometer [95]. They would increase the optical density through an increased light path. Consequently, this would allow us to eliminate the need to heat the cell simplifying the experimental setup. Another way of enhancing the sensitivity of the OPM would be to use a squeezed light source based on an optical parametric oscillator or four-wave mixing methods [96]. The squeezed light method has an experimental drawback of requiring an extensive and comparatively complex laser and optics setup making it impractical for use in miniature sensors. Since the unshielded setup was far from optimal in control and execution, it would be important to reinvestigate the OPM performance in the unshielded environment and determine its fundamental sensitivity.

The work done on the dressed microwave spectroscopy should be further investigated, but in shielded conditions. This would remove significant sources of noise that were present in the unshielded environment where the previous results were taken. Placing the cell in a magnetron cavity [97], or using a microwave horn would further allow us to study the dressed microwave spectrum of the prepared state, as well as explore the use of novel quantum states for magnetometry measurements.

In summary, the system is rich in physics, with many interesting questions and challenges left in both, theoretical and experimental domains. This work has been a consequence of a serendipitous scientific discovery, and the hope is that it will continue as such.

APPENDIX A

Appendix: Light-Matter Interaction

A.1 Optical rate equations for resonant π-polarised pump/repump

The time dependent population for each ground level ρ_n is governed by the following equation of motion [54]

$$\partial_t \rho_n(t) = \sum_{j \neq n} \rho_j(t) \left(\sum_k \Xi_{j,k} \gamma_{j,k} \gamma_{n,k} \right) - \rho_n(t) \sum_k \Xi_{n,k} \gamma_{n,k} (1 - \gamma_{n,k}). \tag{A.1}$$

We begin defining the terms in the equation by computing the transition probabilities for all the possible states for the D1 and D2 lines with the following using $\pi-$polarised pump and repump beams using

$$\gamma_{e,g}(|J_e, I, F_e, m_e\rangle \to |J_g, I, F_g, m_g\rangle) = \gamma_{g,e}(|J_g, I, F_g, m_g\rangle \to |J_e, I, F_e, m_e\rangle) =$$
$$(2F_e + 1)(2J_g + 1)(2J_e + 1) \times \begin{Bmatrix} J_g & I & F_g \\ F_e & 1 & J_e \end{Bmatrix}^2 \times \begin{pmatrix} F_g & 1 & F_e \\ m_g & q & -m_e \end{pmatrix}^2, \tag{A.2}$$

where the curly and round brackets around the matrices represent the Wigner-6j and Wigner-3j symbols respectively. The element q corresponds to the polarisation state such that

$$q = \begin{cases} 0, & \pi\text{-polarisation}, \\ +1, & \sigma^+\text{-polarisation}, \\ -1, & \sigma^-\text{-polarisation}, \end{cases} \tag{A.3}$$

with the natural lifetimes for the D1 and D2 lines given by

$$\Gamma_k = \begin{cases} 2\pi \times 5.746\text{MHz}, & \text{D1-line}, \\ 2\pi \times 6.065\text{MHz}, & \text{D2-line}. \end{cases} \tag{A.4}$$

The branching ratios, $\gamma_{j,k}$ are normalised against the D2 line transition strength

$$|F_g = I + 1/2, m_g = F_g\rangle \rightarrow |F_e = I + 3/2, m_e = F_e\rangle\,, \tag{A.5}$$

to be unity.

Table A.1: $|F = 1\rangle \rightarrow |F' = 2\rangle$ D2 Line

$\pi-$transition	σ^--transition	σ^+-transition
$\gamma_{1,13} = \frac{1}{4}$	$\gamma_{1,14} = \frac{1}{4}$	$\gamma_{2,13} = \frac{1}{12}$
$\gamma_{2,14} = \frac{1}{3}$	$\gamma_{2,15} = \frac{1}{12}$	$\gamma_{3,14} = \frac{1}{4}$
$\gamma_{3,15} = \frac{1}{4}$		

Table A.2: $|F = 2\rangle \rightarrow |F' = 2\rangle$ D2 Line

$\pi-$transition	σ^--transition	σ^+-transition
$\gamma_{5,13} = \frac{1}{12}$	$\gamma_{5,14} = \frac{1}{4}$	$\gamma_{5,12} = \frac{1}{6}$
$\gamma_{6,14} = 0$	$\gamma_{6,15} = \frac{1}{4}$	$\gamma_{6,13} = \frac{1}{4}$
$\gamma_{7,15} = \frac{1}{12}$	$\gamma_{7,16} = \frac{1}{6}$	$\gamma_{7,14} = \frac{1}{4}$

Table A.3: $|F = 2\rangle \rightarrow |F' = 1\rangle$ D1 Line

$\pi-$transition	σ^--transition	σ^+-transition
$\gamma_{5,9} = \frac{1}{4}$	$\gamma_{5,10} = \frac{1}{12}$	$\gamma_{9,4} = \frac{1}{2}$
$\gamma_{6,10} = \frac{1}{3}$	$\gamma_{10,11} = \frac{1}{4}$	$\gamma_{6,9} = \frac{1}{4}$
$\gamma_{7,11} = \frac{1}{4}$	$\gamma_{11,8} = \frac{1}{2}$	$\gamma_{7,10} = \frac{1}{12}$

Table A.4: $|F=1\rangle \rightarrow |F'=1\rangle$ D1 Line

$\pi-$transition	$\sigma^{-}-$transition	$\sigma^{+}-$transition
$\gamma_{1,9}=\frac{1}{12}$	$\gamma_{1,10}=\frac{1}{12}$	$\gamma_{2,9}=\frac{1}{12}$
$\gamma_{2,10}=0$	$\gamma_{2,11}=\frac{1}{12}$	$\gamma_{3,10}=\frac{1}{12}$
$\gamma_{3,11}=\frac{1}{12}$		

The population rate equations read

$$\begin{aligned}
\partial_t\rho_1(t) &= -\rho_1(t)\gamma_{1,13}(\gamma_{13,4}+\gamma_{13,5}+\gamma_{13,6}+\gamma_{13,2})\Xi_1 \\
&\quad + \rho_2(t)\gamma_{2,14}\gamma_{14,1}\Xi_1 + (\rho_5(t)\gamma_{5,9}\gamma_{9,1}+\rho_6(t)\gamma_{6,10}\gamma_{10,1})\Xi_2, \qquad \text{(A.6)}\\
\partial_t\rho_2(t) &= -\rho_2(t)\gamma_{2,14}(\gamma_{14,5}+\gamma_{14,7}+\gamma_{14,1}+\gamma_{14,3})\Xi_1 \\
&\quad + (\rho_1(t)\gamma_{1,13}\gamma_{13,2}+\rho_3(t)\gamma_{3,15}\gamma_{13,2})\Xi_1 \\
&\quad + (\rho_5(t)\gamma_{5,9}\gamma_{9,2}+\rho_7(t)\gamma_{7,11}\gamma_{11,2})\Xi_2, \qquad \text{(A.7)}\\
\partial_t\rho_3(t) &= -\rho_3(t)\gamma_{3,15}(\gamma_{15,8}+\gamma_{15,7}+\gamma_{15,6}+\gamma_{15,2})\Xi_1 \\
&\quad + \rho_2(t)\gamma_{2,14}\gamma_{14,3}\Xi_1 + (\rho_7(t)\gamma_{7,11}\gamma_{11,3}+\rho_6(t)\gamma_{6,10}\gamma_{10,3})\Xi_2, \qquad \text{(A.8)}
\end{aligned}$$

$$\begin{aligned}
\partial_t\rho_4(t) &= \rho_1(t)\gamma_{1,13}\gamma_{13,4}\Xi_1 + \rho_5(t)\gamma_{5,9}\gamma_{9,4}\Xi_2, \qquad \text{(A.9)}\\
\partial_t\rho_5(t) &= -\rho_5(t)\gamma_{5,9}(\gamma_{9,4}+\gamma_{9,6}+\gamma_{9,1}+\gamma_{9,2})\Xi_2 \\
&\quad + \rho_6(t)\gamma_{6,10}\gamma_{10,5}\Xi_2 + (\rho_1(t)\gamma_{1,13}\gamma_{13,5}+\rho_2(t)\gamma_{2,14}\gamma_{14,5})\Xi_1, \qquad \text{(A.10)}\\
\partial_t\rho_6(t) &= -\rho_6(t)\gamma_{6,10}(\gamma_{10,5}+\gamma_{10,7}+\gamma_{10,1}+\gamma_{10,3})\Xi_2 \\
&\quad + (\rho_5(t)\gamma_{5,9}\gamma_{9,6}+\rho_7(t)\gamma_{7,11}\gamma_{11,6})\Xi_2 \\
&\quad + (\rho_1(t)\gamma_{1,13}\gamma_{13,6}+\rho_3(t)\gamma_{3,15}\gamma_{15,6})\Xi_1, \qquad \text{(A.11)}\\
\partial_t\rho_7(t) &= -\rho_7(t)\gamma_{7,11}(\gamma_{11,8}+\gamma_{11,6}+\gamma_{11,3}+\gamma_{11,2})\Xi_2 \\
&\quad + \rho_6(t)\gamma_{6,10}\gamma_{10,7}\Xi_2 + (\rho_3(t)\gamma_{3,15}\gamma_{15,7}+\rho_2(t)\gamma_{2,14}\gamma_{14,7})\Xi_1, \qquad \text{(A.12)}\\
\partial_t\rho_8(t) &= \rho_3(t)\gamma_{3,15}\gamma_{15,8}\Xi_1 + \rho_7(t)\gamma_{7,11}\gamma_{11,8}\Xi_2, \qquad \text{(A.13)}
\end{aligned}$$

where Ξ_1 and Ξ_2 are computed on resonance to their respective transitions, $\Delta = 0$ MHz

$$\Xi_{j,k}(I,\Delta=0) = \frac{I/I_{\text{sat}}}{1+I/I_{\text{sat}}+(2\Delta_{j,k}/\Gamma_k)^2}\frac{\gamma_{j,k}\Gamma_k}{2} = \frac{I/I_{\text{sat}}}{1+I/I_{\text{sat}}}\frac{\gamma_{j,k}\Gamma_k}{2}. \qquad \text{(A.14)}$$

A.2 Optical rate equations for a far-detuned probe

We begin with the same time dependent population for each ground level ρ_n is governed by the following equation of motion [54]

$$\partial_t\rho_n(t) = \sum_{j\neq n}\rho_j(t)\left(\sum_k \Xi_{j,k}\gamma_{j,k}\gamma_{n,k}\right) - \rho_n(t)\sum_k \Xi_{n,k}\gamma_{n,k}(1-\gamma_{n,k}). \qquad \text{(A.15)}$$

In this case we have a probe that has 45° polarisation which can be decomposed into $\pi-$ and $\sigma^{\pm}-$polarisations. The probe addresses $|F=2\rangle \rightarrow |F'=1\rangle$ of the D1 line. The rate equations take the following form

$$\begin{aligned}
\partial_t\rho_1(t) &= \Big((\rho_4(t)\gamma_{4,9} + \rho_5(t)\gamma_{5,9})\gamma_{9,1} + \\
&\quad + (\rho_6(t)\gamma_{6,10} + \rho_7(t)\gamma_{7,10})\gamma_{10,1}\Big)\Xi_2, && \text{(A.16)}\\
\partial_t\rho_2(t) &= \Big(\rho_4(t)\gamma_{4,9} + (\rho_5(t)\gamma_{5,9})\gamma_{9,2} \\
&\quad + (\rho_7(t)\gamma_{7,11} + (\rho_8(t)\gamma_{8,11})\gamma_{11,2}\Big)\Xi_2, && \text{(A.17)}\\
\partial_t\rho_3(t) &= \Big((\rho_8(t)\gamma_{8,11} + \rho_7(t)\gamma_{7,11})\gamma_{11,3} + \\
&\quad + (\rho_6(t)\gamma_{6,10} + \rho_7(t)\gamma_{7,10})\gamma_{10,3}\Big)\Xi_2, && \text{(A.18)}
\end{aligned}$$

$$\begin{aligned}
\partial_t\rho_4(t) &= -\rho_4(t)\gamma_{4,9}(\gamma_{9,5} + \gamma_{9,6} + \gamma_{9,1} + \gamma_{9,2})\Xi_2 \\
&\quad + \rho_5(t)\gamma_{5,9}\gamma_{9,4}\Xi_2 + \rho_6(t)\gamma_{6,9}\gamma_{9,4}\Xi_2, && \text{(A.19)}\\
\partial_t\rho_5(t) &= -\rho_5(t)\gamma_{5,9}(\gamma_{9,4} + \gamma_{9,6} + \gamma_{9,1} + \gamma_{9,2})\Xi_2 \\
&\quad - \rho_5(t)\gamma_{5,10}(\gamma_{10,6} + \gamma_{10,7} + \gamma_{10,1} + \gamma_{10,3})\Xi_2 \\
&\quad + \Big(\rho_4(t)\gamma_{4,9}\gamma_{9,5} + \rho_7(t)\gamma_{7,10}\gamma_{10,5} \\
&\quad + \rho_6(t)\gamma_{6,10}\gamma_{10,5} + \rho_6(t)\gamma_{6,9}\gamma_{9,5}\Big)\Xi_2, && \text{(A.20)}\\
\partial_t\rho_6(t) &= -\rho_6(t)\gamma_{6,10}(\gamma_{10,5} + \gamma_{10,7} + \gamma_{10,1} + \gamma_{10,3})\Xi_2 \\
&\quad - \rho_6(t)\gamma_{6,9}(\gamma_{9,4} + \gamma_{9,5} + \gamma_{9,1} + \gamma_{9,2})\Xi_2 \\
&\quad - \rho_6(t)\gamma_{6,11}(\gamma_{11,7} + \gamma_{11,8} + \gamma_{11,2} + \gamma_{11,3})\Xi_2 \\
&\quad + \rho_4(t)\gamma_{4,9}\gamma_{9,6} + \rho_8(t)\gamma_{8,11}\gamma_{11,6} + \rho_7(t)\gamma_{7,11}\gamma_{11,6} + \rho_7(t)\gamma_{7,10}\gamma_{10,6} \\
&\quad + \rho_5(t)\gamma_{5,9}\gamma_{9,6} + \rho_5(t)\gamma_{5,10}\gamma_{10,6}, && \text{(A.21)}\\
\partial_t\rho_7(t) &= -\rho_7(t)\gamma_{7,11}(\gamma_{11,8} + \gamma_{11,6} + \gamma_{11,3} + \gamma_{11,2})\Xi_2 \\
&\quad - \rho_7(t)\gamma_{7,10}(\gamma_{10,6} + \gamma_{10,5} + \gamma_{10,3} + \gamma_{10,1})\Xi_2 \\
&\quad + \Big(\rho_8(t)\gamma_{8,11}\gamma_{11,3} + \rho_5(t)\gamma_{5,10}\gamma_{10,7} \\
&\quad + \rho_6(t)\gamma_{6,10}\gamma_{10,7} + \rho_6(t)\gamma_{6,11}\gamma_{11,7}\Big)\Xi_2, && \text{(A.22)}\\
\partial_t\rho_8(t) &= -\rho_8(t)\gamma_{8,11}(\gamma_{11,7} + \gamma_{11,6} + \gamma_{11,3} + \gamma_{11,2})\Xi_2 \\
&\quad + \rho_7(t)\gamma_{7,11}\gamma_{11,8}\Xi_2 + \rho_6(t)\gamma_{6,11}\gamma_{11,8}\Xi_2, && \text{(A.23)}
\end{aligned}$$

where the probe is off-resonance $\Delta = -550$ MHz

$$\Xi_{j,k}(I, \Delta = -550\text{ MHz}) = \frac{I/I_{\text{sat}}}{1 + I/I_{\text{sat}} + (2\Delta_{j,k}/\Gamma_k)^2}\frac{\gamma_{j,k}\Gamma_k}{2}. \qquad \text{(A.24)}$$

APPENDIX B

Appendix: Spin Dynamics

B.1 RF-dressed Spin Hamiltonian

The rf-dressed Hamiltonian takes the form

$$\hat{\mathbf{H}} = g_F \mu_B (B_{\mathrm{dc}} \mathbf{e}_z + B_{\mathrm{rf}} \cos(\omega t) \mathbf{e}_x) \cdot \hat{\mathbf{F}}, \tag{B.1}$$

We want to transform the Hamiltonian above into a rotating frame such that we can cancel any time dependencies that exist in it. To do this, we apply a unitary transformation using the following ansatz:

$$\hat{U} = e^{i\omega t \hat{\mathbf{F}}_z}, \tag{B.2}$$

where ω is the angular frequency of the rf-field. Note that this unitary transformation is time dependent. As a result, the transformed Hamiltonian from the original form is given by:

$$\hat{H}' = i\hbar \frac{d\hat{U}}{dt} \hat{U}^\dagger + \hat{U} \hat{H} \hat{U}^\dagger. \tag{B.3}$$

Evaluating the first part gives:

$$i\hbar \frac{d\hat{U}}{dt} \hat{U}^\dagger = -\hbar\omega \hat{F}_z, \tag{B.4}$$

where we have expanded $\hat{U}$ in power series:

$$\hat{U} = e^{i\omega t \hat{\mathbf{F}}_z} = \sum_{n=0}^{\infty} \frac{i^n (\omega t \hat{F}_z)^n}{n!}, \tag{B.5}$$

$$\hat{U} = \sum_{n=0}^{\infty} \frac{(-1)^n (\omega t \hat{F}_z)^{2n}}{(2n)!} + i \sum_{n=0}^{\infty} \frac{(-1)^n (\omega t \hat{F}_z)^{2n+1}}{(2n+1)!}. \tag{B.6}$$

We note the following:

$$\hat{F}_z^{2n+1} = \hat{F}_z, \tag{B.7}$$

$$\hat{F}_z^0 = \mathbb{I}, \tag{B.8}$$

$$\hat{F}_z^{2n} = \begin{bmatrix} 1 & 0 & 0 \\ 0 & 0 & 0 \\ 0 & 0 & 1 \end{bmatrix}. \tag{B.9}$$

From the relation above, we can simplify the unitary transformation. The first term reads

$$\sum_{n=0}^{\infty} \frac{(-1)^n (\omega t \hat{F}_z)^{2n}}{(2n)!} = \mathbb{I} - \frac{(\omega t)^2}{2!}\hat{F}_z^2 + \frac{(\omega t)^4}{4!}\hat{F}_z^4 - ..., \tag{B.10}$$

$$\sum_{n=0}^{\infty} \frac{(-1)^n (\omega t \hat{F}_z)^{2n}}{(2n)!} = \begin{bmatrix} \cos(\omega t) & 0 & 0 \\ 0 & 1 & 0 \\ 0 & 0 & \cos(\omega t) \end{bmatrix}, \tag{B.11}$$

with the second term taking the form

$$\sum_{n=0}^{\infty} \frac{(-1)^n (\omega t \hat{F}_z)^{(2n+1)}}{((2n+1))!} = \omega t \hat{F}_z - \frac{(\omega t)^3}{3!}\hat{F}_z^3 + ..., \tag{B.12}$$

$$\sum_{n=0}^{\infty} \frac{(-1)^n (\omega t \hat{F}_z)^{(2n+1)}}{((2n+1))!} = \begin{bmatrix} \sin(\omega t) & 0 & 0 \\ 0 & 0 & 0 \\ 0 & 0 & -\sin(\omega t) \end{bmatrix}. \tag{B.13}$$

Then, combining the two we obtain:

$$\hat{U} = \begin{bmatrix} \cos(\omega t) & 0 & 0 \\ 0 & 1 & 0 \\ 0 & 0 & \cos(\omega t) \end{bmatrix} + i \begin{bmatrix} \sin(\omega t) & 0 & 0 \\ 0 & 0 & 0 \\ 0 & 0 & -\sin(\omega t) \end{bmatrix}, \tag{B.14}$$

which simplifies to

$$\hat{U} = \begin{bmatrix} e^{i\omega t} & 0 & 0 \\ 0 & 1 & 0 \\ 0 & 0 & e^{-i\omega t} \end{bmatrix}. \tag{B.15}$$

From which we obtain the previously stated result when we evaluate the first term of the Hamiltonian transformation:

$$i\hbar \frac{d\hat{U}}{dt}\hat{U}^\dagger = -\hbar\omega \hat{F}_z. \tag{B.16}$$

Now we perform a unitary transformation on the second term:

$$\hat{U}\hat{H}\hat{U}^\dagger = e^{i\omega t \hat{\mathbf{F}}_z} \mu_B g_F (B_{\mathrm{dc}} \hat{F}_z + B_{\mathrm{rf}} \hat{F}_x) e^{-i\omega t \hat{\mathbf{F}}_z}, \tag{B.17}$$

where the rf-field is given by:

$$B_{\mathrm{rf}}(t) = \frac{B_{\mathrm{rf}}}{2}(e^{i\omega t} + e^{-i\omega t}). \tag{B.18}$$

We separate the two terms in the Hamiltonian and deal with them individually. The first term with the static field in the z-direction gives:

$$e^{i\omega t\hat{\mathbf{F}}_z}\mu_B g_F B_{\mathrm{dc}}\hat{F}_z e^{-i\omega t\hat{\mathbf{F}}_z} = \mu_B g_F B_{\mathrm{dc}}\hat{F}_z, \tag{B.19}$$

which has no effect as there are no time dependent terms and also the fact that it is in the same reference frame. The RF term is more involved:

$$\begin{gathered} e^{i\omega t\hat{\mathbf{F}}_z}\mu_B g_F B_{\mathrm{rf}}(t)\hat{F}_x e^{-i\omega t\hat{\mathbf{F}}_z} = \\ \frac{\hbar\mu_B g_F B_{\mathrm{rf}}}{2\sqrt{2}}\begin{bmatrix} 0 & -i(e^{2i\omega t}+1) & 0 \\ i(1+e^{-2i\omega t}) & 0 & -i(e^{2i\omega t}+1) \\ 0 & i(1+e^{-2i\omega t}) & 0 \end{bmatrix}. \end{gathered} \tag{B.20}$$

We now apply the Rotating Wave Approximation to remove the fast rotating terms in the equation above. After simplification this gives:

$$e^{i\omega t\hat{\mathbf{F}}_z}\mu_B g_F B_{\mathrm{rf}}(t)\hat{F}_x e^{-i\omega t\hat{\mathbf{F}}_z} \approx \frac{1}{2}\mu_B g_F B_{\mathrm{rf}}\hat{F}_x. \tag{B.21}$$

Combining all of these terms yields the new Hamiltonian transformed in the rotating frame:

$$\hat{H}' = i\hbar\frac{d\hat{U}}{dt}\hat{U}^\dagger + \hat{U}\hat{H}\hat{U}^\dagger = \mu_B g_F\left(B_{\mathrm{dc}} - \frac{\hbar\omega}{\mu_B g_F}\right)\hat{F}_z + \frac{1}{2}\mu_B g_F B_{\mathrm{rf}}\hat{F}_x. \tag{B.22}$$

B.2 General case using the Baker-Hausdorff Lemma

The result derived for $\langle\hat{S}'_z(t)\rangle$ was obtained in the Schrödinger picture where the operators are stationary and the states are evolving in time. It is more general to work in the Heisenberg picture where the states are stationary in time and the operators are evolving:

$$\langle\hat{S}_z(t)\rangle = a_2\left\langle\psi_z(0)\right|\hat{F}_y^2(t) - \hat{F}_z^2(t)\left|\psi_z(0)\right\rangle, \tag{B.23}$$

with

$$\hat{F}_i(t) = \hat{U}^\dagger(\theta)\hat{U}^\dagger(\omega t)\hat{F}_i(0)\hat{U}(\omega t)\hat{U}(\theta), \tag{B.24}$$

$$\hat{U}^\dagger(\theta)\hat{U}^\dagger(\omega t)\hat{F}_y(0)\hat{U}(\omega t)\hat{U}(\theta), \tag{B.25}$$

where

$$\hat{U}(\theta) = e^{i\theta\hat{F}_y}, \tag{B.26}$$

$$\hat{U}(\omega t) = e^{i\omega t\hat{F}_z}. \tag{B.27}$$

Using the Baker–Hausdorff Lemma

$$e^{\hat{A}}\hat{B}e^{-\hat{A}} = \hat{B} + [\hat{A},\hat{B}] + \frac{1}{2!}[\hat{A},[\hat{A},\hat{B}]] + ..., \tag{B.28}$$

Expanding this using the Lemma gives:

$$\hat{U}^{\dagger}(\omega t)\hat{F}_y(0)\hat{U}(\omega t) = \hat{F}_y - i\omega t[\hat{F}_z,\hat{F}_y] + \frac{1}{2!}[-i\omega t\hat{F}_z,[-i\omega t\hat{F}_z,\hat{F}_y]] + ..., \tag{B.29}$$

where the commutators read:

$$[\hat{F}_z,\hat{F}_y] = -i\hat{F}_x, \tag{B.30}$$
$$[\hat{F}_y,\hat{F}_z] = i\hat{F}_x, \tag{B.31}$$

we apply this first to the $\hat{F}_y$ operator Evaluating the terms from the Baker–Hausdorff power series for the first 4 terms gives for ωt:

$$-i\omega t[\hat{F}_z,\hat{F}_y] = -\omega t\hat{F}_x, \tag{B.32}$$
$$-i\omega t[\hat{F}_z,[-i\omega t\hat{F}_z,\hat{F}_y]] = -(\omega t)^2\hat{F}_y, \tag{B.33}$$
$$-i\omega t[\hat{F}_z,[-i\omega t\hat{F}_z,[-i\omega t\hat{F}_z,\hat{F}_y]]] = (\omega t)^3\hat{F}_x, \tag{B.34}$$
$$-i\omega t[\hat{F}_z,[-i\omega t\hat{F}_z,[-i\omega t\hat{F}_z,[-i\omega t\hat{F}_z,\hat{F}_y]]]] = (\omega t)^4\hat{F}_y, \tag{B.35}$$

where we have missed additional $i\omega t$ terms in the commutator brackets. Combining these terms gives us the following result for the unitary transformation

$$\hat{U}^{\dagger}(\omega t)\hat{F}_y\hat{U}(\omega t) = \hat{F}_y\cos(\omega t) - \hat{F}_x\sin(\omega t). \tag{B.36}$$

Now we have to apply the Lemma again to evaluate the transformation for the operator $\hat{U}(\theta)$. First, we observe that the first term in the equation above containing $\hat{F}_y$ commutes with $\hat{U}(\theta)$ since it also contains $\hat{F}_y$. As a result, we only need to transform the term containing the $\hat{F}_x$ operator:

$$\hat{U}^{\dagger}(\theta)\hat{F}_x\hat{U}(\theta) = \hat{F}_x - i\theta[\hat{F}_y,\hat{F}_x] + \frac{1}{2!}[-i\theta\hat{F}_y,[-i\theta\hat{F}_y,\hat{F}_x]] + ..., \tag{B.37}$$

where the commutation relations read:

$$[\hat{F}_y,\hat{F}_x] = -i\hat{F}_z, \tag{B.38}$$
$$[\hat{F}_y,\hat{F}_z] = i\hat{F}_x. \tag{B.39}$$

Evaluating the first 4 terms:

$$-i\theta[\hat{F}_y,\hat{F}_x] = -\theta\hat{F}_z, \tag{B.40}$$
$$-i\theta[\hat{F}_y,[-i\theta\hat{F}_y,\hat{F}_x]] = -\theta^2\hat{F}_x, \tag{B.41}$$
$$-i\theta[\hat{F}_y,[-i\theta\hat{F}_y,[-i\theta\hat{F}_y,\hat{F}_x]]] = \theta^3\hat{F}_z, \tag{B.42}$$
$$-i\theta[\hat{F}_y,[-i\theta\hat{F}_y,[-i\theta\hat{F}_y,[-i\theta\hat{F}_y,\hat{F}_x]]]] = \theta^4\hat{F}_x. \tag{B.43}$$

Recognising the cos and sin power series we arrive at:

$$\hat{U}^\dagger(\theta)\hat{F}_x\hat{U}(\theta) = \hat{F}_x\cos\theta - \hat{F}_z\sin\theta. \tag{B.44}$$

Hence, the full transformation reads:

$$\hat{F}_y(t) = \hat{U}^\dagger(\theta)\hat{U}^\dagger(\omega t)\hat{F}_y(0)\hat{U}(\omega t)\hat{U}(\theta) = \hat{F}_y\cos(\omega t) + \hat{F}_x\sin(\omega t)\cos\theta - \hat{F}_z\sin(\omega t)\sin\theta. \tag{B.45}$$

Equivalently, for the $\hat{F}_z$ operator we have:

$$\hat{U}^\dagger(\theta)\hat{U}^\dagger(\omega t)\hat{F}_z(0)\hat{U}(\omega t)\hat{U}(\theta). \tag{B.46}$$

First, we note that the operator $\hat{U}(\omega t)$ commutes with $\hat{F}_z$ hence, the first unitary transformations has no effect. Hence, using the Baker–Hausdorff Lemma we get:

$$\hat{U}^\dagger(\theta)\hat{F}_z(0)\hat{U}(\theta) = \hat{F}_z - i\theta[\hat{F}_y,\hat{F}_z] + \frac{1}{2!}[-i\theta\hat{F}_y,[-i\theta\hat{F}_y,\hat{F}_z]] + ... \quad . \tag{B.47}$$

The first 4 power series terms for θ:

$$-i\theta[\hat{F}_y,\hat{F}_z] = \theta\hat{F}_x, \tag{B.48}$$
$$-i\theta[\hat{F}_y,[-i\theta\hat{F}_y,\hat{F}_z]] = -\theta^2\hat{F}_z, \tag{B.49}$$
$$-i\theta[\hat{F}_y,[-i\theta\hat{F}_y,[-i\theta\hat{F}_y,\hat{F}_z]]] = -\theta^3\hat{F}_x, \tag{B.50}$$
$$-i\theta[\hat{F}_y,[-i\theta\hat{F}_y,[-i\theta\hat{F}_y,[-i\theta\hat{F}_y,\hat{F}_z]]]] = \theta^4\hat{F}_z. \tag{B.51}$$

Combining this gives:

$$\hat{F}_z(t) = \hat{U}^\dagger(\theta)\hat{U}^\dagger(\omega t)\hat{F}_z(0)\hat{U}(\omega t)\hat{U}(\theta) = \hat{F}_z\cos\theta + \hat{F}_x\sin\theta. \tag{B.52}$$

If the differential measurement is done in the $\hat{F}_y^2 - \hat{F}_x^2$ frame, then the DC component of the signal vanishes. To compute this, first we need to find the unitary transformation of

$$\hat{F}_x(t) = \hat{U}^\dagger(\theta)\hat{U}^\dagger(\omega t)\hat{F}_x(0)\hat{U}(\omega t)\hat{U}(\theta). \tag{B.53}$$

First, we compute the inner transformation by applying the Baker-Hausdorff Lemma. The first 4 terms read

$$-i\omega t[\hat{F}_z,\hat{F}_x] = \omega t\hat{F}_y, \tag{B.54}$$
$$-i\omega t[\hat{F}_z,[-i\omega t\hat{F}_z,\hat{F}_x]] = -(\omega t)^2\hat{F}_x, \tag{B.55}$$
$$-i\omega t[\hat{F}_z,[-i\omega t\hat{F}_z,[-i\omega t\hat{F}_z,\hat{F}_x]]] = -(\omega t)^3\hat{F}_y, \tag{B.56}$$
$$-i\omega t[\hat{F}_z,[-i\omega t\hat{F}_z,[-i\omega t\hat{F}_z,[-i\omega t\hat{F}_z,\hat{F}_x]]]] = (\omega t)^4\hat{F}_x. \tag{B.57}$$

Combining this and identifying the series terms:

$$\hat{U}^\dagger(\omega t)\hat{F}_x(0)\hat{U}(\omega t) = \hat{F}_x\cos(\omega t) + \hat{F}_y\sin(\omega t). \tag{B.58}$$

Applying the second unitary transformation:

$$\hat{F}_x(t) = \hat{U}^\dagger(\theta)\left(\hat{F}_x\cos(\omega t) + \hat{F}_y\sin(\omega t)\right)\hat{U}(\theta), \tag{B.59}$$

where we note that the second term above commutes with $\hat{U}(\theta)$. Thus, we want to compute:

$$\hat{F}_x(t) = \hat{U}^\dagger(\theta)\left(\hat{F}_x\cos(\omega t)\right)\hat{U}(\theta) + \hat{F}_y\sin(\omega t). \tag{B.60}$$

Once again, applying the Baker-Hausdorff Lemma and computing the first 4 terms:

$$-i\theta[\hat{F}_y, \hat{F}_x] = -\theta\hat{F}_z, \tag{B.61}$$
$$-i\theta[\hat{F}_y, [-i\theta\hat{F}_y, \hat{F}_x]] = -\theta^2\hat{F}_x, \tag{B.62}$$
$$-i\theta[\hat{F}_y, [-i\theta\hat{F}_y, [-i\theta\hat{F}_y, \hat{F}_x]]] = \theta^3\hat{F}_z, \tag{B.63}$$
$$-i\theta[\hat{F}_y, [-i\theta\hat{F}_y, [-i\theta\hat{F}_y, [-i\theta\hat{F}_y, \hat{F}_x]]]] = \theta^4\hat{F}_x, \tag{B.64}$$

$$\hat{F}_x(t) = \left(\hat{F}_x\cos\theta - \hat{F}_z\sin\theta\right)\cos(\omega t) + \hat{F}_y\sin(\omega t). \tag{B.65}$$

In summary, the full list of transformed operators gives

$$\hat{F}_x(t) = \hat{F}_x\cos(\theta)\cos(\omega t) + \hat{F}_y\sin(\omega t) - \hat{F}_z\sin\theta\cos(\omega t), \tag{B.66}$$
$$\hat{F}_y(t) = -\hat{F}_x\sin(\omega t)\cos\theta + \hat{F}_y\cos(\omega t) + \hat{F}_z\sin(\omega t)\sin\theta, \tag{B.67}$$
$$\hat{F}_z(t) = \hat{F}_x\sin\theta + \hat{F}_z\cos\theta, \tag{B.68}$$

which we can express this as a rotation

$$\mathbf{R}(\omega t, \theta)\cdot\mathbf{F} = \begin{bmatrix} \cos(\theta)\cos(\omega t) & \sin(\omega t) & -\sin\theta\cos(\omega t) \\ -\sin(\omega t)\cos\theta & \cos(\omega t) & \sin(\omega t)\sin\theta \\ \sin\theta & 0 & \cos\theta \end{bmatrix}\cdot\begin{bmatrix}\hat{F}_x\\ \hat{F}_y\\ \hat{F}_z\end{bmatrix}. \tag{B.69}$$

B.3 Raising and lowering spin operators

We define the $\hat{F}_x$ and $\hat{F}_y$ in terms of the raising and lowering operators

$$\hat{F}_y = -\frac{i}{2}\left(\hat{F}_+ - \hat{F}_-\right), \tag{B.70}$$
$$\hat{F}_x = \frac{1}{2}\left(\hat{F}_+ + \hat{F}_-\right), \tag{B.71}$$

with the squares given by:

$$\hat{F}_y^2 = -\frac{1}{4}\left(\hat{F}_+^2 + \hat{F}_-^2 - \hat{F}_+\hat{F}_- - \hat{F}_-\hat{F}_+\right), \tag{B.72}$$
$$\hat{F}_x^2 = \frac{1}{4}\left(\hat{F}_+^2 + \hat{F}_-^2 + \hat{F}_+\hat{F}_- + \hat{F}_-\hat{F}_+\right), \tag{B.73}$$

with

$$\hat{F}_-\hat{F}_+ = \mathbf{F}^2 - F_z^2 - F_z, \tag{B.74}$$
$$\hat{F}_+\hat{F}_- = \mathbf{F}^2 - F_z^2 + F_z, \tag{B.75}$$

where we have set $\hbar = 1$. Here, the operators perform the following operation on our state $|F, F_z\rangle$:

$$\hat{F}_z |F, F_z\rangle = F_z |F, F_z\rangle , \tag{B.76}$$

$$\hat{\mathbf{F}}^2 |F, F_z\rangle = F(F+1) |F, F_z\rangle , \tag{B.77}$$

$$\hat{F}_\pm |F, F_z\rangle = \sqrt{(F \mp F_z)(F \pm F_z + 1)} |F, F_z \pm 1\rangle . \tag{B.78}$$

Before we evaluate the expectation values we notice the following things; the expectation values of the anticommutators will be zero for our chosen $|F, F_z\rangle$ state. This is because, for example for the expectation values involving $\langle F_z, F| \{\hat{F}_i, \hat{F}_z\} |F, F_z\rangle$, where $i = x, y$ the anticommutator will produce orthogonal states to $|F, F_z\rangle$ due to the fact that we have $\hat{F}_{x,y}$ operators which can be expressed as a sum of raising and lowering operators making the new state orthogonal to $|F, F_z\rangle$. On the other hand, the expectation values of anticommutators $\langle F_z, F| \{\hat{F}_x, \hat{F}_y\} |F, F_z\rangle$ will produce products of the raising and lowering operators $\hat{F}_\pm^2$ which again will produce orthogonal states. In addition, the products of raising and lowering operators $\hat{F}_\pm \hat{F}_\mp$ will cancel each other out in the summation since they will have the opposite signs (this can be easily demonstrated by computing the $\{\hat{F}_x, \hat{F}_y\}$ anticommutator in terms of raising and lowering operators which after simplification leaves only the $\hat{F}_\pm^2$ operators in place with the products $\hat{F}_\pm \hat{F}_\mp$ cancelling each other in the sum. We now evaluate the expectation values of $\hat{F}_x^2$, $\hat{F}_y^2$ and $\hat{F}_z^2$:

$$\langle F_z, F| \hat{F}_x^2 |F, F_z\rangle = \frac{1}{2} \left(F(F+1) - F_z^2 \right) , \tag{B.79}$$

$$\langle F_z, F| \hat{F}_y^2 |F, F_z\rangle = \frac{1}{2} \left(F(F+1) - F_z^2 \right) , \tag{B.80}$$

$$\langle F_z, F| \hat{F}_z^2 |F, F_z\rangle = F_z^2 . \tag{B.81}$$

B.4 Derivation of the diffusion coefficients for the Voigt Effect

The Langevin equation of motion has a general solution of the form:

$$u(t) = u(0)e^{-\gamma t} + e^{-\gamma t} \int_0^t e^{\gamma t'} \mathcal{F}_i(t') dt' . \tag{B.82}$$

Thus, if we take our operator equations from the above, we obtain the following general solution:

$$\hat{F}_i(t) = \hat{F}_i(0)e^{-\Gamma_i t} + e^{-\Gamma_i t} \int_0^t e^{\Gamma_i t'} \hat{\mathcal{F}}(t') dt' . \tag{B.83}$$

We assume that the reservoir has no memory i.e. it has a Markov property which is satisfied by the following relation:

$$\langle \hat{\mathcal{F}}_i(t) \hat{\mathcal{F}}_j(t) \rangle = k_{ij} \delta(t - t') . \tag{B.84}$$

If we make an additional assumption that the macroscopic mean value of $\langle \hat{F}_i(t) \rangle$ to be independent of time then we can write [33]

$$i \left\langle \hat{F}_k(t) \right\rangle = i \left\langle \hat{F}_k(t + \Delta t) \right\rangle = \left\langle \left[\hat{F}_i(t + \Delta t), \hat{F}_j(t + \Delta t) \right] \right\rangle . \tag{B.85}$$

Note that the expectation value done here is over quantum states and not time. Here Δt is a small time step and the square brackets represent the commutator relations which follow the standard angular momentum commutator relations

$$\left[\hat{F}_i(t), \hat{F}_j(t) \right] = \epsilon_{ijk} \hat{F}_k(t), \tag{B.86}$$

where ϵ_{ijk} is the Levi-Civita tensor. Expanding the commutator

$$\left\langle \left[\hat{F}_i(t + \Delta t), \hat{F}_j(t + \Delta t) \right] \right\rangle = \left\langle \hat{F}_i(t + \Delta t) \hat{F}_j(t + \Delta t) - \hat{F}_j(t + \Delta t) \hat{F}_i(t + \Delta t) \right\rangle \tag{B.87}$$

Taking the general solution of $\hat{F}_i(t)$ and $\hat{F}_i(t + \Delta t)$ to the commutator. First, we know the general solution for $\hat{F}_i(t)$, we now need to propagate $\hat{F}_i(t + \Delta t)$ and derive its form

$$\hat{F}_i(t + \Delta t) = \hat{F}_i(0) e^{-\Gamma_i (t + \Delta t)} + \int_0^{t + \Delta t} e^{\Gamma_i (t' - t - \Delta t)} \hat{\mathcal{F}}_i(t') dt'. \tag{B.88}$$

Now we note the following

$$\int_0^{t + \Delta t} \ldots dt' = \int_0^t \ldots dt' + \int_t^{t + \Delta t} \ldots dt'. \tag{B.89}$$

Expanding $\hat{F}_i(t + \Delta t)$

$$\begin{aligned} \hat{F}_i(t + \Delta t) = \hat{F}_i(0) e^{-\Gamma_i (t + \Delta t)} + e^{-\Gamma_i (t + \Delta t)} \int_0^t e^{\Gamma_i t'} \hat{\mathcal{F}}_i(t') dt' \\ + e^{-\Gamma_i (t + \Delta t)} \int_t^{t + \Delta t} e^{\Gamma_i t'} \hat{\mathcal{F}}_i(t') dt'. \end{aligned} \tag{B.90}$$

Now if we take a factor of $e^{-\Gamma_i \Delta t}$ out of the equation above, we get

$$\hat{F}_i(t + \Delta t) = e^{-\Gamma_i \Delta t} \left(\underbrace{\hat{F}_i(0) e^{-\Gamma_i t} + e^{-\Gamma_i t} \int_0^t e^{\Gamma_i t'} \hat{\mathcal{F}}_i(t') dt'}_{\hat{F}_i(t)} + e^{-\Gamma_i t} \int_t^{t + \Delta t} e^{\Gamma_i t'} \hat{\mathcal{F}}_i(t') dt' \right). \tag{B.91}$$

Hence

$$\hat{F}_i(t + \Delta t) = \hat{F}_i(t) e^{-\Gamma_i \Delta t} + e^{-\Gamma_i (t + \Delta t)} \int_t^{t + \Delta t} e^{\Gamma_i t'} \hat{\mathcal{F}}_i(t') dt'. \tag{B.92}$$

Now that we know the form of the operator after a step Δt we can work out what the commutator looks like. After some algebra

$$\begin{aligned} \left\langle \left[\hat{F}_i(t + \Delta t), \hat{F}_j(t + \Delta t) \right] \right\rangle = \left\langle \left[\hat{F}_i(t), \hat{F}_j(t) \right] \right\rangle e^{-(\Gamma_i + \Gamma_j) \Delta t} \\ + e^{-(\Gamma_i + \Gamma_j)(t + \Delta t)} \left\langle \int_t^{t + \Delta t} \int_t^{t + \Delta t} e^{(\Gamma_i + \Gamma_j)(t' + t'')} \left[\hat{\mathcal{F}}_i(t'), \hat{\mathcal{F}}_j(t'') \right] dt' dt'' \right\rangle . \end{aligned} \tag{B.93}$$

Note that we can move the brackets inside the integral because it is the expectation value over the states. We know that the product of the Langevin operators satisfy the following

$$\langle \hat{\mathcal{F}}_i(t)\hat{\mathcal{F}}_j(t)\rangle = k_{ij}\delta(t-t'). \tag{B.94}$$

Thus, after the integration and Taylor expansion for small Δt we arrive at

$$\left\langle \left[\hat{F}_i(t+\Delta t), \hat{F}_j(t+\Delta t)\right]\right\rangle = (1-(\Gamma_i+\Gamma_j)\Delta t)\left\langle \left[\hat{F}_i(t), \hat{F}_j(t)\right]\right\rangle + \Delta t\,(k_{ij}-k_{ji})\,. \tag{B.95}$$

The next quantity we want to calculate is the anti–commutator.

$$\left\langle \left\{\hat{F}_i(t+\Delta t), \hat{F}_j(t+\Delta t)\right\}\right\rangle. \tag{B.96}$$

After some algebra and cancelling some terms we get

$$\begin{aligned}\left\langle \left\{\hat{F}_i(t+\Delta t), \hat{F}_j(t+\Delta t)\right\}\right\rangle &= \left\langle \left\{\hat{F}_i(t), \hat{F}_j(t)\right\}\right\rangle e^{-(\Gamma_i+\Gamma_j)\Delta t} \\ &+ e^{-(\Gamma_i+\Gamma_j)(t+\Delta t)}\left\langle \int_t^{t+\Delta t}\int_t^{t+\Delta t} e^{(\Gamma_i+\Gamma_j)(t'+t'')}\left\{\hat{\mathcal{F}}_i(t'), \hat{\mathcal{F}}_j(t'')\right\}dt'dt''\right\rangle,\end{aligned} \tag{B.97}$$

where we have assumed that $i \neq j$ the noise induced by a Langevin force in one quadrature is not correlated in the other one. This is given by

$$\left\langle \hat{F}_i(t)\hat{\mathcal{F}}_j(t)\right\rangle = 0 \quad \text{for} \quad i \neq j. \tag{B.98}$$

In general for a polarised state, that is not a superposition e.g. $|\psi\rangle = |F=2, m_F=2\rangle$ the effect of the anticommutator $\left\langle \left\{\hat{F}_i(t), \hat{F}_j(t)\right\}\right\rangle = 0$ on such a state would give zero. However, experimentally, in our case, the states that we prepare are a set of equal population of mixed states in $|F=2, m_F=-2\rangle$ and $|F=2, m_F=2\rangle$, where it is not the case

$$\left\langle \left\{\hat{F}_i(t), \hat{F}_j(t)\right\}\right\rangle \neq 0. \tag{B.99}$$

Again, applying the same recipe as before, after some algebra and setting Δt to be small we arrive at

$$\left\langle \left\{\hat{F}_i(t+\Delta t), \hat{F}_j(t+\Delta t)\right\}\right\rangle = (1-(\Gamma_i+\Gamma_j)\Delta t)\left\langle \left\{\hat{F}_i(t), \hat{F}_j(t)\right\}\right\rangle + \Delta t\,(k_{ij}+k_{ji})\,. \tag{B.100}$$

The commutator and anticommutator relations will allow us to determine the off–diagonal elements of the matrix k which contains the Langevin force dynamics. We need to calculate the diagonal elements

$$\left\langle \hat{F}_i^2(t)\right\rangle = \left\langle \hat{F}_i(t+\Delta t)\hat{F}_i(t+\Delta t)\right\rangle. \tag{B.101}$$

Substituting the expression for $\hat{F}_i(t)$ into the above and multiplying out the terms gives

$$\begin{aligned}\left\langle \hat{F}_i(t+\Delta t)\hat{F}_i(t+\Delta t)\right\rangle = e^{-2\Gamma_i(t+\Delta t)}\Bigg(&\left\langle \hat{F}_i^2(t)\right\rangle + \int_t^{t+\Delta t} e^{\Gamma_i t'}\left\langle \hat{F}_i(t)\hat{\mathcal{F}}_i(t')\right\rangle dt' \\ &+ \int_t^{t+\Delta t} e^{\Gamma_i t'}\left\langle \hat{\mathcal{F}}_i(t')\hat{F}_i(t)\right\rangle dt' + \int_t^{t+\Delta t}\int_t^{t+\Delta t} e^{\Gamma_i(t'+t'')}\left\langle \hat{\mathcal{F}}_i(t')\hat{\mathcal{F}}_i(t'')\right\rangle dt'dt''\Bigg).\end{aligned} \tag{B.102}$$

The cross terms containing $\langle \hat{F}_i(t)\hat{\mathcal{F}}_i(t')\rangle$ vanish because the operator and the Langevin force are not correlated for different times other than $t' = t$ [58]. Thus, the above reduces to

$$\left\langle \hat{F}_i(t+\Delta t)\hat{F}_i(t+\Delta t)\right\rangle = e^{-2\Gamma_i(t+\Delta t)}\left(\left\langle \hat{F}_i^2(t)\right\rangle + \int_t^{t+\Delta t}\int_t^{t+\Delta t} e^{\Gamma_i(t'+t'')} \left\langle \hat{\mathcal{F}}_i(t')\hat{\mathcal{F}}_i(t'')\right\rangle dt'dt''\right). \tag{B.103}$$

We recognise as before that

$$\langle \hat{\mathcal{F}}_i(t)\hat{\mathcal{F}}_j(t)\rangle = k_{ij}\delta(t-t'). \tag{B.104}$$

Thus, for small Δt we get

$$\left\langle \hat{F}_i(t+\Delta t)\hat{F}_i(t+\Delta t)\right\rangle = (1-2\Gamma_i\Delta t)\left\langle \hat{F}_i^2(t)\right\rangle + k_{ii}\Delta t. \tag{B.105}$$

If we assume steady state conditions over a short time period Δt then the operator values do not vary much in time such that

$$\left\langle \hat{F}_i(t+\Delta t)\hat{F}_i(t+\Delta t)\right\rangle \approx \left\langle \hat{F}_i^2(t)\right\rangle. \tag{B.106}$$

Hence, after some rearrangement and algebra, we can write the diagonal elements as follows

$$k_{ii} = 2\Gamma_i\left\langle \hat{F}_i^2(t)\right\rangle \quad \text{for} \quad i = x, y, z. \tag{B.107}$$

In the same way, after doing some algebra with commutator and anti-commutator terms we get

$$k_{yz} - k_{zy} = i(\Gamma_y + \Gamma_x)\left\langle \hat{F}_x(t)\right\rangle, \tag{B.108}$$

$$k_{zx} - k_{xz} = i(\Gamma_z - \Gamma_x)\left\langle \hat{F}_y(t)\right\rangle, \tag{B.109}$$

$$k_{xy} - k_{yx} = i(\Gamma_x - \Gamma_y)\left\langle \hat{F}_z(t)\right\rangle, \tag{B.110}$$

$$k_{yz} + k_{zy} = (\Gamma_y + \Gamma_z)\left\langle \left\{\hat{F}_z(t), \hat{F}_y(t)\right\}\right\rangle, \tag{B.111}$$

$$k_{xy} + k_{yx} = (\Gamma_x + \Gamma_y)\left\langle \left\{\hat{F}_y(t), \hat{F}_x(t)\right\}\right\rangle, \tag{B.112}$$

$$k_{xz} + k_{zx} = (\Gamma_x + \Gamma_z)\left\langle \left\{\hat{F}_z(t), \hat{F}_x(t)\right\}\right\rangle. \tag{B.113}$$

Now combining the last 6 equations we can calculate the off diagonal elements of the k matrix

$$k_{yz} = (\Gamma_y + \Gamma_z)\left\langle \hat{F}_z(t)\hat{F}_y(t)\right\rangle \quad \text{and} \quad k_{zy} = (\Gamma_z + \Gamma_y)\left\langle \hat{F}_y(t)\hat{F}_z(t)\right\rangle, \tag{B.114}$$

$$k_{zx} = (\Gamma_z + \Gamma_x)\left\langle \hat{F}_z(t)\hat{F}_x(t)\right\rangle \quad \text{and} \quad k_{xz} = (\Gamma_x + \Gamma_z)\left\langle \hat{F}_x(t)\hat{F}_z(t)\right\rangle, \tag{B.115}$$

$$k_{xy} = (\Gamma_x + \Gamma_y)\left\langle \hat{F}_x(t)\hat{F}_y(t)\right\rangle \quad \text{and} \quad k_{yx} = (\Gamma_y + \Gamma_x)\left\langle \hat{F}_y(t)\hat{F}_x(t)\right\rangle. \tag{B.116}$$

Hence, the full $\tilde{\mathbf{\Gamma}}$-matrix reads

$$\tilde{\mathbf{\Gamma}} = \begin{bmatrix} k_{xx} & k_{xy} & k_{xz} \\ k_{yx} & k_{yy} & k_{yz} \\ k_{zx} & k_{zy} & k_{zz} \end{bmatrix} = \begin{bmatrix} 2\Gamma_x\sigma_{xx} & (\Gamma_x+\Gamma_y)\sigma_{xy} & (\Gamma_x+\Gamma_z)\sigma_{xz} \\ (\Gamma_x+\Gamma_y)\sigma_{yx} & 2\Gamma_y\sigma_{yy} & (\Gamma_y+\Gamma_z)\sigma_{yz} \\ (\Gamma_x+\Gamma_z)\sigma_{zx} & (\Gamma_z+\Gamma_y)\sigma_{zy} & 2\Gamma_z\sigma_{zz} \end{bmatrix}. \tag{B.117}$$

B.5 Coherent Dynamics of Spin-1 Particle in a Static External Magnetic Field with RF dressing: Floquet Analysis

We introduce additional weak transverse field to obtain a more complete picture of the dynamics of the Hamiltonian, namely, the field is

$$\vec{B} = B_x \vec{e}_x + \frac{B_y^{\mathrm{rf}}}{2}\left(e^{i\omega t} + e^{-i\omega t}\right)\vec{e}_y + B_y \vec{e}_y + B_z \vec{e}_z. \tag{B.118}$$

The atomic Hamiltonian then reads

$$\hat{H} = \mu_B g_F \hat{F}\cdot\vec{B} = \mu_B g_F \left(\hat{F}_x B_x + \hat{F}_y B_y(t) + \hat{F}_z B_z\right). \tag{B.119}$$

Again, we transform the Hamiltonian into a rotated frame

$$\tilde{H} = i\hbar\frac{d\hat{U}}{dt}\hat{U}^\dagger + \hat{U}\hat{H}\hat{U}^\dagger. \tag{B.120}$$

The unitary transformation of the form

$$\hat{U}(t) = e^{i\omega t\hat{F}_z}. \tag{B.121}$$

Which gives

$$\begin{aligned}\tilde{H} = \mu_B g_F \left(B_x\cos(\omega t) + B_y \sin(\omega t)\right)\hat{F}_x + \mu_B g_F\left(B_z - \frac{\hbar\omega}{\mu_B g_F}\right)\hat{F}_z \\ + \mu_B g_F\left(\frac{1}{2}B_y^{\mathrm{rf}} + B_y\cos(\omega t) - B_x\sin(\omega t)\right)\hat{F}_y.\end{aligned} \tag{B.122}$$

Which we can simplify to

$$\tilde{H} = \alpha(t)\hat{F}_x + \beta(t)\hat{F}_y + \gamma\hat{F}_z. \tag{B.123}$$

The coherent dynamics is then given by

$$\partial_t \hat{F}_i = -\frac{i}{\hbar}\left[\hat{F}_i, \hat{H}\right], \tag{B.124}$$

$$\begin{bmatrix}\partial_t\hat{F}_x\\ \partial_t\hat{F}_y\\ \partial_t\hat{F}_z\end{bmatrix} = \begin{bmatrix}0 & -\gamma & \beta(t)\\ \gamma & 0 & -\alpha(t)\\ -\beta(t) & \alpha(t) & 0\end{bmatrix}\cdot\begin{bmatrix}\hat{F}_x(t)\\ \hat{F}_y(t)\\ \hat{F}_z(t)\end{bmatrix} = M(t)\cdot\begin{bmatrix}\hat{F}_x(t)\\ \hat{F}_y(t)\\ \hat{F}_z(t)\end{bmatrix}. \tag{B.125}$$

Which can further be written as

$$\partial_t\hat{F} = M(t)\hat{F}. \tag{B.126}$$

Note that $M(t) = M(t+p)$ where p is some constant which satisfies the periodicity of $M(t)$. In addition, we can take $M(t)$ and decompose it into its spectral components

$$M(t) = M^0 + \epsilon M^{(-1)} e^{-i\omega t} + \epsilon M^{(+1)} e^{i\omega t}, \tag{B.127}$$

where ϵ is a small dimensionless parameter. The ϵ is justified here because it is proportional to the transverse DC fields B_x and B_y which are by definition very small perturbations relative to the static B_z field. The spectral expressions for M are given by

$$M^0 = \begin{bmatrix} 0 & -\Delta & \delta \\ \Delta & 0 & 0 \\ -\delta & 0 & 0 \end{bmatrix}, \tag{B.128}$$

$$M^{(-1)} = \begin{bmatrix} 0 & 0 & \frac{1}{2}(B_x + B_y) \\ 0 & 0 & \frac{1}{2}(B_y - B_x) \\ -\frac{1}{2}(B_x + B_y) & \frac{1}{2}(B_x - B_y) & 0 \end{bmatrix}, \tag{B.129}$$

$$M^{(+1)} = \begin{bmatrix} 0 & 0 & \frac{1}{2}(B_y - B_x) \\ 0 & 0 & -\frac{1}{2}(B_x + B_y) \\ \frac{1}{2}(B_x - B_y) & \frac{1}{2}(B_x + B_y) & 0 \end{bmatrix}, \tag{B.130}$$

where

$$\Delta = \left(B_z - \frac{\hbar\omega}{\mu_B g_F} \right), \tag{B.131}$$

$$\delta = \frac{1}{2} B_y^{\mathrm{rf}}. \tag{B.132}$$

B.5.1 Floquet Expansion of the second order moment dynamics

The second order moment dynamics in the Liouville space reads

$$\frac{d\mathbf{X}(t)}{dt} = \mathbf{C}(t)\mathbf{X}(t) - 2\Gamma_p(t)\,[\mathbf{X}(t) - \mathbf{X}_{\mathrm{in}}] + \Lambda_{\mathrm{rel}}\,\mathbf{X}_0, \tag{B.133}$$

where we can spectrally decompose the coherent dynamics and the pumping into its harmonics, namely, we can write

$$\mathbf{C}(t) = \mathbf{C}^{(0)} + \mathbf{C}^{(1)}\, e^{i\omega t} + \mathbf{C}^{(-1)}\, e^{-i\omega t}, \tag{B.134}$$

and

$$\Gamma_p(t) = \Gamma_p^{(0)} + \Gamma_p^{(1)} e^{i\omega t} + \Gamma_p^{(-1)} e^{-i\omega t} + \Gamma_p^{(2)} e^{2i\omega t} + \Gamma_p^{(-2)} e^{-2i\omega t} + \cdots = \sum_{n=0} \Gamma_p^{(n)} e^{in\omega t}. \tag{B.135}$$

Using the spectral expansion of our second order moments

$$\mathbf{X}(t) = \mathbf{X}^{(0)}(t) + \mathbf{X}^{(1)}(t)\, e^{i\omega t} + \mathbf{X}^{(-1)}(t)\, e^{-i\omega t} + \mathbf{X}^{(2)}(t) e^{2i\omega t} + \mathbf{X}^{(-2)}(t)\, e^{-2i\omega t} + \cdots, \tag{B.136}$$

and substituting equations (B.134,B.135,B.136) into equation (B.133) and expanding we get

$$\begin{aligned}
\frac{d\mathbf{X}(t)}{dt} &= \frac{d\mathbf{X}^{(0)}(t)}{dt} + \left[\frac{d\mathbf{X}^{(1)}(t)}{dt} + i\omega\right] e^{i\omega t} + \left[\frac{d\mathbf{X}^{(-1)}(t)}{dt} - i\omega\right] e^{-i\omega t} + \cdots \qquad \text{(B.137)}\\
=&[\mathbf{C}^0 + \mathbf{C}^1\ e^{i\omega t} + \mathbf{C}^{-1}\ e^{-i\omega t}][\mathbf{X}^{(0)}(t) + \mathbf{X}^{(1)}(t)\ e^{i\omega t} + \mathbf{X}^{(-1)}(t)\ e^{-i\omega t} + \cdots]\\
&- [\mathbf{\Gamma}_p^{(0)} + \mathbf{\Gamma}_p^{(1)}\ e^{i\omega t} + \mathbf{\Gamma}_p^{(-1)}\ e^{-i\omega t} + \cdots][\mathbf{X}^{(0)}(t) + \mathbf{X}^{(1)}(t)e^{i\omega t} + \mathbf{X}^{(-1)}(t)e^{-i\omega t} + \cdots]\\
&+ [\mathbf{\Gamma}_p^{(0)} + \mathbf{\Gamma}_p^{(1)}\ e^{i\omega t} + \mathbf{\Gamma}_p^{(-1)}\ e^{-i\omega t} + \cdots][\mathbf{X}_{in,F}^{(0)}(t) + \mathbf{X}_{in,F}^{(1)}(t)e^{i\omega t} + \mathbf{X}_{in,F}^{(-1)}(t)e^{-i\omega t} + \cdots\\
&\qquad + \mathbf{X}_{F,in}^{(0)}(t) + \mathbf{X}_{F,in}^{(1)}(t)e^{i\omega t} + \mathbf{X}_{F,in}^{(-1)}(t)e^{-i\omega t} + \cdots]\\
=&(\mathbf{C}^0\mathbf{X}^{(0)}(t) + \mathbf{C}^1\mathbf{X}^{(-1)}(t) + \mathbf{C}^{-1}\mathbf{X}^{(1)}(t)) - \sum_i \mathbf{\Gamma}_p^{(-i)}\mathbf{X}^{(i)}(t)\\
&+ \sum_i \mathbf{\Gamma}_p^{(-i)}[\mathbf{X}_{in,F}^{(i)}(t) + \mathbf{X}_{F,in}^{(i)}(t)]\\
&+ [(\mathbf{C}^0\mathbf{X}^{(1)}(t) + \mathbf{C}^1\mathbf{X}^{(0)}(t) + \mathbf{C}^{-1}\mathbf{X}^{(2)}(t)) - \sum_i \mathbf{\Gamma}_p^{(1-i)}\mathbf{X}^{(i)}(t)\\
&+ \sum_i \mathbf{\Gamma}_p^{(1-i)}[\mathbf{X}_{in,F}^{(i)}(t) + \mathbf{X}_{F,in}^{(i)}(t)]]e^{i\omega t}\\
&+ [(\mathbf{C}^0\mathbf{X}^{(-1)}(t) + \mathbf{C}^{-1}\mathbf{X}^{(0)}(t) + \mathbf{C}^1\mathbf{X}^{(-2)}(t)) - \sum_i \mathbf{\Gamma}_p^{(-1-i)}\mathbf{X}^{(i)}(t)\\
&+ \sum_i \mathbf{\Gamma}_p^{(-1-i)}[\mathbf{X}_{in,F}^{(i)}(t) + \mathbf{X}_{F,in}^{(i)}(t)]]e^{-i\omega t} + \cdots,
\end{aligned}$$

and with the identities given, the compactification in the Floquet space reduces the above equation to

$$\frac{d\mathbb{X}_F(t)}{dt} = [\tilde{\mathbb{C}} - \mathbb{\Gamma}]\ \mathbb{X}_F + \mathbb{\Gamma}_{\text{in}}\mathbb{X}_{\text{in}} + \mathbb{\Lambda}_{\text{rel}}\mathbb{X}_0. \qquad \text{(B.138)}$$

B.6 Spin dynamics using the density matrix formalism

B.6.1 Spin matrices in the F=1 + F=2 manifold

We start with the spin matrix definition in the z-basis for F=1 and F=2 respectively

$$\hat{F}_z = \begin{bmatrix} 1 & 0 & 0 \\ 0 & 0 & 0 \\ 0 & 0 & -1 \end{bmatrix}, \qquad \text{(B.139)}$$

$$\hat{F}_y = \frac{1}{\sqrt{2}} \begin{bmatrix} 0 & -i & 0 \\ i & 0 & -i \\ 0 & i & 0 \end{bmatrix}, \qquad \text{(B.140)}$$

$$\hat{F}_x = \frac{1}{\sqrt{2}} \begin{bmatrix} 0 & 1 & 0 \\ 1 & 0 & 1 \\ 0 & 1 & 0 \end{bmatrix}. \tag{B.141}$$

Equivalently, for F=2 we have

$$\hat{F}_z = \begin{bmatrix} 2 & 0 & 0 & 0 & 0 \\ 0 & 1 & 0 & 0 & 0 \\ 0 & 0 & 0 & 0 & 0 \\ 0 & 0 & 0 & -1 & 0 \\ 0 & 0 & 0 & 0 & -2 \end{bmatrix}, \tag{B.142}$$

$$\hat{F}_x = \begin{bmatrix} 0 & 1 & 0 & 0 & 0 \\ 1 & & \sqrt{\frac{3}{2}} & 0 & 0 \\ 0 & \sqrt{\frac{3}{2}} & 0 & \sqrt{\frac{3}{2}} & 0 \\ 0 & 0 & \sqrt{\frac{3}{2}} & 0 & 1 \\ 0 & 0 & 0 & 1 & 0 \end{bmatrix}, \tag{B.143}$$

$$\hat{F}_y = \begin{bmatrix} 0 & -i & 0 & 0 & 0 \\ i & & -i\sqrt{\frac{3}{2}} & 0 & 0 \\ 0 & i\sqrt{\frac{3}{2}} & 0 & -i\sqrt{\frac{3}{2}} & 0 \\ 0 & 0 & i\sqrt{\frac{3}{2}} & 0 & -i \\ 0 & 0 & 0 & i & 0 \end{bmatrix}. \tag{B.144}$$

Combining them, defines the spin operators for the enlarged F=1+F=2 manifold

$$\hat{F}_i^{\text{Full}} = \begin{bmatrix} \hat{F}_i^{F=1} & 0 \\ 0 & \hat{F}_i^{F=2} \end{bmatrix}, \tag{B.145}$$

which gives the following for all three operators

$$\hat{F}_z^{\text{Full}} = \begin{bmatrix} -1 & 0 & 0 & 0 & 0 & 0 & 0 & 0 \\ 0 & 0 & 0 & 0 & 0 & 0 & 0 & 0 \\ 0 & 0 & 1 & 0 & 0 & 0 & 0 & 0 \\ 0 & 0 & 0 & -2 & 0 & 0 & 0 & 0 \\ 0 & 0 & 0 & 0 & -1 & 0 & 0 & 0 \\ 0 & 0 & 0 & 0 & 0 & 0 & 0 & 0 \\ 0 & 0 & 0 & 0 & 0 & 0 & 1 & 0 \\ 0 & 0 & 0 & 0 & 0 & 0 & 0 & 2 \end{bmatrix}, \tag{B.146}$$

$$\hat{F}_y^{\text{Full}} = \begin{bmatrix} 0 & \frac{1}{2}i\sqrt{2} & 0 & 0 & 0 & 0 & 0 & 0 \\ -\frac{1}{2}i\sqrt{2} & 0 & \frac{1}{2}i\sqrt{2} & 0 & 0 & 0 & 0 & 0 \\ 0 & -\frac{1}{2}i\sqrt{2} & 0 & 0 & 0 & 0 & 0 & 0 \\ 0 & 0 & 0 & 0 & i & 0 & 0 & 0 \\ 0 & 0 & 0 & -i & 0 & i\sqrt{\frac{3}{2}} & 0 & 0 \\ 0 & 0 & 0 & 0 & -i\sqrt{\frac{3}{2}} & 0 & i\sqrt{\frac{3}{2}} & 0 \\ 0 & 0 & 0 & 0 & 0 & -i\sqrt{\frac{3}{2}} & 0 & i \\ 0 & 0 & 0 & 0 & 0 & 0 & -i & 0 \end{bmatrix}, \tag{B.147}$$

$$\hat{F}_x^{\text{Full}} = \begin{bmatrix} 0 & \frac{1}{2}\sqrt{2} & 0 & 0 & 0 & 0 & 0 & 0 \\ \frac{1}{2}\sqrt{2} & 0 & \frac{1}{2}\sqrt{2} & 0 & 0 & 0 & 0 & 0 \\ 0 & \frac{1}{2}\sqrt{2} & 0 & 0 & 0 & 0 & 0 & 0 \\ 0 & 0 & 0 & 0 & 1 & 0 & 0 & 0 \\ 0 & 0 & 0 & 1 & 0 & \sqrt{\frac{3}{2}} & 0 & 0 \\ 0 & 0 & 0 & 0 & \sqrt{\frac{3}{2}} & 0 & \sqrt{\frac{3}{2}} & 0 \\ 0 & 0 & 0 & 0 & 0 & \sqrt{\frac{3}{2}} & 0 & 1 \\ 0 & 0 & 0 & 0 & 0 & 0 & 1 & 0 \end{bmatrix}. \tag{B.148}$$

B.6.2 Wigner D-functions and Angular Momentum Surfaces

The probability surface is defined as

$$\rho_F(\theta,\phi) = \langle F, m \,|\, \hat{\rho} \,|\, F, m \rangle = \sum_{m,m'} \left(D^{(F)}_{m,F}\right)^* (\phi,\theta,0)\hat{\rho}_{m,m'} D^{(F)}_{m',F}(\phi,\theta,0), \tag{B.149}$$

where $D^{(F)}_{m',m}(\phi,\theta,0)$ are the Wigner D-functions which are given by

$$D^{(F)}_{m',m}(\phi,\theta,0) = e^{-i\phi m'} d^{(F)}_{m',m}(\theta), \tag{B.150}$$

and the general form of $d^{(F)}_{m',m}(\theta)$ is given by

$$\begin{aligned} d^{(F)}_{m',m}(\theta) = &\sum_k (-1)^{k-m+m'} \frac{\sqrt{(F+m)!(F-m)!(F+m')!(F-m')!}}{(F+m-k)!k!(F-k-m')!(k-m+m')!} \\ &\times \cos\left(\frac{\theta}{2}\right)^{2F-2k+m-m'} \sin\left(\frac{\theta}{2}\right)^{2k-m+m'}. \end{aligned} \tag{B.151}$$

The form for the Wigner D-function $D^{(F)}_{m,m}(\phi,\theta,0)$ is general, and we want to specify it for our case such that we can calculate the matrix elements directly. In our case, we need to write out the case for $\left(D^{(F)}_{m,F}\right)^* (\phi,\theta,0)\hat{\rho}_{m,m'} D^{(F)}_{m',F}(\phi,\theta,0)$

$$D^{(F)}_{m',m}(\phi,\theta,0) = e^{-i\phi m'} d^{(F)}_{m',m}(\theta) \rightarrow \left(D^{(F)}_{m,F}\right)^* (\phi,\theta,0) = e^{i\phi m'} d^{(F)}_{m,F}(\theta), \tag{B.152}$$

where $d^{(F)}_{m,F}(\theta)$ is given by

$$d^{(F)}_{m,F}(\theta) = \sum_k (-1)^{k-F+m} \frac{\sqrt{(2F)!(F+m)!(F-m)!}}{(2F-k)!k!(F-k-m)!(k-F+m)!} \times \cos\left(\frac{\theta}{2}\right)^{3F-2k-m} \sin\left(\frac{\theta}{2}\right)^{2k-F+m}, \tag{B.153}$$

and equivalently, for $D^{(F)}_{m',F}(\phi,\theta,0)$

$$D^{(F)}_{m',m}(\phi,\theta,0) = e^{-i\phi m'} d^{(F)}_{m',m}(\theta) \rightarrow D^{(F)}_{m',F}(\phi,\theta,0) = e^{-i\phi m'} d^{(F)}_{m',F}(\theta), \tag{B.154}$$

where $d^{(F)}_{m',F}(\theta)$ is given by

$$d^{(F)}_{m',F}(\theta) = \sum_k (-1)^{k-F+m'} \frac{\sqrt{(2F)!(F+m')!(F-m')!}}{(2F-k)!k!(F-k-m')!(k-F+m')!} \times \cos\left(\frac{\theta}{2}\right)^{3F-2k-m'} \sin\left(\frac{\theta}{2}\right)^{2k-F+m'}. \tag{B.155}$$

The code used to calculate the relations is given below.

Listing B.1: SageMath Code calculating $\langle F, m \,|\, \hat{\rho} \,|\, F, m \rangle$

```
def wigner_D(F, beta):

    Wigner_matrix_D = matrix(SR, 2*F+1, 2*F+1)

    k_max = 10
    m1 = range(-F,F+1, 1)
    m2 = m1

    for i in range(2*F+1):
        for j in range(2*F+1):
            for k in range(k_max):

                a = (F + m1[i] - k)
                b = (F - m2[j] - k)
                c = (k - m1[i] + m2[j])
                d = (F + m1[i])
                e = (F - m1[i])
                f = (F + m2[j])
                g = (F - m2[j])

                logic_gate = (a >= 0) * (b >= 0) * (c >= 0) * (d >= 0) *
                    (e >= 0) * (f >= 0) * (g >= 0)

                if logic_gate == 1:
                    Wigner_matrix_D[i,j] += (-1)**(k - m1[i] + m2[j])*
                        sqrt( factorial(d)*factorial(e)*factorial(f)*
                        factorial(g) )/( factorial(a)*factorial(k)*
                        factorial(b)*factorial(c) ) \
```

```
                *cos(beta/2)**(2*F-2*k+m1[i] - m2[j])*sin(beta
                    /2)**(2*k-m1[i] + m2[j])
        else:
            a2 = 1

    return Wigner_matrix_D
```

which is just a simple summation over $m, m' \to i, j$ indices in the $\rho_F(\theta, \phi)$ expression. For $F = 2$ manifold the matrix $d^{(F)}_{m',m}(\theta)$ reads

$$d^{(2)}_{m',m}(\theta) =$$

$$\begin{bmatrix} c^4_{\theta/2} & -2c^3_{\theta/2}s_{\theta/2} & \sqrt{6}c^2_{\theta/2}s^2_{\theta/2} & -2c_{\theta/2}s^3_{\theta/2} & s^4_{\theta/2} \\ 2c^3_{\theta/2}s_{\theta/2} & 4c^4_{\theta/2} - 3c^2_{\theta/2} & (\sqrt{6}c_{\theta/2} - 2\sqrt{6}c^3_{\theta/2})s_{\theta/2} & -4c^4_{\theta/2} + 3c^2_{\theta/2} & -2c^3_{\theta/2}s_{\theta/2} \\ \sqrt{6}c^2_{\theta/2}s^2_{\theta/2} & (2\sqrt{6}c^3_{\theta/2} - \sqrt{6}c_{\theta/2})s_{\theta/2} & 6c^4_{\theta/2} - 6c^2_{\theta/2} + 1 & (\sqrt{6}c_{\theta/2} - 2\sqrt{6}c^3_{\theta/2})s_{\theta/2} & \sqrt{6}c^2_{\theta/2}s^2_{\theta/2} \\ 2c_{\theta/2}s^3_{\theta/2} & 3s^2_{\theta/2} - 4s^4_{\theta/2} & (2\sqrt{6}c^3_{\theta/2} - \sqrt{6}c_{\theta/2})s_{\theta/2} & 4c^4_{\theta/2} - 3c^2_{\theta/2} & -2c^3_{\theta/2}s_{\theta/2} \\ 0 & 2s^3_{\theta/2}c_{\theta/2} & \sqrt{6}c^2_{\theta/2}s^2_{\theta/2} & 2c^3_{\theta/2}s_{\theta/2} & c^4_{\theta/2} \end{bmatrix}. \tag{B.156}$$

B.6.3 Polarisation moment decomposition

For the $F = 2$ manifold, the general density matrix is given by

$$\rho = \begin{bmatrix} \rho_{11} & \rho_{12} & \rho_{13} & \rho_{14} & \rho_{15} \\ \rho_{21} & \rho_{22} & \rho_{23} & \rho_{24} & \rho_{25} \\ \rho_{31} & \rho_{32} & \rho_{33} & \rho_{34} & \rho_{35} \\ \rho_{41} & \rho_{42} & \rho_{43} & \rho_{44} & \rho_{45} \\ \rho_{51} & \rho_{52} & \rho_{53} & \rho_{54} & \rho_{55} \end{bmatrix}. \tag{B.157}$$

The code given below calculates polarisation moments given by the following relation

$$\rho^\kappa_q = \sum_{m,m'} (-1)^{F-m'} \langle F, m\ F, -m' \,|\, \kappa q \rangle \, \rho_{m',m}, \tag{B.158}$$

where $\rho_{m,m'}$ is the density operator element and the $\langle F\ m'\ F, -m \,|\, \kappa q \rangle$ are the corresponding Clebsch-Gordan coefficients which we express and calculate using Wigner-3j symbols.

Listing B.2: SageMath Code calculating polarisation moments, ρ^κ_q

```
F=2
m1_ar = range(-F,F+1, 1)
m2_ar = range(-F,F+1, 1)
k = [0,1,2,3,4]

rho_kq = matrix(SR, len(k),2*len(k)-1)

rho_state = matrix([[1/2, 0, 0, 0, 0], [0, 0, 0, 0, 0], [0, 0, 0, 0, 0],
    [0, 0, 0, 0, 0], [0, 0, 0, 0, 1/2]])

for i in range(len(k)):
```

```
    q = range(-k[i],k[i]+1,1)

    for j in range(len(q)):
        for n in range(2*F+1):
            for l in range(2*F+1):

                j1 = F
                m1 = m1_ar[l]
                j2 = F
                m2 = -m2_ar[n]
                j3 = k[i]
                m3 = q[j]

                rho_kq[i,j] += (-1)**(F-m2)*clebsch_gordan(j1,j2,j3,m1,
                    m2,m3)*rho_state[n,l]
rho_kq
```

This yields the following

$\kappa = 0, q = 0$

$$\rho_0^0 = \frac{\sqrt{5}}{5}(\rho_{11} + \rho_{22} + \rho_{33} + \rho_{44} + \rho_{55}), \tag{B.159}$$

$\kappa = 1, q = -1$

$$\rho_{-1}^1 = \sqrt{\frac{3}{10}}(\rho_{32} + \rho_{43}) + \frac{1}{5}(\rho_{21} + \rho_{54}), \tag{B.160}$$

$\kappa = 1, q = 0$

$$\rho_0^1 = \sqrt{\frac{2}{5}}(\rho_{55} - \rho_{11}) + \frac{1}{\sqrt{10}}(\rho_{44} - \rho_{22}), \tag{B.161}$$

$\kappa = 1, q = +1$

$$\rho_{+1}^1 = -\sqrt{\frac{3}{10}}(\rho_{23} + \rho_{34}) - \frac{1}{5}(\rho_{12} + \rho_{45}), \tag{B.162}$$

$\kappa = 2, q = -2$

$$\rho_{-2}^2 = \sqrt{\frac{2}{7}}(\rho_{31} + \rho_{42} + \rho_{53}), \tag{B.163}$$

$\kappa = 2, q = -1$

$$\rho_{-1}^2 = \frac{1}{\sqrt{14}}(\rho_{43} - \rho_{32}) - \sqrt{\frac{3}{7}}\rho_{21}, \tag{B.164}$$

$\kappa = 2, q = 0$

$$\rho_0^2 = \frac{1}{\sqrt{14}}(2\rho_{11} + 2\rho_{55} - \rho_{22} - 2\rho_{33} - \rho_{44}), \tag{B.165}$$

$\kappa = 2, q = +1$

$$\rho_{+1}^2 = \frac{3}{7}(\rho_{12} - \rho_{45}) + \frac{1}{\sqrt{14}}(\rho_{23} - \rho_{34}), \tag{B.166}$$

$\kappa = 2, q = +2$

$$\rho_{+2}^2 = \sqrt{\frac{2}{7}}(\rho_{13} + \rho_{24} + \rho_{35}), \tag{B.167}$$

$\kappa = 3, q = -3$

$$\rho^3_{-3} = \frac{1}{2}(\rho_{41} + \rho_{52}), \tag{B.168}$$

$\kappa = 3, q = -2$

$$\rho^3_{-2} = \frac{1}{2}(\rho_{53} - \rho_{31}), \tag{B.169}$$

$\kappa = 3, q = -1$

$$\rho^3_{-1} = \sqrt{\frac{3}{10}}(\rho_{21} + \rho_{54}) - \frac{1}{\sqrt{5}}(\rho_{32} - \rho_{43}), \tag{B.170}$$

$\kappa = 3, q = 0$

$$\rho^3_0 = \sqrt{\frac{1}{10}}(\rho_{55} - \rho_{11}) + \sqrt{\frac{2}{5}}(\rho_{22} - \rho_{44}), \tag{B.171}$$

$\kappa = 3, q = +1$

$$\rho^3_{+1} = -\sqrt{\frac{3}{10}}(\rho_{21} + \rho_{54}) + \frac{1}{\sqrt{5}}(\rho_{32} - \rho_{43}), \tag{B.172}$$

$\kappa = 3, q = +2$

$$\rho^3_{+2} = \frac{1}{2}(\rho_{35} - \rho_{13}), \tag{B.173}$$

$\kappa = 3, q = +3$

$$\rho^3_{+3} = -\frac{1}{2}(\rho_{14} + \rho_{25}), \tag{B.174}$$

$\kappa = 4, q = -4$

$$\rho^4_{-4} = \rho_{51}, \tag{B.175}$$

$\kappa = 4, q = -3$

$$\rho^4_{-3} = \frac{1}{\sqrt{2}}(\rho_{52} - \rho_{41}), \tag{B.176}$$

$\kappa = 4, q = -2$

$$\rho^4_{-2} = \sqrt{\frac{3}{14}}(\rho_{31} + \rho_{53}) + \frac{2}{\sqrt{7}}\rho_{42}, \tag{B.177}$$

$\kappa = 4, q = -1$

$$\rho^4_{-1} = \sqrt{\frac{1}{14}}(\rho_{54} - \rho_{21}) + \sqrt{\frac{3}{7}}(\rho_{32} - \rho_{43}), \tag{B.178}$$

$\kappa = 4, q = 0$

$$\rho^4_0 = \frac{1}{\sqrt{70}}(\rho_{11} - 4\rho_{22} + 6\rho_{33} - 4\rho_{44} + \rho_{55}), \tag{B.179}$$

$\kappa = 4, q = +1$

$$\rho^4_{+1} = \sqrt{\frac{1}{14}}(\rho_{12} - \rho_{45}) + \sqrt{\frac{3}{7}}(\rho_{34} - \rho_{23}), \tag{B.180}$$

$\kappa = 4, q = +2$

$$\rho^4_{+2} = \sqrt{\frac{3}{14}}(\rho_{13} + \rho_{35}) - \frac{2}{\sqrt{7}}\rho_{24}, \tag{B.181}$$

$\kappa = 4, q = +3$

$$\rho^4_{+3} = \frac{1}{\sqrt{2}}(\rho_{14} - \rho_{25}), \tag{B.182}$$

$\kappa = 4, q = +4$

$$\rho^4_{+4} = \rho_{15}. \tag{B.183}$$

Using the polarisation moments with the corresponding spherical harmonics, we can write

$$\rho_F(\theta, \phi) = \sqrt{\frac{4\pi}{2F+1}} \sum_{\kappa=0}^{2F} \sum_{q=-\kappa}^{\kappa} \langle F\ F\ \kappa\ 0 \,|\, F\ F\rangle\, \rho^{\kappa q} Y_{\kappa q}(\theta, \phi), \tag{B.184}$$

which we compute using the code below

Listing B.3: SageMath Code calculating angular momentum probability surface using, ρ^κ_q and spherical harmonics $Y_{\kappa q}(\theta, \phi)$

```
k = [0,1,2,3,4]

rho_FF = 0

for i in range(len(k)):

    q = range(-k[i],k[i]+1,1)

    for j in range(len(q)):

        j1 = F
        m1 = F
        j2 = k[i]
        m2 = 0
        j3 = F
        m3 = F

        rho_FF += rho_kq[i,j]*(spherical_harmonic(k[i], q[j], theta, phi
            )).conjugate()*clebsch_gordan(j1,j2,j3,m1,m2,m3)

rho_FF = (rho_FF*sqrt((4*pi/(2*F+1)))).full_simplify()
```

B.6.4 Method 1: Clebsch-Gordan Coefficients for the MW-field states and MW-field operators

We start by expressing $|F, m_F\rangle$ in the product basis

$$|F, m_F\rangle = \sum_{m_S} \sum_{m_I} \langle S, m_S, I, m_I \,|\, F, m_F\rangle\, |S, m_S\rangle\, |I, m_I\rangle\,, \tag{B.185}$$

where $\langle S, m_S, I, m_I \,|\, F, m_F\rangle$ are the Clebsch-Gordan coefficients. We use the Wigner-3j symbols to calculate the Clebsch Gordan coefficients. In the general case, the Clebsch-Gordan coefficients can be related to the Wigner-3j symbols by the following relation

$$C^j_{m_1,m_2} = \langle j_1 j_2 m_1 m_2 \,|\, j_1 j_2 j m\rangle = (-1)^{-j_1+j_2-m}(2j+1) \begin{pmatrix} j_1 & j_2 & j \\ m_1 & m_2 & -m \end{pmatrix}, \tag{B.186}$$

where the angular momenta satisfy the triangular inequalities

$$|j_1 - j_2| \leq j \leq j_1 + j_2, \tag{B.187}$$

and $j_1 + j_2 + J \in \mathbb{Z}$. Now, converting the generalised expression given by to our case gives the following expression for the Clebsch-Gordan coefficients in terms of the Wigner-3j symbols

$$C^F_{m_I,m_S} = \langle I, S, m_I, m_S \,|\, F, m_F \rangle = (-1)^{-I+S-m_F}(2F+1)\begin{pmatrix} I & S & F \\ m_I & m_S & -m_F \end{pmatrix}. \tag{B.188}$$

We use *SageMath*, a *Python* based environment to calculate the Clebsch-Gordan coefficients using the `clebsch_gordan(J, I, F, mJ, mI, mF)` function. We proceed to write out the states in the new basis.

$F = 1$, $|F, m_F\rangle = |S, m_S\rangle\,|I, m_I\rangle$

$$|F=1, m_F=-1\rangle = -\frac{1}{2}\left|\frac{1}{2},-\frac{1}{2}\right\rangle\left|\frac{3}{2},-\frac{1}{2}\right\rangle + \frac{\sqrt{3}}{2}\left|\frac{1}{2},\frac{1}{2}\right\rangle\left|\frac{3}{2},-\frac{3}{2}\right\rangle, \tag{B.189}$$

$$|F=1, m_F=0\rangle = \frac{1}{\sqrt{2}}\left|\frac{1}{2},\frac{1}{2}\right\rangle\left|\frac{3}{2},-\frac{1}{2}\right\rangle - \frac{1}{\sqrt{2}}\left|\frac{1}{2},-\frac{1}{2}\right\rangle\left|\frac{3}{2},\frac{1}{2}\right\rangle, \tag{B.190}$$

$$|F=1, m_F=+1\rangle = -\frac{\sqrt{3}}{2}\left|\frac{1}{2},-\frac{1}{2}\right\rangle\left|\frac{3}{2},\frac{3}{2}\right\rangle + \frac{1}{2}\left|\frac{1}{2},\frac{1}{2}\right\rangle\left|\frac{3}{2},\frac{1}{2}\right\rangle, \tag{B.191}$$

$F = 2$, $|F, m_F\rangle = |S, m_S\rangle\,|I, m_I\rangle$

$$|F=2, m_F=-2\rangle = \left|\frac{1}{2},-\frac{1}{2}\right\rangle\left|\frac{3}{2},-\frac{3}{2}\right\rangle, \tag{B.192}$$

$$|F=2, m_F=-1\rangle = \frac{1}{2}\left|\frac{1}{2},\frac{1}{2}\right\rangle\left|\frac{3}{2},-\frac{3}{2}\right\rangle + \frac{\sqrt{3}}{2}\left|\frac{1}{2},-\frac{1}{2}\right\rangle\left|\frac{3}{2},-\frac{1}{2}\right\rangle, \tag{B.193}$$

$$|F=2, m_F=0\rangle = \frac{1}{\sqrt{2}}\left|\frac{1}{2},\frac{1}{2}\right\rangle\left|\frac{3}{2},-\frac{1}{2}\right\rangle + \frac{1}{\sqrt{2}}\left|\frac{1}{2},-\frac{1}{2}\right\rangle\left|\frac{3}{2},\frac{1}{2}\right\rangle, \tag{B.194}$$

$$|F=2, m_F=+1\rangle = \frac{\sqrt{3}}{2}\left|\frac{1}{2},\frac{1}{2}\right\rangle\left|\frac{3}{2},\frac{1}{2}\right\rangle + \frac{1}{2}\left|\frac{1}{2},-\frac{1}{2}\right\rangle\left|\frac{3}{2},\frac{3}{2}\right\rangle, \tag{B.195}$$

$$|F=2, m_F=+2\rangle = \left|\frac{1}{2},\frac{1}{2}\right\rangle\left|\frac{3}{2},\frac{3}{2}\right\rangle. \tag{B.196}$$

Now to derive the microwave transition operators we have three possibilities, where the transition $F = 1 \to F = 2$ changes the magnetic quantum number of the hyperfine Zeeman states by 0, or ± 1 which correspond to π, and $\sigma^{\pm}$ transitions. The operators governing these properties take the initial state and transform it into the final state times so eigenvalue that normalises the state. These can be computed heuristically. For linearly polarised microwave radiation, the possible transitions between the states are

$$|F=1, m_F=-1\rangle \to |F=2, m_F=-1\rangle, \tag{B.197}$$

$$|F=1, m_F=0\rangle \to |F=2, m_F=0\rangle, \tag{B.198}$$

$$|F=1, m_F=+1\rangle \to |F=2, m_F=+1\rangle. \tag{B.199}$$

This allows us to write a matrix expression for the π-transitions

$$\hat{S}_\pi = \begin{bmatrix} 0 & 0 & 0 & 0 & S_{15} & 0 & 0 & 0 \\ 0 & 0 & 0 & 0 & 0 & S_{26} & 0 & 0 \\ 0 & 0 & 0 & 0 & 0 & 0 & S_{37} & 0 \\ 0 & 0 & 0 & 0 & 0 & 0 & 0 & 0 \\ S_{51} & 0 & 0 & 0 & 0 & 0 & 0 & 0 \\ 0 & S_{62} & 0 & 0 & 0 & 0 & 0 & 0 \\ 0 & 0 & S_{73} & 0 & 0 & 0 & 0 & 0 \\ 0 & 0 & 0 & 0 & 0 & 0 & 0 & 0 \end{bmatrix}, \tag{B.200}$$

where the indices correspond to indices of the density operator transitions. Now we compute the matrix elements for these states

$$\hat{S}_\pi \left| S, m_S \right\rangle = m_F \left| S, m_S \right\rangle, \tag{B.201}$$

$$\begin{aligned} S_{15} &= \left\langle F = 2, m_F = -1 \right| \hat{S}_\pi \left| F = 1, m_F = -1 \right\rangle = \\ &= \left(\frac{1}{2} \left\langle \frac{1}{2}, \frac{1}{2} \right| \left\langle \frac{3}{2}, -\frac{3}{2} \right| + \frac{\sqrt{3}}{2} \left\langle \frac{1}{2}, -\frac{1}{2} \right| \left\langle \frac{3}{2}, -\frac{1}{2} \right| \right) \left| \hat{S}_\pi \right| \\ &\left(-\frac{1}{2} \left| \frac{1}{2}, -\frac{1}{2} \right\rangle \left| \frac{3}{2}, -\frac{1}{2} \right\rangle + \frac{\sqrt{3}}{2} \left| \frac{1}{2}, \frac{1}{2} \right\rangle \left| \frac{3}{2}, -\frac{3}{2} \right\rangle \right) = \frac{\sqrt{3}}{4}, \end{aligned} \tag{B.202}$$

$$S_{26} = \left\langle F = 2, m_F = 0 \right| \hat{S}_\pi \left| F = 1, m_F = 0 \right\rangle = \frac{1}{2}, \tag{B.203}$$

$$S_{37} = \left\langle F = 2, m_F = +1 \right| \hat{S}_\pi \left| F = 1, m_F = +1 \right\rangle = \frac{\sqrt{3}}{4}, \tag{B.204}$$

the same result is obtained for the conjugate elements. Hence, the full matrix takes the form

$$\hat{S}_\pi = \begin{bmatrix} 0 & 0 & 0 & 0 & \frac{\sqrt{3}}{4} & 0 & 0 & 0 \\ 0 & 0 & 0 & 0 & 0 & \frac{1}{2} & 0 & 0 \\ 0 & 0 & 0 & 0 & 0 & 0 & \frac{\sqrt{3}}{4} & 0 \\ 0 & 0 & 0 & 0 & 0 & 0 & 0 & 0 \\ \frac{\sqrt{3}}{4} & 0 & 0 & 0 & 0 & 0 & 0 & 0 \\ 0 & \frac{1}{2} & 0 & 0 & 0 & 0 & 0 & 0 \\ 0 & 0 & \frac{\sqrt{3}}{4} & 0 & 0 & 0 & 0 & 0 \\ 0 & 0 & 0 & 0 & 0 & 0 & 0 & 0 \end{bmatrix}. \tag{B.205}$$

For $\hat{S}_{\sigma^+}$ the operation is defined by a raising operator of the form

$$\hat{S}_\pm \left| S, m_S \right\rangle = \sqrt{(S \mp m_S)(S \pm m_S + 1)} \left| S, m_S \pm 1 \right\rangle, \tag{B.206}$$

$$S_{16} = \left\langle F=2, m_F=0 \middle| \hat{S}_{\sigma^+} \middle| F=1, m_F=-1 \right\rangle = -\frac{\sqrt{2}}{4}, \tag{B.207}$$

$$S_{27} = \left\langle F=2, m_F=+1 \middle| \hat{S}_{\sigma^+} \middle| F=1, m_F=0 \right\rangle = -\frac{\sqrt{6}}{4}, \tag{B.208}$$

$$S_{38} = \left\langle F=2, m_F=+2 \middle| \hat{S}_{\sigma^+} \middle| F=1, m_F=+1 \right\rangle = -\frac{\sqrt{3}}{2}, \tag{B.209}$$

$$S_{41} = \left\langle F=1, m_F=-1 \middle| \hat{S}_{\sigma^+} \middle| F=2, m_F=-2 \right\rangle = \frac{\sqrt{3}}{2}, \tag{B.210}$$

$$S_{52} = \left\langle F=1, m_F=0 \middle| \hat{S}_{\sigma^+} \middle| F=2, m_F=-1 \right\rangle = \frac{\sqrt{6}}{4}, \tag{B.211}$$

$$S_{63} = \left\langle F=1, m_F=+1 \middle| \hat{S}_{\sigma^+} \middle| F=2, m_F=0 \right\rangle = \frac{\sqrt{2}}{4}, \tag{B.212}$$

$$\hat{S}_{\sigma^+} = \begin{bmatrix} 0 & 0 & 0 & 0 & 0 & -\frac{\sqrt{2}}{4} & 0 & 0 \\ 0 & 0 & 0 & 0 & 0 & 0 & -\frac{\sqrt{6}}{4} & 0 \\ 0 & 0 & 0 & 0 & 0 & 0 & 0 & -\frac{\sqrt{3}}{2} \\ \frac{\sqrt{3}}{2} & 0 & 0 & 0 & 0 & 0 & 0 & 0 \\ 0 & \frac{\sqrt{6}}{4} & 0 & 0 & 0 & 0 & 0 & 0 \\ 0 & 0 & \frac{\sqrt{2}}{4} & 0 & 0 & 0 & 0 & 0 \\ 0 & 0 & 0 & 0 & 0 & 0 & 0 & 0 \\ 0 & 0 & 0 & 0 & 0 & 0 & 0 & 0 \end{bmatrix}. \tag{B.213}$$

For $\hat{S}_{\sigma^-}$ we have

$$S_{14} = \left\langle F=2, m_F=-2 \middle| \hat{S}_{\sigma^-} \middle| F=1, m_F=-1 \right\rangle = \frac{\sqrt{3}}{2}, \tag{B.214}$$

$$S_{25} = \left\langle F=2, m_F=-1 \middle| \hat{S}_{\sigma^-} \middle| F=1, m_F=0 \right\rangle = \frac{\sqrt{6}}{4}, \tag{B.215}$$

$$S_{36} = \left\langle F=2, m_F=0 \middle| \hat{S}_{\sigma^-} \middle| F=1, m_F=+1 \right\rangle = \frac{\sqrt{2}}{4}, \tag{B.216}$$

$$S_{61} = \left\langle F=1, m_F=-1 \middle| \hat{S}_{\sigma^-} \middle| F=2, m_F=0 \right\rangle = -\frac{\sqrt{2}}{4}, \tag{B.217}$$

$$S_{72} = \left\langle F=1, m_F=0 \middle| \hat{S}_{\sigma^-} \middle| F=2, m_F=+1 \right\rangle = -\frac{\sqrt{6}}{4}, \tag{B.218}$$

$$S_{83} = \left\langle F=1, m_F=+1 \middle| \hat{S}_{\sigma^-} \middle| F=2, m_F=+2 \right\rangle = -\frac{\sqrt{3}}{2}, \tag{B.219}$$

$$\hat{S}_{\sigma^-} = \begin{bmatrix} 0 & 0 & 0 & \frac{\sqrt{3}}{2} & 0 & 0 & 0 & 0 \\ 0 & 0 & 0 & 0 & \frac{\sqrt{6}}{4} & 0 & 0 & 0 \\ 0 & 0 & 0 & 0 & 0 & \frac{\sqrt{2}}{4} & 0 & 0 \\ 0 & 0 & 0 & 0 & 0 & 0 & 0 & 0 \\ 0 & 0 & 0 & 0 & 0 & 0 & 0 & 0 \\ -\frac{\sqrt{2}}{4} & 0 & 0 & 0 & 0 & 0 & 0 & 0 \\ 0 & -\frac{\sqrt{6}}{4} & 0 & 0 & 0 & 0 & 0 & 0 \\ 0 & 0 & -\frac{\sqrt{3}}{2} & 0 & 0 & 0 & 0 & 0 \end{bmatrix}. \tag{B.220}$$

B.6.5 Method 2: Magnetic Dipole Moment for MW-field operators

For linearly polarised microwave radiation, the possible transitions between the states are

$$|F=1, m_F=-1\rangle \rightarrow |F=2, m_F=-1\rangle, \tag{B.221}$$
$$|F=1, m_F=0\rangle \rightarrow |F=2, m_F=0\rangle, \tag{B.222}$$
$$|F=1, m_F=+1\rangle \rightarrow |F=2, m_F=+1\rangle. \tag{B.223}$$

This allows us to write a matrix expression for the π-transitions

$$\hat{S}_{\pi} = \begin{bmatrix} 0 & 0 & 0 & 0 & S_{15} & 0 & 0 & 0 \\ 0 & 0 & 0 & 0 & 0 & S_{26} & 0 & 0 \\ 0 & 0 & 0 & 0 & 0 & 0 & S_{37} & 0 \\ 0 & 0 & 0 & 0 & 0 & 0 & 0 & 0 \\ S_{51} & 0 & 0 & 0 & 0 & 0 & 0 & 0 \\ 0 & S_{62} & 0 & 0 & 0 & 0 & 0 & 0 \\ 0 & 0 & S_{73} & 0 & 0 & 0 & 0 & 0 \\ 0 & 0 & 0 & 0 & 0 & 0 & 0 & 0 \end{bmatrix}, \tag{B.224}$$

where the indices correspond to indices of the density operator transitions. Following from a previous work[1] we can compute the transition dipole moment elements by writing

$$S^{\pi} = \left\langle F+1, m_F \middle| \hat{S}_{\pi} \middle| F, m_F \right\rangle = \\ = (-1)^{F+m_F-1} \sqrt{\frac{2I(I+1)}{2I+1}} \begin{pmatrix} F+1 & 1 & F \\ -m_F & 0 & m_F \end{pmatrix}, \tag{B.225}$$

[1] https://arxiv.org/pdf/1904.12073.pdf

where the matrix represents the Wigner-3j symbols. Computing the elements explicitly, for example $|F=1, m_F=-1\rangle \rightarrow |F=2, m_F=-1\rangle$ gives the S^{π}_{15} element

$$S^{\pi}_{15} = S^{\pi}_{51} = (-1)^{1+1-1}\sqrt{\frac{15}{8}}\begin{pmatrix} 2 & 1 & 1 \\ 1 & 0 & -1 \end{pmatrix} = \frac{\sqrt{3}}{4}, \tag{B.226}$$

$$S^{\pi}_{26} = S^{\pi}_{62} = \frac{1}{2}, \tag{B.227}$$

$$S^{\pi}_{37} = S^{\pi}_{73} = \frac{\sqrt{3}}{4}. \tag{B.228}$$

Hence the full matrix reads

$$\hat{S}_{\pi} = \begin{bmatrix} 0 & 0 & 0 & 0 & \frac{\sqrt{3}}{4} & 0 & 0 & 0 \\ 0 & 0 & 0 & 0 & 0 & \frac{1}{2} & 0 & 0 \\ 0 & 0 & 0 & 0 & 0 & 0 & \frac{\sqrt{3}}{4} & 0 \\ 0 & 0 & 0 & 0 & 0 & 0 & 0 & 0 \\ \frac{\sqrt{3}}{4} & 0 & 0 & 0 & 0 & 0 & 0 & 0 \\ 0 & \frac{1}{2} & 0 & 0 & 0 & 0 & 0 & 0 \\ 0 & 0 & \frac{\sqrt{3}}{4} & 0 & 0 & 0 & 0 & 0 \\ 0 & 0 & 0 & 0 & 0 & 0 & 0 & 0 \end{bmatrix}. \tag{B.229}$$

For negative circularly polarised microwave radiation, the possible transitions between the states are

$$|F=1, m_F=-1\rangle \rightarrow |F=2, m_F=-2\rangle, \tag{B.230}$$

$$|F=1, m_F=0\rangle \rightarrow |F=2, m_F=-1\rangle, \tag{B.231}$$

$$|F=1, m_F=+1\rangle \rightarrow |F=2, m_F=0\rangle. \tag{B.232}$$

The only non-zero matrix elements for the σ^--transitions are

$$\hat{S}_{\sigma^-} = \begin{bmatrix} 0 & 0 & 0 & S_{14} & 0 & 0 & 0 & 0 \\ 0 & 0 & 0 & 0 & S_{25} & 0 & 0 & 0 \\ 0 & 0 & 0 & 0 & 0 & S_{36} & 0 & 0 \\ S_{41} & 0 & 0 & 0 & 0 & 0 & 0 & 0 \\ 0 & S_{52} & 0 & 0 & 0 & 0 & 0 & 0 \\ 0 & 0 & S_{63} & 0 & 0 & 0 & 0 & 0 \\ 0 & 0 & 0 & 0 & 0 & 0 & 0 & 0 \\ 0 & 0 & 0 & 0 & 0 & 0 & 0 & 0 \end{bmatrix}. \tag{B.233}$$

We can compute the transition dipole moment elements by writing

$$\begin{aligned} S^{\sigma^-} &= \left\langle F+1, m_F-1 \middle| \hat{S}_{\sigma^-} \middle| F, m_F \right\rangle = \\ &= -(-1)^{F+m_F}\sqrt{\frac{4I(I+1)}{2I+1}}\begin{pmatrix} F+1 & 1 & F \\ -(m_F-1) & -1 & m_F \end{pmatrix}, \end{aligned} \tag{B.234}$$

$$S^{\sigma^-} = \left\langle F, m_F \left| \hat{S}_{\sigma^-} \right| F+1, m_F - 1 \right\rangle = \\ = (-1)^{F+m_F} \sqrt{\frac{4I(I+1)}{2I+1}} \begin{pmatrix} F+1 & 1 & F \\ -(m_F-1) & -1 & m_F \end{pmatrix}, \tag{B.235}$$

where the matrix represents the Wigner-3j symbols. Computing the elements explicitly, for example $|F=1, m_F=-1\rangle \rightarrow |F=2, m_F=-2\rangle$ gives the $S_{14}^{\sigma^-}$ element

$$S_{14}^{\sigma^-} = -(-1)^{1+1}\sqrt{\frac{15}{8}} \begin{pmatrix} 2 & 1 & 1 \\ -2 & -1 & -1 \end{pmatrix} = \frac{\sqrt{3}}{4}, \tag{B.236}$$

$$S_{25}^{\sigma^-} = \frac{\sqrt{6}}{4}, \tag{B.237}$$

$$S_{36}^{\sigma^-} = \frac{\sqrt{2}}{4}, \tag{B.238}$$

$$S_{61}^{\sigma^-} = -\frac{\sqrt{2}}{4}, \tag{B.239}$$

$$S_{72}^{\sigma^-} = -\frac{\sqrt{6}}{4}, \tag{B.240}$$

$$S_{83}^{\sigma^-} = -\frac{\sqrt{3}}{2}. \tag{B.241}$$

The full matrix reads

$$\hat{S}_{\sigma^-} = \begin{bmatrix} 0 & 0 & 0 & \frac{\sqrt{3}}{2} & 0 & 0 & 0 & 0 \\ 0 & 0 & 0 & 0 & \frac{\sqrt{6}}{4} & 0 & 0 & 0 \\ 0 & 0 & 0 & 0 & 0 & \frac{\sqrt{2}}{4} & 0 & 0 \\ 0 & 0 & 0 & 0 & 0 & 0 & 0 & 0 \\ 0 & 0 & 0 & 0 & 0 & 0 & 0 & 0 \\ -\frac{\sqrt{2}}{4} & 0 & 0 & 0 & 0 & 0 & 0 & 0 \\ 0 & -\frac{\sqrt{6}}{4} & 0 & 0 & 0 & 0 & 0 & 0 \\ 0 & 0 & -\frac{\sqrt{3}}{2} & 0 & 0 & 0 & 0 & 0 \end{bmatrix}. \tag{B.242}$$

For σ^+-transitions we have the following possibilities

$$|F=1, m_F=-1\rangle \rightarrow |F=2, m_F=0\rangle, \tag{B.243}$$

$$|F=1, m_F=0\rangle \rightarrow |F=2, m_F=+1\rangle, \tag{B.244}$$

$$|F=1, m_F=+1\rangle \rightarrow |F=2, m_F=+2\rangle, \tag{B.245}$$

with the magnetic dipole transition matrix given by

$$\hat{S}_{\sigma^+} = \begin{bmatrix} 0 & 0 & 0 & 0 & 0 & S_{16} & 0 & 0 \\ 0 & 0 & 0 & 0 & 0 & 0 & S_{27} & 0 \\ 0 & 0 & 0 & 0 & 0 & 0 & 0 & S_{38} \\ S_{41} & 0 & 0 & 0 & 0 & 0 & 0 & 0 \\ 0 & S_{52} & 0 & 0 & 0 & 0 & 0 & 0 \\ 0 & 0 & S_{63} & 0 & 0 & 0 & 0 & 0 \\ 0 & 0 & 0 & 0 & 0 & 0 & 0 & 0 \\ 0 & 0 & 0 & 0 & 0 & 0 & 0 & 0 \end{bmatrix}. \tag{B.246}$$

For σ^+ radiation, the dipole moment is given by

$$S^{\sigma^+} = \left\langle F+1, m_F+1 \middle| \hat{S}_{\sigma^+} \middle| F, m_F \right\rangle = \\ = (-1)^{F-m_F} \sqrt{\frac{4I(I+1)}{2I+1}} \begin{pmatrix} F+1 & 1 & F \\ -(m_F+1) & 1 & m_F \end{pmatrix}, \tag{B.247}$$

$$S^{\sigma^+} = \left\langle F, m_F \middle| \hat{S}_{\sigma^+} \middle| F+1, m_F+1 \right\rangle = \\ = -(-1)^{F-m_F} \sqrt{\frac{4I(I+1)}{2I+1}} \begin{pmatrix} F+1 & 1 & F \\ -(m_F+1) & 1 & m_F \end{pmatrix}. \tag{B.248}$$

Computing the elements explicitly, for example $|F=1, m_F=-1\rangle \rightarrow |F=2, m_F=0\rangle$ gives the $S_{16}^{\sigma^+}$ element

$$S_{16}^{\sigma^+} = S_{61}^{\sigma^+} = -(-1)^{1-1} \sqrt{\frac{15}{8}} \begin{pmatrix} 2 & 1 & 1 \\ 0 & 1 & -1 \end{pmatrix} = -\frac{\sqrt{2}}{4}, \tag{B.249}$$

$$S_{27}^{\sigma^+} = -\frac{\sqrt{6}}{4}, \tag{B.250}$$

$$S_{38}^{\sigma^+} = -\frac{\sqrt{3}}{2}, \tag{B.251}$$

$$S_{41}^{\sigma^+} = \frac{\sqrt{3}}{2}, \tag{B.252}$$

$$S_{52}^{\sigma^+} = \frac{\sqrt{6}}{4}, \tag{B.253}$$

$$S_{63}^{\sigma^+} = \frac{\sqrt{2}}{4}, \tag{B.254}$$

(B.255)

$$\hat{S}_{\sigma^+} = \begin{bmatrix} 0 & 0 & 0 & 0 & 0 & -\frac{\sqrt{2}}{4} & 0 & 0 \\ 0 & 0 & 0 & 0 & 0 & 0 & -\frac{\sqrt{6}}{4} & 0 \\ 0 & 0 & 0 & 0 & 0 & 0 & 0 & -\frac{\sqrt{3}}{2} \\ \frac{\sqrt{3}}{2} & 0 & 0 & 0 & 0 & 0 & 0 & 0 \\ 0 & \frac{\sqrt{6}}{4} & 0 & 0 & 0 & 0 & 0 & 0 \\ 0 & 0 & \frac{\sqrt{2}}{4} & 0 & 0 & 0 & 0 & 0 \\ 0 & 0 & 0 & 0 & 0 & 0 & 0 & 0 \\ 0 & 0 & 0 & 0 & 0 & 0 & 0 & 0 \end{bmatrix}. \tag{B.256}$$

APPENDIX C

Appendix: Experimental Apparatus

C.1 Cat-Eye Laser design

The key working principle of the cat-eye laser design is that the wavelength tuning is provided by a low-loss interference filter in contrast to commonly used diffraction gratings in the Littrow ECDL configuration [70, 71, 73]. An interference filter is a passive optical element which reflects and transmits light depending on the wavelength through interference effects between the incident and reflected light at the thin film boundary. Normally, in the grating ECDL design, the grating provides optical feedback as well as the wavelength selection. This tends to result in the output beam steering when the laser wavelength is scanned. The cat-eye laser design avoids this by separating the optical feedback and wavelength selection through the use of two separate optical elements - a partially reflective mirror - outcoupler and an interference filter (see Fig. C.1). This gives the freedom in choosing the optical feedback elements independently of the wavelength tuning, something that the grating based ECDL designs can seldom offer. Another advantage of the cat-eye geometry is that it allows for a linear cavity design for wavelength tuning and feedback which is mechanically more robust than the typical Litrrow type ECDL laser geometry making it passively more robust [73, 76].

Our home made design closely follows the work done in [73–75]. First, our laser diode (LD)[1], is collimated using a high NA, short focal length, $f = 3.1$ mm lens in an adjustable collimation package[2]. The collimation package is mounted inside a small thermal mass cube which is temperature stabilised to ≈ 0.3 mK by four Peltier elements[3], (see Fig. C.3) for temperature stability. The collimated light is then

[1] EagleYard EYP-RWE-0810-03010-1300-SOT02-0000
[2] Thorlabs LTN330-B
[3] RS Stock No. 490-1272

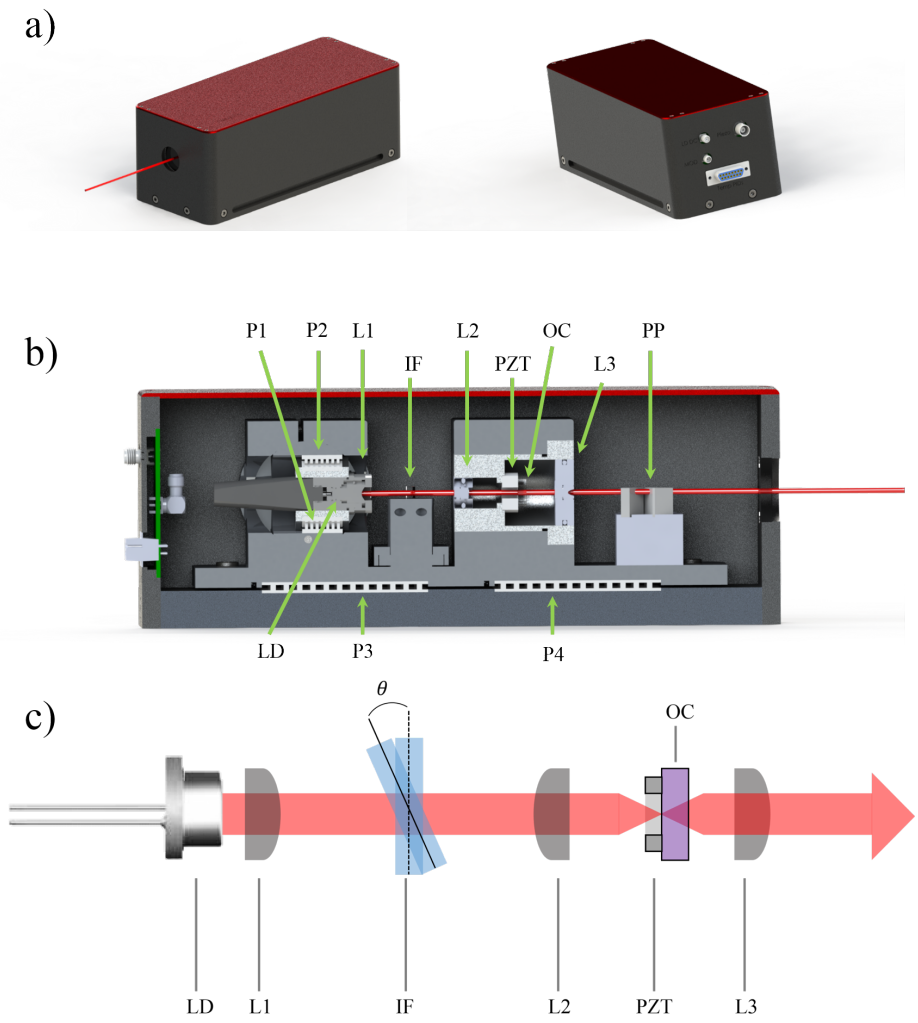

Figure C.1: a) Laser housing. b) Side cross-sectional view of the laser. P1 and P2 - laser head peltiers. LD - laser diode chip. L1 - laser diode collimation lens. P3 and P4 - laser bottom baseplate peltiers. IF - interference filter. L2 - collimation lens which focuses on the cavity outcoupler, OC. PZT - piezo stack that moves the partially reflective cavity mirror. OC - outcoupler, partially reflective cavity mirror which provides optical feedback to LD. L3 - collimation lens. PP - prism pair for beam shaping. c) Top down schematic drawing of the laser components.

incident upon the interference filter, IF[4] at an angle θ. The wavelength tuning as a function of the angle of incidence θ between the incoming light and the interference filter is given by [72]

$$\lambda(\theta) = \lambda_0 \sqrt{1 - \left(\frac{\sin\theta}{n_{\text{eff}}}\right)^2}, \tag{C.1}$$

[4]Radiant Dyes Interference filter for 798 nm

where λ_0 is the wavelength at $\theta = 90°$ and $n_{\text{eff}} \approx 2$ is the refractive index of the interference filter. After the interference filter, a second lens[5] is used to focus the beam onto a planar outcoupler (OC)[6] which provides the optical feedback of the laser. The optical feedback is adjusted by mounting the laser diode into a cylinder which can be rotated to adjust the angle normal to the outcoupler. The outcoupler is glued onto a piezo-electrical ring (PZT)[7]. The loaded piezo of mass m with a loaded outcoupler mass M will have a resonance frequency given by

$$f_{\text{res}} = f_0 \sqrt{\frac{m}{m+3M}} \approx 48 \text{ kHz}, \tag{C.2}$$

where $f_0 = 1/2\pi\sqrt{k/m} \approx 55$ kHz with $k = 720$ N/μm and $m = 6$ g for NAC2124-H06, $M = 0.5$ g for OC. This is the piezo locking bandwidth limit. After the outcoupler, the light is re-collimated with another lens L3[8]. We use an additional anamorphic prism pair[9] after the last lens L3 to correct for the ellipticity of the output beam. The cavity laser baseplate is stabilised independently from the LD head using TEC coolers[10]. This has a large thermal mass and further increases the long term stability to thermal drifts. The temperature sensing is done using small time constant NTCs[11]. To ensure better thermal contact between the peltiers and the contact surfaces we add self-adhering thermally conductive graphite pads. To reduce outgassing, where gluing is required, two component vacuum compatible glue is used[12].

The lasing threshold optimisation is done in a two stage process. First, without any optical feedback, the laser is collimated using the collimator L1. Once the output is collimated, a focussing lens L2 is used to focus on the outcoupler OC and the optical feedback is monitored on the output of the laser. In this case, the interference filter, IF, is not present during this process. The laser head is adjusted by rotating it in order to optimise for the beam alignment relative to the outcoupler - this additionally optimises the optical feedback. Once the feedback is optimised, then a focus-walk method is employed to fine adjust it. In this case, L1 and L2 are adjusted sequentially and iteratively to improve the feedback - this tunes the mode matching condition of the reflected beam from the outcoupler. After the optical feedback is optimised, the interference filter is inserted to adjust the wavelength. The procedure involves setting the laser at an operational current producing sufficient power for the experiments. A wavemeter after an optical isolator is used to monitor the wavelength. The temperature of the laser head is set in the range of $18 - 22$ C° with the cavity temperature set close to the temperature of the lab. The interference filter is then rotated incrementally until we get close to the desired wavelength and then locked in by two fixing screws.

[5]Thorlabs A280TM-B
[6]Laseroptik R= 15% 780 nm/0° (R±2%) with AR 780 nm/0° on $D = 10$ mm, $t = 3$ mm
[7]Noliac NAC2124-H06, 6 mm height, 6.6 μm stroke, 920 nF capacitance
[8]Thorlabs A220TM-B
[9]Thorlabs PS871-B
[10]RS Stock No. 765-0028
[11]Digi-Key 495-75198-ND
[12]Torr Seal Low Vapor Pressure Epoxy

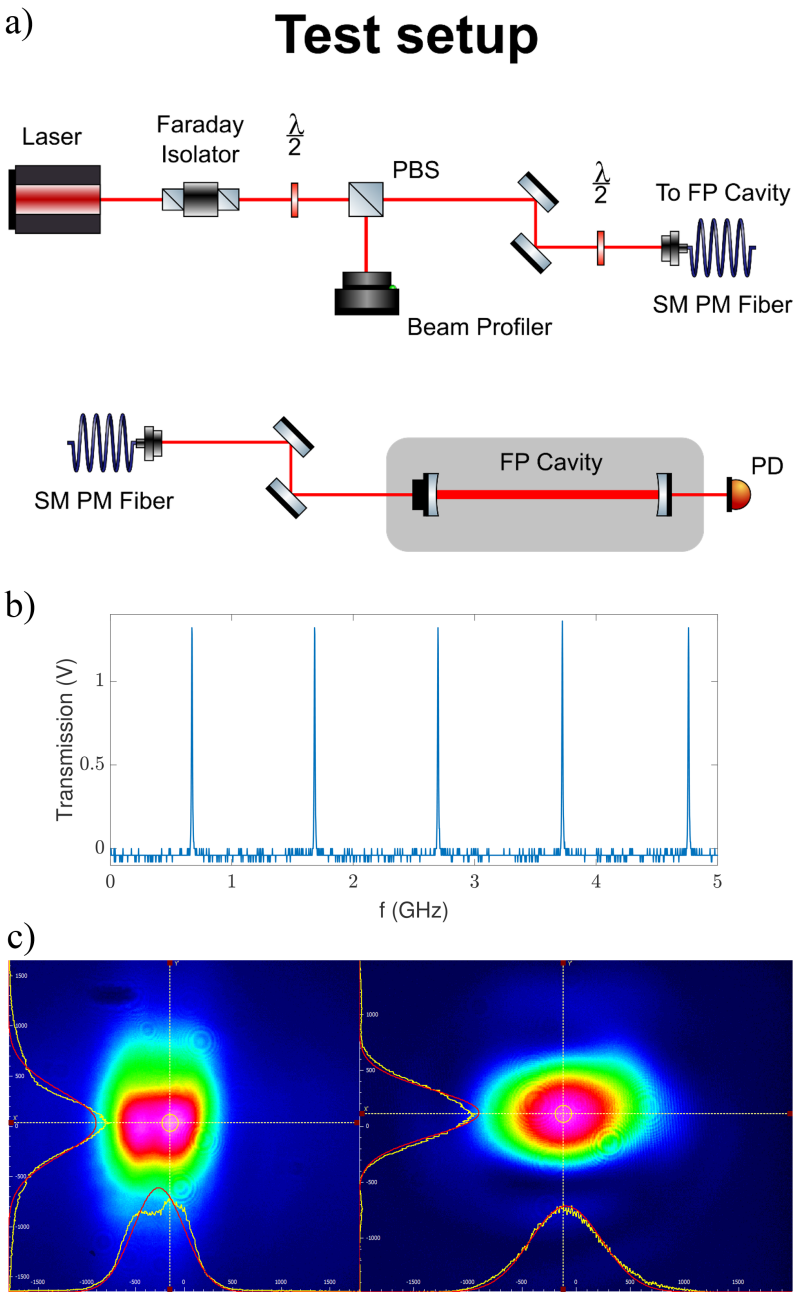

Figure C.2: a) Cavity and beam profiler setup to test and optimise the Cat-Eye laser performance. Here the beam profiler is Thorlabs BC106N-VIS/M and the cavity is Toptica FPI 100. b) Laser cavity scan in free running mode of the laser. Single longitudinal cavity modes are seen. c) Laser beam profile in different running modes. LEFT: No optical feedback, free running. RIGHT: Optimised beam profile with optical feedback at 200 mA.

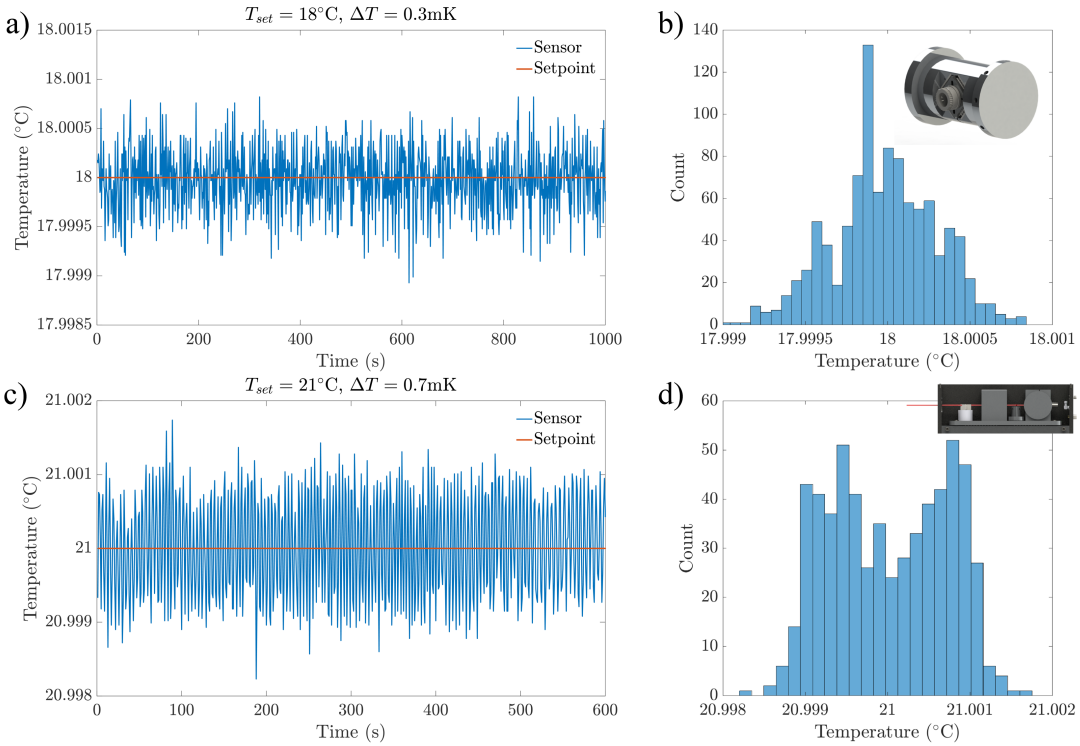

Figure C.3: a) Cat-eye laser head temperature stability over time. b) Histogram showing the binned temperature readings indicating an approximate Gaussian distribution. The inset image shows the laser head of the body that is temperature stabilised. c) Temperature trace of the laser cavity baseplate. d) Histogram showing the binned temperature data indicating a bimodal distribution. The inset shows the baseplate body which the temperature controller stabilises.

Fine adjustments of the wavelength are further done using temperature and current of the laser. We use a Fabry-Perot cavity to confirm that the laser is running single mode, see Fig. C.2. The temperature control of the laser is done using a commercial temperature controller[13]. A key feature of this particular temperature controller is that it has a self-tuning PID function which allows us to avoid the use of heuristic PID tuning methods. Our current controllers are home made and are based on the Hall-Libbrecht-Durfee design [77, 78]. The key feature of this current driver is that the current setpoint is done digitally using a micro-controller and a high resolution DAC which improves current stability and removes long term temperature induced current drifts typical of current drivers which have analog setpoint architectures. To further improve signal stability and reduce EMI noise, our current driver board is designed on a commercially milled 4-layer PCB (instead of the standard 2-layer layout) where each layer plane is used exclusively for signals, ground, positive and negative supply connections. Having 4 separate layers avoids breaking up the ground plane,

[13]Meerstetter Engineering TEC-1091

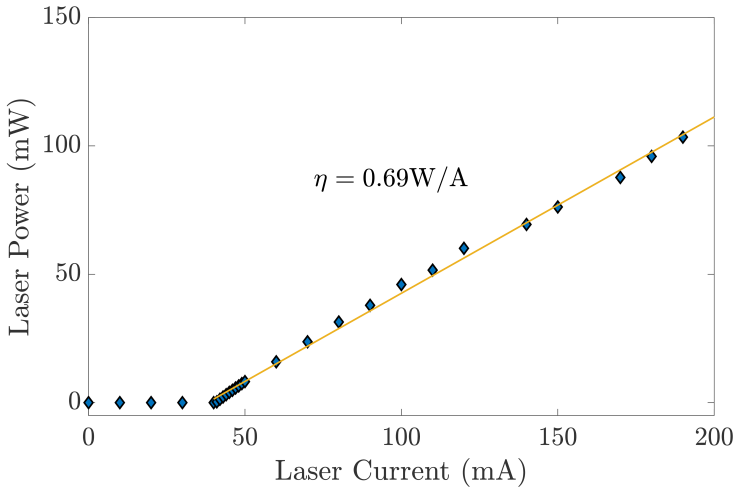

Figure C.4: Laser power as a function of current. The gradient in the linear region is the laser efficiency curve which is characterised as the gradient of the power over the current.

which prevents the formation of current loops which produce noise, especially if the divided planes have different temperatures due to the proximity of different electronic elements. Moreover, having separate ground, supply and signal planes enables better routing reducing additional cross-talk [79].

Over a one year period of continuous operation the only adjustments for optimal operation were small laser current adjustments (typically ± 5 mA). No mechanical (interference filter movement) or temperature adjustments were needed. The warm up time to stability was measured to be typically < 10 mins before locking. The only significant drawback of the current design is the long cavity length which reduces the free spectral range of the laser. This can be trivially circumvented with an improved filter - cavity design.

Bibliography

[1] C. Guillaume, H. Poincaré, 1900, Eds., Congres International de Physique Réuni (Gauthier-Villars, Paris).

[2] D. Budker, W. Gawlik, D. F. Kimball, S. M. Rochester, V. V. Yashchuk, and A. Weis, *Resonant nonlinear magneto-optical effects in atoms*, Rev. Mod. Phys. **74**, 1153, (2002).

[3] A. Kastler, *Some suggestions concerning the production and detection by optical means of inequalities in the populations of levels of spatial quantization in atoms. Application to the Stern and Gerlach and magnetic resonance experiments*, J. Phys. Radium **11**, 255–265, (1950).

[4] Dehmelt, H. *Modulation of a light beam by precessing absorbing atoms*, Phys. Rev. **105**, 1924–1925, (1957).

[5] W. Bell, A. Bloom, *Optical detection of magnetic resonance in alkali metal vapor*, Phys. Rev. **107**, 1559–1565, (1957).

[6] F. A. Hopf, R. F. Shea, and M. O. Scully, *Theory of Optical Free-Induction Decay and Two-Photon Superradiance*, Phys. Rev. A **7**, (2105).

[7] D. Budker, M. Romalis, *Optical magnetometry*, Nature Physics, **3(4)**, 227–234, (2007).

[8] Kominis, I. K., Kornack, T. W., Allred, J. C., Romalis, M. V. *A subfemtotesla multichannel atomic magnetometer*, Nature **422**, 596–599, (2003).

[9] P. Ripka, *Magnetic Sensors and Magnetometers*, Artech House, (2001).

[10] J. Lenz and S. Edelstein, *Magnetic sensors and their applications*, IEEE Sensors Journal, vol. **6**, no. 3, pp. 631-649, (2006).

[11] S. A. Murthy, D. Krause, Jr., Z. L. Li, and L. R. Hunter, *New limits on the electron electric dipole moment from cesium*, Phys. Rev. Lett. **63**, 965–968, (1989).

[12] M. V. Romalis, W. C. Griffith, J. P. Jacobs, and E. N. Fortson, *New Limit on the Permanent Electric Dipole Moment of* ^{199}*Hg*, Phys. Rev. Lett. **86**, 2505, (2001).

[13] D. Budker, S. K. Lamoreaux, A. O. Sushkov, and O. P. Sushkov, *Sensitivity of condensed-matter P- and T-violation experiments*, Phys. Rev. A, **73**, 022107, (2006).

[14] H. Xia, A. Ben-Amar Baranga, D. Hoffman, and M. V. Romalis, *Magnetoencephalography with an atomic magnetometer*, Appl. Phys. Lett., **89**, 211104, (2006).

[15] E. Boto, N. Holmes, J. Leggett, G. Roberts, V. Shah, S. S. Meyer, L. D. Muñoz, K. J. Mullinger, T. M. Tierney, S. Bestmann, G. R. Barnes, R. Bowtell, and M. J. Brookes, *Moving magnetoencephalography towards real-world applications with a wearable system*, Nature, **555** (7698): 657–661, (2018).

[16] K. Jensen, R. Budvytyte, R. A. Thomas, T. Wang, A. M. Fuchs, M. V. Balabas, G. Vasilakis, L. D. M., Hans C. Stærkind, J. H. Müller, T. Heimburg, S.-P. Olesen and E. S. Polzik, *Non-invasive detection of animal nerve impulses with an atomic magnetometer operating near quantum limited sensitivity*, Scientific Reports **6**, 29638, (2016).

[17] R. Fenici, D. Brisinda, and A. M. Meloni, *Clinical application of magnetocardiography*, Exp. Rev. Mol. Diagn., **5**, 291–313, (2005).

[18] R. Wyllie, M. Kauer, R. T. Wakai, and T. G. Walker, *Optical magnetometer array for fetal magnetocardiography*, Opt. Lett., **37**, 2247-2249, (2012).

[19] J. C. Allred and R.N. Lyman, T.W. Kornack and M.V. Romalis, *High-Sensitivity Atomic Magnetometer Unaffected by Spin-Exchange Relaxation*, Phys. Rev. Lett., **89**, 130801, (2002).

[20] J. Kitching, *Chip-scale atomic devices*, Appl. Phys. Rev. **5**, 031302, (2018).

[21] E. B. Alexandrov, M. V. Balabas, V. N. Kulyasov, A. E. Ivanov, A. S. Pazgalev, J. L. Rasson, A. K. Vershovski, and N. N. Yakobson, *Three-component variometer based on a scalar potassium sensor*, Meas. Sci. Technol., **15**, 918–922, (2004).

[22] H. Huang, H. Dong, L. Chen, and Y. Gao, *Single-beam three-axis atomic magnetometer*, Appl. Phys. Lett., **109**, 062404, (2016).

[23] S. J. Seltzer and M. V. Romalis, *Unshielded three-axis vector operation of a spin-exchange-relaxation-free atomic magnetometer*, Appl. Phys. Lett., **85**, 4804, (2004).

[24] B. Patton, E. Zhivun, D. C. Hovde, and D. Budker, *All-Optical Vector Atomic Magnetometer*, Phys. Rev. Lett., **113**, 013001, (2014).

[25] S. J. Ingleby, C. O'Dwyer, P. F. Griffin, A. S. Arnold, and E. Riis, *Orientational effects on the amplitude and phase of polarimeter signals in double-resonance atomic magnetometry*, Phys. Rev. A, **96**, 013429, (2017).

[26] H. C. Huang, H. F. Dong, X. Y. Hu, L. Chen, and Y. Gao, *Three-axis atomic magnetometer based on spin precession modulation*, Appl. Phys. Lett., **107**, 182403, (2015).

[27] S. Jammi, T. Pyragius, M. G. Bason, H. Marin Florez, T. Fernholz, *Dispersive detection of radio-frequency-dressed states*, Phys. Rev. A, **97**, 043416, (2018).

[28] F. Gentile, J. Johnson. K. Poulios, T. Fernholz, *Ring-shaped atom-trap lattices using multipole dressing fields*, arXiv:1909.01186, (2019).

[29] R. Stevenson, M. R. Hush, T. Bishop, I. Lesanovsky, and T. Fernholz, *Sagnac Interferometry with a Single Atomic Clock*, Phys. Rev. Lett. **115**, 163001, (2015).

[30] M. E. Limes, E. L. Foley, T. W. Kornack, S. Caliga, S. McBride, A. Braun, W. Lee, V. G. Lucivero, M. V. Romalis, *Total-field atomic gradiometer for unshielded portable magnetoencephalography*, arXiv:2001.03534, (2020).

[31] J. C. Maxwell, *Illustrations of the dynamical theory of gases*, Philosophical Magazine **19**, 19-32 and Philosophical Magazine **20**, 21-37, (1860).

[32] D. Budker, D. F. Kimball, *Optical Magnetometry*, Cambridge University Press, ISBN: 9781107010352, (2013).

[33] B. Julsgaard, *Entanglement and Quantum Interactions with Macroscopic Gas Samples*, University of Aarhus, PhD Thesis, (2003).

[34] F. L. Pedrotti, L. M. Pedrotti, L. S. Pedrotti, *Introduction to Optics*, 3rd Edition, Pearson International Edition, (2006).

[35] I. S. Grant, W. R. Phillips, *Electromagnetism*, 2nd Edition, Wiley, (1990).

[36] B. E. A. Saleh, M. C. Teich, *Fundamentals of Photonics*, 2nd Edition, Wiley, (2006).

[37] A. Yariv, *Quantum Electronics*, 3^{rd} Edition, Wiley, (1989).

[38] M. Auzinsh, D. Budker, & S. Rochester, *Optically Polarized Atoms*, OUP Oxford, (2010).

[39] J. M. Hollas, *Modern Spectroscopy*, John Wiley & Sons, (2004).

[40] M. Schmitt, *High Resolution Laser Spectroscopy of Dysprosium*, Master Thesis, (2012).

[41] D. Budker, W. Gawlik, D. F. Kimball, S. M. Rochester, V. V. Yashchuk, and A. Weis, *Resonant nonlinear magneto-optical effects in atoms*, Rev. Mod. Phys., **74**, 1153–1201, (2002).

[42] S. R. de Echaniz, M. Koschorreck, M. Napolitano, M. Kubasik, and M. W. Mitchell, *Hamiltonian design in atom-light interactions with rubidium ensembles: A quantum-information toolbox*, Phys. Rev. A, **77**, 032316, (2008).

[43] J.M. Geremia, J. K. Stockton and H. Mabuchi, *Tensor polarizability and dispersive quantum measurement of multilevel atoms*, Phys. Rev. A, **73**, 042112, (2006).

[44] D. V. Kupriyanov, O. S. Mishina, I. M. Sokolov, B. Julsgaard, and E. S. Polzik, *Multimode entanglement of light and atomic ensembles via off-resonant coherent forward scattering*, Phys. Rev. A 71, 032348, (2005).

[45] V. Borisovich Braginsky, F. Y. Khalili, K. S. Thorne, *Quantum Measurement*, (1st Edition), Cambridge University Press, ISBN 978-0521484138, (1992).

[46] H. J. Metcalf and P. van der Straten, *Laser Cooling and Trapping*, Springer, New York, (1999).

[47] W. E. Bell and A. L. Bloom, *Optically Driven Spin Precession*, Phys. Rev. Lett., **6**, 280, (1961).

[48] D. Steck, *Rubidium D Line Data*, http://steck.us/alkalidata/, (2009).

[49] S. J. Seltzer, *Developments in Alkali-Metal Atomic Magnetometry*, PhD Thesis, Princeton University, (2008).

[50] C. B. Alcock, V. P. Itkin, and M. K. Horrigan, *Vapor-Pressure Equations for the Metallic Elements - 298-2500 K*, Canadian Metallurgical Quarterly, **23**, 309, (1984).

[51] H. J. Metcalf and P. van der Straten, *Laser Cooling and Trapping*, Springer Verlag, (1999).

[52] W. Happer, *Optical Pumping*, Rev. Mod. Phys. **44**, 169, (1972).

[53] W. Happer, Yuan-Yu Jau, T. Walker, *Optically Pumped Atoms*, Wiley, ISBN 9783527407071, (2010).

[54] F. Atoneche, A. Kastberg, *Simplified approach for quantitative calculations of optical pumping*, Eur. J. Phys. **38**, 045703, (2017).

[55] J. J. Sakurai , Jim Napolitano, *Modern Quantum Mechanics*, 2nd Edition, Cambridge University Press, ISBN: 9781108527422, (2017).

[56] F. Bloch, *Nuclear Induction*, Physical Review. Vol. 70 (7-8),460474, (1946).

[57] C. Gardiner, *Stochastic Methods*, ISBN 978-3-540-70712-7, Springer, (2009).

[58] C. Cohen-Tannoudji, J. Dupont-Roc, and G. Grynberg, *Atom–Photon Interactions*, 1^{st} Edition, John Wiley and Sons Inc., (1998).

[59] T.O. Levante, M. Baldus, B.H. Meier, R.R. Ernst, *Molecular Physics*, **86**, 1195–1212, (1995).

[60] A. D. Bain R. S. Dumont, *Introduction to Floquet theory: The calculation of spinning sideband intensities in magic-angle spinning NMR*, Magnetic Resonance, **13**, 159–170, (2001).

[61] D. Budker, D. F. Kimball, D. P. DeMille, *Atomic Physics*, Oxford, 2nd Edition, (2008).

[62] Alexandrov, E. B., Auzinsh, M., Budker, D., Kimball, D. F., Rochester, S. M. and Yashchuk, V. V., *Dynamic effects in nonlinear magneto-optics of atoms and molecules: review*, Journal of the Optical Society of America B, **22**, 7, (2005).

[63] M. Auzinsh, R. Ferber, *Optical Polarization of Molecules*, Cambridge University Press, (1995).

[64] G. A. Sinuco-Leon, B. M. Garraway, H. Mas, S. Pandey, G. Vasilakis, V. Bolpasi, W. von Klitzing, B. Foxon, S. Jammi, K. Poulios, T. Fernholz, *Microwave spectroscopy of radio-frequency dressed Rb 87*, arXiv:1904.12073, (2019).

[65] C. J. Foot, *Atomic Physics*, Oxford University Press, Oxford, (2005).

[66] W. Demtröder, *Laser Spectroscopy* Vol. **1**, Basic Principles, Springer, (2008).

[67] D. W. Preston, *Doppler–free saturated absorption: Laser spectroscopy*, Science, **64**, 1432–1436, (1996).

[68] T. Uehara, K. Tsuji, K. Hagiwara, N. Onodera, *Optical beat-note frequency stabilization between two lasers using a radio frequency interferometer in the gigahertz frequency band*, Optical Engineering, **53(12)**, 124109, (2014).

[69] D. Budker, D. F. Kimball, *Optical Magnetometry*, Cambridge, ISBN: 9781107010352, (2013).

[70] C. E. Wieman, L. Hollberg, *Using diode lasers for atomic physics*, Phys. Sci. Inst., **62**, 1–20, (1991).

[71] C. J. Hawthorn, K. P. Weber, and R. E. Scholten, *Littrow configuration tunable external cavity diode laser with fixed direction output beam*, Phys. Sci. Inst., **72**, 4477–4479, (2001).

[72] P. H. Lissberger and W. L. Wilcock, *Properties of All-Dielectric Interference Filters. II. Filters in Parallel Beams of Light Incident Obliquely and in Convergent Beams*, J. Opt. Soc. Am. **49**, 126, (1959).

[73] X. Baillard, A. Gauguet, S. Bize, P. Lemonde, Ph. Laurent, A. Clairon, P. Rosenbusch, *Interference-filter-stabilized external-cavity diode lasers*, Optics Communications, **226**, 2, (2006).

[74] M. Scholl, *Interference fiter stabilized external cavity diode laser*, University of Toronto, (2010).

[75] M. Scholl, W. Caincross, I. Kivlichan, *Interference Filter Stabilized External-Cavity Diode Lasers*, University of Toronto, (2012).

[76] D. J. Thompson, R. E. Sholten, *Narrow linewidth tunable external cavity diode laser using wide bandwidth filter*, Rev. Sci. Inst., **83**, 023107, (2012).

[77] K. G. Libbrecht and J. L. Hall, *A low-noise high-speed diode laser current controller*, Rev. Sci. Inst., **64**, 2133, (1993).

[78] C. J. Erickson, M. Van Zijll, G. Doermann, and D. S. Durfee, *An ultrahigh stability, low-noise laser current driver with digital control*, Rev. Sci. Inst., **79**, 073107, (2008).

[79] *PCB Design Guidelines For Reduced EMI*, Texas Instruments, http://www.ti.com/lit/an/szza009/szza009.pdf, (1999).

[80] U. Rasool, *Biot-Savart Law, MATLAB Central File Exchange*, link https://www.mathworks.com/matlabcentral/fileexchange/70394-biot-savart-law, Retrieved July 12, (2019).

[81] N. Nouri, B. Plaster, *Comparison of magnetic field uniformities for discretized and finite-sized standard*, Nucl. Instrum. Methods Phys. Res. A, **723**, 30, (2013).

[82] C. P. Bidinosti, I. S. Kravchuk, M. E. Hayden, *Active shielding of cylindrical saddle-shaped coils: Application to wire-wound RF coils for very low field NMR and MRI*, Journal of Magnetic Resonance, **1771**, 1, (2005).

[83] F. Bonetto E. Anoardo M. Polello, *Saddle coils for uniform static magnetic field generation in NMR experiments*, Magnetic Resonance Engineering, **29B**, Issue 1, (2006).

[84] J. W. Carlson, *Compact transverse magnetic gradient coils and dimensioning method*, US4755755A patent.

[85] U. Tietze, Ch. Schenk, *Electronic circuits: design and applications*, p775, Springer, ISBN 978-3-540-78655-9, (2008).

[86] J.G. Ziegler, N. B. Nichols, *Optimum settings for automatic controllers*, Transactions of the ASME, **64**, 759—768, (1942).

[87] M. V. Balabas, T. Karaulanov, M. P. Ledbetter, and D.Budker, *Polarized Alkali-Metal Vapor with Minute-Long Transverse Spin-Relaxation Time*, Phys. Rev. Lett., **105**, 070801, (2010).

[88] D. Budker, W. Gawlik, D. F. Kimball, S. M. Rochester, V. V. Yashchuk, and A. Weis, *Resonant nonlinear magneto-optical effects in atoms*, Rev. Mod. Phys.,**74**, 1153, (2002).

[89] Private communication with Dave Newby from Twinleaf LLC, 31st August, (2018).

[90] A. B. Deb, A. Rakonjac, and N. Kjaergaard, *A versatile laser system for experiments with cold atomic gases*, Journal of the Optical Society of America B Vol. **29**, Issue 11, pp. 3109-3113, (2012).

[91] S. J. Seltzer and M. V. Romalis, *High-temperature alkali vapor cells with antirelaxation surface coatings*, Journal of Applied Physics, **106**, 114905, (2009).

[92] D. Budker, D. F. Kimball, S. M. Rochester, V. V. Yashchuk, and M. Zolotorev, *Sensitive magnetometry based on nonlinear magneto-optical rotation*, Phys. Rev. A **62**, 043403, (2000).

[93] S. Pustelny, A. Wojciechowski, M. Gring, M. Kotyrba, J. Zachorowski, and W. Gawlik, *Magnetometry based on nonlinear magneto-optical rotation with amplitude-modulated light*, Journal of Applied Physics, **103**, 063108, (2008).

[94] S. J. Seltzer, D. J. Michalak, M. H. Donaldson, M. V. Balabas, S. K. Barber, S. L. Bernasek, M.-A. Bouchiat, A. Hexemer, A. M. Hibberd, D. F. Jackson Kimball, C. Jaye, T. Karaulanov, F. A. Narducci, S. A. Rangwala, H. G. Robinson, A. K. Shmakov, D. L. Voronov, V. V. Yashchuk, A. Pines, and D. Budker, *Investigation of antirelaxation coatings for alkali-metal vapor cells using surface science techniques*, J. Chem. Phys. **133**, 144703, (2010).

[95] Herbert Crepaz, Li Yuan Ley and Rainer Dumke, *Cavity enhanced atomic magnetometry*, Scientific Reports volume **5**, Article number: 15448, (2015).

[96] F. Wolfgramm, A. Cerè, F. A. Beduini, A. Predojević, M. Koschorreck, and M. W. Mitchell, *Squeezed-Light Optical Magnetometry*, Phys. Rev. Lett. **105**, 053601, (2010).

[97] S. Kang, M. Gharavipour, C. Affolderbach, F. Gruet, and G. Mileti, *Demonstration of a high-performance pulsed optically pumped Rb clock based on a compact magnetron-type microwave cavity*, Journal of Applied Physics, **117**, 104510, (2015).